HZDR-030

Wissenschaftlich-Technische Berichte
HZDR-030 2013 · ISSN 2191-8708

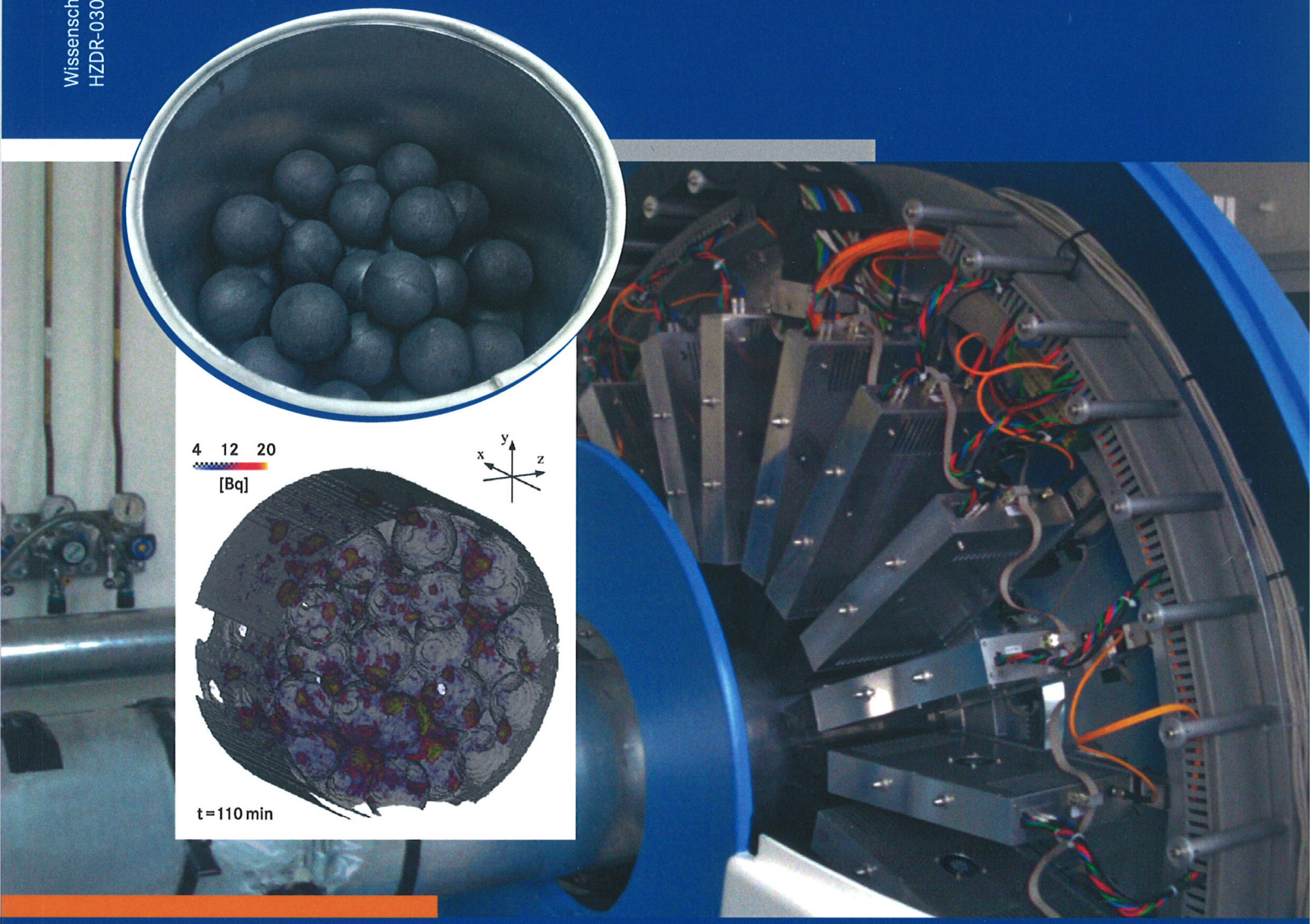

ANNUAL REPORT 2012

INSTITUTE OF RESOURCE ECOLOGY

HZDR

HELMHOLTZ
ZENTRUM DRESDEN
ROSSENDORF

Wissenschaftlich-Technische Berichte
HZDR-030

Annual Report 2012

Institute of Resource Ecology

Editor:
Dr. Vinzenz Brendler

Executive editors:
Dr. Harald Foerstendorf
Dr. Frank Bok
Dr. Anke Richter

HZDR

HELMHOLTZ
ZENTRUM DRESDEN
ROSSENDORF

Print edition: ISSN 2191-8708

Electronic edition: ISSN 2191-8716

Qucosa: http://fzd.qucosa.de/startseite/

Published by Helmholtz-Zentrum Dresden-Rossendorf e.V.

Contact

Helmholtz-Zentrum Dresden-Rossendorf e.V.
Institute of Resource Ecology

Postal Address	*Address for visitors*
P.O. Box 51 01 19	Bautzner Landstraße 400
D-01314 Dresden	D-01328 Dresden
Germany	Germany

Phone: +49 (0) 351 260 3210
Fax: +49 (0) 351 260 3553
e-mail: contact.resourceecology@hzdr.de
http://www.hzdr.de/FWO

This report is also available at http://www.hzdr.de/FWO

Cover picture

The experimental investigation of deposition and resuspension of aerosol particles is a new non-medical Positron Emission Tomography (PET) application jointly conducted by teams from the Reactive Transport Division at the Research Site Leipzig and the Experimental Thermal Fluid Dynamics Division at Dresden-Rossendorf.

The cover picture shows a test facility mounted in the ClearPET-scanner where radioactively labeled aerosol particles are dispersed. The results provide a novel spatiotemporal insight into the formation and removal of graphite particle deposits in a pebble bed and contribute to the field of nuclear safety research (for details see p. 37).

Preface

THE INSTITUTE OF RESOURCE ECOLOGY (IRE) is one of the currently eight institutes of the Helmholtz-Zentrum Dresden-Rossendorf (HZDR). The research activities are fully integrated into the program "Nuclear Safety Research" of the Helmholtz Association and focused on the topics "Safety of Nuclear Waste Disposal" and "Safety Research for Nuclear Reactors". With the integration of the division of "Reactor Safety" from the former "Institute of Safety Research" nuclear research at HZDR is now mainly concentrated within this institute.

In addition, various activities have been started investigating chemical and environmental aspects of processing and recycling of strategic metals, namely rare earth elements. Here, a knowledge transfer from the nuclear to the non-nuclear community, branching thermodynamics and spectroscopy, has been established. This also strengthens links to the recently established "Helmholtz-Institute Freiberg for Resource Technology".

The research objectives are the protection of humans and the environment from hazards caused by pollutants resulting from technical processes that produce energy and raw materials. Treating technology and ecology as a unity is the major scientific challenge in assuring the safety of technical processes and gaining their public acceptance. Namely we investigate the ecological risks exerted by radioactive and non-radioactive metals in the context of nuclear waste disposal, the production of energy in nuclear power plants and in processes along the value chain of metalliferous raw materials. A common goal is to generate better understanding about the dominating processes essential for metal mobilization and immobilization on the molecular level. This in turn enables us to assess the macroscopic phenomena, including models, codes and data for predictive calculations, which determine the transport and distribution of contaminants in the environment.

Special emphasis is put on the biological mediated transport of long-lived radionuclides and heavy metals in the geosphere and their interaction with different biota up to human organism for a better calculation of environmental and health risks as well as for the development of detoxification strategies.

Advanced knowledge is needed for description of the processes dominating at the interfaces between geo- and bio-systems related to the distribution of long-lived radionuclides in various bio-systems along the food chain.

One highlight of the year 2012 was the organization and hosting of the "International Workshop on Advanced Techniques in Actinide Spectroscopy" (ATAS) in November, attracting more than 70 contributors.

Another issue of paramount importance was the intermediate evaluation of our scientific work, initiated by the Helmholtz Association and carried out by the HZDR Scientific Advisory Board and additional international experts. Our whole team performed very well and is thus optimally positioned for the upcoming tasks. A big "Thank you" to all who contributed to this success.

More than 120 scientists, technicians, and students, working on their Ph.D., diploma, master, or bachelor thesis, were employed at the Institute of Resource Ecology in 2012. More than 30 Ph.D. students are working at the institute. Promotion of young scientists is an important requirement to ensure the competence and further scientific excellence in future times. We obtained many new scientific results in the past year, which are presented in this Annual Report, and almost 60 original papers were published in peer-reviewed international scientific journals.

I would like to thank the visitors, German and international ones, for their interest in our research and for their participation in the institute seminars. We further like to thank our scientific collaborators and the visiting scientists for coming to Dresden/Rossendorf in 2012 to share their knowledge and experience with us. We will continue to strongly encourage the collaborations and visits by scientists in the future. Special thanks are due to the Executive Board of the HZDR, the Ministry of Science and Arts of the Free State Saxony (SMWK), the Federal Ministry of Education and Research (BMBF), the Federal Ministry of Economics and Technology (BMWi), the Deutsche Forschungsgemeinschaft (DFG), the European Commission, and other organizations for their support.

Finally, I would like to express my sincerest respect to Prof. Gert Bernhard, who retired end of March last year. He was the founder of this institute 20 years ago, served it in different positions throughout the years, and is definitely the one single person that most distinctly shaped our research profile. The workshop on occasion of his 65th birthday was another impressing event in 2012.

Dr. Vinzenz Brendler
Acting director
of the Institute of Resource Ecology

Contents

SCIENTIFIC CONTRIBUTIONS

PART I: LONG-LIVED RADIONUCLIDES IN BIOLOGICAL SYSTEMS

PART II: LONG-LIVED RADIONUCLIDES IN FINAL DISPOSAL SYSTEMS

PART III: NUCLEAR REACTOR SAFETY & TRANSMUTATION

PUBLICATIONS

SCIENTIFIC ACTIVITIES

LONG-LIVED RADIONUCLIDES IN BIOLOGICAL SYSTEMS

Complex formation of U(VI) with 1,3-β-diketones in methanolic solution investigated by UV-vis spectroscopy

A. Günther, G. Bernhard

The interaction of 1,3-β-diketones with uranium(VI) in methanolic solution were investigated using different spectroscopic methods, namely UV-vis, IR spectroscopy and laser-induced methods. Up to now, only the obtained UV-vis spectra were suited for a quantitative analysis and the determination of the stability constants of formed organic uranyl complexes. In addition, the single spectra of the complex species could be obtained using analysis program HypSpec.

EXPERIMENTAL. The sample preparation was performed using the method of the continuous variation of contents of metal and ligand (Job-Plot) [1]. The total concentration of the involved reactants (uranyl perchlorate and diketone) in methanol was constant in each of 21 samples of the series. Only the concentration ratios were varied. The total concentration was 1×10^{-4} M in the case of 2,4-pentanedione (Acac) and 1-phenyl-1,3-butanedione (Phe). The substance concentration in the U(VI)/1,3-diphenyl-1,3-propanedione (DiPhe) system was 8×10^{-5} M. All experiments were performed at an ionic strength of 0.1 M ($NaClO_4$) and at a voltage of 0, 120 and 240 mV (Ag/AgCl reference system with ethanolic LiCl solution). The spectrophotometer Cary 50 Bio (Varian) and the UV-vis-NIR spectrophotometer 3600 (Shimadzu) were used for the UV-vis measurements.

RESULTS. Figure 1 shows the UV-vis spectra of a series of methanolic complex solutions in dependence of the mole fraction of DiPhe at weak basic conditions as an example. The shifts of the absorption at 250 and 342 nm as well as the detection of a new absorption band at about 395 nm demonstrate the interaction between uranium(VI) and the selected 1,3-β-diketone under the given experimental conditions.

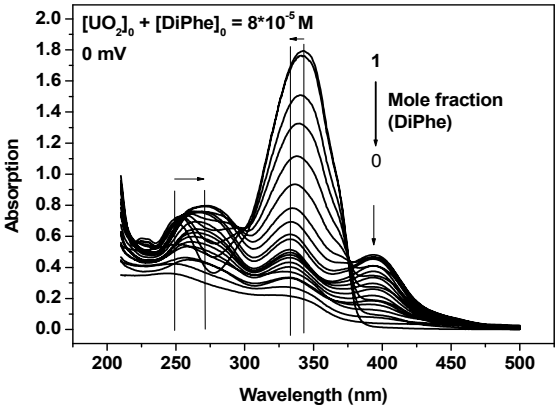

Fig. 1: UV-vis spectra of methanolic complex solutions with different U(VI) /1-Phenyl-1,3-butadione (DiPhe) concentration ratios (Job-Plot).

The composition of the formed complex species (number of the ligand molecules b) and the corresponding complex formation constant K_b could be calculated by analysis of the different Job-Plots (example in Fig. 2). In all investigated systems we found a 1 : 1 uranyl complex at 240 mV (weak acidic conditions). At lower voltage up to 0 mV (weak basic conditions) we could determine 1 : 2 U(VI) complexes with the selected 1,3-β-diketones. Comparable

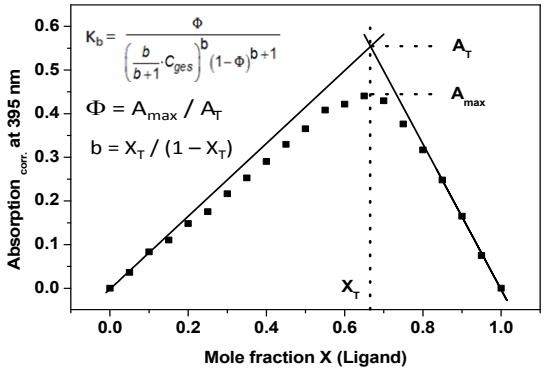

Fig. 2: Job-Plot analysis of measured spectra from Figure 1.

Tab. 1: Formation constants of uranyl complexes with 1,3-β-diketones in methanolic solution at the voltage range between 0 and 240 mV (Job-Plot analysis and HypSpec).

1,3-β-diketone (L)	UO_2+L→UO_2L	UO_2+2L→UO_2L_2
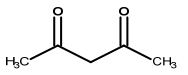	4.67 ± 0.04	9.65 ± 0.07
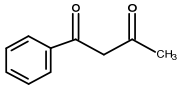	5.15 ± 0.03	10.08 ± 0.02
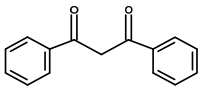	5.48 ± 0.01	10.46 ± 0.01

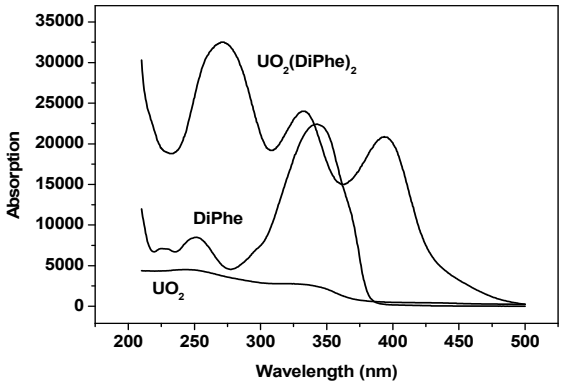

Fig. 3: Molar single component spectra of U(VI) and corresponding complex species calculated by HypSpec.

results could be obtained by applying the factor analysis program HypSpec [2]. The weighted averages of the constants are summarized in Table 1. The formed complexes are more stable if the number of aromatic phenyl rings in the diketone molecule is higher.
Figure 3 shows the corresponding single component spectra of the selected example from Fig. 1 as another result of the factor analysis.

ACKNOWLEDGEMENTS. This work was supported by the Federal Ministry of Education and Research under the contract number 02NUK014B.

[1] Job, P. (1928) *Ann. Chim. Appl.* **9**, 113–203.
[2] Gans, P. et al. (2008) *Protonic Software*, Leeds, U.K.

Interaction of U(VI) and Eu(III) with Schiff Bases investigated by laser-induced spectroscopic methods in methanol

K. Lindner, A. Günther, G. Bernhard

We investigated the complexation behavior of U(VI) and Eu(III) with Schiff Bases by time-resolved laser-induced fluorescence spectroscopy (TRLFS). The formed complexes show no significant fluorescence signal in methanolic solution.

The development of new supramolecular complexing agents with N, O, S donor function is important to selectively separate d- and f-elements and to enrich rare earth elements. Schiff Bases are essential basic components of these new organic ligands. The investigated Schiff Bases are shown in Fig. 1.

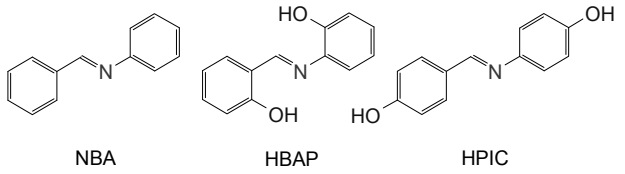

Fig. 1: Structure of the used Schiff Bases: N-benzylidenaniline (NBA), 2-(2-Hydroxybenzylidenamino)-phenol (HBAP), Alpha- (4-hydroxyphenylimino)-p-cresol (HPIC).

EXPERIMENTAL. As methanol strongly quenches the luminescence of U(VI), the TRLFS experiments were carried out at low temperatures (−120 °C). The U(VI) concentration was fixed at 50 µM and the Schiff Base concentration was varied between 0 and 0.1 mM. The TRLFS spectra of U(VI) were recorded using Nd : YAG laser system (Minilite laser, Continuum, USA) with an excitation wavelength at 266 nm and an averaged pulse energy of 300 µJ. The TRLFS measurements for Eu(III) were performed under room temperature and at a fixed metal concentration at 10 µM. The Schiff Base concentration was varied between 0 and 0.25 mM. The luminescence of the Eu(III) was measured with a Nd : YAG-OPO laser system (Powerlite Precision II 9020 laser equipped with a Green PANTHER EX OPO from Continuum, Santa Clara, U.S.A.) with a laser pulse at 394 nm and an averaged pulse energy of 3 mJ. Further details about the laser system can be found in [1]. All samples were prepared in methanol at 0, 120 and 240 mV (Ag/AgCl reference system with ethanolic LiCl solution) and 0.1 M $NaClO_4$ was used as background electrolyte. In the following only the results for the ligand HPIC at 240 mV are represented.

RESULTS. Figure 1 shows the luminescence spectra of U(VI) as function of the total HPIC concentration in methanol at −120 °C. The intensity of U(VI) luminescence decrease with increasing HPIC concentration, but no shifts of the emission bands were detected. From TRLFS results, we conclude that the formed U(VI)/HPIC complex shows no appropriate fluorescence signal under the given experimental conditions. At this time, the time-resolved spectra are not reliable evaluated because of the high background noise.

The luminescence spectra of Eu(III) in water and methanol are depicted in Fig. 3A. The intensity of the hypersensitive $^5D_0$-$^7F_2$ transition (at 616 nm) increases strongly with the transition from water to methanol. The appearance of the symmetry-forbidden $^5D_0$-$^7F_0$ transition (at 578.6 nm) in methanol shows that the Eu(III)-methanol

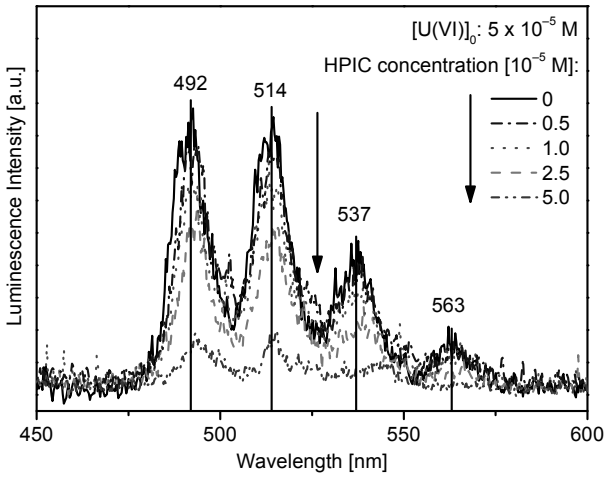

Fig. 2: Luminescence spectra of U(VI) with HPIC at 240 mV.

complex is asymmetrical. The time-resolved fluorescence decay of Eu(III) in water is mono-exponential with a lifetime of 107 µs. The lifetime of the aqua ion corresponds to nine water molecules in the first hydration shell of Eu(III) [2]. The luminescence lifetime in methanol is prolonged to 266 µs. A similar lifetime (267 µs) was found by Billard [3].

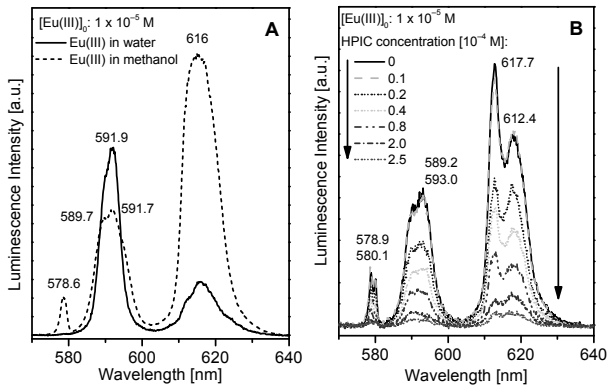

Fig. 3: Luminescence spectra of Eu(III) in water and methanol (A) and as function of the HPIC concentration at 240 mV (B).

After addition of HPIC to the Eu(III) methanolic solution (see Fig. 3B), the intensity decreases. It is noteworthy that the chemically inert $^5D_0$-$^7F_1$ transition (at 591.9 nm) is considerably degraded. Furthermore, there is a splitting of the peaks indicating the presence of two species in solution. The lifetime is reduced to 213 µs after HPIC addition.

ACKNOWLEDGEMENTS. This work was supported by the Federal Ministry of Education and Research under contact number 02NUC014B.

[1] Moll, H. et al. (2008) *Biometals* **21**, 219–228.
[2] Kimura, T. et al. (1996) *Radiochim. Acta* **72**, 61–64.
[3] Billard, I. (2003) *Handbook on the Physics and Chemistry of Rare Earths* **33**, 465–514.

Complexation and photoreactivity of U(VI) with the natural flavonoid quercetin

E. Attia, S. Tsushima, K. Fahmy

Quercetin is a ubiquitous natural UV-absorbing polyphenolic plant pigment present in fruit and vegetable. As it is part of the daily diet and at the same time capable of chelating a variety of transition metals. Here, we have studied its interaction with U(VI). Quercetin provides not only act as a ligand but may also affect the redox state of Uranium through photochemical processes which are of radioecological importance, related to the abundance of flavonoids in sunexposed soils. In this work, UV-visible spectroscopy has been used to explore the complexation of U(VI) with quercetin in aqueous and non-aqueous states.

EXPRIMENTAL. Absorption spectra of quercetin (3,3',4',5,7-pentahydroxyflavone) were determined at 2.1×10^{-5} M concentration with a Cary spectrophotometer at 2 nm bandwidth. The measurements were performed in a quartz cuvette with an optical path length of 10 mm at ambient temperature. ATR-FTIR spectra were recorded with a Vector22 (Bruker) and photoreactivity induced with a Xe-lamp (Rapp, OptoElectronic).

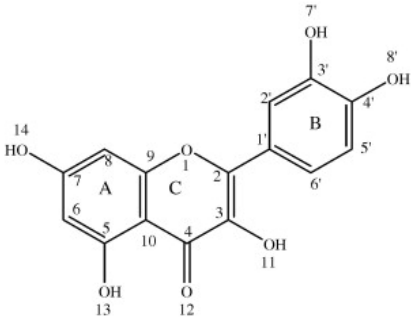

Fig. 1: Molecular structure and chemical numbering of quercetin.

RESULTS. The changes in UV-vis absorption of quercetin in the presence of increasing concentrations of U(VI) were measured in acetone (Fig. 2.A). Quercetin shows absorption maxima at 369 nm (band I) and 251 nm (band II). Band I is related to ring B (cinnamoyl system) and band II to ring A (benzoyl system) (Fig. 1) [1]. The intensity of the 369 nm band decreased gradually with addition of U(VI), and new absorption peaks arised at 431 and ~495 nm indicating complex formation (with isosbestic points at 344 and 385 nm). Second derivative spectra show that there is an additional effect on a narrow absorption line at 347 nm which we assign to a transition in U(VI) which is affected by complexation with quercetin (Fig. 1 inset). The 3- and 5-hydroxyls and the 4-carbonyl are prime candidates for coordinating U(VI). By analogy to other complexes, the peak at 431 nm suggests that U(VI) binds at the 3-OH and 4-carbonyl of ring C [2]. This agrees with a large number of experimental data on metal complexes that involve the same groups and particularly the 3-OH exhibits greater chelation power and larger effect on Π electron delocalization, thus mediating the red shift of the UV-vis absorption [3, 4] as seen here also with U(VI). The coordination of U(VI) with the 4-keto group is supported by FT-IR spectra. Based on DFT calculations (not shown) intensity in the 1620–1590 cm^{-1} range (Fig. 3A) is assigned to the 4-keto C=O stretching mode. In agreement with DFT calculations, it shifts down by upon U(VI) binding to ~1530 cm^{-1} (Fig. 3B, arrow)

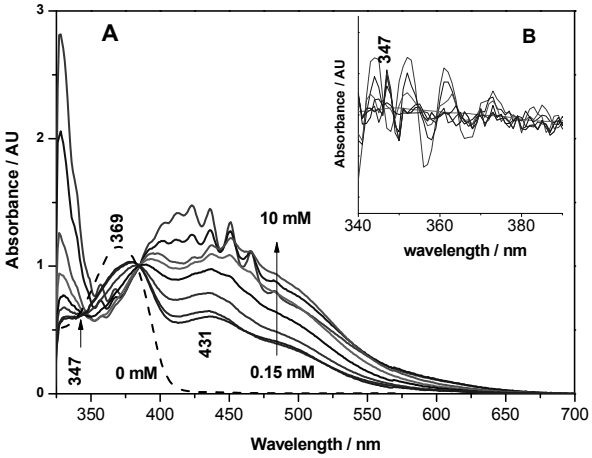

Fig. 2: (A) Absorption spectra of quercetin (21 μM) in the presence of U(VI) (at 0, 5, 2.5, 1.25, 0.625, 0.3125, 0.156 mM) corresponding to the curves from 1 to 8. (B) The second derivative spectra indicate identify the overlaying U(VI) peaks showing an affect of quercetin on a uranyl transition at 347 nm.

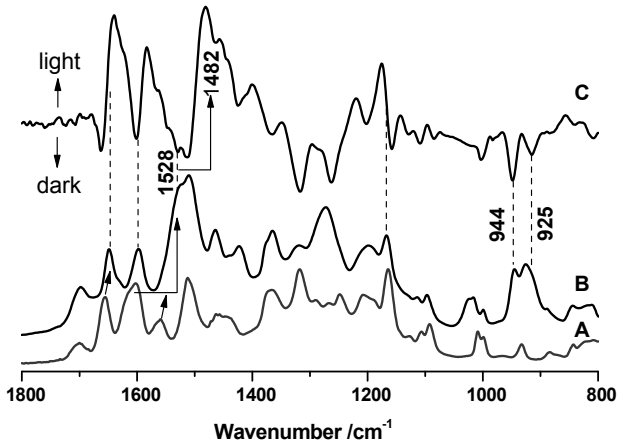

Fig. 3: (A) FT-IR spectra of a quercetin film dried from acetone solution. (B) equivalent film in the presence of U(VI) nitrate (1 : 1 ratio). (C) UV-light-induced difference spectrum of the quercetin-U(VI) complex. Light-induced vibrational features are positive, absorption bands of the initial state negative.

supporting the proposed binding site. We have addressed the photoreactivity of the complex by measuring light-induced FT-IR difference spectra. Illumination causes stable vibrational frequency changes (Fig. 3C), evidencing a U(VI)-dependent chemical reactivity. The salient light dependent change is a further down shift in the 1530 to 1480 cm^{-1} range (Fig. 3C, arrow). Remarkably, the IR absorption of U(VI) at 950–920 cm^{-1} is partially bleached, indicative of a light-driven photoreduction of U(VI) in dry films of the complex.

[1] Kang, J.W. et al. (2004) *Biochim. Biophys. Acta* **1674**, 205–214.
[2] Kang, J.W. et al. (2004) *J. Inorg. Biochem.* **98**, 79–86.
[3] Boudet, A.C. et al. (2000) *Spectrochim. Acta A* **56**, 829–839.
[4] Zhang, G. et al. (2010) *Sensors and Actuators B* **144**, 239–246.

Photocatalytic decomposition of diclofenac by platinum/palladium doped ZnO

C. Bobeth, S. Matys, M. Vogel, J. Raff

ZnO-nanoparticles immobilized on S-layer coated stainless steel were doped with platinum and/or palladium to improve the photocatalytic efficiency. The photocatalytic activity of the created biocomposite materials was tested by decomposition of the pharmaceutical diclofenac (DCF).

Although water treatment technology in Germany is leading, there are some toxic and not biodegradable chemicals, especially pharmaceuticals which are widely distributed in surface water [1]. To eliminate such substances from waste water, photocatalysis is gaining on importance. The photocatlaytic decomposition is based on the formation of hydroxyl radicals. For this ZnO or TiO_2 are well known as sensitive photocatalysts with a large band gap. However, usually UV radiation is needed as energy source. To expand the photoresponse of photocatalysts to visible light region the semiconductor can be doped with precious metals. Furthermore, for water treatment it is necessary to immobilize the catalyst. In this work the ZnO particles were immobilized on stainless steel plates by surface layer proteins and doped with platinum and/or palladium. The produced biocomposites were firstly tested for decomposition of diclofenac (DCF) during irradiation with UV light.

EXPERIMENTAL. Stainless steel plates with a diameter of 5 cm were used as carriers for the biocomposite materials. The surface of the plates was cleaned with isopropanol and modified with three alternating layers of the polyelectrolytes (PE) polyethyleneimine and polystyrenesulfonate by layer-by-layer techniques [2]. S-layer proteins were isolated from Bacillus sp. JG-B53 [3] and recrystallized within 24 h on the PE-coated carriers using 0.3 mg/mL S-layer proteins in 1.5 mM Tris, 10 mM $CaCl_2$ at pH 8. For immobilization of ZnO particles, the activated plates were incubated in 20 mM $Zn(NO_3)_2(H_2O)_6$, 30 mM Tris-buffer at pH 8 for 4 h at room temperature [4]. The last step was repeated three times. The photocatalysts were calcinated at 300 °C for 24 h. For the chemical deposition of platinum and palladium particles, the plates were shaken in 8 mL 24 h old 0.05 mM Na_2PdCl_4 and 0.05 mM K_2PtCl_4 (80/20) for 9.5 h and reduced with 100 µM $NaBH_4$ for 24 h. Photocatalyst doping by sputtering was realized by a Pt/Pd template (80/20) with a layer thickness of 0.2–0.3 nm. For the third method of doping, separately synthesized nanoparticle-solutions [5] were used by incubating the plates in the solutions for 4 h at room temperature. Finally, the coated plates were shaken with 5 mL 0.1 mM DCF in culture dishes and treated with 5 W/m² light at a wavelength of 365 nm. Before treating with UV light, the plates were incubated in the dark for 30 min. The DCF decomposition was analyzed by HPLC according to [6].

RESULTS. The experiments showed that the model pharmaceutical DCF was totally degraded by three of four tested Pt/Pd doped carriers after 6 h, whereas a residual concentration of 15% DCF was detected for the carrier material with Pt/Pd doping by chemical deposition. The latter is only slightly more efficient than the reference without doping which showed a residual DCF concentration of 20%. The fastest decomposition result could be realized with photocatalyst doped by sputtering. Already after 3 h, more than 90% of DCF was degraded. There is no significant difference between the tested sputtering times. Finally, the doped ZnO-carriers show a higher catalytically efficiency to degrade DCF as without Pt/Pd. The amount of immobilized Pt/Pd differs in dependence of the used method (data not shown). To separate degradation from sorption at the beginning, the plates were shaken without light for 30 min. All biocomposites show a low sorption affinity of DCF. Finally, the decreasing of DCF complies with the degradation of the pharmaceutical.

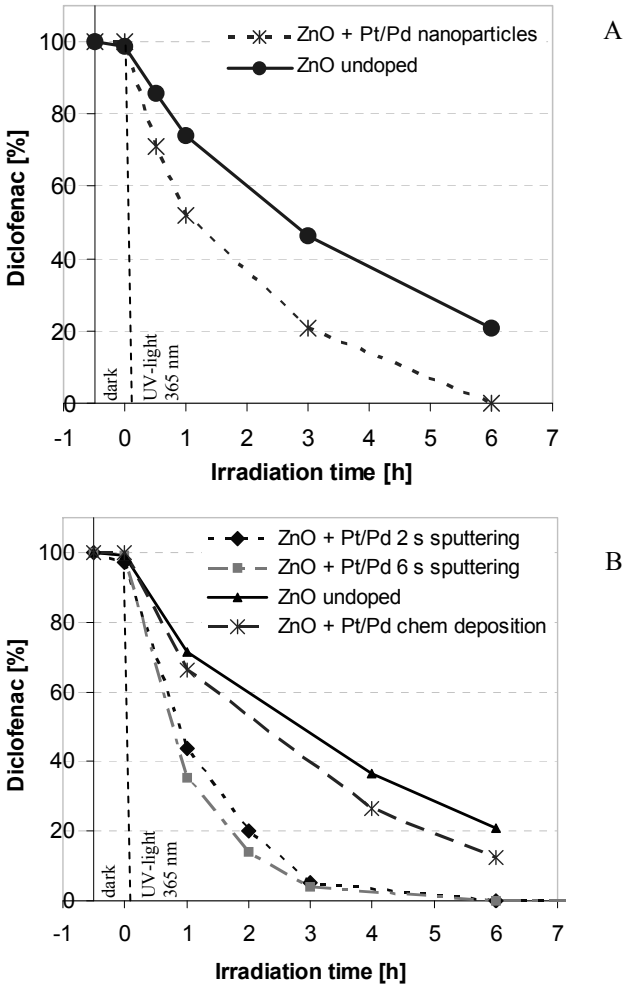

Fig. 1: Decomposition of DCF by Pt/Pd doped ZnO-nanoparticles immobilized on S-layer-coated carriers under UV-irradiation with nanoparticle solutions (A) and by sputtering or chemical deposition (B).

CONCLUSIONS. Experiments have demonstrated the higher decomposition efficiency of doped catalysts under UV irradiation. As next step the photocatalytic activity under day light will be investigated.

[1] Kümmerer, K. (2009) *Chemosphere*. **75**, 417–434.
[2] Decher, G. et al. (1997) *Science* **277**, 1232–1237.
[3] Raff, J. et al. (2003) *Chem. Mater.* **15**, 240–244.
[4] Bauermann, L.P. et al. (2007*) Int. J. Mat. Res.* **98**, 879.
[5] Bigall, N.-C. (2009) Ph.D. Theses, Technische Universität Dresden, Dresden, Germany.
[6] Pollmann, K. et al. (2009) *Report FZD-511*, p. 24.

A biochemical approach to single particle X-FEL studies on membrane proteins

J. Oertel, A. Keller,[1] S. Weiß, F. Stellato,[2] A. Barty,[2] K. Fahmy

[1]Institute of Ion Beam Physics and Materials Research, Helmholtz-Zentrum Dresden-Rossendorf, Dresden, Germany; [2]Center for Free Electron Laser Science, DESY, Hamburg, Germany

The development of a technology that allows resolving structural transitions in single membrane proteins by the use of ultra-short X-ray pulses from X-ray free electron lasers (X-FELs) will represent a significant advance in studies of membrane protein structure and dynamics. The successful use of X-FEL radiation for Structural Biology has been proven for nanocrystals [1]. In contrast, the potential for a fully crystallization-independent analysis of large protein structures at the single molecule level has not been explored experimentally.

Membrane proteins are vital for making cells responsive to environmental stimuli as well as in controlling the exchange of ions between the cytoplasm and the extracellular space. Both processes depend on proteins containing multiple transmembrane helices that rearrange during function. Engineered phospholipid nanodiscs (NDs), which are lipid-protein complexes surrounded by a helical protein belt of two membrane scaffold proteins (MSPs) provide a completely soluble nanoscale section of a lipid bilayer designed for functional investigations of membrane proteins. A single ND consists of approximately 120 phospholipid molecules and has a diameter and thickness of about 10 nm and 5.5 nm, respectively [2]. Exploring their suitability for single particle X-ray diffraction will have a strong impact on X-FEL applications in Structural Biology, particular for the crystallization-independent structure determination of membrane proteins. Here, we are interested in the mechanism of metal-transporting ATP-ases. These membrane proteins confer metal resistance to microorganisms. Their efficiency is critical for the ecology of microorganisms at mining sites and for their potential use in biotechnological processes for recovering metallic resources. Sufficiently high concentrations of NDs have been obtained for preliminary X-ray diffraction experiments and reconstitution of an expressed functional Copper-ATPase is underway.

EXPERIMENTAL. NDs are formed by a self-assembly process, initiated by solubilization of lipids into a detergent containing micellar solution, mixing with MSP at the gel-liquid crystalline phase transition temperature and subsequent removal of the surfactant (Fig. 1). Specifically, DMPC (Avanti) or DPPE Nanogold lipids (Nanoprobes) were solubilized in cholate buffer (25 mM ammonium acetate, cholate : lipid = 2 : 1). The respective lipid/sodium cholate solution and MSP1 were mixed to give final concentrations of 6 mM lipid and 0.1 mM MSP1. The mixture was incubated for 1 h at 25 °C. The detergent was removed by Detergent Removal spin columns (Pierce).

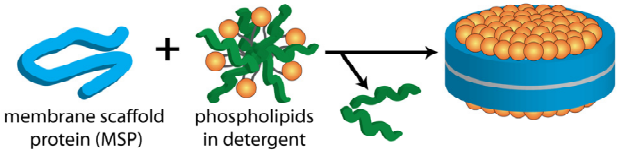

Fig. 1: Formation of Nanodisc initiated by mixing of MSP with detergent solubilized phospholipids followed by detergent removal.

Native MSP protein structure was confirmed by CD-spectroscopy, the expected 10 nm particle size was verified by AFM-Microscopy and further confirmed by Dynamic Light Scattering (DLS) and TEM.

RESULTS. To demonstrate the adaptability of the ND-technology as a platform for single particle X-FEL analysis, NDs were first characterized by spectroscopic and microscopic methods (Fig. 2A–D). From these samples preliminary X-FEL diffraction data have been obtained. Preliminary experiments carried out at the CXI beam line at LCLS at SLAC in 2012 July using gold-labeled NDs devoid of a membrane protein have revealed diffraction patterns of the ~ 10 nm-sized particles when injected as a liquid jet into the X-FEL beam (Fig. 2E).

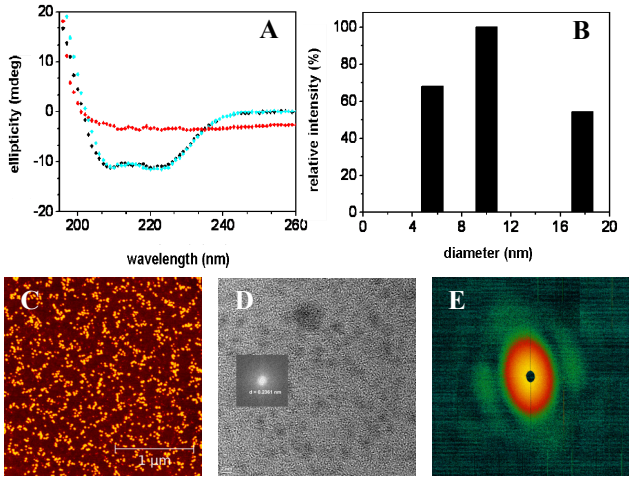

Fig. 2: (A) CD spectra of MSP and Nanodiscs. Black: pure MSP, cyan: MSP signal after formation of NDs, red: magnetic CD signal of the DMPC lipid moiety. (B) Size distribution of Nanodiscs according to DLS data, indicating the main ND-fraction with diameter size of 10 nm. (C) AFM topography image of Nanodiscs. (D) TEM characterization of gold-labeled NDs. Disks were unstained and are not visible in this preparation. (E) Low resolution X-FEL diffraction from NDs containing gold-labeled lipids. The pattern was obtained with 4 mJ pulses at 1.2 keV energy, focused to a 3 µm diameter spot in an experiment at the AMO beamline.

Studies of heterogeneity in crystals suffer from superimposed electron densities (when differences are not at unit cell contacts), or impose artificial state selection (when changes are at the unit cell contacts). Adopting a single-particle approach frees us from these limitations.
Future work will include the characterization by Grazing Incidence Small Angle X-ray Scattering (GISAXS) of oriented NDs. These data will guide the evaluation of later X-FEL-based diffraction data, particularly when obtained with magnetic alignment. Based on the known structure of reference proteins we will be able to proof the validity of a general bioinorganic platform for crystal-free membrane protein structure determination.

[1] Schlichting, I. et al. (2012) *Curr. Opin. Struc. Biol.* **22**, 613–626.
[2] Bayburt, T.H. *et al.* (2010) *FEBS Lett.* **584**, 1721–1727.

Investigations on the stability of S-layer proteins towards OH-radicals by means of diamond electrode

S. Matys, M. Vogel, C. Bobeth, T. Dittmar,[1] C. Schmoock,[1] J. Raff
[1]Institute of Water Chemistry, Technische Universität Dresden, Dresden, Germany

The structural stability of bacterial S-layers towards OH-radicals was investigated with respect to their application as support for photocatalytically active nanoparticles. SDS-PAGE and fluorescence spectroscopy proved the intermolecular crosslinking of the proteins and their high structural stability.

S-layer proteins serve as an excellent template for fixation or generation of defined photocatalytically active nanoparticles such as ZnO or TiO_2 which are suitable for the decomposition of persistent organic residues in waste water [1]. These oxides evolve under UV irradiation or even under day light reactive oxygen species (ROS) [2]. To get information about the stability of S-layer proteins under attack of ROS, suspensions of JG-B 62 have been exposed to diamond electrodes (DE) which are composed of metallic or semiconducting base materials covered with polycrystalline diamond with a thickness in the micrometer scale. The electrical conductivity will be provided by doping with boron [3]. In contrast to other commercial electrodes, DE generate the highest known overpotential for the evolution of oxygen and hydrogen from water. In comparison to photocatalytically active materials, the amount of ROS evolved by DE is at least thousandfold enhanced. Using this measurement setup, the degree of structural changes of the S-layer protein in relation to the amount of evolved radicals has been determined.

EXPERIMENTAL. Lyophilized S-layer protein of the *Lysinibacillus* isolate JG-B 62 was dissolved in 8 M urea and dialyzed against seralpur water for 24 hours at 4 °C. The concentration was adjusted to 0.56 mg/mL immediately before the experiment. As a reference bovine serum albumin of the same concentration was chosen. Both suspensions were adjusted to 16 mS/m conductivity with solid $NaNO_3$. Five mL of the protein suspension were filled into the electrolysis cell with opened fittings for the collection of the emerging protein foam and subjected to an electrical current of 0.5 A (galvanostatic mode). The observed voltage during the experiment was around 6 V. At fixed intervals, the cell was poured out and the protein containing samples checked by SDS gel electrophoresis. After each measurement the cell was rinsed thoroughly with water.

RESULTS. During the measurements a remarkable amount of protein foam expelled trough the fittings leading to reduced volumes of resting protein suspension in the electrolysis cell in dependence on the reaction time (data not shown). The SDS-PAGE revealed that the protein underwent a crosslink by the evolved radicals as indicated by additional occurring bands on the top of the gel (Fig. 1). Samples derived from the resting solution in the electrolysis cell appeared of intact size but with lower intensity in the gel. This could be attributed to a loss of protein in the cell due to the foam evolution and was evaluated by the estimation of the protein concentration (not shown). Additionally, fluorescence spectroscopic measurements (see Fig. 2A and B) proved the intermolecular protein crosslinking by showing the characteristic fluorescence peak of

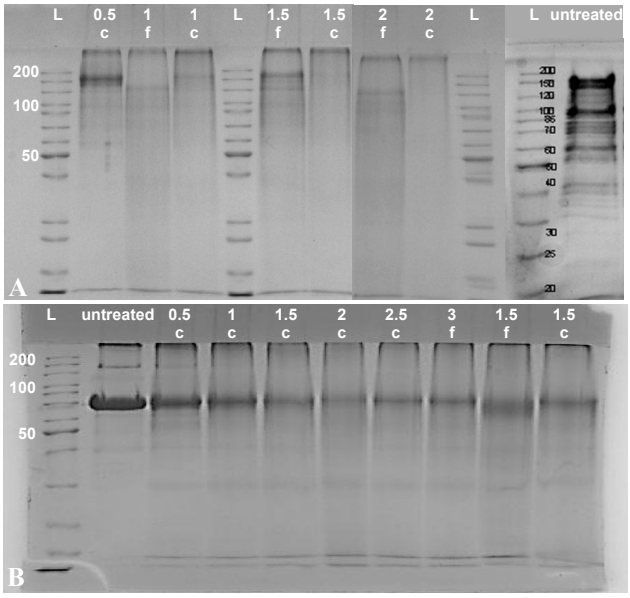

Fig. 1: SDS-PAGE of S-layer protein JG-B 62 (A) and bovine serum albumin (BSA) (B) after treatment with diamond electrode. The given numbers indicate time intervals in minutes; f = foam; c = chamber.

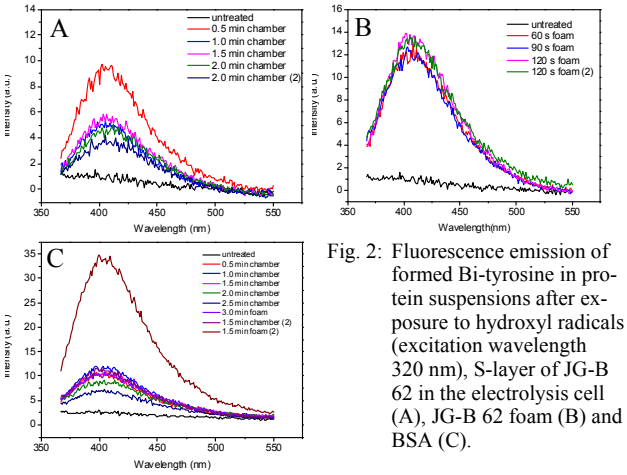

Fig. 2: Fluorescence emission of formed Bi-tyrosine in protein suspensions after exposure to hydroxyl radicals (excitation wavelength 320 nm), S-layer of JG-B 62 in the electrolysis cell (A), JG-B 62 foam (B) and BSA (C).

Bi-tyrosine at 406 nm. Similar effects could be detected for the reference protein BSA, as shown in Fig. 2C. However, the SDS-PAGE revealed for BSA a protein band at 10 kDa which relates to partially occurring decomposition processes and which was not observed for the S-layer protein.

Diamond electrodes are well suited for stability investigations of protein solutions while exposure to ROS. The S-layer protein JG-B 62 was crosslinked and stabilized as evidenced by tyrosine dimerization. In contrast, BSA underwent partial decomposition processes as revealed by SDS-PAGE.

ACKNOWLEDGEMENTS. This work was supported by the Federal Ministry of Education and Research (BMBF 03X0094G).

[1] Vogel, M. et al. (2012) *HZDR Report-013*, p. 25.
[2] Pollmann, K. et al. (2011) *HZDR-Report-001*, p. 25.
[3] Rehman, S. et al. (2009) *J. Hazard. Mater.* **170**, 560 –569.
[4] Kraft, A. (2007) *Int. J. Electrochem. Sci*. **2**, 355–385.

Heterologous expression of Calmodulin in *E. coli* for interaction studies of actinides with Ca-binding proteins

B. Drobot, H. Moll, J. Raff

Calmodulin (CaM) is a ubiquitous protein of the calcium dependent signal cascade. Regulated by calcium binding CaM can interact with more than 300 intercellular interaction partners. Therefore, CaM is a possible target for all calcium analogue elements including also trivalent actinides.

In 1970, Cheung et al. discovered a calcium depending activator of the phosphodiesterase [1]. Due to its calcium depending properties it was named Calmodulin (CALcium MODULated proteIN). This 149 amino acid containing protein appears in all higher organisms and it is highly conserved in the vertebrates. The binding motif of CaM is a so called EF-hand. CaM consists of two domains with two EF-hands, respectively.
In addition to calcium, CaM has also a high affinity to other bi- and trivalent cations [2]. It is thought that the toxicity of some metal ions is caused by their opportunity to activate CaM [3].
Actinides are harmful in two different aspects, that is radiotoxicity and chemotoxicity. CaM is a potential target for actinide ions. Therefore, it is necessary to understand the actinide-CaM-interaction to estimate the risk of actinide exposure. The present study describes the establishment of a reliable method to produce large amounts of CaM and is part of a general study on the interaction of trivalent actinides with Ca-binding proteins.

EXPERIMENTAL. A plasmid containing the Calmodulin gene (pET 23d, Novagen) was transformed in *E. coli* (BL21(DE3)pLysS, Novagen). 200 µL cell culture were thawed on ice for 10 min and 2 µL plasmid was added. Subsequently the cells were heated for 30 s at 42 °C and immediately placed on ice for 2 min. 150 µL preheated (37 °C) SOC-Medium was added. The cells were incubated at 37 °C at 300 rpm. Cells were plated out on agar containing 34 and 100 µg/mL Chloramphenicol and Ampicilin, respectively. Single colonies were transferred in LB medium and cryostocks were prepared.
For the heterologous expression, an overnight culture was prepared in 25 mL LB medium with antibiotics. The culture was transferred in 375 mL LB medium. At an OD_{600} of 0.5 the overexpression was induced with IPTG (1 mM). After 6 h the culture was harvested by centrifugation (20 min, at 6000 g).
CaM was purified as described previously [4] with minor modifications. The pellet was resolved in buffer (20 mL 50 mM TRIS pH 7.5) and freeze-thawed three times with additional sonification. The suspension was heated for 5 min up to 70 °C. After centrifugation (1 h at 40,000 g), the pellet was discarded. 2.5 M ammonium sulfate was added and the suspension was centrifuged (10 min at 12,500 g). The supernatant was saturated with ammonium sulfate and centrifuged (10 min at 12,500 g). The pellet was resolved in buffer (40 mL 50 mM TRIS, 200 mM ammonium sulfate, 1 mM EDTA at pH 7.5).
An FPLC was used for further purification. A Phenyl-Sepharose column pre-equilibrated with buffer was loaded with the sample. The flow-through was collected. The column was washed and preequilibrated with buffer (50 mM TRIS, 200 mM ammonium sulfate, 2 mM calcium chloride at pH 7.5). Calcium chloride (2.5 mM) was added to the sample. The sample was loaded onto the column. After washing the column with the same buffer CaM was eluted with a further buffer (50 mM TRIS, 1 M NaCl, 2.5 mM EGTA). Fractions with high absorbance at 280 nm were collected.
To remove calcium and EGTA from the sample, it was ultrafiltrated eight times (Vivaspin 20 VS2052 with an MWCO of 3000 Da) and diluted with calcium free buffer.

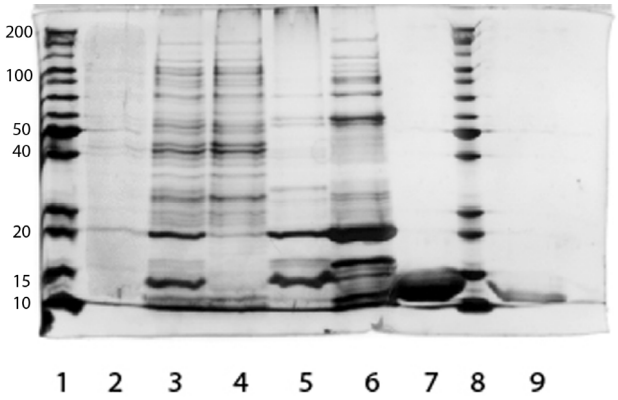

Fig. 1: SDS gel CaM purification: marker (1), uninduced cells (2), cells induced for 6 h (3), pellet after thermal denaturation (4), supernatant after thermal denaturation (5), pellet after salting out with 2.5 M ammonium sulphate (6), CaM purified with FPLC (7), marker (8), CaM purchased from Sigma-Aldrich (9).

RESULTS. The transformation of *E. coli* cells grew on agar with antibiotics, indicating a successful transformation. The purification was documented by SDS-Page and silver staining. As can be seen from Fig. 1, Calmodulin can be effectively overexpressed and purified.
FPLC is a useful tool to optimize the purification. The yield of CaM from 400 mL cell culture is about 80 mg.

ACKNOWLEDGEMENTS. We like to thank Dr. Neal Waxham for kindly supplied me the CaM plasmid.

[1] Cheung, W.Y. et al. (1970) *Biochem. Biophys. Res. Commun.* **38**, 533–538.
[2] Ouyang, H. et al. (1998) *Biometals* **11**, 213–222.
[3] Kursula, P. et al. (2007) *Acta Crystallogr. Sect. F Struct. Biol. Cryst. Commun.* **63**, 653–656.
[4] Park, H.Y. et al. (2008) *Proc. Natl. Acad. Sci. U.S.A.* **105**, 542–547.

Isolation, characterization and biosorption of heavy metals with membrane lipids of *Lysinibacillus* sp. JG-B53

M. Suhr, J. Raff, K. Pollmann[1]

[1]Helmholtz-Zentrum Dresden-Rossendorf, Helmholtz Institute Freiberg for Resource Technology, Dresden, Germany

The investigation of interactions of distinct cell wall components like surface layer, peptidoglycan, membrane lipids and secondary cell wall polymers (SCWP) with heavy metals is challenging. The metal interaction with the biosphere is important not only from an ecological point of view but also from an application oriented one. Experiments with surface-layer (S-layer) proteins showed a high metal binding capacity [1]. In this study, the focus is set to membrane lipids their isolation, characterization, and the sorption behavior.

EXPERIMENTAL. Exponential growth phase cells [2] of *Lysinibacillus* sp. JG-B53 were used for the isolation procedure. The wet biomass (160 g) was washed twice with buffer. After removal of flagella, the cells were disrupted under high pressure (1000 bar). The lipids were isolated with a combined and adapted method of solvent extraction and mechanical-biochemical process [3, 4].
The reddish pellet obtained by centrifugation was suspended by ultrasonic, washed 4 times with ultra-pure water, and the crude lipids were obtained by ultracentrifugation steps. For protein digest, Proteinase K was added and incubated for 24 h at 4 °C. The crude extract was washed 4 times with ultra-pure water and by means of long term ultracentrifugation. The pellet was dissolved in a mixture of chloroform, methanol and water, and the lipids were transferred to organic phase. After filtration and removal of $CHCl_3$, the purified lipids were lyophilized for characterization. The membrane lipids were characterized by thin layer chromatography (TLC-silica plates with fluorescence indicator, eluent: $CHCl_3/CH_3OH/H_2O$) and GC-FID. For the GC analysis it was necessary to crack the lipids, derivatize with methanolic boron trifluoride and to transfer the derivates into an n-hexane phase. The sorption experiments were done in batch mode. Lipids were dissolved in a concentration of 0.5 g/L, the metal salt solution (Au, Pb or Pd) was added to an final concentration of 1 mM and incubated for 48 h. The metal concentration was analyzed by ICP-MS.

RESULTS. Different extraction procedures where combined for the best quantitative and qualitative isolation of membrane lipids from JG-B53. The yield was 3.1% (see ref. [5]: 4%) of the dry biomass. The SDS-PAGE picture shows the extract after protein removal (Fig. 1a).
For TLC, model substances with different polar head groups e.g. phosphatidylcholine (PC), -ethanolamine (PE) were used to indicate the functional hydrophilic groups of the lipids by using ninhydrin solution. TLC indicates PC as the dominating species with a retention factor (R_f) of 0.6 (Fig. 1b). The fatty acid profile of the lipids was determined by gas chromatography (Tab. 1). It could be shown that 4 saturated fatty acids from C-14 to C-16 dominate the lipid content. Only one unsaturated fatty acid, the *cis*-9-Octadecenoic acid, is present with ~ 0.5%.
The sorption experiments (Fig. 2) show a fast metal binding to the lipids within the first 10 minutes at high amount, presumably through interaction with hydrophilic phosphatidyl groups and carbonyl groups. For palladium and gold, the sorption maximum is reached after 4–6 h. The sorption of Pb increased until 24 h. Further incubation with Pd and Au shows a stable metal binding up to 48 h.

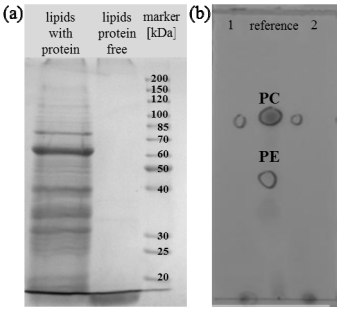

Fig. 1: (a) SDS-PAGE picture, (b) TLC picture of purified lipids.

Tab. 1: Fatty acid profile of membrane lipids of JG-B53 measured by GC-FID (isolation batch no. 1–3).

No.	Fatty acid ratio [%]								
	14:0	**15:0 iso**	**15:0 ante-iso**	**16:0 iso**	**16:0**	**17:0 ante-iso**	**18:0**	**18:1 *cis* d9**	∑
1	30.43	17.64	0.19	17.91	27.48	5.13	0.68	0.53	100
2	30.49	17.85	0.74	17.06	27.77	5.06	0.67	0.36	100
3	30.30	17.51	0.62	17.55	27.06	5.47	0.91	0.59	100

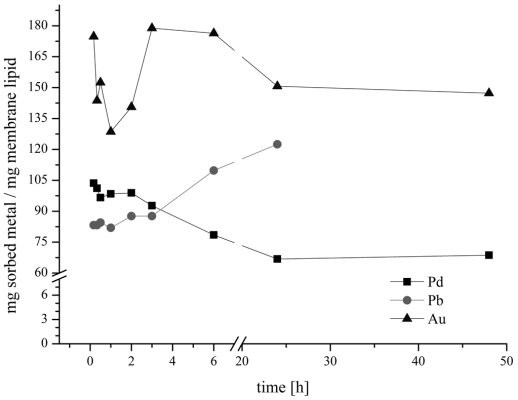

Fig. 2: Sorption process of Pd, Pb, Au with JG-B53 membranes lipids.

CONCLUSION. With the modified two isolation procedures for lipids it was possible to get the membrane lipids in a good yield and purity. With the usage of TLC and GC-FID it was possible for the first time to show the composition of the JG-B53 membrane lipids. The following sorption experiments show that these biological compounds are able to bind high amounts of heavy metals e.g. palladium, lead, and gold. These results open a wide field for applications, e.g. template for filter materials as well as a new base for fundamental research.

ACKNOWLEDGEMENTS. Thanks to N. Drechsel (University of Applied Science, Mittweida) for her support and to Dr. H. Heipieper (UFZ, Leipzig) for the GC-FID measurements.

[1] Raff, J. et al. (2003) *Chem. Mater.* **15**, 240–244.
[2] Kutschke, S. et al (2010) *Report FZD-530*, p. 21.
[3] Bligh, E.G. et al. (1959) *Can. J. Biochem. Physiol.* **37**, 911–917.
[4] Drechsel, N. (2012) Bachelor thesis, HSMW, Mittweida.
[5] Hahn et al. (2009) *Medizinische Mikrobiologie und Infektiologie,* Springer Medizin Verlag, Heidelberg.

Low dose effects of uranyl on the metabolic activity of bacteria isolated from mining waste piles

M. H. Obeid, K. Fahmy, J. Oertel

Metabolic monitoring of bacterial cell growth was established using microcalorimetry to measure metabolic reaction heats as a function of low doses of Uranium nitrate in four different bacterial strains: *Paenibacillus* sp. JG-TB8, *Bacillus sphaericus* sp. JG-A12, *Bacillus sphaericus* sp. and JG-B53 which were isolated from a uranium mining waste pile at Johann-Georgenstadt, Saxony. The *E. coli* strain W3110 served as a reference. Here, the toxicity of a radionuclide is defined as a measurable effect on the metabolic activity. The objective is to quantify low dose toxicity under well-defined native conditions rather than predicting toxicity from a limited number of hypothetical assumptions on speciation or bioavailability. Here, we are interested in 1. concentration thresholds of uranyl(VI) for induction of metabolic responses and 2. uranyl-induced changes in the general bacterial growth pattern. This is exemplified for the strain JG-B53 and the *E. coli* reference.

To improve the knowledge about the toxicity of radionuclides in bio-systems, the mechanisms of the interaction between microorganisms and radionuclides should be studied more intensively. The study of microorganisms-(radioactive) heavy metals interactions has opened new doors for novel bioremediation programs [3, 4]. These interactions affect the metabolic activity of the bacterial cell. In this sense, monitoring the metabolic activity of the cell will develop ecotoxicological biomonitors that provide a physical readout based on measurable metabolic effects. It is a major challenge to develop such biomonitors rather than extrapolating risks from the cell survival curves that account neither for the bioavailability nor the metabolic responses to toxicity. It has been shown that monitoring the heat from metabolic reactions in a microorganism allows studying even subtle influences of physical and chemical factors on metabolism [1, 2, 5]. The high sensitivity and thermal stability of modern instrumentation may thus enable radiotoxicity measurements at much lower than lethal doses as required for environmentally relevant low dose risk assessment.

METHODS. Liquid cultures of the bacterial strains were grown in R2A 50% media at 30 °C and exposed to micromolar concentrations (0, 10, 50, 100 µM) of uranium nitrate $UO_2(NO_3)_2$ salt. The metabolic heat release was measured as a function of time and temperature using a TAMIII (TA-Instruments). Inductively coupled plasma mass spectrometry (ICP-MS) was performed to detect the absorbed amounts of metals by the bacterial cells.

RESULTS. Reproducible distinct effects of uranium on the time-dependent heat release were observed already at a threshold of 10 µM in JG-B53 and *E. coli*. In JG-A12 and JG-TB8, uranium decreases the maximal heat flow with increasing uranium salt concentration (not shown). In contrast, JG-B53 and *E. coli* (Fig. 1) release more heat at 50 µM than at 10 µM uranyl(VI). For *E. coli* also the maximal heat flow at 150 µM uranium is higher than at 100 µM. This indicates that these organisms may activate metal-induced detoxification pathways at [U] > 50 µM

Tab. 1: Summary of growth rate constants k, evaluation of the first max. heat flow and the U adsorption to cellular fraction depending on the $UO_2(NO_3)_2$ concentration.

$UO_2(NO_3)_2$ [µM]	0	10	50	100	150
k [s^{-1}]	0.27646	0.26864	0.26975	0.25859	0.26084
first max. heat flow [µW]	48.01	49.99	56.10	48.71	52.98
% U in biomass	---	90.20446	97.51606	96.55193	94.93619

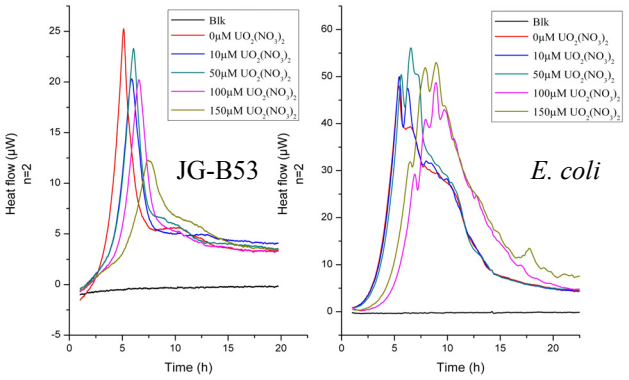

Fig. 1: Thermograms of the bacterial strain *E coli* and JG-B53 grown in R2A 50% at 30 °C under different concentrations of $UO_2(NO_3)_3$. Pure R2A media with heavy metals were used as negative controls (zero-line). Blk: blank (only medium).

which produce a surplus of metabolic heat. In this regard, JG-B53 appears to be unique among the three isolates. Initial growth rates have been calculated and ICP-MS revealed that more than 90% of the total uranium was associated with the cellular fractions (Tab 1).

CONCLUSIONS.

- Microcalorimetric monitoring is an extremely sensitive tool to investigate low dose toxicity of heavy metals and radionuclides in microorganisms.
- JG-B53 and *E. coli* respond with increased metabolic activity to uranium above 50 µM.
- Initial growth rates were determined with high accuracy in real time.
- Metabolic monitoring may be extended to higher soil-inhabitating organisms in the context of mining technologies.

[1] Xie, W.-H. et al. (1992) *Thermochim. Acta* **195**, 297–302.
[2] Xie Chang-Li, T.H.K. et al. (1988) *Thermochim. Acta* **123**, 33–41.
[3] Pollmann, K., et al. (2006) *Biotechnol. Adv.* **24**, 58–68.
[4] Keith-Roach, M. et al. (2002) *Interactions of microoganisms with radionuclides 2*, Elsevier, Munich.
[5] Forrest, W.W. (1972) *Methods in Microbiology*, p. 285–318, Elsevier, Munich.

Encapsulation of *Bacillus* sp. B5T in electrospun microtubes

M. Vogel, T. Lehrer,[1] R. Avrami,[1] S. Tarre,[1] E. Zussman,[1] M. Green,[1] J. Raff, K. Pollmann[2]
[1]Technion, Israel Institute of Technology, Haifa, Israel; [2]Helmholtz Institute Freiberg for Resource Technology, Freiberg, Germany

Encapsulation of whole bacterial cells for water treatment using advanced technologies is the objective of this research project. Bacterial cells of *Bacillus* sp. B5T were successfully encapsulated in electrospun polymeric microtubes for use in bioremediation purpose like toxic metal removal.

In this study, the focus is on the development of innovative biocomposite materials for biotechnologically applications, e.g. for the removal of contaminants from water. As an example *Bacillus* sp. B5T was chosen which was isolated from a uranium mining waste pile in Saxony and is able to bind large amounts of heavy metals. As an immobilization technique for the production of a biocomposite material electrospinning was used. The bacteria should be encapsulated inside polymeric microtubes as described by Klein et al. [1]. The produced biocomposite material should be evaluated according to microtube performance, stability and uranium removal efficiency.

EXPERIMENTAL. *Bacillus* sp. B5T was cultivated overnight at 30 °C in conical flasks containing 50 mL nutrient broth (5 g peptone, 5 g meat extract, 2.5 g NaCl per liter). An amount of 10–12 mL cell culture with an OD_{600} of 1.8–2.5 was centrifuged for 15 min, washed three times and resuspended in 0.5 mL of deionized water.
The core solution for the electrospinning consists of 1.5 mL 20% polyvinylpyrrolidone (PVP) and 0.5 mL bacterial suspension. The shell solution is made of polyvinylidene fluoride-cohexa-fluoropropylene (PVDF-HFP) dissolved in a mixture of tetrahydrofuran and dimethylformamide. Core-shell-fibres were fabricated using the co-electrospinning process described by Dror et al. [2]. The spinning parameters were previously published [1] with subsequent modifications. The flow rates of both shell and core solution were controlled by syringe pumps and were 5 mL/h for the shell and 0.5 to 2 mL/h for the core, respectively. The fibers were collected in a water bath and then as a strip on the edge of a vertical rotating wheel [3] at a velocity of 1.2 m/s. For confocal laser scanning microscopy (CLSM), microtube walls were stained with Syto9, dead bacteria with propidium iodide (PI) and living bacteria with 5-Cyano-2,3-ditolyl tetrazolium chloride (CTC).

RESULTS. The bacteria were successfully incorporated into PVP-PVDF-HFP microfibers. Parameters like cell concentration and core flow rate were varied in order to determine optimal conditions for the encapsulation of *Bacillus*. The influence of the parameter variation during spinning on the tube performance is summarized in Tab. 1. The core flow rate influenced the microtube diameter, cell distribution and cell density as can be seen in Fig. 1 on CLSM images. The fibers with a core flow rate of 0.5 mL/h show around 4 µm in diameter. The amount of bacteria inside seems to be low. The higher core flow rate of 2 mL/h created wider tubes around 7 µm accompanied by a higher concentration of living bacteria inside. However, the fibers seemed weak and unstable. The Z axis sectioning (Fig. 1, bottom) in both examples shows round tubes with bacterial cells located definitely inside the tubes.

Tab. 1: Influence of core flow rate on microtube performance.

Parameter	core flow rate [mL/h]		
	0.5	1.0	2.0
Microtube diameter (µm)	2–4	4–6	5–8
Microtube form	++	+	0
B5T in microtube	+	+	+
Distribution of B5T	++	++	0
B5T living	+	++	++

++ very good, + good, 0 satisfactory, – sufficient, –– deficient.

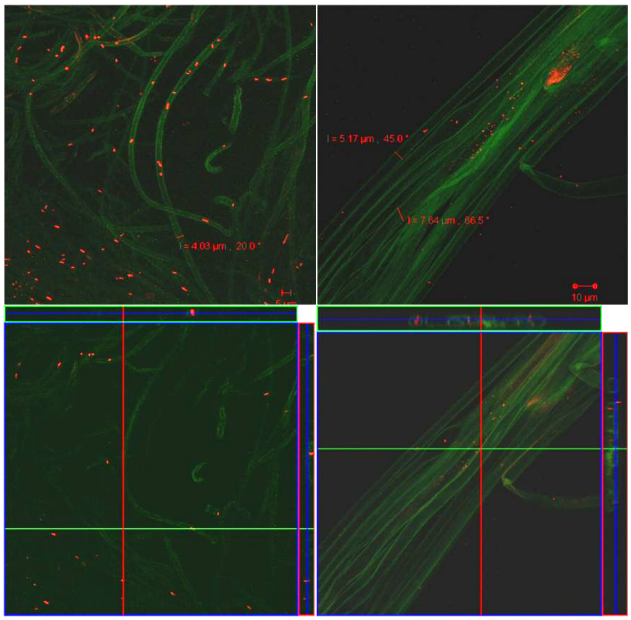

Fig. 1: CLSM-Images of microtubes with *Bacillus* sp. B5T. Core flow rate 0.5 mL/h (left) and 2.0 mL/h (right). Green microtube walls stained with Syto9. Red fluorescence shows dead cells stained with PI (left) or living cells stained with CTC (right).

In conclusion, electrospinning is a suitable technique for the encapsulation of bacteria of the genus *Bacillus*. However, due to low biomass content inside the tubes the removal efficiency of the biocomposite material for uranium was not significantly better than that one of the reference material without biomass (data not shown). Therefore, it remains still challenging to produce stable microtubes with an adequate amount of encapsulated biomass for the efficient removal of heavy metals from water being part of future work.

ACKNOWLEDGEMENTS. The authors thank the BMBF-MOST German-Israeli Water Technology Research Fund (WT1103/02WA1223).

[1] Klein, S. et al. (2012) *J. Ind. Microbiol. Biotechnol.* **39**, 1605–1613.
[2] Dror, Y. et al. (2008) *Macromolecules* **41**, 4187–4192.
[3] Theron, A. et al. (2001) *Nanotechnology* **12**, 384–390.

The impact of the Mont Terri isolate *Paenibacillus* sp. on the U(VI) speciation

L. Lütke, H. Moll, V. Bachvarova,[1] S. Selenska-Pobell, G. Bernhard
[1]Center for Medical Biotechnology/ Faculty of Biology, University of Duisburg-Essen, Essen, Germany

Potentiometry combined with Time-resolved Laser-induced Fluorescence Spectroscopy (TRLFS) were employed to study the binding of U(VI) onto cells of the novel Mont Terri isolate *Paenibacillus* sp. with respect to the U(VI) surface complexes formed and their stability constants.

Besides the prominent processes influencing the migration of actinides in the environment, e.g. sorption onto mineral surfaces, there is growing attention to the influence of indigenous microorganisms on actinide speciation. The investigated bacterial strain, *Paenibacillus* sp. MT-2.2, has been isolated from Opalinus clay (Mont Terri, Switzerland) [1] currently studied as candidate host rock for nuclear waste storage.

EXPERIMENTAL. *Paenibacillus* sp. MT-2.2 was grown anaerobically in R2A medium at 30 °C. Culture purity was ensured by light microscopy and *in situ* PCR with subsequent RFLP. The characterization of the bacterial cell surface functional groups as well as the determination of the U(VI) surface species and corresponding stability constants by potentiometry combined with HYPERQUAD [2] analysis was carried out as described previously [3]. TRLFS was employed to verify the U(VI) surface complexes formed, for details see [4].

RESULTS. A three-site model is commonly used to describe the bacterial cell surface functional groups and was applied to the titration data of *Paenibacillus* sp. cells. HYPERQUAD analysis yielded the following pK_a values (densities in $mmol/g_{dry\ weight}$) of the binding sites: 4.90 ± 0.05 (0.55 ± 0.12), 6.66 ± 0.10 (0.24 ± 0.01), and 9.20 ± 0.03 (1.19 ± 0.26). The respective surface functional groups are attributable to carboxyl, phosphate and amine moieties [5]. An excellent agreement was found comparing our results to the pK_a values published for cyanobacteria [6].

Figure 1 illustrates the titration curve of U(VI) and *Paenibacillus* sp. and the HYPERQUAD fit. Input parameters for the fit were the pK_a values and site densities of the bacteria and the log β values of relevant uranyl hydrolytic species. Extracted U(VI) surface complexes and stability constants using HYPERQUAD are given in Tab. 1.

The calculated stability constants imply a moderate to strong interaction of U(VI) with the surface functional groups of the investigated strain. Based on the determined stability constants the U(VI) species distribution in presence of the bacteria in dependency on pH using environmentally relevant concentrations was calculated with HySS 2009 (Fig. 2).

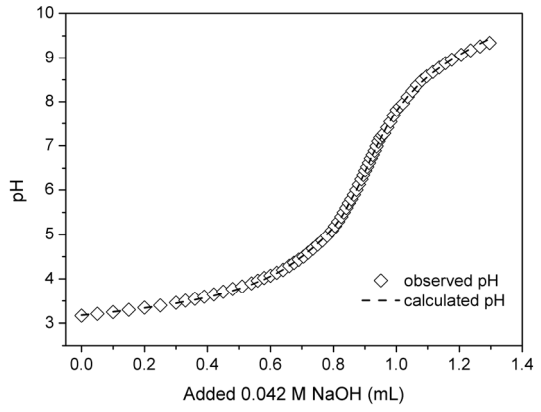

Fig. 1: Titration of 1×10^{-4} M UO_2^{2+} and 0.3 g/L cells in 0.1 M $NaClO_4$ with 0.042 M NaOH under N_2 atmosphere. Data (◊), fit (---).

Tab. 1: Calculated U(VI) surface complexes and stability constants.

Complex	xyz*	Log β (± SD)
$R–COO–UO_2^+$	110	5.33 ± 0.08
$R–O–PO_3–UO_2$	110	8.89 ± 0.04
$R–O–PO_3H–UO_2^+$	111	12.92 ± 0.05
$(R–O–PO_3)_2–UO_2^{2-}$	120	13.62 ± 0.08

*ratio metal : ligand : proton.

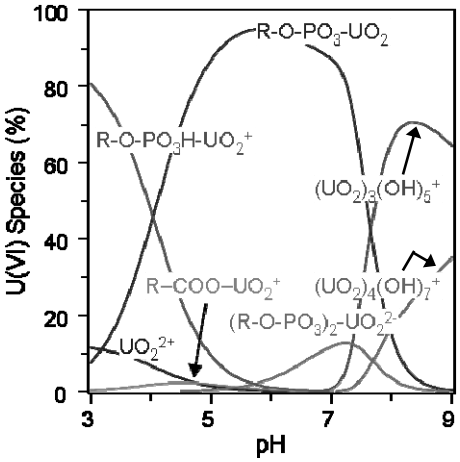

Fig. 2: U(VI) species distribution in presence of *Paenibacillus* sp. cells in dependence on pH. [U(VI)] = 1×10^{-6} M, [dry biomass] = 0.02 g/L. CO_2-free system.

This species distribution reveals that U(VI) is dominantly coordinated by the phosphoryl surface sites over a wide pH range up to pH 7.5. At environmental [U(VI)] and [dry biomass] carboxyl complexation is almost neglectable due to the higher stability of U(VI) complexed by phosphoryl residues. Using TRLFS, the different phosphoryl complexes were distinguishable by their different lifetimes and appearance in dependency on pH. The $R–O–PO_3–UO_2$ complex is characterized by a quite short lifetime for U(VI) species (0.57 µs) as found also for another strain, *P. fluorescens* [3]. For the complexes $R–O–PO_3H–UO_2^+$ and $(R–O–PO_3)_2–UO_2^{2-}$ significantly longer lifetimes of 2.69 and 2.34 µs, respectively, were found [4].

ACKNOWLEDGEMENTS. The authors thank the BMWi for financial support (contract no.: 02E10618) and the BGR for providing the clay samples.

[1] Bachvarova, V. et al. (2010) *Report FZD-530*, p. 18.
[2] Gans, P. et al. (1996) *Talanta* **43**, 1739–1753.
[3] Lütke, L. et al. (2012) *Dalton Trans.* **41**, 13370–13378.
[4] Lütke, L. et al. (2013) *Dalton Trans.*, submitted.
[5] Cox, J. S. et al. (1999) *Environ. Sci. Technol.* **33**, 4514–4521.
[6] Yee, N. et al. (2004) *Environ. Sci. Technol.* **38**, 775–782.

Evidence of meta-autunite formation in *Pseudomonas fluorescens* biofilms by EXAFS spectroscopy

E. Krawczyk-Bärsch, H. Moll, L. Lütke, A. Rossberg

***Pseudomonas fluorescens* bacteria, which were isolated in the Äspö HRL (Sweden) at a depth of 70 m [1], were used as a slime forming bacterium in uranium(VI) sorption experiments. Analysis refer to a immobilization of U(VI) from the nutrient media by the *Pseudomonas fluorescens* biofilm. EXAFS measurements confirmed the microbial mediated retention of U(VI). The similarities of the EXAFS oscillation features especially in k-space between 8 and 12 $Å^{-1}$ observed in the biofilm sample and in the meta-autunite reference points to the beginning formation of meta-autunite in the *Pseudomonas fluorescens* biofilm.**

EXPERIMENTAL. *Pseudomonas fluorescens* (CCUG 32456 A) was cultivated in a synthetic nutrient medium consisting of 5 g/L peptone and 3 g/L meat extract (pH 7). Glucose was absent and the phosphate amount was low (PO_4^{3-} = 12.7 mg/L). In the mid-exponential growth phase a volume of 3.6 mL of the *Pseudomonas fluorescens* culture were added to 400 mL of the synthetic nutrient medium, kept in a glass plunger. The experiments were performed in air atmosphere under sterile condition. After a 400 µm thick slimy biofilm has formed as homogeneous surface pellicle on the interface between air and nutrient medium, $UO_2(ClO_4)_2$ was added to the nutrient medium to a final U(VI) concentration of 23.8 mg/L (1×10^{-4} M). After 48 hours, a biofilm sample was taken and prepared for EXAFS measurements at the ROBL beamline (BML20), ESRF, Grenoble. The sample was measured at 15 K in a closed-cycle He cryostat using a water-cooled Si(111) double-crystal monochromator in channel cut mode (5–35 keV). The spectra were collected either in fluorescence mode using a 13-element Ge solid-state detector [2] or in transmission mode using ionization chambers and compared with the meta-autunite reference [3].

RESULTS. At the end of the experiment, the uranium concentration was determined to have declined to 12.9 mg/L (5.4×10^{-5} M) indicating that uranium has been removed from solution and immobilized. EXAFS spectroscopy was used to determine and identify the structure of uranium associated with the biofilm and especially to judge if solid uranium phases were formed in the biofilm. Based on the XAS data obtained at the uranium L_{III}-edge good analyzable uranium EXAFS oscillations could be achieved in the biofilm sample (see Fig. 1). The coordination number (N) of the axial oxygen of the linear uranyl(VI) unit was held constant at two during the fitting procedure. The mean U–O_{ax} distance (R) was measured at 1.78 ± 0.01 Å. The Debye-Waller factor (σ^2) of the U–O_{ax} shell of the biofilm sample contacted with 0.05 mM uranium(VI) is similar to the value of the crystalline meta-autunite sample. Compared to the meta-autunite reference, there is a tendency of larger Debye-Waller factors measured in the biofilm sample for the higher shells probably due to higher disorder of the respective shells. The similarities of the EXAFS oscillation features especially in k-space between 8 and 12 $Å^{-1}$ observed in the biofilm sample and in the meta-autunite reference points to the beginning formation of meta-autunite like U(VI) structure in the biofilm sample.

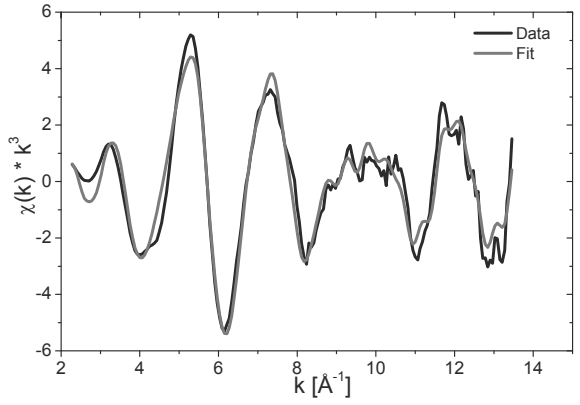

Fig. 1: U L_{III} k^3-weighted EXAFS spectrum including the best theoretical fit (gray) of the 0.05 mM U(VI) biofilm sample at pH 7.

There are strong indications especially for heavier backscatterer like U(VI) at distance values above 4 Å (see Fig. 2). The structural parameters are in agreement with the corresponding meta-autunite values.

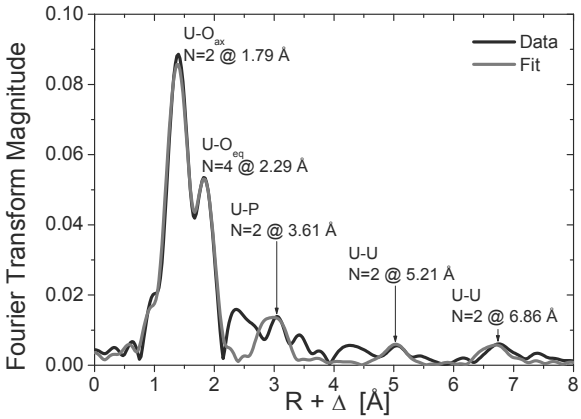

Fig. 2: Corresponding Fourier transformation including the best theoretical fit (gray) of the 0.05 mM U(VI) biofilm sample at pH 7.

ACKNOWLEDGEMENTS. This work was funded by BMWi under contract number 02E10618. We thank Ursula Schaefer and Carola Eckardt for analysis. Stephan Weiß skilfull work on sample preparation for EXAFS is gratefully acknowledged.

[1] Pedersen, K. (2005) *J. Nucl. Radiochem. Sci.* **6**, 11–15.
[2] Rossberg, A. et al. (2009) *Environ. Sci. Technol.* **43**, 1400–1406.
[3] Makarov, E.S. et al. (1960) DOKLADY AKADEMII NAUK SSSR **132**, 673–676.

The impact of the Äspö-strain *Pseudomonas fluorescens* on the speciation of plutonium

H. Moll, L. Lütke, G. Bernhard

This study focuses on the unknown interaction between plutonium in mixed oxidation states (60% Pu(VI) and 18% Pu(IV)-polymers) and cell-suspensions of the Äspö strain *P. fluorescens*. Accumulation experiments were performed in order to obtain information about the amount of Pu bound by the bacteria. We used solvent extraction and UV-vis-NIR absorption spectroscopy to determine the speciation of Pu oxidation states.

Since microbes are well known to affect the mobility of actinides, dominant microbial strains from sites destined for future nuclear waste deposition have to be investigated regarding their interaction mechanisms with soluble actinides [1, 2]. Pu is one of the hazardous components of nuclear waste (radio- and chemical toxicity). Pu experiments are challenging because it can coexist in several oxidation states in aqueous solutions. The investigated subsurface groundwater strain *P. fluorescens* (CCUG 32456A) has been isolated from the Äspö site, Sweden [3].

EXPERIMENTAL. *P. fluorescens* cells were harvested in the mid-exponential growth phase washed and suspended in 0.9% NaCl solution. The experiments were performed at [dry biomass] of 0.2 $g_{dry\ weight}$/L and pH 6 under N_2 atmosphere at 25 °C in 0.1 M $NaClO_4$ solution. $[^{242}Pu]_{initial}$ was varied between 0.2 and 100 mg/L. The ^{242}Pu present in a) blank (no cells added), b) supernatant, and c) washed biomass suspension at pH 0 was analyzed using UV-vis-NIR spectroscopy, solvent extraction, and liquid scintillation counting (LSC) as described in [4].

RESULTS. The amount of Pu sorbed by *P. fluorescens* increased with time as shown in Fig. 1. Steady state conditions were reached after approximately 8 days. The data could be successfully fitted to a bi-exponential law. This suggests that at least two different processes occur after adding Pu to the biomass. A higher Pu binding capacity of dead biomass was detected at larger contact times.
At $[Pu]_{initial}$ 0.2 mg/L 67% of the initially present Pu was removed by the cells. Whereas at $[Pu]_{initial}$ 100 mg/L the removal efficiency dropped down to 27%. Hence, we found a strong dependence of the amount of Pu associated with *P. fluorescens* cells on the initial Pu concentration in the test solutions.

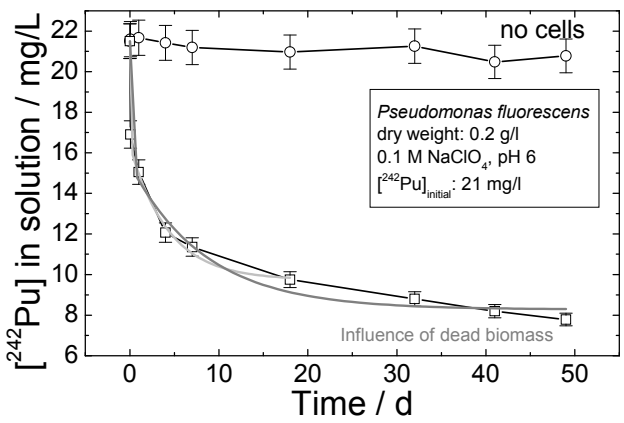

Fig. 1: Decrease of the Pu concentration in solution at $[Pu]_{initial}$: 21 mg/L at pH 6.

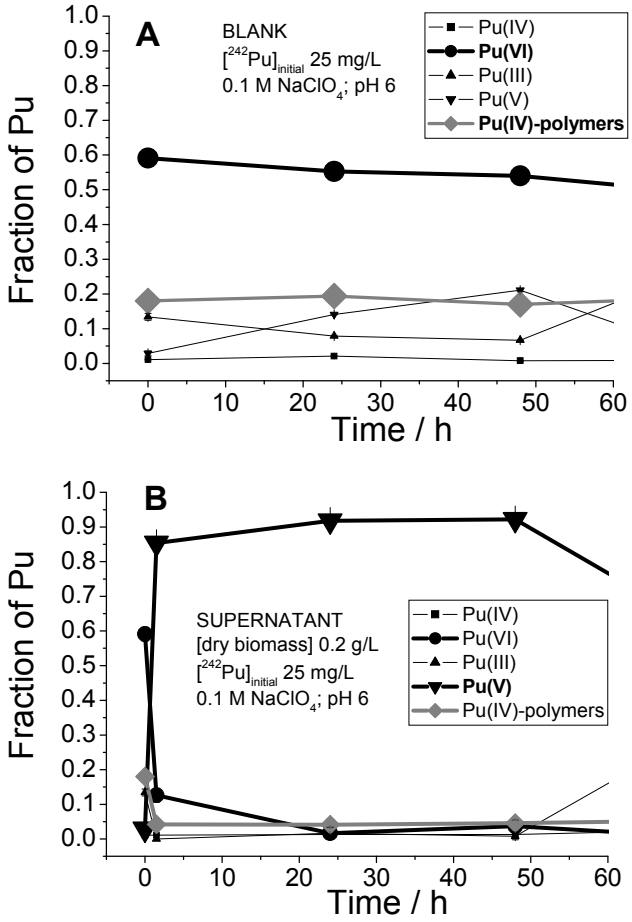

Fig. 2: Time dependent Pu oxidation state distribution in the samples (a) blank and (b) supernatant determined by solvent extraction.

The time dependent Pu oxidation state distribution depicted in Fig. 2 demonstrates the strong impact of the Äspö strain *P. fluorescens* on the Pu speciation [5]. In the first step, a fast binding of the Pu(VI) and Pu(IV)-polymers on the biomass occurred. Approximately 85% of the initially present Pu(VI) is reduced to Pu(V) due to the activity of the cells within the first 24 h of contact time (no electron donor added). Most of the formed Pu(V) dissolves from the cell envelope back to the aqueous solution due to the weak complexation properties of this plutonium oxidation state. Pu(IV)-polymers dominated the Pu oxidation state distribution on the biomass showing the good binding properties of Pu(IV)-polymers on functional groups of the cell envelope.

ACKNOWLEDGEMENTS. The authors thank the BMWi for financial support (Contract no.: 02E10618).

[1] Neu, M.P. et al. (2005) *Radiochim. Acta* **93**, 705–714.
[2] Ohnuki, T. et al. (2010) *Geomicrobiol. J.* **27**, 225–230.
[3] Pedersen, K. (1997) *FEMS Microbiol. Rev. 20*, 399–414.
[4] Moll, H. et al. (2006) *Radiochim. Acta* **94**, 815–824.
[5] Moll, H. et al. (2012) *Plutonium Futures - The Science 2012*, p. 44.

Bioaccumulation of uranium by the acidophilic protozoan *Euglena mutabilis* studied by Transmission Electron Microscopy (TEM)

S. Brockmann,[1] T. Arnold, G. Bernhard
[1]Radiochemistry,Technische Universität Dresden, Dresden, Germany

Uranium was identified by TEM/EDX in *Euglena mutabilis* cells. This indicated an active transport of uranium into the cell and precipitation of uranium in vacuoles or vacuole-like vesicles.

EXPERIMENTAL. The *Euglena* cells were cultivated in a 2 L reactor at room temperature under constant slow stirring and supply of sterile filtered air. More details are provided in [1]. The harvested cells were washed and finally resuspended in a prepared sterile filtrated U-solution (5×10^{-4} mol/L $UO_2(NO_3)_2$ in 3.48 g/L Na_2SO_4, pH = 3). The experiments were carried out by testing the bioaccumulation of living and heat killed cells. After 10 days, the cells were washed to remove unbound adhering uranium and fixed in 2.5% glutaraldehyd and contrasted for at least 1 h in 1% OsO_4. Subsequently, the cells were dehydrated in a graded ethanol/acetonitrile series and finally embedded in Agar Low Viscosity Resin (Plano GmbH, Germany). After polymerization, the samples were cut into 40 nm slices and positioned on carbon coated copper grids.

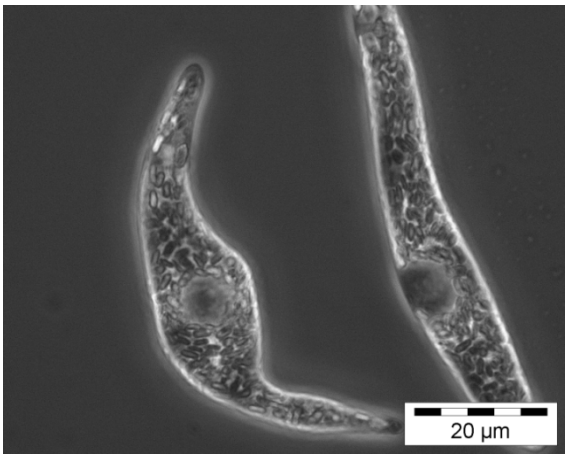

Fig. 1: TEM of a living *Euglena mutabilis* cells.

RESULTS. Transmission electron microscopy (TEM) investigations with the *Euglena* cells (see Fig. 1) in contact with uranium for 10 days showed regions with high contrast (displayed in white) in the cells which were attributed to elements with high atomic weight. EDX measurements of these regions (see Fig. 2) identified bioaccumulated uranium. In addition, Cu, C, and P were detected. Cu is related to the Cu grid on which the TEM specimen was positioned and C originates from the organic material of the sample. The P signal could be an indication for a coordination of uranium with phosphate groups. The localization of uranium inside the *Euglena* cells is a strong indication for the active transport of uranium into the cell. Additional EDX measurements at the pellicle of the cells showed no further U peaks. Thus, an intensive accumulation on the *Euglena* pellicle could not be detected. However, homogeneously distributed uranium on the cell surface could not be excluded. The U-accumulations inside the cells are located in round or oval shaped cell compartments. These compartments may be vacuoles or vacuole-like vesicles which are filled with gas or liquid. In [2] the existence of phospholipid vesicles in cells of *Euglena spirogyra* is described. Thus, uranium may have been accumulated in such vesicles and could be coordinated to phosphate groups.

TEM/EDX measurements of dead cells after treatment with 5×10^{-4} mol/L U for 10 days were also performed. However, in these studies no U could be visualized or detected with EDX. There are two possibilities why there was no uranium detected: (1) the uranium was only slightly bound to the cells and was flushed away during the numerous washing steps in sample preparation, or (2) the bound uranium was homogeneously distributed at the cell surface without local accumulations, so that the U concentrations were below detection limit for EDX.

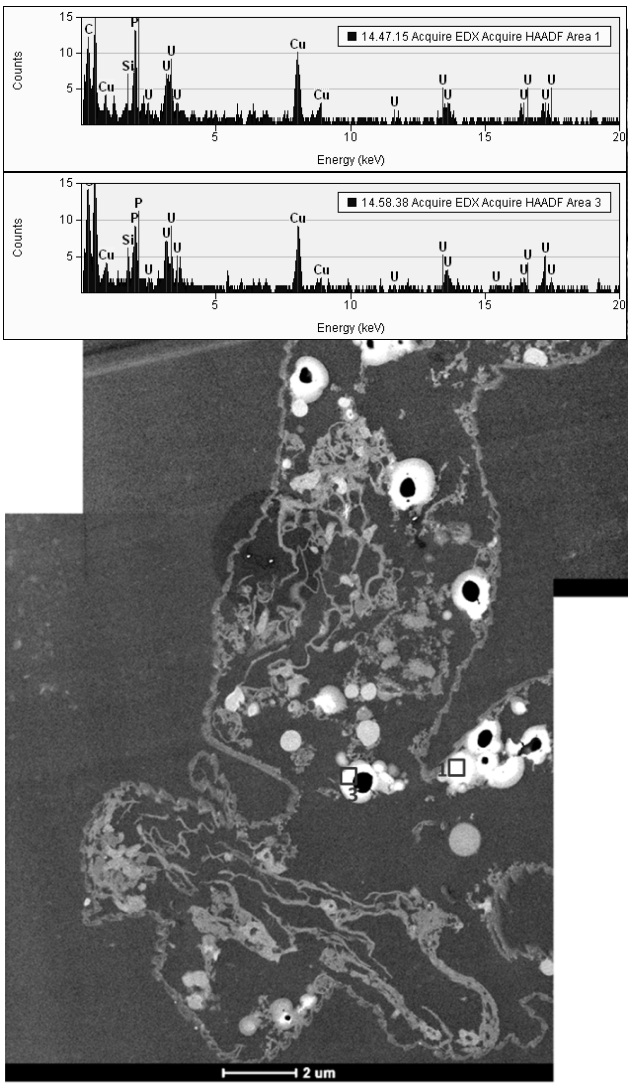

Fig. 2: EDX (above) and TEM photomicrographs (below) of a *Euglena mutabilis* cell.

ACKNOWLEDGEMENTS. The Bundesministerium für Bildung und Forschung (project no. 02NUK002F) is thanked for funding.

[1] Brockmann, S. et al. (2013) *Environ. Sci. Pollut. Res.*, submitted.
[2] Leedale, G.F. et al. (1965) *Archiv für Mikrobiologie* **50**, 68–102.

Formation of Se(0) nanoparticles by *Azospirillum brasilense*

R. Steudtner, M. Vogel, C. Franzen

In the present study, we investigated the reduction of SeO_3^{2-} by *Azospirillum brasilense*. The formation of fairly soluble Se(0) nanoparticles during this process might be of interest for both bioremediation of Se-contaminated sites and for nanobiotechnology.

In the environment, the oxyanions selenate [SeO_4^{2-}, Se(VI)] and selenite [SeO_3^{2-}, Se(IV)] represent soluble species in aqueous media, whereas the reduced species Se(0), Se(−I) and Se(−II) mainly form colloidal particles or fairly soluble precipitations. This results in a more sufficient retardation of the reduced species. Reactions between Se and microorganisms can significantly influence the Se oxidation state and, therefore, the transport behavior in geological environment.

EXPERIMENTAL. *Azospirillum brasilense* has been precultured overnight at 30 °C. 5 mL of preculture were added to 25 mL of fresh medium. After addition of 1 mM Se(IV), the samples were placed in a 30 °C shaking (100 rpm) incubator for 3 days. Afterwards, cellular material was removed from the evolved precipitation by using a modified procedure of Oremland [1]. The cleaned particles were then resuspended in deionized water.
For selective Se(IV) quantification in the culture media we used HG-AAS [2]. The evolved nanoparticles were characterized by SEM-EDX, PCS and zeta potential measurements.

RESULTS. After *Azospirillum brasilense* being exposed to Se(IV), the bacterial growth continued subsequent to a prolonged lag-phase. After a cultivation time of 3 days, a (clearly reddish) staining of the sample was observed and a (bright red) precipitate occurred, indicating the formation of Se(0) nano-particles (see samples 2–5 in Fig. 1).

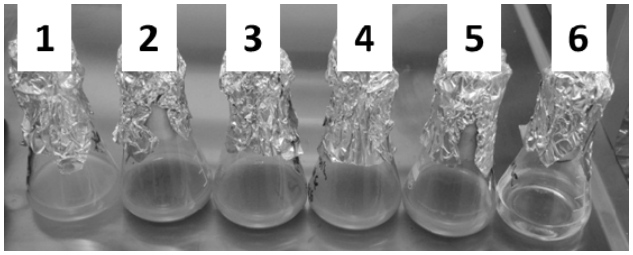

Fig. 1: Se(IV)-reduction to Se(0) within 3 days in presence of *A. brasilense.* Sample 1: bacteria without Se(IV); samples 2–5: Se(IV) plus bacteria; sample 6: Se(IV) without bacteria.

The SEM-EDX spectra derived from the nano-spheres (Fig. 2) indicated that they mainly consist of selenium.
In addition, only 10% of the initial Se(IV) concentrations was recovered in culture media by means of HG-AAS, indicating a Se(IV) removal from the media.
The isolated and resuspended Se(0) nanoparticles showed a long time stability of some hours, which is sufficient for the PCS and the zeta potential measurements. In contrast, Se(0) chemically formed by reduction with hydroxylamine solution produced amorphous aggregates with a rapid sedimentation behavior. The PCS measurement of the Se(0) particles showed a particle size distribution between 100 and 300 nm with an averaged particle diameter of 200 nm (Fig. 3).

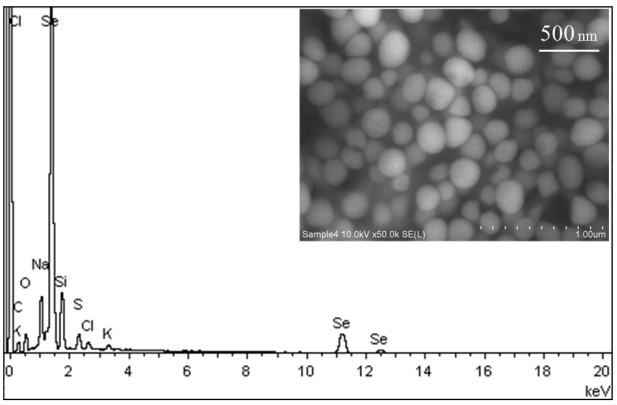

Fig. 2: EDX spectrum of the nano-spheres and SEM image of the precipitated nano-spheres (inset).

The size was further confirmed by SEM imaging which demonstrated that the Se(0) particles possess spherical forms and a particle size distribution between 140 and 300 nm (Fig. 2, inset).
The isoelectric point of Se(0) particles was found at pH 2.8 ± 0.2 (Fig. 3). The preference of forming Se(0) particles with a negative charge agree very well with the literature [3].

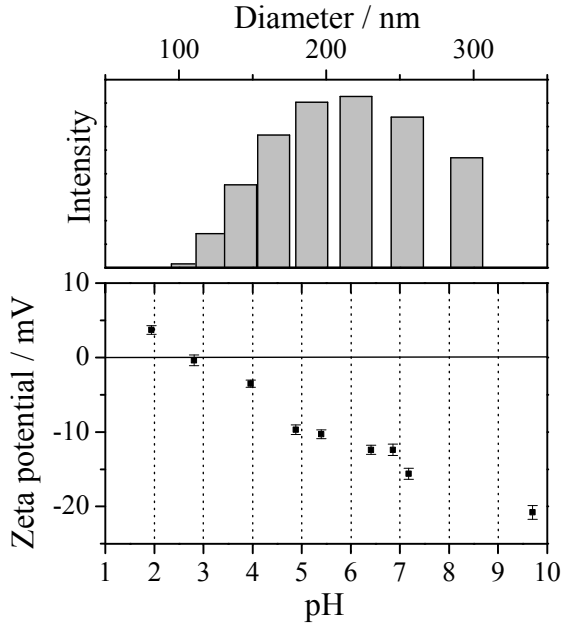

Fig. 3: Characterization of the Se(0) particles. Top: Particle size distribution via PCS. Bottom: Zeta potential of Se(0) particles as function of pH. Error bars indicate 95% confidence level.

This study showed the reduction of selenite and the formation of Se(0) nanoparticles in the presence of *Azospirillum brasilense*. This might be of interest for both bioremediation of Se-contaminated sites and for nanobiotechnology.

[1] Oremland, R.S. et al. (2004) *Appl. Environ. Microbiol.* **70,** 52–60.
[2] Niedzielski, P. et al. (2002) *Pol. J. Environ. Stud.* **11**, 219–224.
[3] Dhanjal, S. et al. (2010) *Microb. Cell Fact.* **9,** 1–11.

Study of the Eu(III) uptake by FaDu cells as a function of the nutrient composition

S. Sachs, A. Heller

The Eu(III) uptake by FaDu cells was studied in the presence and absence of fetal bovine serum. Eu(III) seems to be bound onto the cell surface and does not significantly enter the cells.

In case of the release of long-lived radionuclides into the environment, knowledge about their behavior in biosystems is necessary to assess and prevent health risks for humans. Objective of our work is the study of interaction processes of actinides with mammalian cells. In continuation of our previous studies [1, 2], the uptake of Eu(III), serving as analog for trivalent actinides, by FaDu cells is studied as a function of the Eu(III) concentration and the nutrient composition. In parallel, the speciation of Eu(III) in the cell culture media is studied by time-resolved laser-induced fluorescence spectroscopy (TRLFS) in order to correlate the metal ion uptake by cells with their chemical speciation, thus enabling a better understanding of their bioavailability and toxicity.

EXPERIMENTAL. FaDu cells (human squamous cell carcinoma cell line) were grown in Dulbecco's modified eagle medium (DMEM; w/o sodium pyruvate, with stable glutamine, 4.5 g/L D-glucose; Biochrom) supplemented with 10% fetal bovine serum (FBS; Sigma), 0.7 mM non-essential amino acids, 20 mM HEPES, penicillin/streptomycin (100 U/mL/100 µg/mL), and 1 mM sodium pyruvate (all from Biochrom) and subcultured as described in [1]. The Eu(III) toxicity onto FaDu cells was studied in the presence and absence of FBS in the concentration range between 5 and 2000 µM as described in [1]. To study the Eu(III) uptake by cells, 8.55×10^4 cells/well were seeded in 6 well plates (CELLSTAR®, Greiner). After 48 h of incubation (37 °C, 5% CO_2, 95% humidity), the nutrient was removed from the cells and about 10 or 1000 µM Eu(III) dissolved in complete cell culture medium or in cell culture medium w/o FBS (pH 7.7 ± 0.1) were added in this work. In the case of the studies w/o FBS, the cells were rinsed with FBS-free nutrient medium before Eu(III) addition. Cells were incubated with Eu(III) for 24 or 48 h. After that, the nutrient was removed and the cells were washed six times with 0.9% NaCl solution. Cells were detached from wells for 8 min at 37 °C using 2 mL trypsin/EDTA (0.05%/0.02%) in phosphate buffered saline solution (w/o Ca^{2+}, Mg^{2+}; Biochrom). To stop trypsinization, 2 mL complete medium were added. An aliquot of this solution was used for cell counting; the remaining solution was centrifuged (5 min, 200 g, 4 °C) to pellet the cells. Then, the supernatant was carefully removed. The isolated cells were resuspended in water and lysed by fivefold freeze/thaw lysis. After lysis, the solution was centrifuged (6000 rpm, 15 min, 4°C). The resulting supernatant, the last washing solution, and the trypsin/EDTA supernatant was analyzed for its Eu(III) content by ICP-MS. The protein-bound Eu(III) in complete medium was assessed by ultrafiltration using 10 kD Microsep filters (Pall) and subsequent ICP-MS analyses of the filtrates. The Eu(III) speciation in complete and FBS-free medium was studied by TRLFS as described in [2].

RESULTS. As already described in [1], the Eu(III) toxicity onto FaDu cells is significantly lower in the presence of FBS than in the absence. Eu(III) concentrations that reduce the cell viability to 50% after 24 h of incubation amount to about 1700 and 200 µM Eu(III) in the presence and absence of FBS, respectively. This difference can be caused by the different Eu(III) speciation in the nutrient media and points to a different bioavailability of Eu(III). In FBS presence, Eu(III) is stabilized in solution by complexation with FBS constituents [2], most probably proteins, which could be verified by ultrafiltration. Almost 100% of Eu(III) are retained from solutions with initial concentrations of 10 and 1000 µM Eu(III) by 10 kD filters, indicating the predominance of protein-bound Eu(III). In the absence of FBS, the Eu(III) solubility is very low. Already at 10 µM, Eu(III) precipitates from the cell culture medium. ICP-MS analysis of the Eu(III) precipitates as well as TRLFS measurements point to the occurrence of ternary or higher Eu(III) complexes with phosphate as the dominating ligand. The identification of these complexes is still subject of ongoing studies.

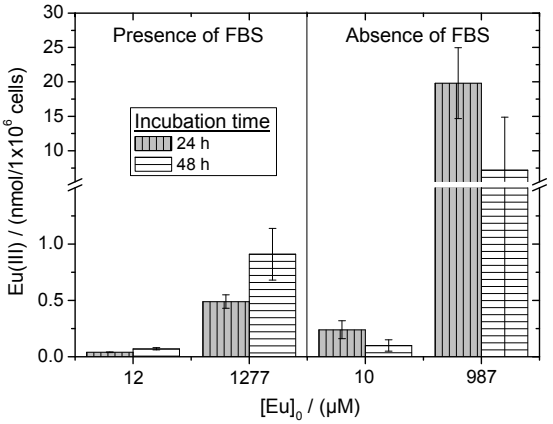

Fig. 1: Eu(III) uptake by FaDu cells in the absence and presence of FBS.

Figure 1 shows results of the Eu(III) uptake by FaDu cells in FBS absence and presence. Independent from the initial Eu(III) speciation, the Eu(III) uptake by the cells is very low. It seems to be increased with increasing Eu(III) concentration and in FBS absence. The incubation time has no significant effect. Comparing the Eu(III) content of the last washing solutions, the trypsin/EDTA solutions and the solutions after cell lysis with each other, the most significant Eu(III) contents were found in the trypsin/EDTA fractions. This points to the fact that Eu(III) initially bound in protein or phosphate complexes is located on the cell surface. By trypsinization, the surface-bound Eu(III) is removed, which was already reported for the plutonium uptake by cells [3]. Only a very low amount of Eu(III) appears to be able to enter the cells. However, especially for the FBS-free medium, it has to be confirmed if this Eu(III) fraction represents Eu(III) really taken up by the cells or Eu(III) which was not completely removed from the cell surface by trypsinization.

ACKNOWLEDGEMENTS. We thank J. Seibt and S. Heller for performance of the experiments and A. Ritter for ICP-MS analyses.

[1] Sachs, S. et al. (2012) *Report HZDR-013,* p. 12.
[2] Heller, A. et al. (2012) *Report HZDR-013,* p. 13.
[3] Planas-Bohne, F. et al. (1988) *Int. J. Radiat. Biol.* ***53***, 489–500.

Retrieval of biofilms from flooding water of the underground uranium mine Königstein

I. Zirnstein, T. Arnold, I. Röske[1]

[1]Institute of Microbiology, Technische Universität Dresden, Dresden, Germany

Biofilms had grown in the underground uranium mine Königstein (Germany) before the mine was flooded in 2010 and thus is no longer accessible for sampling today. To analyze microorganisms in the flooding water different systems for retrieval were used. Molecular based methods detected bacteria, archaea and eukarya in the flooding water.

To analyze the microorganisms in the flooding water of the underground Königstein mine, we used different systems to retrieve microorganisms as single cells (e.g. vacuum filtration with CA-membranes) and as biofilm (e.g. flow-cell with glass slides and biofilm-reactor with HDPE carriers).

EXPERIMENTAL. To determine the biodiversity of the flooding water after flooding the mine the following two DNA based methods were used: 16S /18S rDNA PCR and cloning/sequencing.
The water samples (10 L) and the biofilm samples on the flow-cell slides were taken two times in 2011 and 2012. The samples were analyzed by extracting the total DNA using the NucleoSpin®Soil Kit (Marchery-Nagel) and the PowerWaterExtraction Kit (MoBIO) followed by 16S rDNA PCR to analyze Archaea (seminested PCR: 21Fa-1513R; 21Fa-Arch958R) and Bacteria (27F-1492R) and 18S rDNA PCR to analyze Eukarya (EUK20F-EUKBr). The purified amplified rDNA fragments were cloned into *E. coli* (chemical competently TOP 10 F') using the Topo T/A CloningKit (Genaxxon BioScience) and following the manufacturers' recommendations. The recombinant clones (82 clones) were selected by blue-white colony selection. Representative clones were selected for sequencing to enable the phylogenetic classification of the predominant populations.

RESULTS AND DISCUSSION. Positive PCR-amplicons show (Fig. 1), that the water (W) and the biofilm on the flow cell slides (B) contained microorganisms belonging to all three domains bacteria, archaea and eukarya.
Sequencing analysis showed the bacterial diversity of water and biofilm samples (shown in Fig. 2). 82 clones resulted in 47 different species, which were grouped together (Fig. 2). It is supposed that these data of the bacterial diversity is a part of the real composition, that is why samples will further analyze by pyrosequencing and

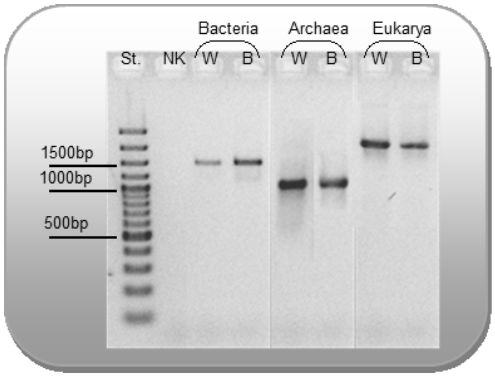

Fig. 1: PCR products from water samples (W) and biofilm samples (B) of the flooding water Königstein.

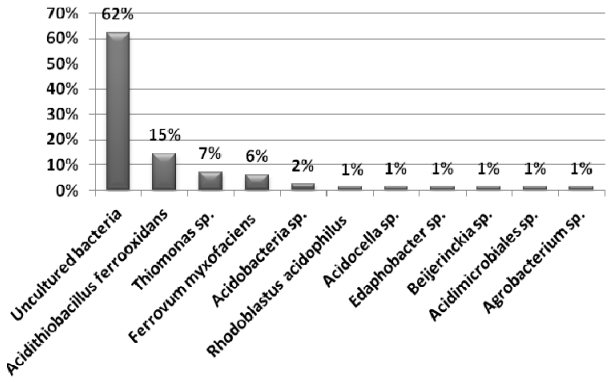

Fig. 2: Bacterial composition of water and biofilm samples (2011 and 2012) detected by 16S rDNA based sequencing.

CARD-FISH (catalyzed-reporter deposition *in situ* hybridization).
Many "uncultured bacteria" were detected by sequencing analysis. Typical acidophilic and iron-oxidizing bacteria e.g. *Acidithiobacillus ferrooxidans* and *Ferrovum myxofaciens* were established, which has been proven also in the biofilm samples before flooding. Representatives of sulfate-oxidizing bacteria were found e.g. *Thiomonas* species. Iron oxidizing bacteria oxidize Fe(II) to Fe(III) and sulfur-oxidizing bacteria oxidize S-compounds to sulfate.

$$FeS_2 + 3.5\ O_2 + H_2O \rightarrow Fe^{2+} + 2\ SO_4^{2-} + 2\ H^+$$
$$14\ Fe^{2+} + 3.5\ O_2 + 14\ H^+ \rightarrow 14\ Fe^{3+} + 7H_2O\ (Fe(OH)_3)\downarrow$$
$$FeS_2 + 14\ Fe^{3+} + 8\ H_2O \rightarrow 2\ SO_4^{2-} + 15\ Fe^{2+} + 16\ H^+$$

For using these iron-oxidizing and sulfate-reducing/oxidizing bacteria to clean the contaminated water of the Königstein mine, the flooding water is channeled directly from the underground through a biofilm-reactor (139 cm high, 39 cm in diameter) including biofilm-carriers (9 mm in diameter). The surplus water in the reactor is discharged to waste water treatment. The reactor takes 100 L flooding water and 60 L of biofilm-carriers (Fig. 3, [1]). Two months later, the carriers looked brownish and slimy, and a macroscopically visible biofilm has formed.

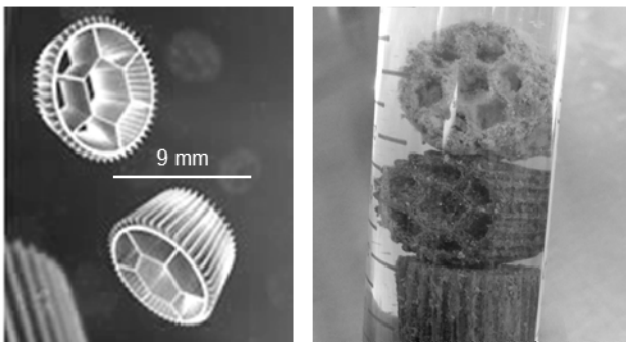

Fig. 3: Left: biofilm-carriers itself. Right: biofilm-carriers after attaching of microorganisms.

[1] Bergmann Abwassertechnik; wsb®*clean*.

First results on the microbial diversity of mine water from two flooded underground uranium mines

C. Gagell, T. Arnold, U. Jenk,[1] I. Röske[2]

[1]Wismut GmbH, Chemnitz, Germany; [2]Institute of Microbiology, Technische Universität Dresden, Dresden, Germany

The underground mine water of the two former uranium mines, Pöhla and Schlema, in the Erzgebirge were investigated with respect to their chemical composition and microbial diversity. The analysis of anions and cations of the mine water revealed higher uranium and sulfate concentrations for Schlema than for Pöhla. Interestingly, based on the 16S rRNA gene analysis seven bacterial classes could be identified from mine Schlema compared to only three for Pöhla, indicating a higher diversity of bacteria in Schlema. In contrast to Schlema archaea were identified in the Pöhla mine showing the presence of methane-producing microorganisms.

After the German reunification the Wismut GmbH, formerly the 3rd largest uranium producer of the world, started to remediate the legacies of their uranium mining activities. As a part of the remediation, the whole pit body of the mine was flooded. Although flooding of the Pöhla and Schlema mine was already finished about ten years ago, the mine waters still contain elevated concentrations of toxic metals such as uranium, arsenic and radium. Thus, expensive water monitoring and cleaning is required. Since microorganisms can influence the toxicity of metals directly or indirectly, one alternative approach is to use them for bioremediation [1]. To this end, it is necessary to characterize the microbial community of the mine in terms of diversity.

EXPERIMENTAL. The mine water was analyzed with respect to major anions and cations by ICP-MS. Complex anions such as sulfate were analyzed by ion chromatography. For the analysis of the microbial diversity, a flow cell was installed on site to allow the collection of natural biofilms. After two months, microorganisms were harvested and genomic DNA was extracted using the NucleoSpin Soil Kit (MarcheryNagel) according to manufacturer's instructions. A bacteria specific 16S rDNA PCR was performed with the primers 27F (5'-AGAGTTTGATCCTG GCTCAG-3') and 1492R (5'-GGTTACCTTGTTACGAC TT-3') [2]. The 16S rDNA of archaea was amplified by a semi-nested PCR with the primers 21Fa (5'-TTCCGGTT GATCCYGCCGGA-3', [3]) and 1513R (5'-TACGGYTA CCTTGTTACGACTT-3', [4]) for the first PCR reaction and the primers 21Fa and Arch958r (5'-YCCGGCGTTG AMTCCAATT-3', [3]) for the second reaction. The analyzed PCR product was inserted into a vector by cloning by means of the TOPO TA cloning Kit for Sequencing (Invitrogen) following the manufacturer's instructions. Clones were screened by blue-white selection and subsequent *in situ* PCR with vector specific M13 primers. 16S rDNA PCR fragments were sequenced by GATC and the sequences were aligned to those of the NCBI and RDP database.

RESULTS. The chemical analysis of the mine waters revealed differences between the Pöhla and the Schlema mine. Mine water from Schlema showed a 100-fold and 1000-fold higher concentration of uranium and sulfate, respectively, compared to Pöhla. However, Fe, As and the pH values are similar for both sites (Tab. 1). Analyzing the microbial community revealed three bacterial classes for Pöhla and seven for Schlema indicating a higher bacterial diversity at the Schlema site. All three classes, namely Alpha-, Betaprotebacteria and Sphingobacteria identified in the Pöhla mine water were also found for the Schlema site. Betaproteobacteria are the dominant class (Tab. 2). In terms of the archaeal diversity, the class of Thermoprotei, which belongs to the Crenarchaeota, accounts for about one half or more of the analyzed sequences from both sites. For the Pöhla mine, almost one half of the sequences represents the class of methanomicrobia which are methane producers grouped in the phylum of Euryarcheaota (Tab. 3). High sequence homologies were found for members of the genus Methanolinea *sp.* and Methanosaeta *sp.* ´

Tab. 1: Chemical composition of mine water from the Pöhla and Schlema mine. Only selected anions and cations are listed. All values are given in mg/L.

Analyte	Pöhla	Schlema
Mn	0.23	2.61
Fe	5.63	5.05
As	1.95	1.15
U	0.02	1.74
nitrate	2.61	1.13
sulfate	< 0.5	638
carbonate	292.5	542.5
pH	6.705	6.605

Tab. 2: Bacterial community structure of mine water from the Pöhla and Schlema mine. All values are given in %.

Bacterial Class	Pöhla	Schlema
Alphaproteobacteria	11	9
Betaproteobacteria	45	40
Gammaproteobacteria	0	9
Deltaproteobacteria	0	12
Epsilonproteobacteria	0	6
Acidobacteria	0	3
Sphingobacteria	44	6
unknown	0	15

Tab. 3: Archaeal community structure of mine water from the Pöhla and Schlema mine. All values are given in %.

Archaeal Class	Pöhla	Schlema
Thermoprotei	51	83
Methanomicrobia	44	0
unknown	5	17

ACKNOWLEDGEMENTS. We thank Aline Ritter and Carola Eckardt for ICP-MS and ion chromatography analysis.

[1] Anderson R. T. et al. (2003) *Appl. Environ. Microbiol.* **69**, 5884–5891.
[2] Lane, D. J. et al. (1991) *Nucleic acid techniques in bacterial systematics*, p. 115–175, John Wiley & Sons, Chichester.
[3] Delong, E. F. et al. (1992) *Proc. Natl. Acad. Sci. U.S.A.* **89**, 5685–5689.
[4] Selenska-Pobell S. et al. (2001) *Antomie van Leeuwenhoek* **79**, 149–161.

Response of bacteria in pore water of opalinus clay to addition of nitrate and acetate

S. Selenska-Pobell, G. Radeva,[1] A. Geissler, H. Moors,[2] N. Leys[2]
[1]Institute of Molecular Biology, Sofia, Bulgaria, [2] Belgian Nuclear Research Centre SCK•CEN, Mol, Belgium

Nitrate, nitrite, and acetate addition to opalinus clay (OC) pore water (PW) strongly influence intrinsic bacterial community. One day after the supplementation, the initially present bacteria are overgrown by species not identified in the untreated water. Noticeable is the extreme proliferation of *Pseudomonas stutzeri* capable to reduce NO_3^-/NO_2^- with acetate. We suggest that *P. stutzeri* plays a major role in the earlier measured removal of the supplements from the (OC-PW).

The *in situ* BN experiment performed at the international underground laboratory Mont Terry in Switzerland estimates the risks of release of NO_3^- and organic molecules into the OC due to the weathering of the bitumen containers, foreseen for disposal of long-living radioactive waste. The changes induced by the bitumen degradation products in the OC have many different bio-geo-chemical aspects which may facilitate migration of radionuclides. For this reason, the BN experiment exploits a set of interdisciplinary (chemical, technical, and biological) approaches [1]. Response of bacteria present in the Mont Terri OC-PW to addition of NO_3^-, NO_2^-, and acetate is reported here.

EXPERIMENTAL. Total DNA was recovered from three samples: BN2, representing artificial pore water (APW) which was circulating for 3 months in the interval 2 of the BN test system [1]. The second one (BN2-1) was collected from the interval 2, 24 hours after circulation of APW supplemented with 70 mg/L NO_3^-, 35 mg/L NO_2^- and 46 mg/L acetate; and the third one (BN2-5) was collected at the 5th day after the supplementation. Analyses of bacterial communities in the studied samples were performed by ribosomal intergenic amplification (RISA) using two bacterial primers 16S $rDNA_{968}$ and 23S $rRNA_{130}$, consequent cloning and sequencing of the 16S rRNA gene parts of the amplicons as described in [2].

RESULTS. In the frames of the BN-experiment, complete reduction of NO_3^- to NO_2^- was monitored 3 days after the supplementation with NO_3^-, NO_2^-, and acetate, while the full consumption of acetate was registered at the 5th day [1]. Between 3rd and 5th day, rapid reduction of almost the whole newly accumulated NO_2^- occurred followed by a further slow reduction and removal of the whole NO_2^- two weeks after the treatment (1). Due to the increased turbidity in the analyzed APW and the fast reaction rates of the NO_3^- reduction and acetate consumption, it was concluded that some natural microbial populations supported the above described changes in the APW (1).
In order to answer the question: "Who is involved in NO_3^- and NO_2^- reduction?", we performed direct molecular RISA-analyses of the samples BN2, BN2-1 and BN2-5. The RISA patterns of the three APW samples presented in Fig. 1 designate that the structure of bacterial community in the APW was drastically changed only 24 hours after the supplementation. Differences in the position and the intensity of the predominant RISA bands of the samples BN2-1 and BN2-5 indicate that additional shifting in the bacterial community occurred between the first and the fifth day after the treatment as well.

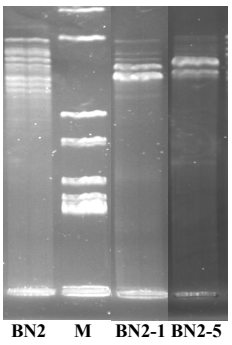

Fig. 1: RISA profiles of the samples collected from interval 2 before (**BN2**), 24 h (**BN2-1**), and 5 days (**BN2-5**) after addition of NO_3^-, NO_2^- and acetate, **M**-molecular marker.

The 16S rRNA gene sequence analyses of the three samples demonstrated that 24 h after the supplementation bacterial community structure of the APW was strongly shifted to α-*Proteobacteria* and newly appeared γ-*Proteobacteria* (compare BN2 and BN2-1 in Fig. 2). In the sample BN2-5 γ-*Proteobacteria* were even more predominant (Fig. 2). In both cases, γ-*Proteobacteria* were limited to one and the same species, namely *P. stutzeri*. As *P. stutzeri* can use acetate as electron donor for NO_3^- reduction our results clearly demonstrate that this species is involved in the reported in [1] rapid reduction of NO_3^- to NO_2^- during the first 3 days after the treatment. The predominance of *P. stutzeri* in the sample BN2-5 is evidence that this bacterium plays the major role also in the monitored in [1] rapid reduction of NO_2^- between the 3rd and 5th days after the treatment. Our suggestion is in agreement with the published capability of *P. stutzeri* to perform fast reduction of NO_2^- to N_2 with acetate under conditions similar to ours [3]. Further analyses will clarify the role (if any) of the other members of the bacterial community in the fast NO_3^- and NO_2^- reduction and also in the slow NO_2^- reduction occurring after the 5th day of the supplementation, after complete consumption of acetate.

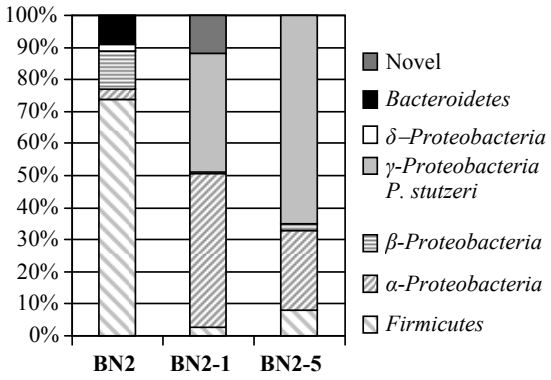

Fig. 2: Shifting in bacterial community structure (percentage of clones) in the pore water of interval 2 (**BN2**), 24 h (**BN2-1**) and 5 days (**BN2-5**) after the addition of nitrate and acetate.

[1] Bleyen, N. et al. (2012) *Clays in natural and engineered barriers for radioactive waste confinement*, p. 755.
[2] Selenska-Pobell, S. et al (2001) *Ant. Van Leeuvenhoek.***79**, 149–161.
[3] Strohm, T.O. et al. (2007) *Appl. Environ. Microbiol*. **73**, 1420–1424.

Uranium in mushrooms related to the iron and manganese concentrations

N. Baumann, T. Arnold, G. Haferburg[1]

[1]Institute of Microbiology, Friedrich-Schiller-University Jena, Germany

Anion contents in the dry masses of nine fruiting body mushroom samples were analyzed. These samples were collected from a test field in a uranium contaminated area in Eastern Thuringia. It turns out, that proximate as more uranium is in the fruiting bodies of mushrooms, as more manganese and iron they have. This could be important in the expectation for evaluable uranium (VI) laser-induced fluorescence signals from material of these fruiting bodies of mushrooms.

The test site, where samples were collected, was installed by the Friedrich-Schiller-University Jena for investigation the interactions between biosphere and heavy metals in soil [1]. From this test site, the uranium speciation in surface water and in pore water samples was identified by time-resolved laser-induced spectroscopy as the $UO_2SO_{4(aq)}$-speciation [2].

EXPERIMENTAL. The collected fruiting bodies from mushrooms were washed, shopped in small chips and dried in an oven at 105 °C, milled in an agate mortar and digested in a mixture of nitric acid and hydrogen peroxide within a microwave. After chemical digestion, the anions were measured with ICP-MS, the values for iron additional were controlled with Graphite furnace AAS.

RESULTS. The uranium concentrations in dry masses from nine mushroom fruiting body samples collected from a heavy metal contaminated site are confronted with their manganese concentrations and their iron contents. The samples are tableted with increasing uranium content in the dry mass. Because the water content on fruiting bodies of mushrooms is 92% or more [3], the uranium concentrations in the dried masses are much higher than in saps of mushrooms. It turns out, as higher the uranium concentration, proximate as higher are the concentrations in the uranium(VI) fluorescence quenching elements iron and manganese.

Tab. 1: Uranium contents in dry masses of different mushrooms collected from the test site, to the opposites to contents in iron and manganese (concentrations in ppb).

	U	Mn	Fe
Tricholoma sulphureum (sulphur knight)	30	30,040	79,470
Leccinum versipelle (orange birch bolete)	35	6,070	304,290
Lactarius torminosus (woolly milkcap)	130	14,870	247,010
Amanita phalloides (death cap)	260	33,770	386,970
Pisolithus arhizus (dyeball)	500	5,970	923,930
Leccinum scabrum (brown birch bolete)	900	72,480	5,077,520
Laccaria laccata (deceiver)	950	69,480	1,017,270
Thelephora terrestris (earthfan)	1,200	98,950	2,79,905
Paxillus involutus (brown roll-rim)	3,470	114,930	10,020,450

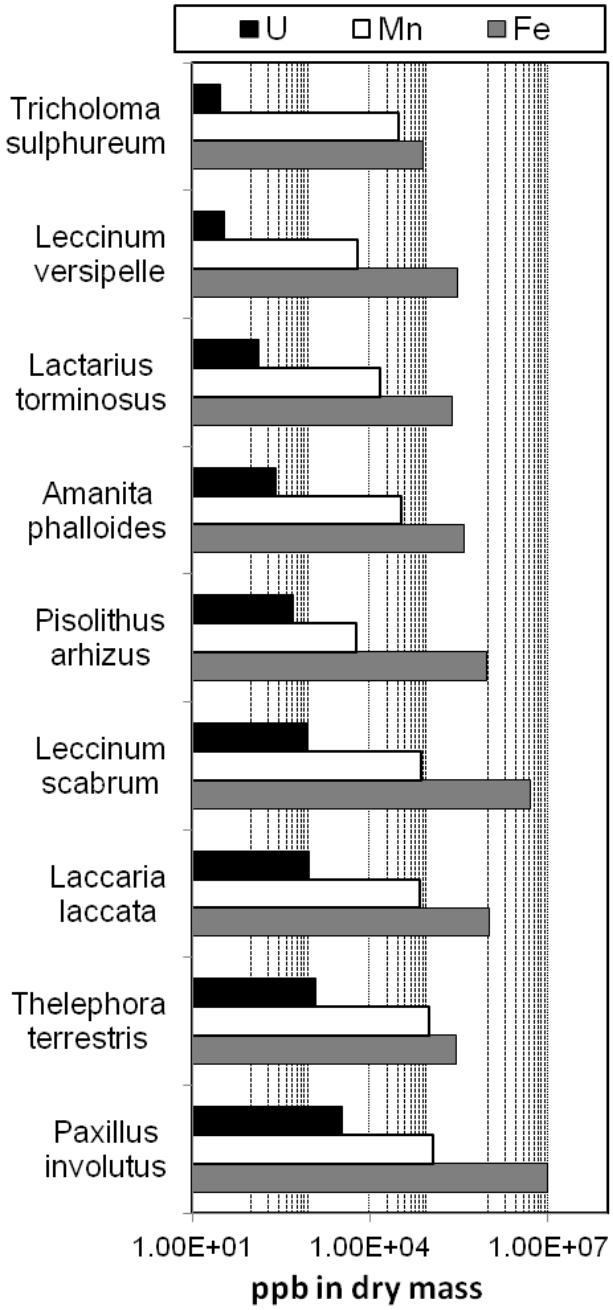

Fig. 1: Uranium contents in dry masses of mushrooms collected from the test site together with contents of iron and manganese. In general, as more uranium as more iron and manganese.

ACKNOWLEDGEMENTS. The authors are grateful to A. Ritter for ICP-MS measurements, EU for funding within the UMBRELLA project, and the Bundesministerium für Bildung und Forschung (BMBF), Project No 02NUK015F, also for support.

[1] Baumann, N. et al. (2012) *Report HZDR-013*, p. 15.
[2] Baumann, N. et al. (2012) *J. Radioanal. Nucl. Chem.* **291**, 673–679.
[3] Donker, H.C.W. et al. (1999) *Biochim. Biophys. Acta-Gen. Subj.* **1427**, 287–297.

LONG-LIVED RADIONUCLIDES IN

FINAL DISPOSAL SYSTEMS

Thermodynamic reference database THEREDA: 4. Implementation of Surface Complexation Modeling

F. Bok, A. Richter, M. Stockmann, V. Brendler

A holistic view of geochemical processes in the context of a safety analysis requires the inclusion of sorption calculations. A thermodynamically consistent treatment of these processes is only possible with surface complexation modeling (SCM). The prospective aim of THEREDA is the provision of a comprehensive and consistent database for both thermodynamic and sorption data for geochemical modeling.

The tabular structure of the thermodynamic reference database THEREDA [1–5] has been enhanced to enable the input and internal conversion of SCM data.

SUPPORTED MODELS. THEREDA will support the following Surface Complexation Models: Diffuse Double Layer Model (DDL), the Constant Capacitance Model (CC), the Non-electrostatic Model (NE), and the 1pK-Basic Stern model (1pK-BS). Most of them are implemented in a variety of speciation codes, namely by PHREEQC and Geochemist's Workbench (both supported by THEREDA).

STORED DATA. For every mineral, the specific surface area (A), the surface site density (N_S), and the equilibrium constants ($\log K$) of the protolysis reaction(s) will be stored. Additionally mineral-specific capacitance values (C) will be kept for the CC and the 1pK-BS model. Equilibrium constants ($\log K$) of the surface complex formations are entered for given combinations of mineral, ligand, and model.
Log K values of protolysis or surface complexation reactions are usually determined at a constant ionic strength (fixed by a background electrolyte). They are entered in THEREDA after extrapolation to infinite dilution using the Davies equation:

$$\log K_0^\circ = \log K_I + \sum_{i=1}^{n} \nu_i \cdot z_i^2 \cdot \left[-A \cdot \left(\frac{\sqrt{I}}{1+\sqrt{I}} - b \cdot I \right) \right] \quad (1)$$

All stored SCM data are valid for 298.15 K only. However, the THEREDA database can be adapted to temperature-dependent surface complexation modeling in the future if required (and sufficient data sets are available).

INTERNALLY CALCULATED DATA. To support Gibbs free energy minimizing speciation codes such as GEMS, the Standard Molar Gibbs Energy of Formation ($\Delta_f G_i^0$) is stored for every surface species. This value is set to 0 J/mol for the neutral surface hydroxyl group by definition. The value for (de)protonated species and surface complexes will be calculated using the equation:

$$\Delta_f G_{i\neq j}^0 = -\mathrm{R}T \ln(10) \log K - \sum_{j\neq i} \nu_j \Delta_f G_j^0 \quad (2)$$

The $\Delta_f G^0$ values for the aqueous species correspond to the thermodynamic values of the Extended Debye-Hückel interaction model.

DATA ASSESSMENT. For a particular combination of mineral and sorbing ligand many different datasets of assumed surface complexation reactions can be found in literature. This leads to completely different surface complex speciation. Figure 1 shows the different results of the SCM calculation of UO_2^{2+} onto goethite using three different sets of $\log K$ values for SCM reactions [6–8].
The drastic differences in the results of these calculations illustrate the need for a comprehensive and self-consistent SCM database. Respective data compiled in RES³T [9] have to be critically evaluated and the refined data to be included in THEREDA.

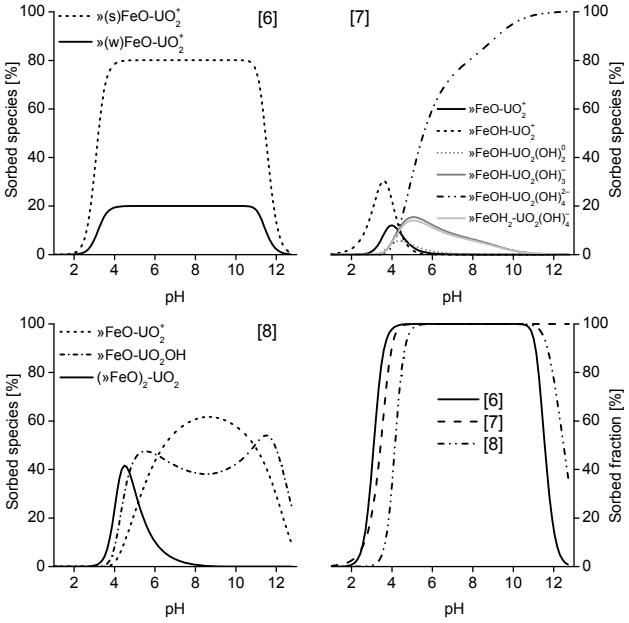

Fig. 1: Surface species diagrams of a 0.1 mM U(VI) solution (I = 0.1 m $NaClO_4$) with 1 g/L goethite using three different data sets of surface complex species [6-8], calculated with Geochemist's Workbench. Only species with an amount >1% were included. Lower right: accumulated fractions of sorbed species.

ACKNOWLEDGEMENTS. The authors wish to thank Steffen Leske for his support in programming various functions of the database.

[1] THEREDA – Thermodynamic Reference Database (2011), *Report GRS-265*.
[2] Richter, A. et al. (2007) *Report FZD-459*, p. 71.
[3] Richter, A. et al. (2009) *Report FZD-511*, p. 57.
[4] Gester, S. et al. (2009) *Report FZD-511*, p. 58.
[5] Richter, A. et al. (2012) *Report HZDR-013*, p. 55.
[6] Dzombak, D.A., Morel, F.F.M. (1990) *Surface Complexation Modeling, Hydrous Ferric Oxide,* Wiley, New York.
[7] Turner, D.R., Sassmann, S.A. (1996) *J. Contamin. Hydrol.* **21**, 311–332.
[8] Missana, T. et al. (2003) *J. Colloid Interface Sci.* **260**, 291–301.
[9] Brendler, V. et al. (2003) *J. Contamin. Hydrol.* **61**, 281–291.

Ranking factors that determine distribution coefficients of radionuclides

M. Stockmann, V. Brendler, J. Flügge,[1] U. Noseck[1]
[1]GRS mbH, Braunschweig, Germany

In order to treat the radionuclide sorption processes in natural systems realistically, the smart K_d concept was implemented into the transport code r³t [1] which is applied to large model areas and very long time scales in long-term safety assessments. This approach has been developed in the framework of the ESTRAL project for the sedimentary overburden of the Gorleben salt dome [2].

The sorption of radionuclides (RN) onto relevant mineral phases of Gorleben sediments was calculated as a function of the most important environmental parameters pH, dissolved inorganic carbon (DIC), ionic strength (IS) and total concentration of [Ca] and [RN] [3, 4]. A bottom-up approach based on surface complexation was used to calculate the smart K_d values, i.e. the sorption of each RN is described as the sum of the competitive sorption of the RN onto each mineral fraction in the different sedimentary units. By coupling the computer codes PhreeqC, UCODE and SimLab, variable smart K_d values were obtained and implemented in the transport code r³t [5]. Sensitivity and uncertainty analysis provided information about the influence of each environmental parameter on the sorption.

RESULTS. The obtained average smart K_d values [6] are in good agreement with the temporally constant conservative K_d values given by Suter et al. (1998) [7], which were previously used in r³t for the retention of RN at the Gorleben site, but now realistic environmental conditions are considered.
In order to test the modified code r³t and to analyze the influence of each environmental parameter on the radionuclide sorption, transport calculations have been performed for a potential future climate transition (seawater transgression). The results of the transport simulations were verified qualitatively for specific points in time and space, and the correlation between the environmental parameters and the smart K_d values was analyzed. These simulations show that

- the implementation of the concept for transport of the environmental parameters works well. Generally, these parameters follow expected trends and major dependencies. The changes in pH, ionic strength, concentrations of [Ca] and [DIC] and dissolution/precipitation of calcite are plausible and can be explained according to the concept for the different states of the climate transition.
- the smart K_d concept also works well and is in accordance with the major dependencies and trends of all considered elements, which were identified in sensitivity analysis. All smart K_d values change according to the changes in environmental parameters. The pH value has the most dominant effect on the smart K_d values for most of the regarded RN, except for Th (and as an analogue Pu), for which the DIC concentration has the strongest impact (Fig. 1).

Under the considered conditions for a possible future climate evolution the smart K_d values of Cs, Ni, Am and Np(V) increase, those of Se(VI) and U(VI) decrease with increasing pH. The smart K_d values of Pu and Th decrease with increasing DIC concentrations. These dependencies can be observed at different points in time, for which different flow and transport patterns are dominant.

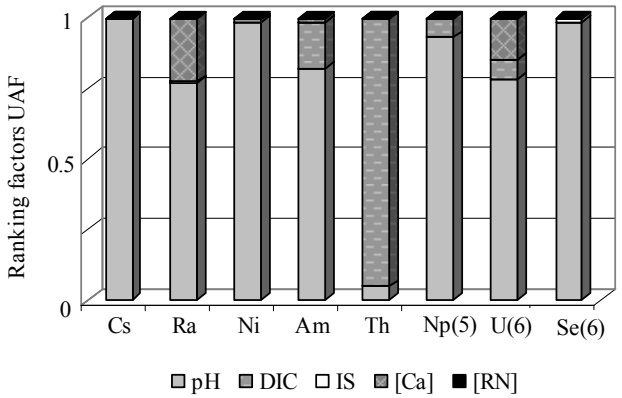

Fig. 1: Ranking factors for the upper aquifer (UAF) at the Gorleben site.

Comparing simulations employing the smart K_d concept with those employing the conservative K_d values [7], it can be shown that the new concept features higher smart K_d values than the conventional K_d values especially in hydrogeological units with higher clay contents. Therefore, the radionuclide distribution is spatially restricted and smaller for the smart K_d concept.
Nevertheless, some of the smart K_d values, calculated on the basis of available thermodynamic sorption data (e.g. for Cs and Ra), seem to be very high. This observation needs to be verified in future studies. Further, additional processes such as redox reactions and ionic exchange as well as the impact of additional competing cations and complexing ligands on RN sorption should be considered in more detail in a follow-up project. Finally, the possibility to apply the concept on highly mineralized solutions using the Pitzer formalism should be investigated.

ACKNOWLEDGEMENTS. This project was funded by the German Federal Ministry of Economics and Technology (BMWi) under contract number 02 E 10518 and 02 E 10528.

[1] Fein, E. (2004) *Report GRS-192*.
[2] Noseck, U. et al. (2012) *Report GRS-297*.
[3] Stockmann, M. et al. (2010) *Report FZD-530*, p. 33.
[4] Stockmann, M. et al. (2011) *Report HZDR-001*, p. 71.
[5] Schikora, J. et al. (2012) *Report HZDR-013*, p. 57.
[6] Stockmann, M. et al. (2012) *Report HZDR-013*, p. 58.
[7] Suter, D. et al. (1998) *Proceedings DisTec 98*.

Data mining with self-organizing maps

A. Rossberg, K. Domaschke

Self-organizing maps (SOM), as a kind of artificial neuronal networks, are used for classification and visualization of height dimensional data. After unsupervised learning, the SOM enables a visualization of these data in lower dimensions, typically by using a two-dimensional map. For a set of spectral mixtures, the standard SOM algorithm yields up to now only rough estimates for the spectral fraction of the spectral components and is not able to extrapolate the spectra of components. We modified the standard algorithm in such a way that these drawbacks are eliminated by a novel supervised learning algorithm [1] so that the modified SOM becomes a complementary method to factor analysis. When compared with factor analysis the SOM shows a higher robustness over experimental error and outliers and has the main advantage that additional physicochemical parameters (pH, concentrations, etc.) can be directly included in the analysis.

EXPERIMENTAL. SOM [1, 2] is tested with a set of 12 spectral mixtures (Fig. 1, left, upper half) calculated by a linear combination of four different sine-functions (Fig. 1, left, lower half), which serve as theoretical component spectra, and the corresponding theoretical spectral fractions (Fig. 1, right). For supervised learning the fractions are given only for spectrum 1, 5, 8 and 12 and the pH is given for all spectra. The SOM consists of 40× 40 neurons. Each neuron contains a spectrum, the fractions of the components, and one pH-value. The SOM-extrapolated component spectra and the determined fractions are compared with the theoretical component spectra and fractions. For two theoretical spectral mixtures (A and B) the "unknown" fractions of the components and pH-values are predicted by using the trained SOM as a look-up table and are compared with the theoretical values (Tab. 1).

Tab. 1: Theoretical and predicted fractions of the four components (C1-C4) and pH-values for spectrum A and B.

	pH	C1	C2	C3	C4
Spectrum A					
Theoret.	1.89	0.64	0.30	0.06	0.01
Predicted	1.79	0.63	0.30	0.05	0.02
Spectrum B					
Theoret.	2.47	0.22	0.37	0.25	0.17
Predicted	2.49	0.21	0.36	0.24	0.18

RESULTS. During training, the SOM with the known entries, i.e. the 12 spectra, the pH-values and the fractions for four spectra, the unknown fractions are determined and the spectra of the four components are extrapolated. The deviation between the theoretical and determined fractions (Fig. 1, right) is 0.6% and the extrapolated component spectra agree perfectly with the theoretical component spectra (Fig. 1, left, lower half). For the determination of the unknown fractions and pH-values for the spectral mixture A and B the neurons are searched on the trained map (Fig. 2) for which the contained spectrum gives the best match with spectrum A and B. When the best matching neurons are localized then the fractions and pH-values can be read out from these neurons. As summarized in Tab. 1, the predicted fractions and pH-values agree very well with the theoretical values (1% and 0.1–0.02 pH units).

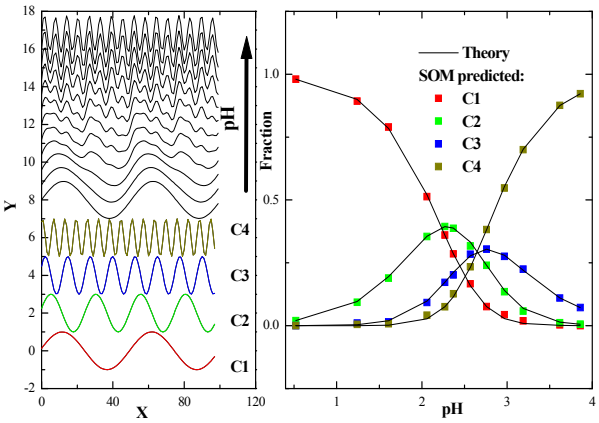

Fig. 1: Left: theoretical component spectra and extrapolated component spectra C1–C4 (lower half), series of spectral mixtures (upper half), right: theoretical (line) and SOM predicted fractions (squares).

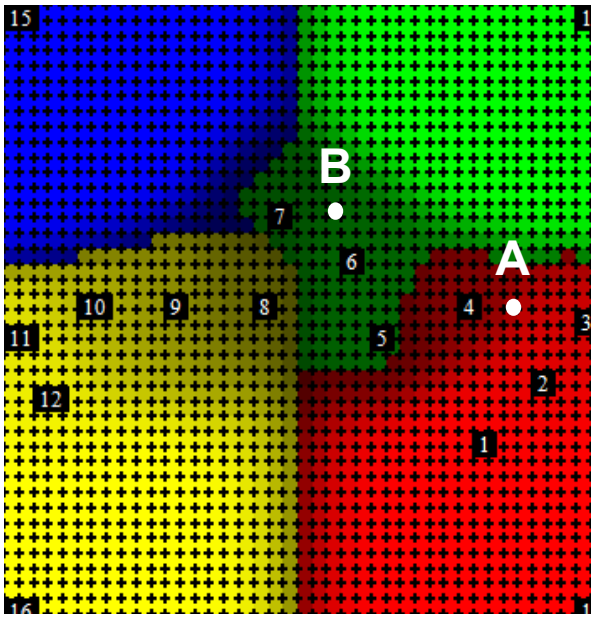

Fig. 2: SOM generated map of the fractional distribution of the components. Each point on the map corresponds to one neuron. The colours correspond to the colours of the components in Fig. 1. As higher the brightness the higher is the fraction of a component. The numbers give the positions of the 12 mixtures on the map (the numbering follows increasing pH). No. 13–16 are the positions of the extrapolated components. A and B are the best matching neuron positions for the mixture A and B.

SUMMARY. In a chemical sense, this theoretical example shows the capability of SOM for the quantification of coexisting chemical species and for the extraction of the spectra of the pure end-member species from spectral mixtures. Moreover, it is shown that physicochemical parameters (pH, etc.), can be directly included as additional information, which would be impossible in the case of factor analysis [3].

[1] Domascke, K. (2013) *Diploma Thesis*, Zittau/Görlitz.
[2] Kuzmanovski, I. et al. (2008) *Chemometr. Inell. Lab.* **90**, 84–91.
[3] Rossberg, A. et al. (2003*) Anal. Bioanal. Chem.* **376**, 631–638.

Numerical simulation of anisotropic diffusion process in Opalinus Clay drill cores and matching with long-term spatio-temporal observations with GeoPET

J. Schikora, J. Kulenkampff, M. Gründig, J. Lippmann-Pipke

In the course of the past decade we established the GeoPET-method allowing the direct, non-destructive, quantitative spatiotemporal visualization of (e.g.) diffusion processes in natural geological media on drill-core scale [1–3]. Here, we couple it with the parameterization of heterogeneous and anisotropic effective diffusion parameters by means of inverse modeling with a finite element based code.
The modeling was done in COMSOL Multiphysics V4.2a which is capable of solving the necessary 3D partial differential equation for anisotropic diffusion and adsorption. The least squares fitting of the diffusion tensor on the GeoPET images was done with the COMSOL Optimization Module using the Levenberg-Marquardt algorithm and parameter sweep for sensitivity analysis [4].
The experimental data were reproduced quite well, but the obtained parameter values for diffusion parallel and normal to the bedding are slightly larger than reported [5].

EXPERIMENTAL. Diffusion experiments were conducted on Opalinus clay drill cores from the Mont Terri Rock Laboratory which were casted into epoxy resin (10 cm diameter, 8 cm length). An axial drill hole (1 mL) was filled with synthetic Opalinus pore water (OPW). After re-saturation of the sample over 3 months the OPW was labeled with ^{22}Na ($T_{1/2}$ = 4.602 a). The propagation of this PET-tracer was monitored with > 20 3D-GeoPET-images in the cause of 7 months. Then the specific activity fell below the detection threshold.

MODELLING. We modeled this experiment with COMSOL Multiphysics® 4.2a (3D convection-diffusion equation, PDE mode, PARDISO solver) for reproducing the observed spatiotemporal concentration distribution data with the differential equation for anisotropic diffusion and adsorption (Fig. 1). The best fit values e.g. of the diffusion tensor were efficiently determined by importing Geo-PET images from various time steps and using then the Levenberg-Marquardt algorithm of the Optimization Module to minimize the sum of squared residuals [4].
Combined with the parameter sweep operation the sensitivity analysis is performed in parallel [4] and covers the range of literature values for porosity and K_d values for $^{22}Na^+$ sorption on Opalinus clay [5].

RESULTS. The simulation reproduced the experimental data quite well (Fig 1, bottom row). From this one sample, the apparent diffusion coefficients normal *and* parallel to the bedding are obtained. The anisotropy value is reasonable and slightly increasing in time (Tab. 1). The obtained parameter values for diffusion parallel and normal to the bedding are slightly larger than reported in [5]. This is in accordance with our observations of an emerging gas bubble in the tracer reservoir. In spite of the long re-saturation period, suction tensions caused by unsaturated clay zones must have significantly influenced the transport regime by an additional advective component. In Tab. 1 the best-fit values of the diffusion coefficients for the GeoPET images of days 3 and 13 are presented. We used the (local) sensitivity test to calculate relative sensitivity indices (SI) as a measure of importance. The larger the SI of a parameter, the larger is the impact of uncertainties in its value on the fitted diffusion tensor. These indices are calculated as the ratio between the resulting relative change of the diffusion coefficient and the relative change of the parameter. The sensitivity analysis was carried out for the parameters: initial tracer concentration c_0, distribution coefficient K_d and porosity ε, separately for the diffusion coefficient parallel and normal to the bedding.
The sensitivity analysis revealed that uncertainties about the initial PET-tracer concentration have a large impact on both diffusion coefficients. The SI`s for the diffusion coefficient parallel to the bedding for the days 3 and 13 are presented in Tab. 2.

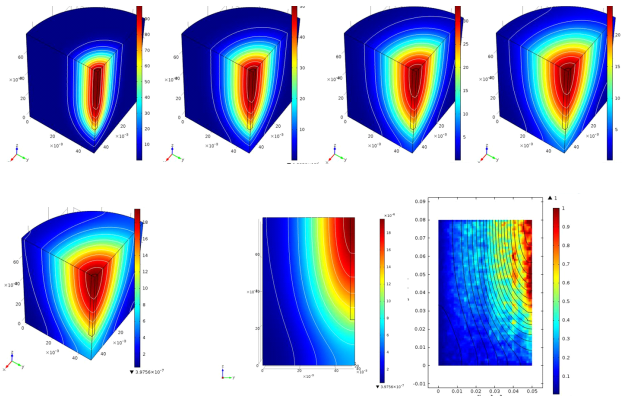

Fig. 1 Top row: 3D-simulation results of Na^+-diffusion in Opalinus clay (from left to right: day 1, 3, 5, 7). Bottom row: Simulated data from day 10: 3D simulation results (left), simulated c(x,z,t) (centre) and GeoPET obtained c(x,z,t) merged with simulated isolines (right). High concentrations are shown in red.

Tab. 1: Best-fit values for diffusion coefficients parallel and normal to the bedding as obtained by least squares fitting of the numerical model to the GeoPET images of day 3 and 13.

	3 d	**13 d**
$D_{parallel}$ [10^{-12} m²/s]	2.65 ± 0.72	2.10 ± 0.36
D_{normal} [10^{-12} m²/s]	2.01 ± 0.62	1.31 ± 0.31
Anisotropy (D_{xx}/D_{yy}) [–]	1.32 ± 0.03	1.60 ± 0.31

Tab. 2: Relative sensitivity indices (SI) for the diffusion coefficient parallel to the bedding.

Parameter	**Change [%]**	**SI (3 d)**	**SI (13 d)**
c_0	+20	1.36	0.86
	−20	1.32	0.78
K_d	+20	−0.27	0.17
	−20	−0.28	0.13
ε	+20	−0.11	0.04
	−20	−0.06	0.04

[1] Richter, M. et al. (2005) *Radiochim. Acta* **93**, 643–651.
[2] Gründig, M. et al. (2007) *App. Geochem.* **22**, 2334–2343.
[3] Kulenkampff, J. et al. (2008) *Phys. Chem. Earth* **33**, 937–942.
[4] Schikora, J. (2012) Diploma thesis, p. 95, Technische Universität Dresden, Dresden, Germany.
[5] Gimmi, T. et al. (2011) *Sci. Tech.* **45**, 1443–1449.

Study of particle deposition and resuspension in pebble beds using PET

T. Barth[1], J. Kulenkampff, M. Gründig, K. Franke, J. Lippmann-Pipke, U. Hampel[1,2]

[1]Institute of Fluid Dynamics, Helmholtz-Zentrum Dresden-Rossendorf, Dresden, Germany; [2]AREVA Endowed Chair of Imaging Techniques in Energy and Process Engineering, Technische Universität Dresden, Germany

The deposition and resuspension of graphite particles in a pebble bed was studied by means of positron emission tomography (PET). Background motivation is the nuclear safety research of graphite dust transport in High Temperature Reactors (HTR). A small-scale test facility was designed to produce a particle laden flow through a model pebble bed. The particles were labeled with the radioisotope fluorine 18 (^{18}F) and the spatiotemporal distribution of the particle deposits was recorded using PET. The existing data set gives a novel 3D insight into the formation of multi-layer deposits in the pebble bed during different accidental scenarios.

Considering a pebble bed type HTR the reactor core is formed out of several thousand graphite pebbles. Carbonaceous dust is formed during reactor operation mainly due to friction between the pebbles and the dust deposits on the inner surfaces of the HTR primary circuit [1, 2]. Fission products diffuse through the graphite matrix and the dust becomes a carrier of radioactivity [3]. In case of a depressurisation of the primary circuit it is of general interest how much of this radioactive dust will be resuspended and might escape the primary circuit.

EXPERIMENTAL. The turbulent flow field was generated by an air-driven small-scale test facility (Fig. 1) consisting of steel pipes, the pebble bed, a particle filter (HEPA) and a radial fan. The outer diameter was adjusted to the inner diameter of the ClearPET™ scanner and the pebbles were fluid dynamically downscaled by the Reynolds similarity. Fluid velocity and particle concentration measurements were performed at the side locations *1* and *2* using an inclined tube manometer to characterize the turbulent flow field. The pebble bed was analyzed by a gamma CT for the determination of the pebble orientation and bed porosity.

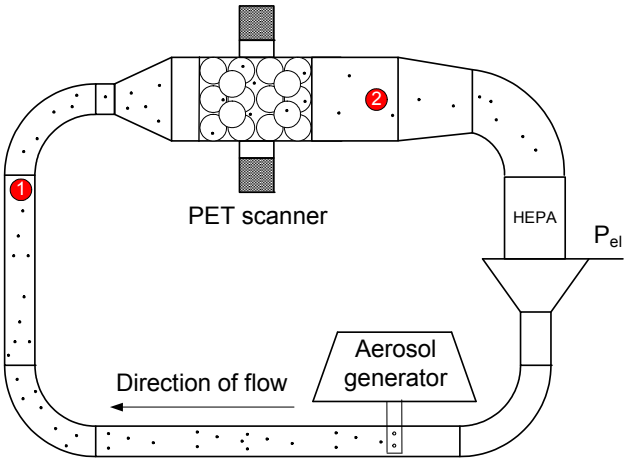

Fig. 1: Schematic drawing of the Pebble Bed Loop.

RESULTS. Two different sets of experiments were performed. In a preliminary study, monodisperse liquid aerosol particles were injected into the flow field. The condensation nuclei were labeled with ^{18}F and the formation of particle deposits in the pebble bed was recorded by means of PET. The use of oil particles allowed to study pure particle deposition over a wide velocity and particle size range. A PET-CT overlay gives an insight into the spatiotemporal distribution of the particles in the pebble bed [4].

In a second study, the oil particles were replaced by technical graphite dust. The graphite particles were also labeled with ^{18}F before being dispersed into the turbulent flow field. Firstly, particle deposition was studied at rather low fluid velocities. Figure 2 displays a PET-CT overlay over $t = 110\ min$ of pure deposition. Activity spots are found on the front sides of the single pebble indicating that the particles enter the pebble bed and deposit on the single pebbles due to inertia impaction. After the deposition scenario the aerosol dispersion was stopped and the fluid velocity was stepwise increased to induce particle resuspension. Once a critical velocity was exceeded, the count rates of the PET scanner instantly dropped down indicating particle resuspension. The present data set gives a completely novel and fully 3D insight into the formation of particle deposits in a pebble bed [5]. The results can be used for CFD code development to simulate the release of carbonaceous dust during accidental scenarios in HTRs.

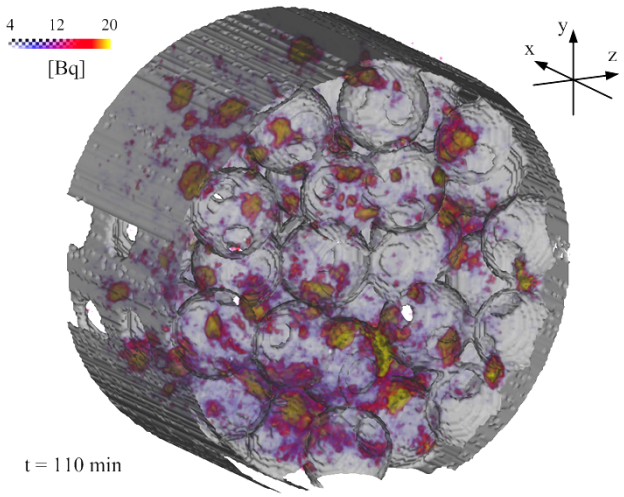

Fig. 2: PET-CT overlay of a graphite particle deposition experiment, mean flow along x-axis, gravity in counter y-direction.

ACKNOWLEDGEMENTS. This work was supported by the EC (Project ARCHER, grant agreement no. 269892).

[1] Kissane, M.P. (2009) *Nucl. Eng. Des.* **239**, 3076–3091.
[2] Moormann, R. (2008) *Science and Technology of Nuclear Installations*, 2008, 1–14.
[3] Seeger, O. et al. (2012) *6th International Topical Meeting on High Temperature Reactor Technology*, HTR2012-3-036, Tokyo Japan.
[4] Barth, T. et al. (2012) *6th International Topical Meeting on High Temperature Reactor Technology*, HTR2012-8-001, Tokyo, Japan.
[5] Barth, T. et al. (2013) *15th International Topical Meeting on Nuclear Reactor Thermal Hydraulics,* 280, Pisa, Italy.

4D process monitoring of reactive tracer transport of [^{64}Cu]Cu(MCPA)$_2$ in a synthetic soil with PET and alignment with numerical flow path evaluation

J. Kulenkampff, A. Mansel, M. Stoll,[1] M. Gründig, K. Franke, J. Lippmann-Pipke
[1]Institute for Geosciences, Johannes Gutenberg University, Mainz, Germany

The pure MCPA (2-methyl-4-chlorophenoxyacetic acid), which is a widely used herbicide, is almost insoluble in water and, thus, immobile. However, traces of metal complexes of MCPA could migrate through soils, depending on the chemical conditions [1, 2]. We observed the propagation of [^{64}Cu]Cu(MCPA)$_2$ in artificial soil columns composed of sand, goethite and illite. The spatiotemporal tracer propagation in the column was observed with Positron Emission Tomography (PET), break-through-curves at the outlet have been recorded.

EXPERIMENTAL. A homogeneous soil column (length: 94.5 mm, diameter: 40 mm, composition by mass: 94% sand, 5% illite, 1% goethite, porosity: 29%) was prepared under CO_2-atmosphere. The column was flushed for 12 days with synthetic pore water (10^{-3} M $NaNO_3$ + 10^{-2} M KF, pH = 6.8).
MCPA was labeled with ^{64}Cu which was cyclotron-produced. The labeling was conducted with 2 mL ^{64}Cu in 0.1 M HNO_3, 1 mg $Cu(NO_3)_2{\cdot}3H_2O$, 2 mg MCPA in synthetic pore water. Then a volume of 5 mL 8×10^{-4} M [^{64}Cu]Cu(MCPA)$_2$ was obtained at adjusted pH 5.
The sample was preconditioned for 4 days with synthetic pore water at pH 5 at a constant flow rate of 0.1 mL/min prior to tracer injection. A tracer pulse of 4 mL, labeled with 235 MBq ^{64}Cu was applied into the column, which had no former contact to Cu(MCPA)$_2$.
The decay time of ^{64}Cu of 12.7 h allowed an observation period with PET of five days. The break-through-curve (BTC) at the outlet of the column could be recorded both with a flow-through-counter and a gamma-counter for 10 days, which corresponds to roughly 400 times the pore volume.
The column experiments were accompanied by batch experiments, in order to study the adsorption of the Cu(MCPA)$_2$-complex. These resulted in a K_D of 3.1 mL/g at pH = 5. Precipitation and dissolution at pH 6.4 have to be considered as well.
The column had to be installed vertically within the field-of-view of the PET scanner, which had been shown adverse effects on image quality, strong circular artifacts, when the standard reconstruction procedure was applied. A more thorough bin-wise normalization and absorption correction procedure and filtering during the iterative reconstruction with the osmaposl-procedure from STIR2.1 [3] resulted in a more satisfying image quality, although no correction of the strong Compton-scatter component was conducted yet.

RESULTS. As anticipated from the results of the batch experiments, both PET-images and the BTC are showing strong retardation of the tracer. The PET-images are showing that the dispersion, which is derived from the BTC is not only caused by the homogeneous packing of the soil, but also by a fraction of faster preferential flow along the wall, where the homogeneity is disturbed. We have to account for this effect by modeling of the flow field and considering a smaller effective volume for chemical interactions.

One special effect occurred at the beginning of the experiment, when the tracer pulse at first rapidly entered the sample and then stagnated as clearly bounded structure for roughly 24 hours. We attribute this effect to the pH-gradient within the sample, because the pH at the outlet was neutral at the start and slowly decreasing, while the injected pH value of the injected fluid was 5. Thus, the structure followed the slowly moving precipitation pH-threshold of 6.4.

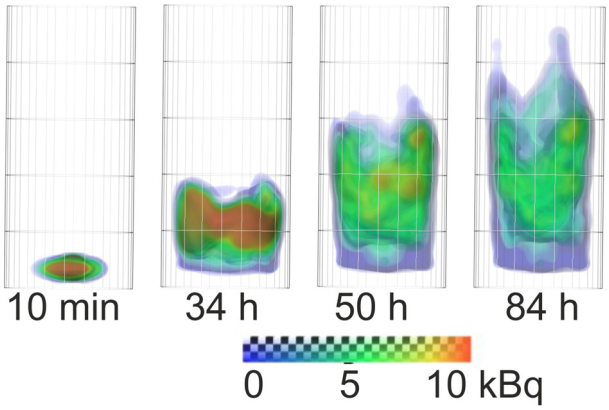

Fig. 1: PET-images of the tracer distribution.

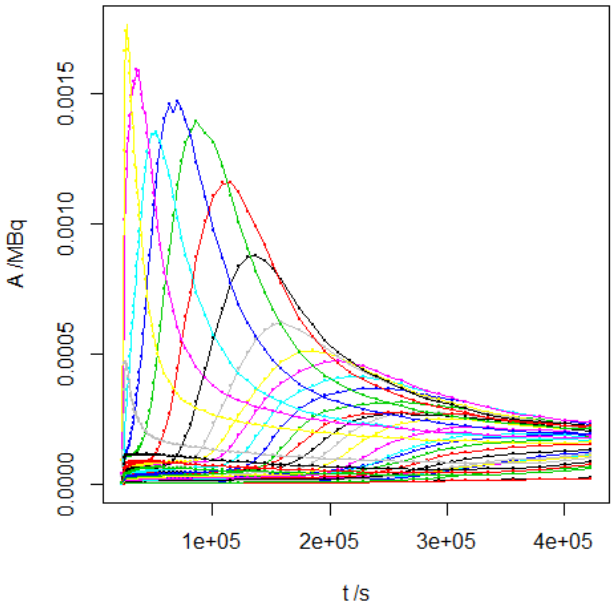

Fig. 2: "Break-through-curves" inside the sample derived by integration of activity over 3.5 mm thick slices of the PET-images.

ACKNOWLEDGEMENTS. This work was supported by grant from DFG within the Priority Program 1315.

[1] Kobylecka, J. et al. (2003) *Thermochim. Acta* **407**, 25–31.
[2] Kobylecka, J. et al. (2008) *Polish J. Environ. Stud.* **17**, 895–901.
[3] Thielemans, K. et al. (2012) *Phys. Med. Biol.* **57**, 867–883.

Equilibrium characteristics of adsorption of humic matter onto kaolinite as revealed by radiotracer studies

H. Lippold, J. Lippmann-Pipke

Interaction with aquatic humic substances can be decisive for the mobility of radionuclides or other contaminants in the subsurface hydrosphere. For a realistic assessment of migration processes, retardation of the humic carriers must be considered. Their behaviour in flow systems is, however, poorly understood. In particular, reversibility of adsorption (prerequisite of a steady local equilibrium) is an open question. In tracer exchange studies by means of ^{14}C-labelled humic material, we were able to demonstrate that a dynamic equilibrium actually exists for the first time. This is in contrast to desorption experiments indicating irreversibility.

In models on reactive humic-bound transport (see [1] for an overview), reaction rates of adsorption and desorption are commonly assumed to be high enough to ensure a dynamic equilibrium under flow conditions. Slow kinetics can be considered, but reversibility remains a prerequisite. For humic matter as a polydisperse system of highly charged colloids, however, it is unclear whether this requirement is actually met. Strong hysteresis [2] and low recoveries in column experiments suggest a limited reversibility of the adsorption process on geomaterials.

EXPERIMENTAL. Kaolinite suspensions (5 g L^{-1} in 0.1 M $NaClO_4$, pH 4.7) were contacted with humic acid at a range of concentrations (4 mg L^{-1} - 180 mg L^{-1}) to cover an adsorption isotherm, including the plateau region. The systems were completed by adding a small amount (0.1 mg L^{-1}) of ^{14}C-labelled humic acid as a tracer, which was prepared by an azo coupling reaction with [^{14}C]aniline [3]. The tracer was either introduced simultaneously together with the non-labelled material (conventional adsorption experiment) or subsequently after an equilibration period of 48 hours (exchange experiment), admitting different exchange periods (6 hours to 4 weeks). The suspensions were rotated end-over-end during these periods. The adsorbed or exchanged amount of humic acid was then determined from the decrease in the concentration of the tracer in the supernatant. Figure 1 shows which information is expected from this experimental approach.

RESULTS. In Fig. 2, adsorption isotherms are shown for both experimental procedures – simultaneous and subsequent addition of radiolabelled humic acid. In the first case, a conventional adsorption isotherm is obtained. It reaches a plateau value at equilibrium concentrations higher than 30 mg L^{-1}, indicating that all available sites are occupied (section B). If the adsorption process is irreversible, the tracer will not be bound when subsequently introduced into these systems. However, adsorption is observed even though the tracer is confronted with saturated surfaces. This clearly shows that there is an exchange between adsorbed state and dissolved state, i.e., the process is reversible.

This dynamic equilibrium is not quantitatively represented by the tracer; the plateaus are situated at intermediate levels, depending on the time of equilibration. The more time the tracer is given for exchange, the more it can progress, and finally approaches the equilibrium state. This kinetic hindrance is in fact limited to the region of surface saturation, as can be seen from the occurrence of a maximum in section A of the isotherms for low times of exchange.

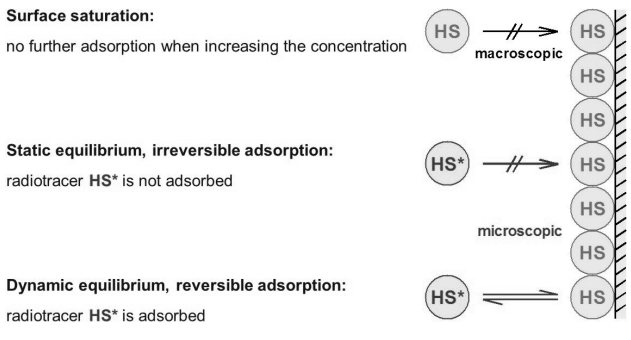

Fig. 1: Principle of radiotracer exchange experiments on the reversibility of adsorption of humic substances (HS) onto geomaterials.

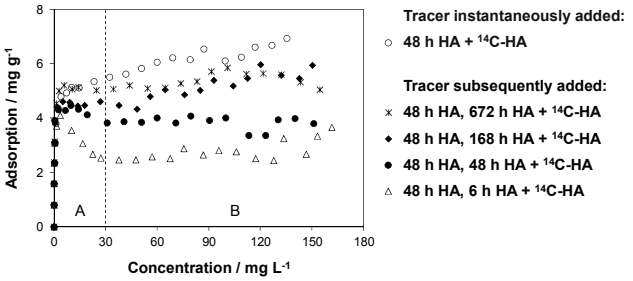

Fig. 2: Isotherms of adsorption of humic acid (HA) onto kaolinite, obtained with ^{14}C-labelled HA as a radiotracer, which was added instantaneously or subsequently after an equilibration period.

Albeit the exchange process takes much more time than attaining the adsorption equilibrium at the bare surface (~ 2 days), these findings are surprising. Earlier desorption experiments, initiated by diluting the supernatant, had not shown any desorption within the same time frame of 4 weeks. Obviously, this is not indicative of a static equilibrium without any exchange. Models for humic-bound transport are thus applicable under comparable conditions.

ACKNOWLEDGEMENTS. This work was funded by the German Federal Ministry of Economics and Technology (BMWi), project agency PTKA-WTE, contract no. 02 E 10176.

[1] Lippold, H. et al. (2009) *J. Contam. Hydrol.* **109**, 40–48.
[2] Gu, B. et al. (1994) *Environ. Sci. Technol.* **28**, 38–46.
[3] Mansel, A. et al. (2007) *Appl. Radiat. Isot.* **65**, 793–797.

On the stability of thorium(IV)-silica colloids

H. Zänker, S. Weiß, C. Hennig

Thorium(IV)-silica nanoparticles show a much higher colloidal stability at near-neutral pH than thorium(IV)-oxyhydroxide colloids. The DLVO contributions and non-DLVO contributions to the forces causing this increased stability are discussed.

The classical approach to explain colloidal stability is the application of the theory developed by Derjaguin, Landau, Verwey and Overbeek (DLVO theory). This theory is based on a superposition of repulsive electrostatic double layer forces and the attractive Van der Waals force [1–3]. Many colloidal systems obey the DLVO theory. However, there are also lots of colloidal systems which do not follow this theory. The latter primarily refers to very hydrophobic and very hydrophilic colloids [4]. In these cases, "hydration forces" between particles may play a role. These forces can be attributed to hydrogen bonding [1] and are also called "structural forces" because they are closely related to the structure of the water close to the particles [1, 2, 4]. Other types of interactions counteracting the DLVO theory are "hydrophobic interactions" or steric interactions. For oxide colloids, Koopal [5] suggested to distinguish between

(i) colloids with gibbsite-type surfaces and
(ii) colloids with silica-type surfaces.

The gibbsite-type colloids, which include colloids of ThO_2 and its analogs ZrO_2 and TiO_2, are amphoteric and show the typical charge *vs.* pH curves with a point of zero charge more or less in the middle of the pH scale. For low electrolyte concentrations, they follow the classical DLVO theory quite well. The silica-type colloids are acidic and can only carry negative charge according to Koopal. They are more stable than gibbsite-type colloids and deviate significantly from the DLVO behavior [6]. A variety of models have been developed to explain the puzzling non-DLVO phenomena that are encountered in the case of silica colloids namely the *hydration force model for silica*, the *gel layer model*, the *hairy layer model* or the *roughness model* (cf. [7] and references therein). Only a few studies exist so far analyzing the stability behavior of colloids consisting of both metal oxide and silica (ZrO_2/silica [8], ferrihydrite/silica [9], UO_2/silica [10]). The aim of this study is to classify the Th(IV)-silica colloids and to assign them to the colloids of type (i) or type (ii).

EXPERIMENTAL. Th(IV)-silica colloids were synthesized as described in [7] and [10]. The zeta potential was determined by laser Doppler velocimetry using a Zetasizer Nano ZS (Malvern).

RESULTS. Figure 1 shows the zeta potential *vs.* pH curves for colloids of pure Th oxyhydroxide, pure SiO_2 and Th(IV)-silica colloids. The zeta potential is a measure of the surface charge of the particles. For oxides such as heavy metal oxides or silica, protons are the potential-determining ions, i.e. the surface charge (and thus the zeta potential) is controlled by the dissociation or association of H^+ [11]. The figure demonstrates that the admixture of silica to the Th(IV) oxyhydroxide changes the zeta potential *vs.* pH curve. The curve becomes shifted toward the curve of pure silica colloids but does not reach the silica curve. Similar results were obtained by Dyer et al. (2010) for the admixture of silica to ferrihydrite particles by Fe(III) precipitation in aqueous silicate solutions. From their zeta potential vs. pH curves Dyer et al. concluded that the surfaces of the particles were a "mixture" of ferrihydrite and silica. Likewise, the surfaces of our Th(IV)-silica particles reflect both the Th(IV) oxyhydroxide behavior and the silica behavior. The negative charge of the colloids gained by the admixture of silica (Fig. 1) will contribute to the repelling force stabilizing the particles in near-neutral solutions.

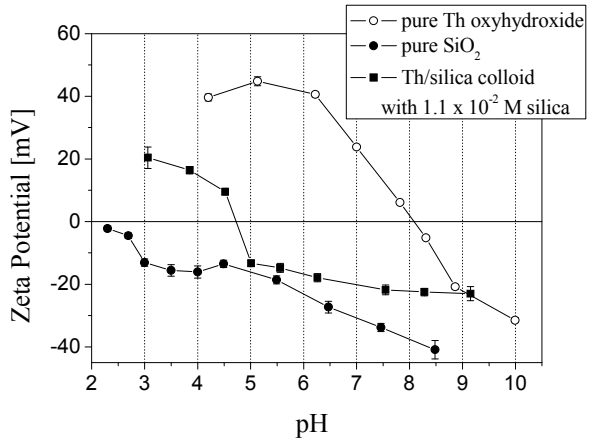

Fig. 1: Zeta potential of Th(IV) oxyhydroxide, SiO_2 and Th(IV)/silica colloids as function of pH (conditions: $[Th] = 1 \times 10^{-3}$ M; $[CO_3]_{ini} = 5 \times 10^{-2}$ M, IS = 5×10^{-2} M $NaClO_4$.

However, the admixture of silica to the colloidal Th(IV) oxyhydroxide also reflects a transition from metal oxide type colloids (or, according to Koopal's terminology, from "gibbsite type" colloids) to silica type colloids (types i and ii). Even though electrostatic repulsion plays an important role for the colloidal stabilization of these particles in the near-neutral pH region, also significant influences of non-DLVO forces such as hydration force and/or other "structural forces" are expected to be of importance. They could explain why the negatively charged Th(IV)-silica colloids are much more stable at pH values around 7 than the positively charged Th(IV) oxyhydroxide colloids (although the absolute value of the zeta potential is very similar for the Th-silica and the Th oxyhydroxide colloids, cf. Fig. 1). Experiments to quantify the DLVO contributions and non-DLVO contributions to the stabilization of Th(IV)-silica colloids are in preparation.

[1] Grasso, D. et al. (2002) *Rev. Environ. Sci. Biotechnol.* **1**, 17–38.
[2] Eastman, J. (2005) *Colloid Science. Principles, methods and applications*, p. 36–49, Blackwell Publishing, Oxford.
[3] Kobayashim, M. et al. (2005) *Langmuir* **21**, 5761–5769.
[4] Yotsumoto, H. et al. (1993) *J. Colloid Interface Sci.* **157**, 426–433.
[5] Koopal, L.K. (1996) *Electrochim. Acta* **41**, 2293–2305.
[6] Yotsumoto, H. et al. (1993) *J. Colloid Interf. Sci.* **157**, 434–441.
[7] Hennig, C. et al. (2013) *Geochim. Cosmochim. Acta* **103**, 197–212.
[8] Kagawa, M. et al. 1986) *J. Am. Ceram. Soc.* **69**, C50–C51.
[9] Dyer, L. et al. (2010) *J. Colloid Interf. Sci.* **348**, 65–70.
[10] Dreissig, I. et al. (2011) *Geochim. Cosmochim. Acta* **75**, 352–367.
[11] Riley, J. (2005) *Colloid Science. Principles, methods and applications*, p. 14–35, Blackwell Publishing, Oxford.

The chemical persistency of thorium(IV)-silica nanoparticles

H. Zänker, S. Weiß, C. Hennig

Thorium(IV)-silica nanoparticles are chemically resistant to multiple washing with pure water.

Tetravalent actinides, An(IV), are sparingly soluble at near-neutral pH and are, therefore, often regarded as immobile in nature. However, insoluble An(IV) compounds can also be mobile in the aquatic environment if they occur as colloids. The following conditions must be fulfilled to generate mobilizing effects of colloids on radionuclide subsurface transport [1–3]:

(iii) colloids must be present in a non-negligible concentration,
(iv) the colloids must be mobile and in stable suspension,
(v) there must be stable binding between the colloids and the radionuclides (slow reversibility or irreversibility).

If one of these conditions is not fulfilled, the role of colloids is negligible. If they all are fulfilled, colloids can significantly influence radionuclide transport. Model calculations for the proposed high-level nuclear waste geologic repository at Yucca Mountain, for instance, imply that colloid-facilitated transport of americium and plutonium leads to a 60-fold increase in the total effective dose equivalent for the relevant population after a delay time of > 10 000 years [4]. Among the three conditions, condition (iii) is of special importance [1, 5, 6]. Therefore, we started experiments to test the chemical persistency of the recently discovered An(IV)-silica colloids (cf. [7, 8]). As a first step, we studied the influence of pure water on thorium(IV)-silica colloids.

EXPERIMENTAL. Silica-containing Th(IV) colloids of different molar Si/Th ratio were prepared according to the methods described in [7, 8]. The particles were subjected to washing experiments. First, the waterborne state was destroyed by acidification of the solutions to pH 6 and centrifugation. Subsequently, the nanoparticles (subnatants of the centrifugations) were re-suspended in pure water and centrifuged again. This was repeated three times (contact time of the particles with the pure water ca. 50 min per washing step). The molar Th/Si ratios before and after the threefold washing were determined by ICP-MS.

RESULTS. Figure 1 demonstrates the stability of the material the thorium(IV)-silica colloids are made of. The molar Si/Th ratio of three initial solutions, of the Th(IV)-silica colloids produced by these solutions, and of these Th(IV)-silica colloids after threefold washing with pure water are compared. One can see that the washing does not noticeably influence the composition of the colloids, i.e. that the colloids are chemically stable insofar as that they do not readily dissolve and no individual component is incongruently washed out under the conditions of the experiment. This seems in direct correspondence with the result of the EXAFS experiments on An(IV)-silica colloids reported in [7, 8] according to which the An-O-An bonds of the colloids are replaced by An-O-Si bonds with increasing silicate concentration, i.e. a relatively stable non-stoichiometric chemical compound of An(IV) and silica is formed.

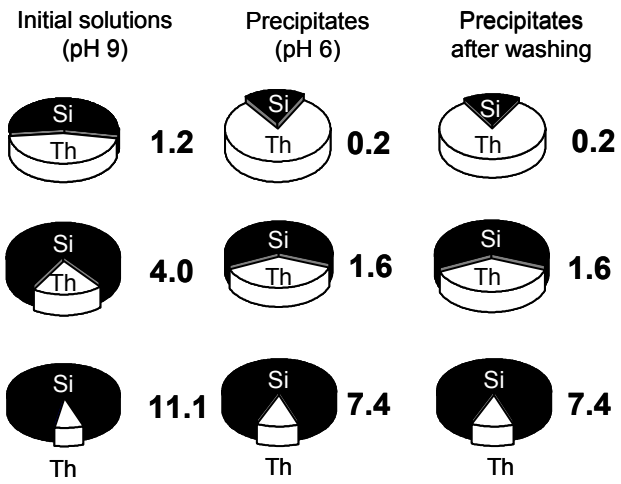

Fig. 1: Molar composition of initial solutions and solid Th(IV)-silica precipitates before and after three-fold washing with water. The numbers give the molar Si/Th ratios.

As mentioned above, the question of chemical persistency is crucial for the behavior of contaminant-containing nanoparticles in geochemical scenarios. As particles that are not persistent are carried beyond a region in which the dissolved and colloid-borne contaminants are in equilibrium, the particles will release their contaminants (or will completely dissolve) and equilibrium between the mobile phases and the stationary rock or sediment phases will re-establish. However, as the strength of the contaminant-colloid association increases, the time to reach equilibrium increases, resulting in increased distances for colloid-facilitated transport [1]. The results of Fig. 1 do not indicate fast destruction of the Th(IV)-silica particles.
Nevertheless, we are still far from being able to draw definitive conclusions on the issue of persistency of these colloids in subsurface actinide transport. First, the time frame of our washing experiments was too short to allow conclusions on geochemical scenarios. Second, we used pure water as the "leachant", pure water is not encountered in nature. Natural waters, i.e. silicate-containing waters should be less "aggressive" to the Th(IV)-silica colloids than pure waters. In former experiments, we showed that silicate-containing waters of relatively low Si concentration (0.24×10^{-3} or 0.5×10^{-3} M; cf. Tab. 3 in [7]) did not cause *destruction* of U(IV) colloids but, on the contrary, *formation* of U(IV)-silica colloids. Washing experiments with both pure waters and silica-containing waters applying significantly longer contact times between particles and water are underway.

[1] Ryan, J.N. et al. (1996) *Coll. Surf. A: Physicochem. Eng. Aspects* **107**, 1–56.
[2] Missana, T. et al. (2004) *Appl. Clay Sci.* **26**, 137–150.
[3] Geckeis H. et al. (2011) *Actinide Nanoparticle Research*, p. 1, Springer, Berlin.
[4] Contardi, J.S. et al. (2001) *J. Cont. Hydrol.* **47**, 323–333.
[5] Vilks, P. et al. (2001) *J. Cont. Hydrol.* **47**, 197–210.
[6] Kurosawa, S. et al. (2006) *J. Colloid Interf. Sci.* **298**, 467–475.
[7] Dreissig, I. et al. (2011) *Geochim. Cosmochim. Acta* **75**, 352–367.
[8] Hennig, C. et al. (2013) *Geochim. Cosmochim. Acta* **103**, 197–212.

Recoil labeling of nanoparticulate TiO_2, Ag^0 and multiwall carbon nanotubes with ^7Be

H. Hildebrand, S. Schymura, I. Cydzik,[1] F. Simonelli,[1] A. Bulgheroni,[1] U. Holzwarth,[1] J. Kozempel,[1] N. Gibson,[1] K. Franke

[1] European Commission, DG Joint Research Centre, Institute for Health and Consumer Protection, Nanobiosciences Unit, Ispra, Italy.

Radiolabeling techniques provide the great opportunity of highly sensitive traceability and detectability of nanoparticles (NP) in small quantities and complex matrices. Recoil labeling is one option to implement radiotracers inside the NP inner structure which is also feasible for nanomaterials that cannot be easily directly activated due to a lack of suitable nuclear reactions. Within this study, nanoparticulate TiO_2, Ag^0 and multiwall carbon nanotubes (MWCNT) were radiolabeled with ^7Be ($t_{1/2}$ = 53.12 d) that was produced via proton irradiation of a LiH/NP mixture using the nuclear reaction $^7Li(p,n)^7Be$. Successful radiolabeling of all three types of NPs could be achieved.

EXPERIMENTAL. Recoil labeling was conducted by proton irradiation of powdered mixtures of NPs and LiH in order to use the nuclear reaction $^7Li(p,n)^7Be$ for implementation of ^7Be inside the NPs [1, 2]. Briefly, powdered targets were prepared by mixing LiH in a ratio of 2 : 1 (w/w) with TiO_2-NPs (P25, Evonik Degussa, d_p = 21 nm), 1 : 1 (w/w) with MWCNT (SES research, d_p = 10–30 nm, l = 1–2 µm) and 3 : 1 (w/w) with Ag^0-NPs (Sigma-Aldrich, d_p < 100 nm). Figure 1 shows the experimental setup, detailed information is given in reference [3]. The NP/LiH mixtures are filled in a sealed capsule (1–4). This capsule is inserted in a holder (5) that allows the capsule to be fully immersed in cooling water flowing across the front and rear side. The capsule holder is inserted in the target block (7), sealed by an O-ring (6) and fixed by screws. The target block is inserted in a vacuum chamber connected to the beam line of the cyclotron (Scanditronix MC40, JRC), centered on the beam axis and connected to the cooling system (8).

Irradiation parameters were chosen as the following: TiO_2-NP: Ep = 4.34 MeV, Ip = 2.5 µA, 17.5 µAh; Ag^0-NP: Ep = 4.34 MeV, Ip = 1.0 µA, 8.0 µAh; MWCNT: Ep = 4.34 MeV, Ip = 10.0 µA, 55.5 µAh. During irradiation ^7Be is emitted from LiH and implemented inside the NPs due to recoil energies. Active NP targets were further processed by subsequent washing (10 washing steps) of the powders with ethanol, ethanol/water mixtures and finally with pure water to eliminate LiH and unbound ^7Be. Radiolabelling stability and yield were quantified using gamma spectrometry measurements. NP size and size distribution and zeta potential in aqueous media was compared before and after radiolabeling using scanning electron microscopy and dynamic light scattering techniques (Zetasizer Nano, Malvern). Limits of detection were determined using either a gamma counter (TiO_2 and Ag^0, 1480 Wallac wizard 3'', Perkin Elmer) or liquid scintillation counting (MWCNT).

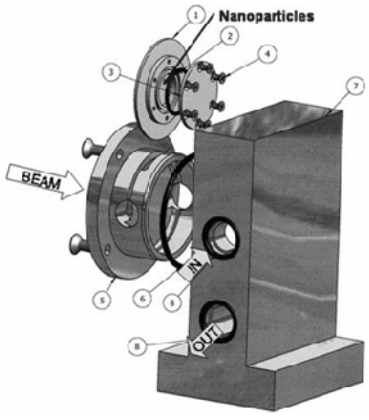

Fig. 1: Design of a target system for activating NPs by use of proton beams [3]. Numbers are explained in the experimental section.

RESULTS. Successful radiolabeling of all three types of NPs under study could be achieved using the ^7Be recoil implantation method. Concerning the radiolabeling yield and radiolabel stability, significant differences between the three nanomaterials became obvious. For TiO_2 and Ag^0 NPs, those are considered as dense materials; about 20% of the initial ^7Be generated was implemented inside the NPs. Within the first three washing steps, LiH and unbound ^7Be were completely washed away and activity concentrations of [^{7}Be]Be-TiO_2 and [^{7}Be]Be-Ag^0 NPs remained stable within the following 7 washing steps. For MWCNT, linear ^7Be release could be observed within the first 7 washing steps and stability of the activity concentration of [^{7}Be]Be-MWCNT was finally found within the last 3 washing steps. This could be explained by the fact that ^7Be can only be implemented in the space between the walls of the MWCNTs (Fig. 2).

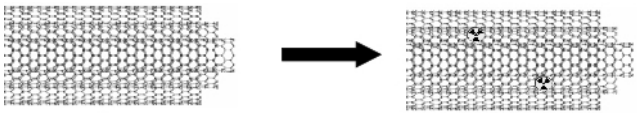

Fig. 2: ^7Be implantation in MWCNTs via proton irradiation of ^7Li and recoil labeling.

Final activity concentrations were determined as 8.7×10^4 Bq/mg for [^{7}Be]Be-TiO_2, 3.8×10^4 Bq/mg for [^{7}Be]Be-Ag^0 and 5.5×10^4 Bq/mg for [^{7}Be]Be-MWCNT. Detection limits were found to be in the range of 100 µg/L for all NPs under study and aqueous NP suspensions. Stability of the NP properties such as particle size and morphology were analyzed and compared with the pristine materials. For TiO_2 and MWCNTs, no significant change of particle properties could be detected. SEM imaging clearly showed that especially the morphology of the MWCNTs remained unaltered. Radiation damage of the nanotubes, potentially caused by the recoil implantation of ^7Be, could not be observed. Zeta potential remained unaltered in the range of pH 2–10. For Ag^0-NPs, slight changes in particle size distribution could be observed. Although intensive cooling and low energy input into the sample was ensured, some sintering of the NPs occurred. Nevertheless, this recoil labeling technique proved to be feasible for generating radiolabeled NPs with useful activity concentrations for various experimental setups.

ACKNOWLEDGEMENTS. This work was financially supported by the QNano Transnational Access program (JRC-TAF-13 and JRC-TAF-23).

[1] Cydzik, I. et al. (2011) *3rd-INCC*, 18–23.09.11, Palermo, Italy.
[2] Kozempel J. et al. (2012) *NRC 8*, 16–18.09.12, Como, Italy.
[3] Holzwarth, U. et al. (2012) *J. Nanopart. Res.* **14**, 880.
[4] Schymura, S. et al. (2012) annual *Cycleur Meeting*, 29.–30.11.12 JRC, Ispra, Italy.

Radiolabeling of carbon nanotubes using the Iodogen reaction

S. Schymura, F. Schörg,[1] A. Sanchez-Castillo,[1] K. Franke
[1]Institute of Physical Chemistry, University of Stuttgart, Stuttgart, Germany

The risk assessment of a nanoparticle release into the environment is dependent on a suitable method for tracking said particles. We here report the possible route of radioiodination using the one-pot Iodogen method for the radiolabeling of carbon nanotubes.

Carbon nanotubes (CNT), cylinders of sp^2-hybridized carbon, show intriguing physical properties. Since their discovery in 1991 [1], a substantial amount of research was put into their application. A critical assessment of their mobility and fate in the geosphere and their ingestion by living organisms is mandatory. However, the monitoring of nanoparticles in complex natural systems like geological formations, ground water or organisms is nearly impossible using conventional methods, especially in the low concentrations which are environmentally relevant. In order to investigate these issues, a rapid, reproducible way of radiolabeling is highly desirable. Most radiolabeling processes for CNT, like binding radiolabeled chemicals on the CNT sidewall [2] or synthesizing them using radiolabelled precursors [3], are in need of elaborate chemistry and often also greatly influence the properties of the CNT due to large substituents. The radioiodination of CNT is a versatile method minimizing the intrusion.

EXPERIMENTAL. The carbon nanotubes were radiolabeled using the Iodogen (1, 3, 4, 6-tetrachloro-3α-6α-diphenylglycouril) method adopted from protein labeling [4]. Iodogen (25 µL of a 2 mg/mL solution in chloroform) was coated onto the inner wall of an Eppendorf tube by evaporation of the chloroform. A dispersion of 200 µg of CNT in 200 µL of phosphate buffered water as well as typically 200 kBq of [$^{125/131}$I]NaI was added into the tube. The tube was put into an ultrasonic bath to keep the CNT in dispersion during the 4 h labeling process. Transferring the reaction mixture into another uncoated tube finished the reaction. Remaining unreacted iodine was washed away in 2–4 washing steps until the radiolabeled particles remained stable in the absence of light.

RESULTS. It was possible to stable label carbon nanotubes using the procedure outlined above. In general, the Iodogen acts as oxidizing agent which converts the unreactive iodide I^- into the reactive species I_2 or I^+ [5] which then perform an electrophilic attack onto the CNT side wall forming a covalent carbon-iodine bond [6]. Single wall CNT proved to be more reactive than multi wall CNT, as their higher curvature renders them more reactive. Corresponding to that the yield further decreases for graphite. The yield was independent of the pH value in case of ^{125}I in the tested pH range of 6–8.
No change of the ζ potential or the D : G Raman band ratio could be observed confirming the non-intrusiveness of the method.

CONCLUSION. A versatile method for CNT radiolabeling was developed without the setback of largely changing the CNT properties. The possible use of ^{124}I enables PET-studies.

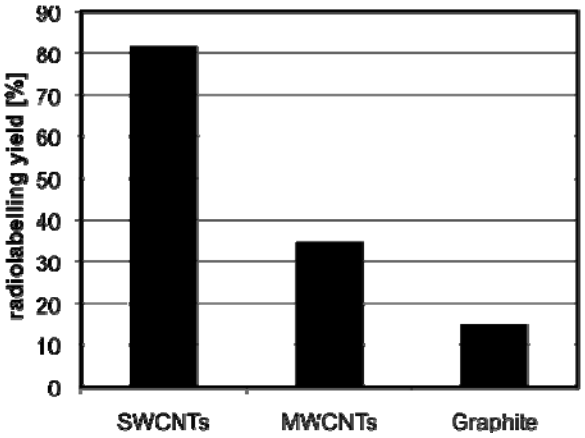

Fig. 1: Radiolabeling yields for 200 µg carbon nanoparticles reacted with 200 kBq [^{131}I]NaI in distilled water.

ACKNOWLEDGEMENTS. Financial support by the Deutsche Forschungsgemeinschaft is gratefully acknowledged (support code: FR1643/3-1).

[1] Iijima, S. (1991) *Nature* **345**, 56–58.
[2] Singh, R. et al. (2006) *Proc. Natl. Acad. Sci. U.S.A.*. **103**, 3357–3362.
[3] Petersen, E.J. et al. (2008) *Environ. Sci. Technol.* **42,** 3090–3095.
[4] Fraker, P.J. et al. (1978) *Biochem. Biophys. Res. Comm.* **80**, 849–857.
[5] Preedy, V.R. et al. (2009) *Comprehensive Handbook of Iodine*, Academic Press, London.
[6] Deng, X. et al. (2008) *Nanotechnology* **19**, 075101.

Interfacial reactions of Sn(II) with anatase (TiO_2): EXAFS and surface complexation modeling

S. Dulnee, B. Merkel,[1] A. C. Scheinost
[1]Department for Geology, TU Bergakademie Freiberg, Freiberg, Germany

Sn(II) is a contaminant of general environmental interest, but little is known about its interaction and retention by mineral surfaces. We have selected the redox-inactive mineral anatase (TiO_2) to study the surface complexation mechanism by combining EXAFS-derived surface structures with surface complexation modeling to model the macroscopic sorption behavior. Three adjustable parameters required for diffuse double layer model were determined in this study: the surface site density (16 sites/nm^2), and two log K^+ values (4.76 ± 0.36 and −9.90 ± 0.42) of the protolysis reactions. EXAFS spectra show Sn(II)–Ti distances at 3.26 and 3.60 Å indicating the formation of monodentate and bidentate inner-sphere sorption complexes. Four surface complexes, Anat_sOSn$^+$, Anat_sSnOH, Anat_sOH(Anat_sO)Sn$^+$, and (Anat_sO)$_2$Sn, with log K values of 3.66, 3.68, 4.63, and 4.41, respectively, were required to model the sorption data.

EXPERIMENTAL. Anatase was obtained from [1]. It was equilibrated in 0.01 M NaCl at least 24 h before use in sorption experiments and acid-base titrations.
Sorption experiments were conducted in the pH range 2 to 9 in a Jacomex glove box with O_2 level less than 2 ppm. All test tubes were wrapped in aluminum foil to prevent photocatalytic redox reactions. We used 2 g/L anatase and 10 µM Sn(II) initial solution concentration. After equilibration for 24 h, suspensions were centrifuged and Se(II) in the supernatant was determined by ICP-MS, while the wet-pastes were used to determine the interfacial reaction of Sn(II) with anatase by X-ray absorption spectroscopy (XAS) at The Rossendorf Beamline at ESRF using the Sn K-edge (29,200 eV). Surface complexation modelling and estimation of log k values was carried out by using PHREEQC and PEST codes and the MINTEQ.V4 database.

RESULTS.
Interfacial reactions of Sn(II) on anatase. The XANES edge energy of 29,203 keV and a fit of the EXAFS coordination shell with 3 to 4 O atoms at a distance of 2.09 Å confirmed that the divalent oxidation state of Sn(II) was maintained in all samples. Two Sn–Ti distances of about 3.26 and about 3.58 Å were found, indicative of two different binding coordinations. For the sample prepared with the shortest reaction time of 4 h under neutral pH, Sn(II) is coordinated to only one Ti atom at 3.60 Å indicative for the formation of a monodentate surface complex. A stronger Sn–Ti scattering at 3.26 and 3.58 Å with coordination numbers of 2 to 4 indicated formation of bidentate surface complexes. These surface complexes were found in the samples prepared with longer reaction times (>4 h). The bidentate complexes may form either at two acid surface OH groups (bridging OH groups) or at two basic surface OH groups (terminal OH groups), exchanging H^+ with cations and OH^- with anions, respectively. The possible Sn(II) surface complexation structures are shown in Fig. 1. The first scheme in Fig. 1 depicts the formation of a Sn(II) complex on an O-vacancy of anatase.

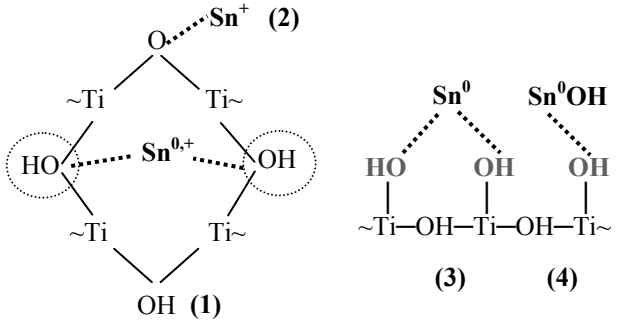

Fig. 1: Scheme of the possible Sn(II) surface complexation structures.

Surface complexation modeling. The surface site density of anatase as investigated by fast backward titration was determined to be 15.94 sites/nm^2. The two equilibrium constants of the protolysis reactions were optimized as 4.76 ± 0.36 and −9.90 ± 0.42, which are in the expected range in line with previous work [2, 3]. Equations (1) to (3) describe the acid-base surface sorption of anatase and equations (4) to (7) represent the surface complexation reactions.

$$C_a - C_b = H^+ - OH^- + Anat\_sOH_2^+ - Anat\_sO^- \quad (1)$$
$$Anat\_sOH + H^+ \rightarrow Anat\_sOH_2^+ \quad (2)$$
$$Anat\_sOH \rightarrow Anat\_sO^- + H^+ \quad (3)$$
$$Anat\_sOH + Sn^{+2} \rightarrow Anat\_sOSn^+ + H^+ \quad (4)$$
$$Anat\_sOH + Sn(OH)_2 \rightarrow Anat\_sOSnOH + H_2O \quad (5)$$
$$2Anat\_sOH + Sn^{+2} \rightarrow Anat\_sOH(Anat\_sO)Sn^+ + H^+ \quad (6)$$
$$2Anat\_sOH + Sn(OH)_2 \rightarrow (Anat\_sO)_2Sn + 2H_2O \quad (7)$$

Note that positive and zero charges of the Sn(II) complexes Sn^{+2} and $Sn(OH)_2$ facilitate the formation of inner-sphere surface complexes. Not only monodentate but also bidentate complexes are feasible. Their optimized logarithmic equilibrium constants are 3.66, 3.68, 4.63, and 4.41, which provide a good fitting of the observed data (Fig. 2). Moreover, the formation of a bidentate complex without the release of H^+ may take place (Eq. (6), as was also proposed by Gunneriusson [4].

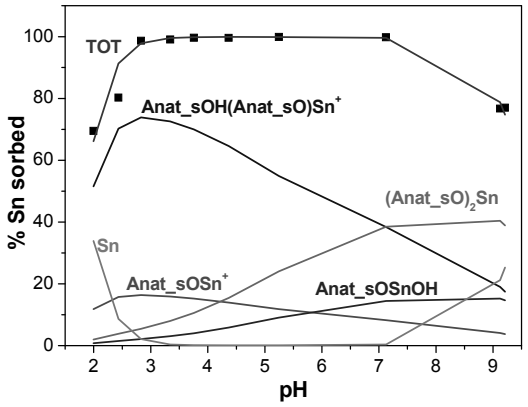

Fig. 2: Distribution of Sn(II) surface species.

[1] Comarmond, M.J. et al. (2011) *Environ. Sci. Technol.* **45**, 5536–5542.
[2] Ludwig, C. et al. (1995) *J. Colloid Interf. Sci.* **169**, 284–290.
[3] Weng et al. (1997) *Wat. Sci. Tech.* **35**, 55–62.
[4] Gunneriusson , L. (1993) *PhD thesis.*

Sorption of Se(IV) oxyanions onto maghemite

N. Jordan, A. Ritter, S. Weiß, A. C. Scheinost

The sorption of Se(IV) onto maghemite was investigated. It was found to decrease upon increasing pH, while no impact of ionic strength could be noticed. Zeta potential measurements showed that the pH_{IEP} of maghemite was significantly shifted towards lower pH values upon Se(IV) sorption. EXAFS measurements revealed the formation of bidentate binuclear and bidentate mononuclear inner-sphere complexes (IS) during the sorption process, whose proportion were pH-dependent.

In the context of nuclear waste management, ^{79}Se could be one of the major isotopes contributing to the global radioactivity potentially reaching the biosphere. Maghemite (γ–Fe_2O_3) is a ubiquitous iron oxide in the environment and is also part of the corrosion products of stainless steel canisters. In addition, maghemite ability to remove inorganic pollutants like U(VI), As(V), Cr(VI), Mo(VI), U(VI) was already shown and its magnetic properties eases the separation process. Thus, this study was aiming at characterizing at both macroscopic and molecular levels the sorption process of Se(IV) onto maghemite.

EXPERIMENTAL. Maghemite was purchased from Alfa Aesar and has a specific surface area of 38 m^2 g^{-1}. The detailed description of the performance of batch sorption studies, zeta potential measurements and EXAFS experiments is given elsewhere [1].

RESULTS. The sorption of Se(IV) onto maghemite is at maximum in the acidic pH range and decreases with increasing pH. However, no impact of the ionic strength was observed (Fig. 1). EXAFS evidenced the absence of heterogeneous reduction of Se(IV) at the maghemite surface, showing that only sorption processes are responsible for its removal from the aqueous phase.

Upon Se(IV) sorption, the pH_{IEP} of maghemite was significantly shifted towards lower pH values (Fig. 2). Observations from batch and zeta potential measurements are both strong macroscopic indications of inner-sphere complexation mechanism [1, 2].

EXAFS measurements (Fig. 3) revealed the formation of two inner-sphere complexes, namely bidentate binuclear corner sharing ^2C and bidentate mononuclear edge-sharing complex ^1E. At low surface loading (i.e. pH 8), the ^1E complex is predominant while the formation of ^2C takes place upon increasing surface loading (i.e. lowering pH). Based on structural information [3–5], we hypothesize that edge sites, located e.g. at the (110) facet, are high energy sites and active at low surface loading, while the formation of ^2C complexes takes place at facets having rows of octahedra with singly coordinated oxygens (low energy sites), namely the (100) facet.

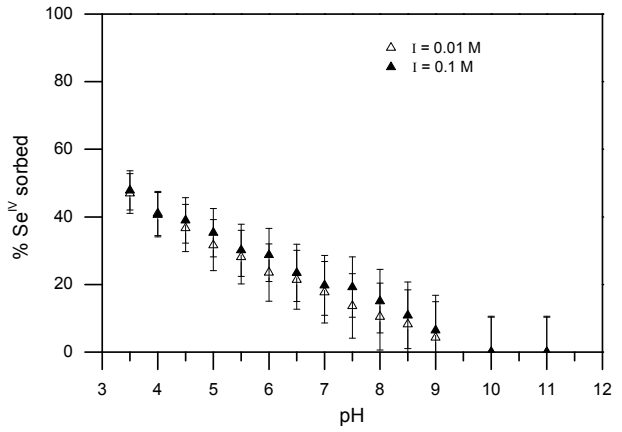

Fig. 1: Sorption edges of Se(IV) onto maghemite. m/v = 0.25 g L^{-1}, 0.1 and 0.01 M NaCl, $[Se^{IV}]_{initial} = 5 \times 10^{-5}$ M, 2 days of shaking.

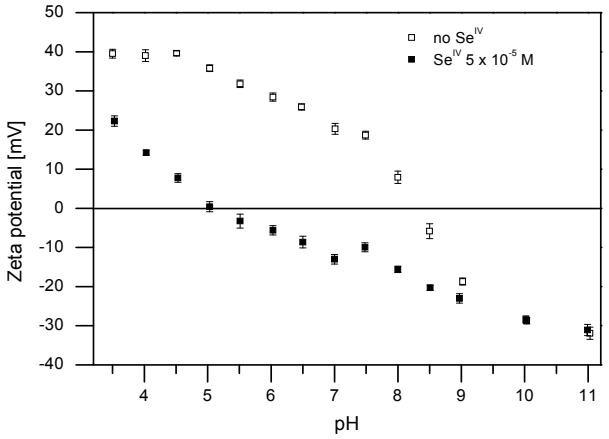

Fig. 2: Zeta potential of maghemite (open diamonds) and the effect of Se(IV) sorption (filled squares), m/v = 0.25 g L^{-1}, $[Se^{IV}]_{initial} = 5 \times 10^{-5}$ M, 0.1 M NaCl, 2 days of shaking.

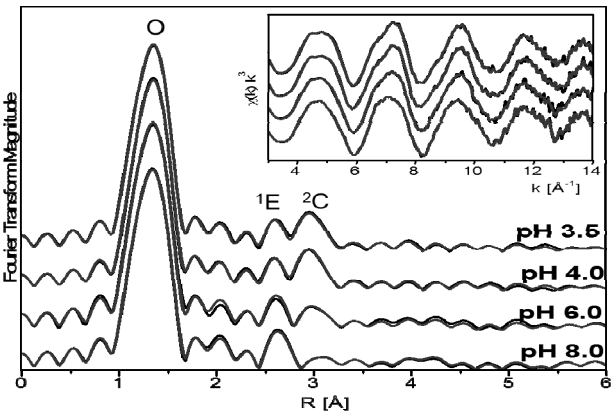

Fig. 3: Fourier transform magnitude spectra of maghemite-reacted selenium(IV) at different pH, m/v = 0.25 g L^{-1}, $[Se^{IV}]_{initial} = 5 \times 10^{-5}$ M, 0.1 M NaCl, 3 days of stirring.

Due to incompatible structure, the formation of a tridentate hexanuclear corner-sharing complex ^3C on vacant tetrahedral sites located at the (111) facet was not noticed, contrary to former observations during As(III), As(V) and Sb(III) sorption onto magnetite and maghemite [3–6].

[1] Jordan, N. et al. (2013) *Geochim. Cosmochim. Acta* **103**, 63–75.
[2] Elzinga, E.J. et al. (2009) *J. Colloid Interf. Sci.* **340**, 153–159.
[3] Wang, Y. et al. (2011) *Environ. Sci. Technol.* **45**, 7258–7266.
[4] Wang, Y. et al. (2008) *Geochim. Cosmochim. Acta* **72**, 2573–2586.
[5] Auffan, M. et al. (2008) *Langmuir* **24**, 3215–3222.
[6] Kirsch, R. et al. (2008) *Miner. Mag.* **72**, 185–189.

Impact of salinity on the sorption of selenate onto aged γ-Al_2O_3 in the context of salt dome repositories

C. Franzen, D. Hering,[1] N. Jordan
[1]University of Applied Sciences, Zittau/Görlitz, Germany

Sorption of Se(VI) onto γ-Al_2O_3 was investigated at different ionic strengths (NaCl) within the reaction fluid. The decrease of Se(VI) sorption at higher salt concentrations can be attributed to a change in the surface charge of γ-Al_2O_3.

^{79}Se is expected to be one of the fission products most contributing to the potential radiation dose according to safety assessments of nuclear waste underground repositories. Its retardation is influenced by background salts which are important with regard to salt domes as potential deposits.

EXPERIMENTAL. Batch experiments were conducted at a solid-to-solution ratio of 1 g L^{-1} and an initial Se(VI) concentration of 2×10^{-5} mol L^{-1}. The suspensions were equilibrated for 48 hours. All experiments were conducted in N_2-atmosphere. After centrifugation during two hours at 6,800 g, the remaining selenium concentration in the supernatant was determined by ICP-MS. The selenate sorption reactions onto γ-Al_2O_3 were investigated by *in situ* ATR FT-IR spectroscopy. The stability of γ-Al_2O_3 in solution at different pH was investigated by XRD after an equilibration of seven days, followed by subsequent centrifugation and lyophilisation. Additionally, ATR FT-IR was conducted to characterize the mineral.
The impact of salinity on the variable surface charge of γ-Al_2O_3 (−log H^+: 3.5–11) was evaluated by zeta potential measurements using laser Doppler electrophoresis. For batch experiments and zeta potential measurements, corrections for H^+ concentrations due to the high ionic strengths were done by the method of Altmaier et al. [1].

RESULTS. The characterization of the mineral demonstrates that the phase is pure γ-Al_2O_3 and no phase transformation occurs in aqueous suspensions (Fig. 1). This is in contrast to literature data, where a pH dependent transformation to gibbsite or bayerite was observed [2].

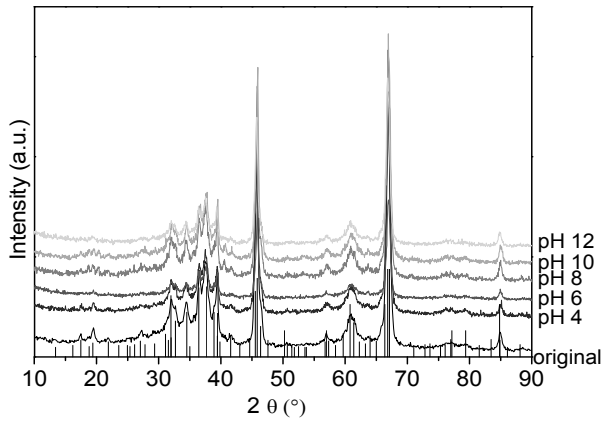

Fig. 1: XRD patterns of the solid as purchased and of the solid after equilibration with 0.1 M NaCl solution of different pH.

From IR spectra (data not shown), a change in the symmetry of the aqueous tetrahedral selenate anion upon sorption can be derived evidencing the formation of a surface complex on γ-Al_2O_3. From batch experiments, a decreased sorption of selenate is observed with increasing

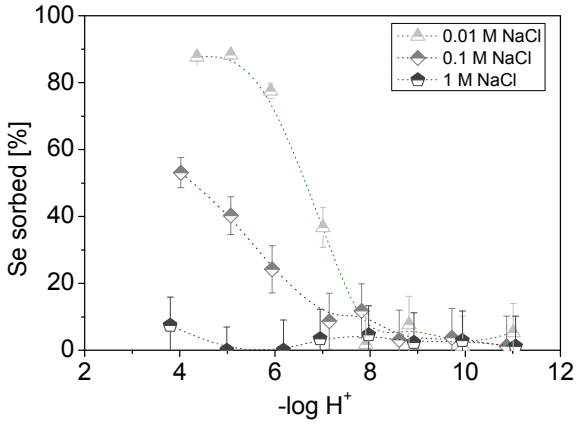

Fig. 2: Se(VI) sorption edges onto γ-Al_2O_3 in NaCl solution at different ionic strengths ($[Se(VI)]_{ini} = 2\times10^{-5}$ mol L^{-1}, m/v = 1 g L^{-1}).

ionic strengths and pH of the aqueous suspensions (Fig 2).
The isoelectric point (pH_{IEP}) of γ-Al_2O_3 is observed at pH 9.6 for low NaCl background electrolyte concentration (0.01 and 0.1 M; Fig. 3). The increase of ionic strength (up to I = 1 M) results in a decrease of the magnitude of the zeta potential for both the acidic and alkaline pH range, which is consistent with the observed decrease of selenate sorption (Fig. 2). However, in the alkaline range, the decrease of the zeta potential is more pronounced (Fig. 3).

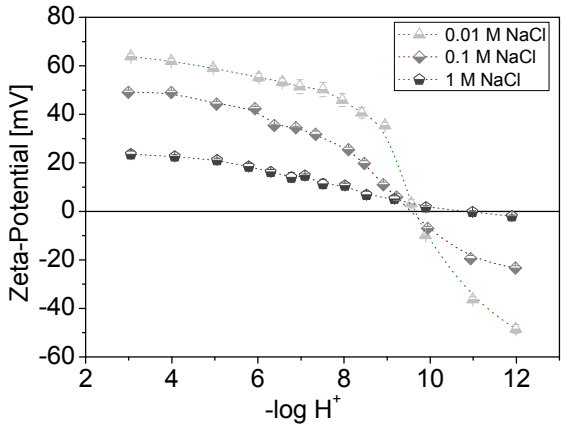

Fig. 3: Zeta potential of the neat surface of γ-Al_2O_3 in NaCl solution at different ionic strengths (m/v = 0.2 g L^{-1}).

Additionally, it could be observed that at high ionic strength the pH_{IEP} is shifted to more alkaline values and finally no charge reversal is found. These findings are accordant to literature [3]. To what extent these changes in the surface charge advance the sorption of selenate in the alkaline range has to be checked in detail.

ACKNOWLEDGEMENTS. This work is part of the VESPA project, funded by the German Federal Ministry of Economics and Technology (No. 02E10790).

[1] Altmaier, M. et al. (2003) *Geochim. Cosmochim. Acta*. **67**, 3595–3601.
[2] Carrier, X. et al. (2007) *J. Colloid Interf. Sci.* **308**, 429–437.
[3] Kosmulski, M. et al. (2004) *Adv. Colloid Interface Sci.* **112**, 93–107.

A study of the sorption of U(VI) onto SiO_2 in the presence of phosphate by ATR FT-IR spectroscopy

H. Foerstendorf, M. J. Comarmond,[1] K. Gückel, K. Müller, K. Heim, V. Brendler, T. E. Payne[1]

[1]Australian Nuclear Science and Technology Organisation, Lucas Heights, Australia

The aqueous speciation of U(VI)/PO_4 and the ternary sorption system U(VI)/PO_4/SiO_2 were investigated by in situ vibrational spectroscopy. The spectra obtained suggest the formation of a uranylphosphate species in solution which is also formed on the SiO_2 surface most probably as a surface precipitate.

Phosphate is known to influence uranium sorption in natural systems and model minerals [1–3] and a number of possible mechanisms have been proposed. While studies at the molecular level have recently been reported for iron oxides and aluminium oxides (e.g. [3]), this is not the case for SiO_2, a major component of soils and rocks. This study investigates sorption of an aqueous solution of U(VI) onto SiO_2 in the presence of phosphate by *in situ* vibrational spectroscopy.

EXPERIMENTAL. The ATR FT-IR accessory and the procedure for the *in situ* sorption measurement were described in detail previously [4]. All experiments were performed with 20 µM U(VI) and 20 µM NaH_2PO_4 in 0.1 M NaCl at pH 4 unless where noted.

RESULTS. Prior to the sorption experiments, aqueous solutions of the U/PO_4 system were investigated. From chemical speciation modeling, the aqueous speciation of the solutions used in this study is predicted to be predominated by the fully hydrated UO_2^{2+} species (Tab. 1).

Tab. 1: Result of the aqueous speciation modelling for the U(VI)/PO_4 system ([U] = [PO_4] = 20 µM) at pH 4 (0.1 M NaCl) using EQ3/6 code and NEA database.

Species*	Fraction [%]
UO_2^{2+}	86.9
UO_2HPO_4(aq.)	4.8
UO_2Cl^+	4.4
UO_2OH^+	2.5
$UO_2H_2PO_4^+$	1.1

*The solution is predicted to be slightly oversaturated with $(UO_2)_3(PO_4)_2 \cdot 4H_2O$.

The corresponding vibrational spectra of the U/PO_4 containing solutions and of the precipitate found are shown in Fig. 1A-D. The band representing the $\nu_3(UO_2)$ mode is observed at 919 cm^{-1} irrespective of absence or presence of precipitate. The bands at 1532 and 1455 cm^{-1}, previously observed for aqueous hydroxo species [5], have yet to be assigned to distinct modes. Interestingly, all spectra show bands assigned to phosphate modes at the same frequencies, i.e. at 1125 and 993 cm^{-1}, which are significantly shifted compared to the aqueous phosphate species (HPO_4^{2-}) [6] indicating the presence of a dissolved uranylphosphate species (most probably $UO_2HPO_4^0$).
From the sorption experiments, it was found that phosphate did not sorb onto SiO_2 unless U(VI) was present (data not shown). This can be explained by the isoelectric point of SiO_2 which is found to be around pH 2.5 resulting in an overall negatively charged surface at pH 4 which is unfavorable for sorption of anions.

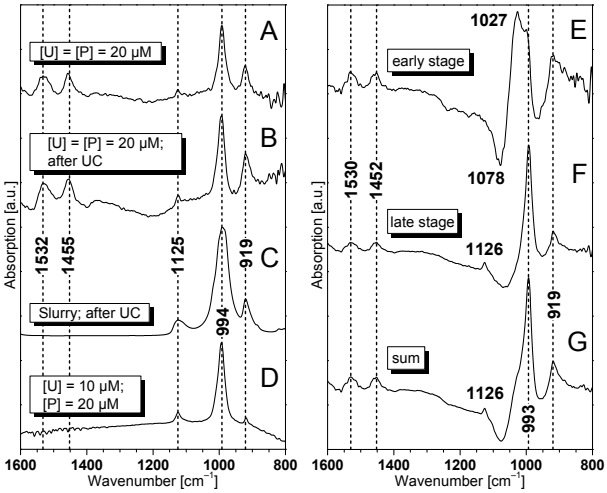

Fig. 1: IR spectra of the aqueous U(VI)/PO_4 system (left panel, concentration given in the panel) and of the ternary sorption system U(VI)/PO_4/SiO_2 (right panel). IR spectra of the solutions (A, B, D) before (A,D) and after ultracentrifugation (UC) (B). Spectrum of the slurry after UC is shown in (C). IR spectra of the simultaneous sorption process of 20 µM U(VI)/PO_4 obtained a few minutes after induced sorption (E) and at a later sorption stage (F). The spectrum summarizing the entire sorption process is also given (G).

During the early stage of simultaneous sorption of U(VI) and phosphate, bands at 919, 1027, 1452 and 1530 cm^{-1} are observed suggesting the formation of a transient uranyl species at the SiO_2 surface (Fig. 1E). With ongoing sorption, the IR spectra (Fig. 1F) become quite similar to those of the solutions and the precipitate (Fig. 1A-D). In addition, the relatively small band widths – in particular those of the uranyl mode – suggest the formation of a surface precipitate. Such sharp bands were already observed for surface precipitates from previous *in situ* sorption experiments [7].

CONCLUSIONS. The predicted predominance of the UO_2^{2+} ion in aqueous solution under the prevailing conditions was not confirmed by IR spectroscopy. Whether this is due to questionable data sets of the NEA database for the U/PO_4 system or due to the weak absorption coefficient of the fully hydrated UO_2^{2+} ion, which might be overlapped by the bands of the aqueous uranylphosphate species, has to be verified in future experiments.
Nevertheless, the sorption of U(VI) on SiO_2 in the presence of inorganic phosphate is predominantly characterized by surface precipitation. These findings corroborate results from concurrent batch experiments of the U(VI)/SiO_2 sorption system where an increase of U(VI) uptake in the presence of phosphate has been observed.

[1] Payne, T.E. et al. (1998) *Adsorption of Metals by Geomedia*, p. 75–97, Academic Press, San Diego, U.S.A.
[2] Zhang, H., Tao, Z. (2001) *J. Rad. Nucl. Chem.* **254**, 103–107.
[3] Del Nero, M. et al. (2010) *J. Colloid. Interface Sci.* **342**, 437–444.
[4] Müller, K. et al. (2009) *Environ. Sci. Technol.* **43**, 7665–7670.
[5] Müller, K. et al. (2008) *Inorg. Chem.* **47**, 10127–10134.
[6] Tejedor-Tejedor, M.I. et al. (1990) *Langmuir* **6**, 602–611.
[7] Gückel, K. et al. (2012) *Chem. Geol.* **326–327**, 27–35.

Uranium(VI) sorption onto Äspö diorite in Äspö groundwater

K. Schmeide, S. Gürtler, K. Müller, R. Steudtner, C. Joseph, V. Brendler

U(VI) sorption onto diorite obtained from Äspö Hard Rock Laboratory (HRL, Sweden) was studied by batch sorption experiments in dependence on grain size, temperature and atmosphere using synthetic Äspö groundwater as background electrolyte. Distribution coefficients, K_d values, were determined. $Ca_2UO_2(CO_3)_3(aq)$ was detected as dominating U(VI) species in solution by time-resolved laser-induced fluorescence spectroscopy (TRLFS). As surface species on diorite, $UO_2(CO_3)_3^{4-}$ was identified by attenuated total reflection (ATR) IR spectroscopy.

Granitic subsurface environments are considered as potential host rock formations for the deep underground disposal of radioactive waste [1]. Diorite from Äspö HRL was chosen as crystalline rock material in this sorption study. It was sampled, transported and crushed under anoxic conditions [2]. The objective was to determine the retention behavior of this anoxic diorite toward U(VI) and to identify U species in solution and sorbed onto the rock matrix by spectroscopic methods.

EXPERIMENTAL. Conditions of batch sorption experiments: $[^{233}U(VI)] = 1 \times 10^{-6}$ M; S/L = 200 g/L; Äspö diorite (size fractions: cf. Tab. 1); Äspö groundwater [3]: I = 0.178 M, pH 7.8; N_2 atmosphere or $pCO_2 = 10^{-3.5}$ atm; 25 or 10 °C. The diorite suspensions were pre-equilibrated for 10 d. The U sorption time was 21 d. The samples were analyzed by liquid scintillation counting.

Tab. 1: Specific surface areas of various grain size fractions of diorite.

Grain size fraction (mm)	Specific surface area (m^2/g)
0.063–0.2	0.249 ± 0.014
0.5–1	0.079 ± 0.003
1–2	0.065 ± 0.004

RESULTS. According to speciation calculations (cf. [3]), the U(VI) speciation in the Äspö groundwater at pH 7.8 is dominated by 99% $Ca_2UO_2(CO_3)_3(aq)$ [4]. This is verified by TRLFS [3].

The U(VI) sorption onto diorite decreases with increasing grain size (cf. Fig. 1). This is attributed to decreasing specific surface areas (cf. Tab. 1). Compared to U(VI) sorption under anaerobic conditions, the U(VI) sorption is lower under aerobic conditions indicating a change of the inventory of sorbing minerals in oxidized diorite samples. Furthermore, the U(VI) sorption determined at 10 °C is lower than that at room temperature.

Desorption tests with 0.1 M HCl (5 min) showed that about 74% of the U can again be desorbed. The desorbed U occurred predominantly as U(VI) (94%) as shown by solvent extraction [5].

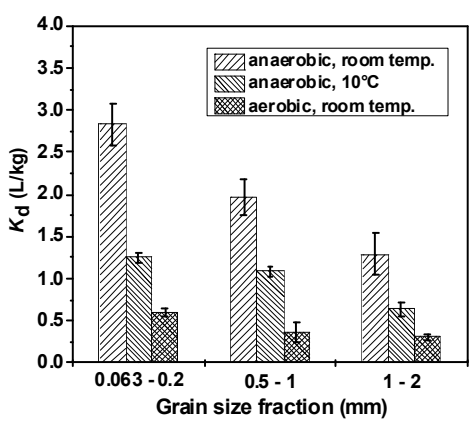

Fig. 1: U(VI) sorption onto diorite in Äspö groundwater in dependence on grain size, atmosphere and temperature.

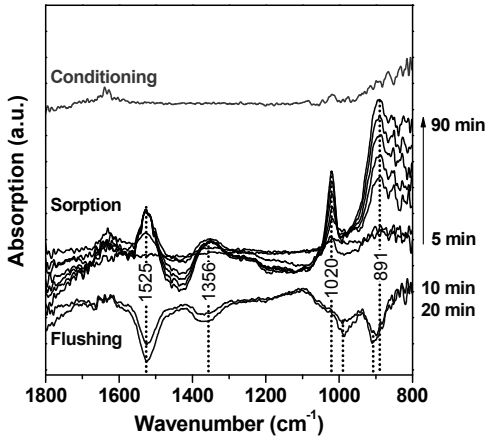

Fig. 2: *In situ* time-resolved IR spectra of U(VI) sorption onto diorite in Äspö groundwater.

The IR spectra obtained during U(VI) sorption onto diorite (Fig. 2) show increasing bands at 1525, 1356, 1020 and 891 cm^{-1} with sorption time. Since the absorption bands at 891 cm^{-1} as well as at 1525 and 1356 cm^{-1} are also observed in the spectrum obtained for U(VI) equilibrated in Äspö groundwater (cf. [3]) and no shift of the absorption bands occurs, it is assumed that the aqueous complexes present in solution are accumulated at the mineral surface. The band at 891 cm^{-1} represents the antisymmetric U–O stretching vibration of the uranyl ion. The bands at 1525 and 1356 cm^{-1} can be assigned to the antisymmetric and symmetric stretching vibration of the carbonate ion, respectively. Consequently, the sorption spectra indicate the accumulation of the $UO_2(CO_3)_3^{4-}$ complex at the mineral surface. This seems to be confirmed by the band at 1020 cm^{-1} which can be assigned to Si–OH surface modes which undergo significant alterations during the sorption reactions. During the flushing of the diorite film with Äspö groundwater, negative bands are observed, reflecting the release of a weakly bound $UO_2(CO_3)_3^{4-}$ complex.

The study showed that the speciation of U(VI) in solution and thus, its sorption onto diorite is strongly influenced by the groundwater composition. From the ions leached out of diorite, Ca^{2+} and CO_3^{2-} have the strongest impact.

ACKNOWLEDGEMENTS. This work was funded by the European Union's European Atomic Energy Community's (EURATOM) Seventh Framework Programme FP7/2007-2011 (contract no. 269658, CROCK project). We also thank KIT-INE for providing the diorite.

[1] Bäckblom, G. (1991) *Tunn. Undergr. Space Technol.* **4**, 463–467.
[2] Schäfer, Th. et al. (2012) *KIT Scientific Reports 7629*, 63–72.
[3] Schmeide, K. et al. (2012) *KIT Scientific Reports 7629*, 169–180.
[4] Bernhard, G. et al. (2001) *Radiochim. Acta* **89**, 511–518.
[5] Bertrand, P.A. (1982) *Radiochim. Acta* **31**, 135–137.

Uranium(VI) sorption on montmorillonite in an NaCl medium of high ionic strength

K. Fritsch, K. Schmeide

The sorption of uranium(VI) onto the clay mineral montmorillonite was studied in dependence on pH and ionic strength. While there is an overall trend of the ionic strength decreasing the uranium sorption at pH values lower than 6, there is no discernible difference in uranium sorption under neutral and alkaline conditions. Furthermore, leaching studies of the clay were conducted.

There are generally three types of host rock that are considered for radioactive waste disposals: crystalline rock, salt dome and argillaceous rock, with the last two being relevant for the German radioactive waste management concept [1]. The North German clay deposits are of special interest but in contrast to the well-researched South German and Swiss Opalinus clay deposits, their pore water has a much higher ionic strength.
Montmorillonite, a smectite, is used as a model clay. As well as representing the smectite fraction of natural argillaceous rock, it is also very important as the main component of bentonite, which is used as sealing material in radioactive waste repositories in argillaceous rock as well as crystalline rock. Montmorillonite has the ability to strongly swell – in fact, 30 g of montmorillonite can take up as much space as 2 dm³ at low ionic strengths.

EXPERIMENTAL. The clay was cleaned according to the procedures of Poinssot and Bradbury and Baeyens [1, 2]. Subsequent characterization of the montmorillonite gave a cation-exchange capacity (CEC) of 85.0 ± 22.4 $mmol_c\ (100\ g)^{-1}$ and a specific surface area of 41.1 ± 0.8 $m^2\ g^{-1}$ (N_2-BET). Analysis of the composition of the clay was in excellent agreement with the literature [4–6]. The sorption and leaching experiments were conducted under the following conditions: S/L = 4.00 ± 0.01 g L^{-1}, background electrolyte NaCl, I = 1…3 mol kg^{-1}, pH = 4…10, room temperature, atmospheric conditions, $c_{U(VI)} = 1\times10^{-6}$ mol kg^{-1}, sorption time 5 days.

RESULTS. Figure 1 shows the influence of ionic strength and pH on the U(VI) sorption on montmorillonite. There is no significant difference between the sorption values in neutral and alkaline media. At acidic pH values, there is a marked difference between the sorption at an ionic strength of I = 1 mol kg^{-1} and the two higher ionic strengths.

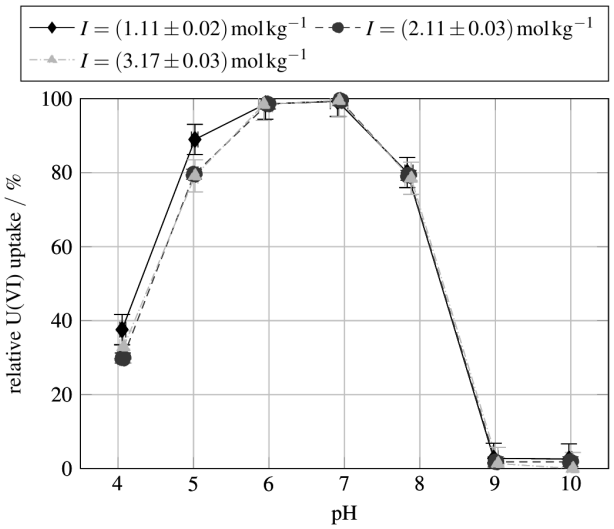

Fig. 1: U(VI) sorption on montmorillonite in NaCl.

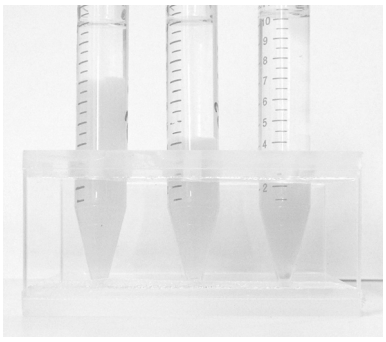

Fig. 2: Swelling of montmorillonite in NaCl (pH = 7). From left to right: 1, 2 and 3 mol kg^{-1}.

Montmorillonite swelling is highly dependent on ionic strength. At an ionic strength of I = 1 mol kg^{-1}, montmorillonite shows swelling properties that correspond to swelling at low ionic strength, while there is no marked difference between the swelling at I = 2 mol kg^{-1} and I = 3 mol kg^{-1} (see Fig. 2).
Leaching experiments were conducted under the aforementioned conditions. Clays are considered to be unstable at pH values below 4 because there the solubility of alumina oxides increases. The leaching experiments confirm this, as there is aluminum present in the solution at pH 4 but not at higher pH values. Silicon on the other hand is better soluble at high pH values. Consequently, there is a strong increase in solved silicon at higher pH values, particularly at pH 10. Furthermore, a number of cation exchange reactions can be observed: The calcium contents in the solution and the clay are in equilibrium. If no calcium is present in the background electrolyte, calcium originating from the clay exchanges against sodium and calcium becomes detectable in the solution. If calcium is added to the background electrolyte, some of this calcium migrates into the clay, with the concentration profiles of the calcium in the clay and in the liquid being roughly similar. This process is also observable on a greater scale – only montmorillonites without notable calcium content are able to fully swell, which is why the swelling properties of montmorillonite in a calcium-enriched background electrolyte are visibly decreased compared to pure Na-montmorillonite. There is also an increase of magnesium and manganese content in the background electrolyte, with more ions released from the clay at lower pH values. Uranium is present in montmorillonite in small amounts (1.47 µg U/g clay) and is released at low and high pH values.

ACKNOWLEDGEMENTS. This work is funded by the BMWi (No. 02 E 10971).

[1] BGR (2007) *Endlagerung radioaktiver Abfälle in Deutschland.*
[2] Poinssot, C. et al. (1999) *Nagra Technical Report 99–04.*
[3] Bradbury, M. et al. (2009) *Geochim. Cosmochim. Acta* **73**, 990–1003.
[4] Olphen, H.V. et al. (1979) *Data handbook for clay materials and other non-metallic minerals*, Pergamon Press, Oxford.
[5] Mermut, A. et al. (2001) *Clay Clay Min.* **49**, 381–386.
[6] Vogt, K. et al. (1978) *Clay Min.* **13**, 25–43.

Investigation of the neptunium(V) sorption onto gibbsite by means of ATR FT-IR spectroscopy

K. Gückel, H. Foerstendorf

The sorption of neptunium(V) on gibbsite was investigated in the presence and absence of equivalent added carbonate by *in situ* attenuated total reflection (ATR) infrared spectroscopy.

Carbonate ions play an important role for the migration behavior of heavy metal contaminants, due to their high concentration in groundwater and their strong complexation ability towards metal ions [1]. In consequence, the thermodynamic properties of Np carbonate species in the aqueous solution system with high carbonate concentrations have been extensively investigated by many researchers for the last decades. Limited data exists for the influence of atmospheric carbon dioxide on the sorption of NpO_2^+ on aluminum oxides and hydroxides [2].

EXPERIMENTAL. The synthesis of the gibbsite was described before [3]. A BET value of 4.5 m²/g and an IEP at pH 8.3 were determined. The experimental setup, the preparation of the mineral film and parameter of the data acquisition are already described [4,5]. The Np(V) solution (50 µM NpO_2^+, 0.1 M NaCl) was adjusted to pH 7.5. All solutions were prepared in a glove box under inert gas atmosphere and in D_2O.

RESULTS. The NpO_2^+ ion shows a characteristic absorption band representing the $\nu_3(NpO_2)$ mode at 818 cm^{-1} which can be assigned to the fully hydrated NpO_2^+ ion [5]. The IR spectrum of an aqueous Np(V) solution equilibrated at ambient atmosphere at pH 7.5 is shown in Fig. 1A. The absorption band representing the $\nu_3(NpO_2)$ mode is now observed at 796 cm^{-1} due to the formation of a hydrolysis species, namely $NpO_2CO_3^-$.

In the absence of carbonate, the time-resolved spectra are dominated by two absorption bands at 1070 and 789 cm^{-1} (Fig. 1B) representing vibrational surface modes of gibbsite and the $\nu_3(NpO_2)$ mode, respectively . The frequency of the $\nu_3(NpO_2)$ mode is shifted about 28 cm^{-1} to lower frequencies compared to those of the fully hydrated ion [5]. From the frequency of the band (789 cm^{-1}), the formation of an inner-sphere surface complex can be suggested because it is further bathochromically shifted compared to the aqueous species. A similar frequency of this vibrational mode was observed for NpO_2^+ sorption complexes on TiO_2 [5].

Prior to the experiments performed in the presence of equivalent atmospherically derived carbonate, the interactions of the dissolved carbonate ions with the gibbsite surface were investigated (Fig. 1C). The spectrum obtained exhibits two bands at 1507 and 1383 cm^{-1} representing the $\nu_{3,as}$ and $\nu_{3,s}$ mode of the carbonate ions sorbed onto the gibbsite phase, respectively.

The time-resolved spectra of the sorption of Np(V) on gibbsite in the presence of carbonate (Fig. 1D) are dominated by absorption bands at 1495, 1405, 1070 and 789 cm^{-1}. In the spectral range above 1300 cm^{-1}, the band pattern of the $\nu_3(CO_3)$ modes is changed in the presence of Np(V) (Fig. 1C/D). With respect to the sorption spectrum of the binary carbonate-gibbsite system , the band of the $\nu_{3,as}$ mode is shifted to lower wavenumber whereas the $\nu_{3,s}$ mode shows up at higher frequencies and are now observed at 1495 and 1405 cm^{-1}, respectively. Consequently, it is assumed that the carbonate ions coordinate to the neptunyl ions sorbed on the gibbsite surface resulting in ternary surface complexes. The band at 1070 cm^{-1} represents vibrational surface modes of gibbsite and was discussed before [3]. During the time of sorption, no changes of the ν_3 mode of NpO_2^+ at 789 cm^{-1} occur indicating the formation of a single surface species. With respect to frequency shifted about 7 cm^{-1} to lower wavenumbers in comparison to those of the aqueous $NpO_2CO_3^-$ species (Fig. 1A), the formation of an inner-sphere complex can be suggested.

In summary, irrespective of the atmospheric conditions neptunyl(V) inner-sphere complexes are formed on the surface of gibbsite.

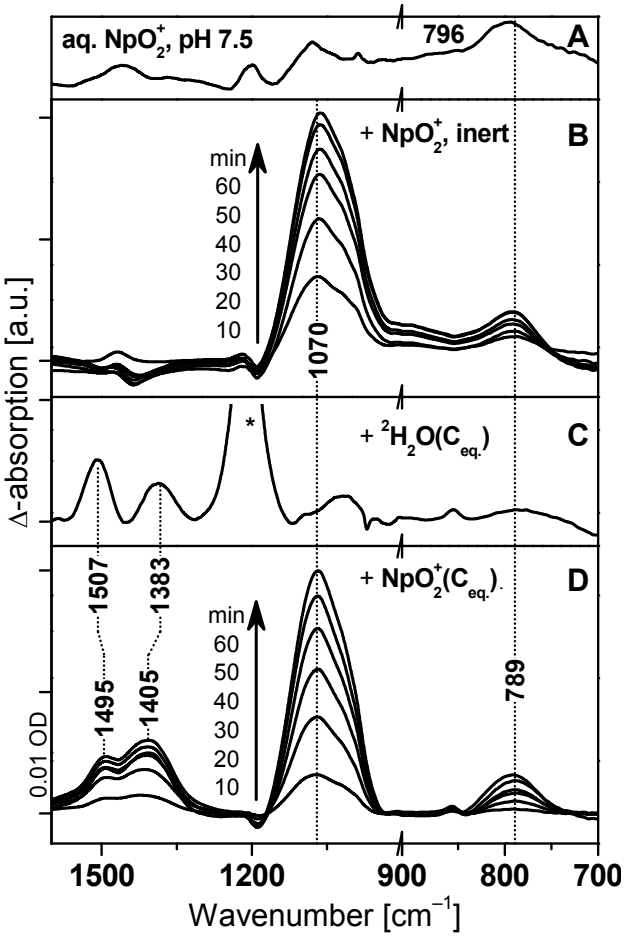

Fig. 2: IR spectrum of an Np(V) solution containing equivalent atm. carbonate (A); IR spectra of *in situ* Np(V) sorption experiments on gibbsite under inert gas conditions (B), sorption of equivalent atm. carbonate (C), sorption of Np(V) in the presence of carbonate (D). $[Np(V)]_{init.}$= 50 µM. All aqueous solutions in D_2O, 0.1 M NaCl, pH 7.5.

[1] Ikeda-Ohno, A. (2009) *Inorg. Chem.* **48**, 11779–11787.
[2] Del Nero, M. et al. (1998) *Radiochim. Acta* **81**, 133–141.
[3] Gückel, K. et al. (2012) *Chem. Geol.* **326–327**, 27–35.
[4] Meusel, T. et al. (2009) *Report FZD-511*, p. 48.
[5] Müller, K. et al. (2009) *Environ. Sci. Technol.* **43**, 7665–7670.

Sorption of neptunium(V) onto hematite studied by in situ ATR FT-IR spectroscopy

K. Müller, A. Gröschel

The Np(V) sorption onto commercial hematite has been studied in situ by application of ATR FT-IR spectroscopy. A simultaneous formation of inner- and outer-sphere complexes is derived from the spectra.

Iron oxides play a decisive role in regulating the mobility of contaminants in rock and soil formations particularly because of their tendency to form coatings on mineral surfaces [1]. In this work, Np(V) sorption on α-Fe_2O_3 is investigated as a function of different surface loadings, pH, and ionic strength.

EXPERIMENTAL. Hematite from US Research Nanomaterials Inc. (USA) was used. Particle size is homogenous around 70 nm and the BET specific surface area was found to be 41.1 m^2/g. The isoelectric point (IEP) determined by zeta potential is at pH 9.2.
For sorption experiments, Np(V) concentration was set to 50 µM at an ionic strength of 0.1 M adjusted by NaCl at pH 7.6 and N_2 atmosphere. All measurements were performed with D_2O (Sigma Aldrich, isotope purity > 99%) The ATR FT-IR accessory and the procedure for the in-situ sorption measurement were described in detail previously [2].

RESULTS. The obtained IR spectra are shown in Fig. 1. Since no negative bands below 1000 cm^{-1} were observed in the difference spectrum of the conditioning, the stability of the prepared hematite film on the ATR crystal under the given conditions is confirmed. The bands at 1491 and 1356 cm^{-1} represent the removal of carbonate by rinsing the hematite film, prepared in air with the CO_2 free solution.

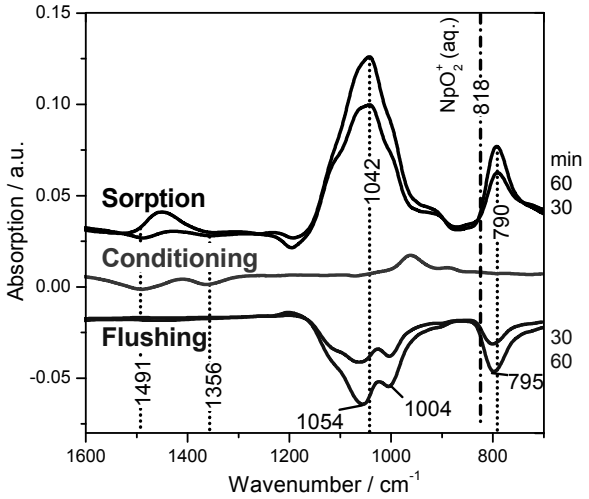

Fig. 1: ATR FT-IR spectra of 50 µM Np(V) sorbed onto α-Fe_2O_3 at pH 7.6, 0.1 M NaCl, D_2O, N_2. Indicated values are in cm^{-1}.

Upon Np(V) sorption, several bands increase with time. The band at 790 cm^{-1} is assigned to the antisymmetric stretching vibrational mode (ν_3) of the neptunyl ion. The IR spectrum obtained from an aqueous solution at 50 µM Np(V), 0.1 M, pH 6 shows the absorption of $\nu_3(Np^VO_2)$ at 818 cm^{-1}. The red shift of ν_3 to 790 cm^{-1} upon sorption can be assigned to an inner-sphere monomeric sorption complex, as previously reported for TiO_2, SiO_2 and ZnO [2]. The band at 1042 cm^{-1} is due to rearrangement processes at the mineral oxide surface upon sorption and are similarly observed for interactions with U(VI), Cs(I) and CO_3^{2-} [2].
In the flushing stage, a weakly bound species is released from the stationary phase, reflected by a negative band at 795 cm^{-1} in the respective spectra.
Additional experiments were performed at varied values of pH (5.6–12) and ionic strength (0.001–0.1) (Fig. 2). Upon increasing the pH from 5.6 to 8.6, no shifts of the bands at 1041 and 790 cm^{-1} are observed. But the intensities of these spectral features are considerably increased at higher pH values indicating an enhanced sorption capacity close to the IEP at pH 9.2. At pH > 10, the aqueous Np(V) speciation changes and NpO_2OH_{aq} is formed and distinctly changes the sorption behavior. The band of $\nu_3(Np^VO_2)$ is shifted to 773 cm^{-1}.

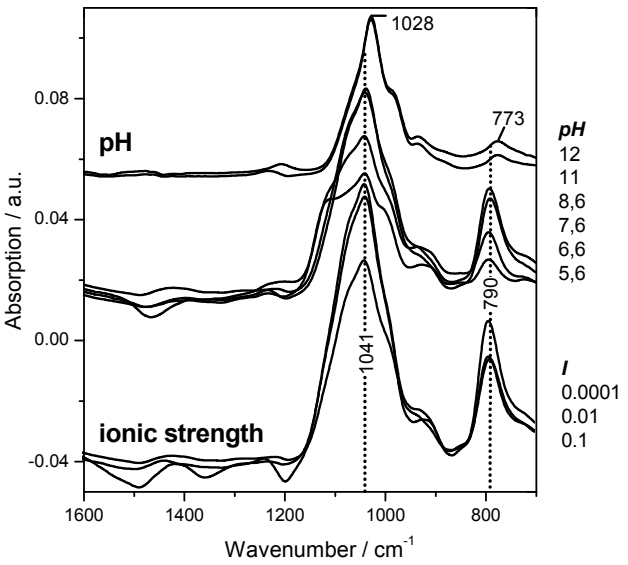

Fig. 2: ATR FT-IR spectra of 50 µM Np(V) sorbed onto α-Fe_2O_3 at a variation of pH (5.6-12) and ionic strength (0.1-0.0001). The other parameters remained constant: pH 7.6, 0.1 M NaCl, D_2O, N_2. Indicated values are in cm^{-1}.

The variation of ionic strength between 0.1 and 0.01 does not change the spectral characteristics. The higher intensities observed at 0.0001 M NaCl can be attributed to contributions of an outer-sphere complex which has to be verified by future experiments.
In summary, the IR spectra evidence the formation of Np surface complexes on hematite which can be easily removed to a considerable extent by flushing with blank solution. From this behavior, the simultaneous formation of an inner-sphere species with significant contributions of an outer-sphere complex is suggested.

ACKNOWLEDGEMENTS. The authors are grateful to C. Eckardt and S. Domaschke. The funding of this work by Deutsche Forschungsgemeinschaft (MU 3207/1-1) is greatly acknowledged.

[1] Dixon, J.B. et al. (1989) *Minerals in soil environments*, Soil Science Soc. of America, Madison, U.S.A.
[2] Müller, K. et al. (2009) *Environ. Sci. Technol.* **43**, 7665–7670.

Investigations of the formation of neptunium(IV)-silica colloids

R. Husar, S. Weiß, H. Zänker, G. Bernhard

Neptunium(IV) forms silicate-containing colloids when the limit of solubility is exceeded in presence of dissolved silicate.

Detailed knowledge of the migration behavior of actinides is an important issue in predicting the potential release of radiotoxic elements from nuclear waste repositories. Under the reducing conditions expected for the disposal zone, the tetravalent form of the actinides An (An = Th, U, Np, Pu) is predominant. Due to the low solubility at neutral pH, the An(IV) are considered as immobile under these conditions. Nevertheless, high environmental mobility has been found e.g. for Pu(IV) [1, 2]. This is obviously related to the formation of An(IV) eigencolloids or the sorption of Pu onto other colloids.
Several investigations revealed the occurrence of $An(IV)O_2{\times}H_2O$ colloids at concentrations of several orders of magnitude higher than the limit of solubility [3, 4]. During colloid formation, there is also a potential interaction with other compounds ubiquitous in groundwaters as e.g. humic acids, carbonates or silicates, which may influence the mobility of the actinides in aquifers. For Th(IV) and U(IV), there is evidence that silica stabilizes such colloids at alkaline and neutral pH up to An(IV) concentrations of 10^{-3} M. EXAFS measurements indicate a replacement of Th–O–Th and U–O–U bonds by Th–O–Si and U–O–Si bonds [5, 6].
In the case of neptunium the formation of Np(IV) silicate colloids has never been reported so far.

RESULTS. Np(IV)-silicate colloids prepared from Np(IV) carbonate solutions by dilution with silicate solutions at alkaline pH (8.9–9.9) were investigated by ultrafiltration, LSC, ICP-MS, UV-vis and Dynamic Light Scattering (DLS) under exclusion of oxygen to maintain anaerobic conditions. Colloid samples with concentrations up to 2×10^{-3} M Np(IV) and $1–9 \times 10^{-3}$ M silicate and a background carbonate concentration of 1×10^{-1} M $NaHCO_3$ were produces.
The presence of silicate stabilizes the precipitated Np(IV) as colloids in the solutions while rapid sedimentation occurs in the absence of silicate. The diameter of such stabilized particles was estimated by DLS at < 20 nm. The colloids were found to be stable for at least 30 days, and their size increased with time.
The UV-vis spectra obtained show appreciable absorption band shifts which can be assigned to the reaction of soluble Np(IV)-carbonate to form polymerized Np(IV) species.

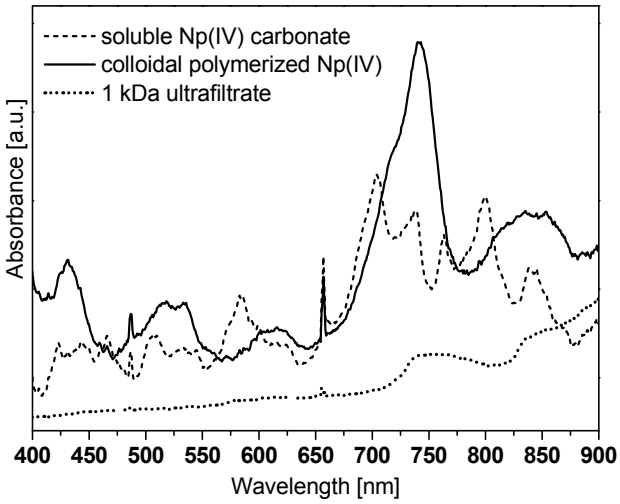

Fig. 1: UV-Vis spectra of the soluble Np(IV) carbonate (1.82×10^{-3} M, 1 M $NaHCO_3$), the polymerized Np(IV) (1.72×10^{-3} M, 3.2×10^{-3} M Si, 1×10^{-1} M $NaHCO_3$), and the ultrafiltrate of the colloidal solution.

Polymerized Np(IV) was almost completely removed by 1 kDa ultrafiltration resulting in the disappearance of an adsorption band at 741 nm (Fig. 1). A molar Np/Si ratio of the formed solids of approximately 1 : 1.4–1 : 1.5 was determined by this method (Tab. 1). Higher silica contents results in more stable and smaller colloids. The formation of Np(IV)-silica colloids might increase the mobility of neptunium.

Tab. 1: Results of concentration of Np and silica in example samples.

Analyte	Np [mM]	Si [mM]
	Initial solution	
Sample 1	1.04	8.6
Sample 2	1.05	5.4
	Supernatant of 1 kDa filtered samples	
Sample 1	0.12	5.3
Sample 2	0.12	3.0
	Np-Si-ratio in colloids [mol/mol]	
Sample 1	1 : 3.6	1 : 3.6
Sample 2	1 : 2.6	1 : 2.6

[1] Buddemeier, R. et al. (1988) *Appl. Geochem.* **3**, 535–548.
[2] Utsunomiya, S. et al. (2009) *Environ. Sci. Technol.* **43**, 1293–1298.
[3] Altmaier, M. et al. (2004) *Radiochim. Acta* **92**, 537–543.
[4] Neck, V. et al. (2001) *Radiochim. Acta* **89**, 439–446.
[5] Dreissig, I. et al. (2011) *Geochim. Cosmochim. Acta* **75**, 352–367.
[6] Hennig, C. et al. (2013) *Geochim. Cosmochim. Acta* **103**, 197–212.

Radionuclide sorption studies of Co, Cs and Sr onto soils from an Australian legacy low-level radioactive waste disposal site

K. Gückel, M. J. Comarmond,[1] T. E. Payne[1]

[1]Australian Nuclear Science and Technology Organisation, Locked Bag 2001, Kirawee DC, Australia

The work focuses on sorption studies of the radionuclides Co, Cs and Sr on a soil profile taken from the Little Forest Burial Ground located within the ANSTO Buffer Zone Boundary in South Eastern Australia.

This site was used by the former Australian Atomic Energy Commission (AAEC) during the 1960's to dispose of waste containing low levels of radioactivity in a series of shallow trenches. There has been regular environmental monitoring of the site since 1966, during which measurable amounts of Co-60, Sr-90, Cs-137 have been observed in some soils, groundwater and vegetation samples taken in close proximity to the disposal area. An intensified research program, including a series of field studies, has been implemented during recent years. Moreover, an extensive core-drilling program was undertaken in 2009.

EXPERIMENTAL. The studies were conducted on bulk samples (< 1 mm) with a mass loading of 10 g/L, ionic strength of 0.01 M (NaCl) in the presence of air. The soil suspensions were adjusted to pH 3–7 and equilibrated in a shaker for one day under ambient atmosphere. Then 500 Bq of each tracer were added. During the contact time of 48 h the samples were placed back in the shaker at room temperature, followed by centrifugation at 8000 rpm for 20 min. The remaining tracer activities in the supernatant were determined by gamma-counting.

RESULTS. Strong sorption (> 80%) was observed for Cs over the entire pH range studied, whereas the sorption of Co and Sr on the soils was pH dependent with sorption edges between pH 3 and pH 6. The sorption behavior was similar for all four depth intervals and all tracer nuclides, respectively. Figure 1 shows exemplarily the sorption curves for Cs, Co and Sr for the depth interval 1.4–1.6 m. Distribution coefficients (K_d values) for Cs sorption were similar for each soil over the entire pH range, with variations of less than one order of magnitude between samples (800–4700 mL/g). However, the K_d values for Sr and Co sorption varied over two and three orders of magnitude, respectively, over the pH range studied. For Sr the K_d values range between 10 and 2000 mL/g and for Co between 5 and 4500 mL/g. With increasing pH values the K_d values increases, indicating a decrease in the mobility of these radionuclides.

The bulk mineralogy of the soils was found to be similar with quartz, kaolinite and interstratified illite/smectite to be the main mineralogical phases with iron oxides and anatase as minor minerals in some soils. The BET surface values of the bulk samples varied from 27 m^2/g to 47 m^2/g and no strong correlation of surface area with sorption was observed. The CEC of the bulk samples range between 10 and 24 cmol/kg and the clay mineral fraction between 67.8 and 31.2%.

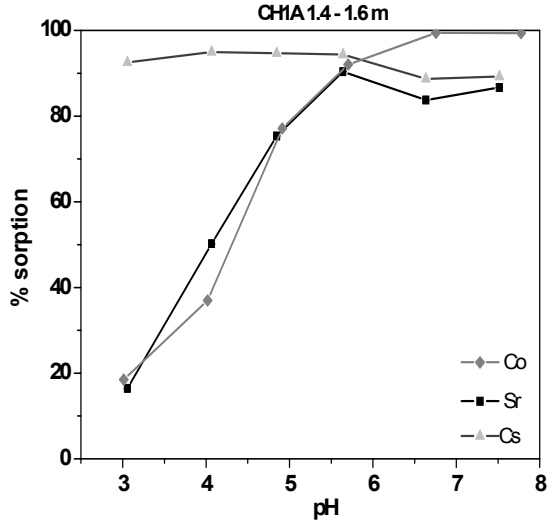

Fig. 1: Sorption curve for Cs, Co and Sr on the depth interval 1.4-1.6 m.

Tab. 1: Sample parameters, bulk fraction.

Sample description	CEC* [cmol/kg]	BET surface area [m^2/g]	Clay mineral fraction [%]
CH1A 0.4–0.6 m	19.4	40.2	67.8
CH1A 1.4–1.6 m	23.7	47.1	47.8
CH1A 2.4–2.6 m	10.0	36.2	31.2
CH1A 3.4–3.6 m	10.9	27.2	36.5

*Cation exchange capacity.

ACKNOWLEDGEMENTS. We would like to thank the ANSTO project team who completed the field sampling program and sample preparation, E. Chong for undertaking the sorption studies of Co and L. Mokhber-Shahin for the gamma measurements and analysis.

Extraction studies of Co-56, Cu-64 and Zn-65 in the presence of calix[4]arenes

M. Poetsch, A. Mansel, R. Schnorr,[1] S. Haupt,[1] B. Kersting[1]

[1]Institute of Inorganic Chemistry, Faculty of Chemistry and Mineralogy, University of Leipzig, Leipzig, Germany

The long-lived radionuclides ^{60}Co and ^{65}Zn are produced in nuclear energy and medical facilities. Exposed to living organisms, they show radiotoxic properties. In case of release in the biosphere, efficient and selective extraction methods from environmental samples (e.g. groundwater) are necessary. In an ongoing cooperation project, we investigate the extraction behavior of particularly designed calixarenes in respect to radionuclides of cobalt, copper and zinc. The radionuclides used for extraction were either produced at the Leipzig 18 MeV cyclotron of the HZDR (^{56}Co, ^{64}Cu) or purchased by commercial suppliers (^{65}Zn). These studies represent an implementation of radiotracer technique within a cooperation project.

EXPERIMENTAL. ^{56}Co ($T_{1/2}$ = 77 d) and ^{64}Cu ($T_{1/2}$ = 12 h) were produced by using the nuclear reactions ^{56}Fe(p,n)^{56}Co [1] and ^{64}Ni(p,n)^{64}Cu. After irradiations of the target materials, the iron and nickel were dissolved with concentrated HCl [2]. The radionuclides were seperated by liquid-liquid extraction with methyl-tert-butylether (MTBE) and an anionic exchange with DOWEX 1x8 [3]. The extractions yields amount to 82% and 86%. As a ligand for the extraction experiments, a lower rim substituted calix[4]arene was used. The 25,27-Bis-{2-[N-(2-hydroxybenzyliden)amino]ethoxy}-26,28-dihydroxy-calix [4]arene was synthesized at the Leipzig University as shown in Fig. 1. 25,27-Bis(aminoethoxy)-26,28-dihydroxy-calix[4]arene was suspended in ethanol. While stirring, a solution of salicylaldehyde, dissolved in ether, was added dropwise. The mixture was refluxed and afterwards cooled down. The precipitation was filtered, washed with methanol and dried in an oven.

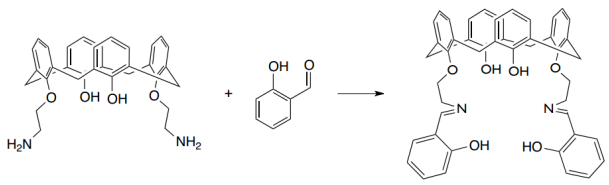

Fig. 1: Scheme of the synthesis route to 25,27-Bis-{2-[N-(2-hydroxybenzyliden)amino]ethoxy}-26,28-dihydroxy-calix[4]arene.

Due to the high solubility of the extractant in typical unpolar organic solvents, a simple chloroform-water system was used for the liquid-liquid extraction experiments. In general, 0.1 mM aqueous solutions of either cobalt nitrate, copper nitrate and zinc chloride were extracted with 0.5 mM chloroform solutions of the extractants. The aqueous phases were traced by addition of the corresponding radionuclide. pH values were adjusted using an ammonium acetate/ammonia buffer. After extraction, the remaining concentrations of radionuclides in the aqueous phases were determined via γ-spectrometry and Liquid Scintillation Counting.

RESULTS. Screening experiments on the effect of pH on the extraction yield were investigated first (Fig. 2). Below a pH of 7, metal extraction yields under 15% were observed. At pH 9, metal extraction yields ranged between

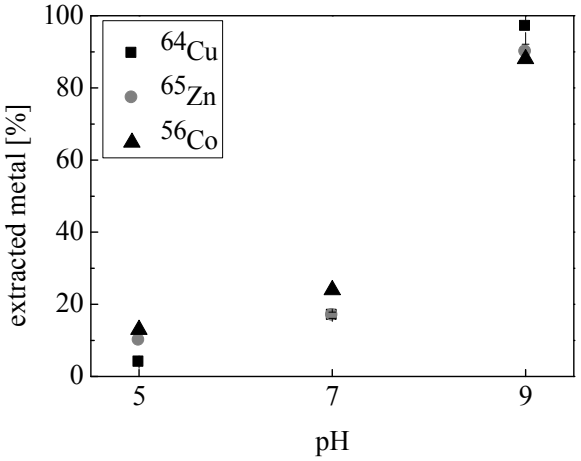

Fig. 2: Extraction yields for ^{56}Co, ^{64}Cu and ^{65}Zn by using the extractant at different pH values.

90% and 99%. All further extraction studies were consequently conducted at pH 9.

The influence of typical organic and inorganic groundwater compounds (NaCl, $CaCl_2$, $FeCl_3$, HCO_3^-, HSO_4^-) on the selective metal extraction yields was studied. Results for equimolar additions of these competing compounds are shown in Fig. 3.

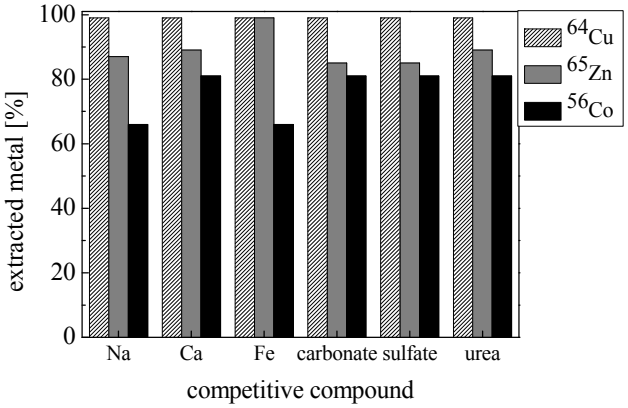

Fig. 3: Extraction yields obtained for ^{56}Co, ^{64}Cu and ^{65}Zn with addition of equimolar concentrations of different competing compounds similar to groundwater.

It is evident that the effect of most of the competing compounds on the extraction yield is of minor importance. Still, Co, Cu and Zn extraction yields amount larger than 60% although iron and sodium lead to a decrease of extracted ^{56}Co by approximately 10%.

To summarize, the studied calixarene was found to be a surprisingly efficient extractant for the tested dissolved transition metal ions. In turn, a selectivity for a special ion could not be shown.

ACKNOWLEDGEMENTS. The authors gratefully thank the German Federal Ministry of Education and Research (BMBF) for financial support of this study (project no. 02NUK014).

[1] Jenkins, I.L. et al. (1970) *J. Inorg. Nucl. Chem.* **32**, 1419–1425.
[2] Lagunas-Solar, M.C. et al. (1979) *Int. J. Appl. Radiat. Isot.* **30**, 25–32.
[3] Kozempel, J. et al. (2007) *Radiochim. Acta* **95**, 75–80.

Probing Eu^{3+} with NMR spectroscopy – A helpful tool in tracking binding sites

J. Kretzschmar, A. Barkleit, V. Brendler

The paramagnetic europium ion (Eu^{3+}) can be used as a very helpful probe to determine the binding sites of a molecule of interest by means of the interaction of the metal ion with the molecule's functional groups. Glutathione (GSH), a ubiquitous tripeptide possessing different types of functional groups, serves as a model system to show the usefulness of paramagnetic ions in NMR spectroscopy. The closer (the stronger) the ion is attached to a distinct binding site, the stronger is the impact on the spectral changes of the respective signals of adjacent nuclei.

Lanthanides have become a useful tool in NMR (nuclear magnetic resonance) spectroscopy within the last 40 years. Due to their paramagnetism they can be utilized as probes to determine the binding sites of biologically or environmentally relevant organic molecules as they cause significant line broadenings and/or paramagnetic induced shifts [1–3].

Lanthanides such as europium can easily be used as inactive analogues for trivalent actinides in consequence of their similar chemistry.

GSH (Fig. 1) is a tripeptide consisting of the amino acids glutamate (Glu), cysteine (Cys) and glycine (Gly). It is a highly concentrated intracellular reducing agent, playing a major role in detoxification processes. Important targets are electrophiles such as heavy metal ions. With its high natural abundance, different functional groups and reducing capability, this tripeptide provides outstanding characteristics for actinide complexation research.

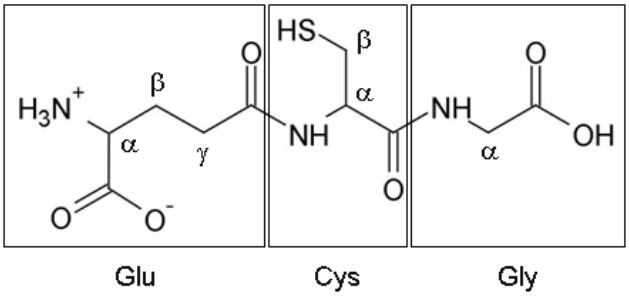

Fig. 1: Lewis structure of glutathione at pH 3 and indication of its constituents.

EXPERIMENTAL. Samples containing 300 mM GSH and different concentrations (0–300 mM) $EuCl_3$ were prepared at pH 3 and ambient conditions (T = 22 °C, $p(CO_2) = 10^{-3.5}$ atm).

The samples were investigated by 1D and 2D NMR methods, *e.g.* ^{1}H- and ^{13}C- as well as H,H-COSY (Correlation Spectroscopy) and H,C-HSQC (Hetero-nuclear Single Quantum Coherence). NMR spectra were recorded on a Varian Unity Inova 400 spectrometer with a field strength of 9.4 T and resonance frequencies of 400 and 100 MHz for ^{1}H and ^{13}C, respectively, using an ATB $^{1}H/^{19}F/\{^{15}N\text{-}^{31}P\}$ PFG 5 mm broadband probe.

RESULTS. As shown in Fig. 2, the ^{1}H-NMR signals are shifted and broadened by the strong distance dependent interactions between nuclear spins and electron unpaired spins. This is due to the $4f^6$ electron configuration of the paramagnetic Eu^{3+} ions. The closer the binding site, the bigger is the effect on the respective signal.

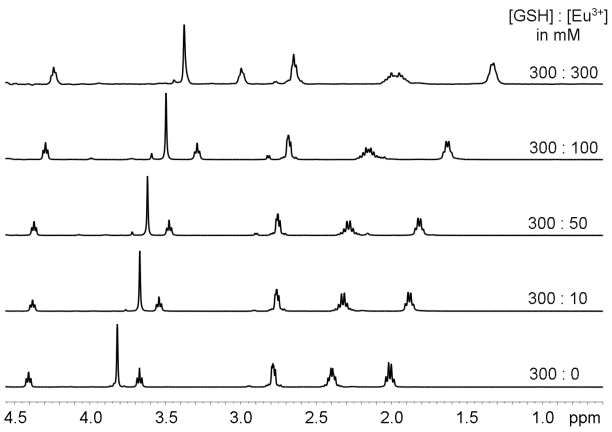

Fig. 2: ^{1}H-NMR spectra of 300 mM glutathione containing different Eu^{3+} concentrations at pH 3.

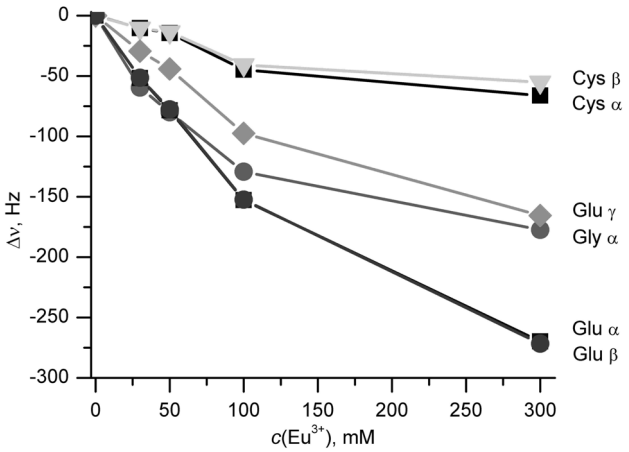

Fig. 3: Shift of the ^{1}H-NMR signals of glutathione in dependence on the europium concentration.

Figure 3 shows the change in the signals' positions (resonance frequencies) in dependence on the Eu^{3+} concentration. The α and β protons of the glutamate residue are shifted to the largest extent, indicating a low distance to Eu^{3+}, whereas the respective γ proton is less affected. The protons of the glycine moiety are moderately and that of cysteine are hardly shifted.

From these findings, the carboxylate group of the glutamate residue is identified as the most potential binding site for Eu^{3+} at pH 3. According to the aqueous speciation, the glycine carboxylic acid group is only partially deprotonated and therefore less involved in complexation. The thiol group does not seem to interact with the metal ion at all.

[1] Hinckley, C.C. (1969) *J. Am. Chem. Soc.* **91**, 5160–5162.
[2] Gansow, O.A. et al. (1971) *J. Am. Chem. Soc.* **93**, 4295–4297.
[3] Bertini, I. et al. (2001) *Solution NMR of paramagnetic molecules, Vol. 2, in: Current methods in inorganic chemistry*, Elsevier, Amsterdam.

Borate speciation at pH 5 and pH 6 determined by ^{11}B-NMR spectroscopy

J. Schott, J. Kretzschmar, A. Barkleit, M. Acker,[1] S. Taut,[1] V. Brendler
[1]Central Radionuclide Laboratory, Technische Universität Dresden, Dresden, Germany

The borate speciation at pH 5 and 6 was investigated using ^{11}B-NMR spectroscopy. Additionally, the influence of the concentration of different salts ($NaClO_4$, NaCl) was studied.

Boric acid ($B(OH)_3$) and borates are of great interest regarding the mobilization of trivalent actinides in the environment of nuclear waste repositories (salt deposits) [1]. The aqueous chemistry of boric acid/borates is very complex. Up to a critical boric acid concentration of 25 mM, only the dissociation of $B(OH)_3$ is observed, whereas at higher concentrations also polymerization reactions occur, that is the formation of polyborate species, such as tri-, tetra and pentaborate species. In the past, investigations concerning the borate speciation in aqueous solution were carried out (Raman spectroscopy [2], NMR [3]).
The aim of this work is the identification of the predominant aqueous polyborate species at pH 5 and 6 and the impact of the electrolyte (type of salt, concentration) on the borate speciation using ^{11}B-NMR spectroscopy.

EXPERIMENTAL. Samples with different $B(OH)_3$ concentrations (0.2–0.7 M) and $c(NaClO_4) = 0.1$ M were prepared at pH 5 and 6 under ambient conditions (22 °C, $p(CO_2) = 10^{-3.5}$ atm). $NaClO_4$ or NaCl was added to aliquots of the prepared $B(OH)_3$ stock solutions until a final salt concentration of 0.1 m, 1 m and 3 m was obtained.
^{11}B-NMR spectra were recorded with a Varian Unity Inova 400 spectrometer with a field strength of 9.4 T and a corresponding ^{11}B resonance frequency of 128.4 MHz with a ATB ^{1}H/^{19}F/{^{15}N-^{31}P} PFG 5 mm broadband probe. The ^{11}B chemical shifts (δ) are referenced externally with respect to BF_3 etherate in $CDCl_3$.

RESULTS. At pH 6 and an initial boric acid concentration of 0.4 M (or higher), three boron species can be observed (Fig. 1, bottom). According to [3] these signals at δ = 19.4 ppm , δ = 13.3 and δ = 1.2 ppm can be assigned to boric acid $B(OH)_3$, the triborate $[B_3O_3(OH)_4]^-$ and the pentaborate $[B_5O_6(OH)_4]^-$, respectively. With increasing initial boric acid concentration, the formation of these polyborate species increases (Fig. 1, Tab. 1) and no further polyborates are formed. This speciation is affected neither by salt concentration ($NaClO_4$, Tab. 1) nor by the investigated electrolyte systems ($NaClO_4$, NaCl, Fig. 2, Tab. 1). Moreover, the six months aged 0.7 M $B(OH)_3$, 0.1 m $NaClO_4$, shows no differences in the borate speciation compared to the freshly prepared one (Fig. 2). At pH 5 and up to 0.5 M initial $B(OH)_3$ concentration no polyborate species are formed (Fig. 1, top). The only boron species found is the undissociated boric acid. Above 0.5 M $B(OH)_3$, marginal amounts of polyborates occur (detection limit).
These results of the borate speciation serve as a reference data set for further investigations. For instance, it can be shown that due to the presence of polyborates an Eu(III) borate solid species is formed [4].

ACKNOWLEDGEMENTS. This work is funded by BMWi under contract number 02E11021.

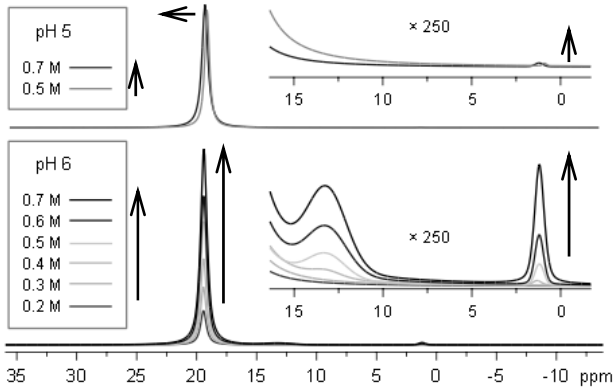

Fig. 1: ^{11}B-NMR spectra at different initial $B(OH)_3$ concentrations at pH 5 and 6, 1 m $NaClO_4$.

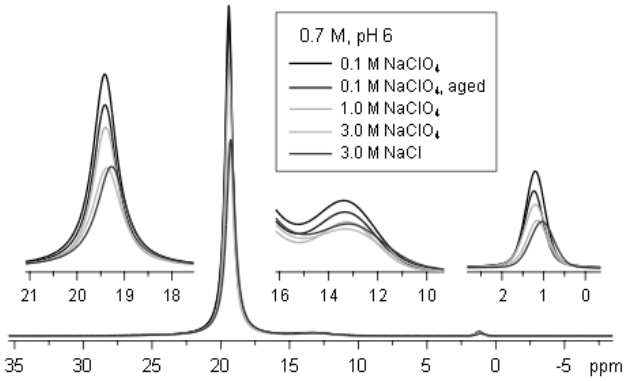

Fig. 2: ^{11}B-NMR spectra showing systems with an initial $B(OH)_3$ concentration of 0.7 M at pH 6 ($B(OH)_3$ stock solution) for different electrolyte concentrations.

Tab. 1: Molar fractions (calculated from peak areas) of borate species, pH 6 ($B(OH)_3$ stock solution).

initial $B(OH)_3$ concentration, electrolyte	molar fraction [%]		
	$B(OH)_3$	triborate	pentaborate
0.7 M $B(OH)_3$, 0.1 m $NaClO_4$	98.1	0.91	1.03
0.7 M $B(OH)_3$, 1 m $NaClO_4$	98.1	0.86	1.09
0.7 M $B(OH)_3$, 3 m $NaClO_4$	98.2	0.81	0.94
0.7 M $B(OH)_3$, 3 m NaCl	98.0	1.11	0.90
0.6 M $B(OH)_3$, 0.1 m $NaClO_4$	98.8	0.64	0.57
0.6 M $B(OH)_3$, 1 m $NaClO_4$	98.8	0.67	0.52
0.6 M $B(OH)_3$, 3 m $NaClO_4$	99.0	0.42	0.56
0.5 M $B(OH)_3$, 0.1 m $NaClO_4$	99.3	0.43	0.30
0.5 M $B(OH)_3$, 1 m $NaClO_4$	99.3	0.44	0.29
0.5 M $B(OH)_3$, 3 m $NaClO_4$	99.5	0.31	0.23
0.4 M $B(OH)_3$, 0.1 m $NaClO_4$	99.6	0.27	0.09
0.4 M $B(OH)_3$, 1 m $NaClO_4$	99.8	0.09	0.08
0.4 M $B(OH)_3$, 3 m $NaClO_4$	99.96	0.01	0.03
< 0.4 M $B(OH)_3$, 0.1 m / 1 m / 3 m $NaClO_4$	100.0	–	–

[1] Borkowski, M. et al. (2010) *Radiochim. Acta* **98**, 577–582.
[2] Hirao, T. et al. (1979) *J. Inorg. Nucl. Chem.* **41**, 1217–1220.
[3] Hertam, A. (2011) Diploma Thesis, TU Bergakademie Freiberg, Freiberg, Germany.
[4] Schott, J. et al. (2012) this report, p. 57

The formation of an Eu(III) borate solid species in aqueous solution

J. Schott, A. Barkleit, M. Acker,[1] S. Taut,[1] V. Brendler
[1]Central Radionuclide Laboratory, Technische Universität Dresden, Dresden, Germany

The Eu(III)-$B(OH)_3$ system was investigated by varying the pH, initial boric acid ($B(OH)_3$) and electrolyte ($NaClO_4$) concentration. An Eu(III) borate solid species was identified by filtration and fluorescence spectroscopy.

Although the interaction of trivalent actinides with borates might be relevant for the safety and risk assessment of a nuclear waste repository (salt deposit), this system is still investigated insufficiently. Borkowski et al. report on a moderate Nd(III) borate complex [1]. Furthermore, structures of solid borate compounds of trivalent actinides and lanthanides obtained from hydrothermal syntheses are well characterized [2, 3].
This work describes the formation of an Eu(III) borate solid species in aqueous solution under ambient conditions where Eu(III) is used as an analog for trivalent actinides.

EXPERIMENTAL. Samples with different $B(OH)_3$ concentrations (0.2–0.7 M) and c($NaClO_4$) = 0.1 M were prepared at pH 5 and 6 under ambient conditions (22 °C, $p(CO_2) = 10^{-3.5}$ atm). Eu(III) (3×10^{-5} M) and $NaClO_4$ (0.1–3 m salt concentration) were added to aliquots of the prepared $B(OH)_3$ stock solutions. The samples were investigated by time-resolved laser-induced fluorescence spectroscopy (TRLFS) and membrane filtration (0.2 µm pore size). TRLFS was carried out with a Nd:YAG-OPO laser system (Continuum). Static and time-resolved spectra of the solutions were recorded (delay times: 10–75 µs, pulse energy: 4 mJ, excitation wavelength: 394 nm).

RESULTS. Filtration experiments confirm the formation of a solid Eu(III) borate species at pH 6 which was not observed at pH 5 after 71 days observation time of the samples. The involvement of polyborate species in the solid formation is assumed. Due to ^{11}B-NMR spectroscopy it can be shown that at pH 6 and above 0.4 M $B(OH)_3$ polyborate species occur and at pH 5 in marginal (detection limit) amounts at higher concentrations (> 0.5 M $B(OH)_3$) [4]. Furthermore, only in presence of Eu(III) a solid formation is observable.
The solid formation at pH 6 was confirmed by TRLFS (Fig. 1). A characteristic band splitting of the $^5D_0 \rightarrow {}^7F_1$ and $^5D_0 \rightarrow {}^7F_2$ transition of the Eu luminescence during the formation of the solid species occur. The Eu luminescence lifetime τ, which can be used as a marker of the solid formation progress, increases with time to a constant value of around ~ 650 µs. From this result, a formation mechanism can be postulated. Starting from a soluble weak Eu borate complex (τ ~ 150 µs) a clustering of this species occurs, followed by a nucleation and precipitation of the Eu borate solid species (τ ~ 650 µs).
The solid formation depends on the polyborate concentration (Fig. 2). The smaller the initial $B(OH)_3$ (polyborate) concentration the slower the formation of the solid species. The solid formation can be detected for $B(OH)_3$ concentrations ≥ 0.4 M, which is consistent with the borate speciation at pH 6 [4].
Furthermore, the solid formation depends on the salt ($NaClO_4$) concentration (Fig. 3). This was not expected because of the salt independence of the borate speciation under these conditions [4]. During the formation phase a minimum of the Eu luminescence lifetime τ at ~ 0.5 m $NaClO_4$ is observable. This minimum is planished with the solid formation progress. Very high salt concentrations (~ 3 m $NaClO_4$) lead to a rapid solid formation.

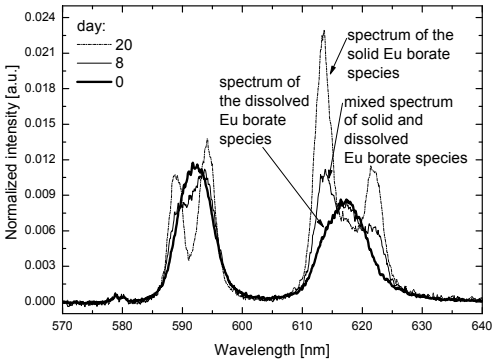

Fig. 1: Luminescence spectra of Eu representing the formation of the Eu borate solid species; sample contains 3×10^{-5} M Eu(III), 0.65 M $B(OH)_3$, 0.1 m $NaClO_4$, pH 6.

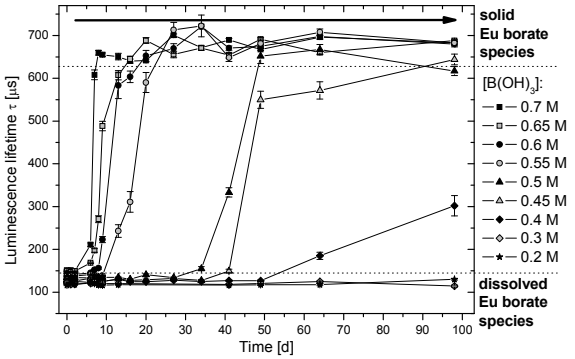

Fig. 2: Evolution of the Eu luminescence lifetime τ with time in dependence on initial [$B(OH)_3$]; samples contain 3×10^{-5} M Eu(III), 0.1 m $NaClO_4$, pH 6; arrow indicates decreasing [$B(OH)_3$].

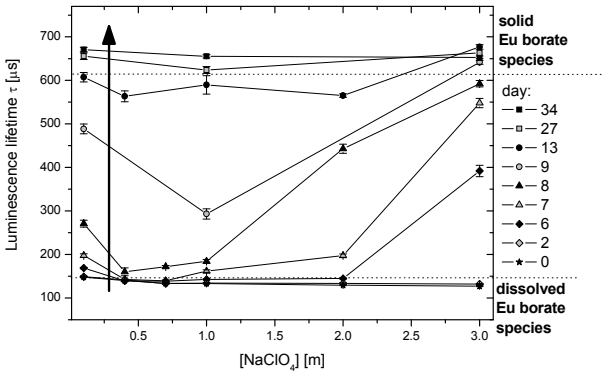

Fig. 3: Evolution of the Eu luminescence lifetime τ in dependence on [$NaClO_4$]; sample contains 3×10^{-5} M Eu(III), 0.65 M $B(OH)_3$, pH 6 ($B(OH)_3$ stock solution); arrow indicates increasing observation time.

ACKNOWLEDGEMENTS. This work is funded by BMWi under contract number 02E11021.

[1] Borkowski, M. et al. (2010) *Radiochim. Acta* **98**, 577–582.
[2] Polinski, M. J. et al. (2011) *Angew. Chem. Int. Ed.* **50**, 8891–8894.
[3] Polinski, M. J. et al. (2012) *J. Am. Chem. Soc.* **134**, 10682–10692.
[4] Schott, J. et al. (2012) this report, p. 56.

Formation of a hexanuclear Th(IV)-glycine complex in aqueous solution

C. Hennig, S. Takao,[1] K. Takao,[2] S. Weiß, W. Kraus,[3] F. Emmerling,[3] A .C. Scheinost

[1]Department of Engineering Science, University of Electro-Communications, Tokyo, Japan; [2]Department of Materials and Life Science, Seikei University, Tokyo, Japan; [3]BAM Federal Institute for Materials Research and Testing, Berlin, Germany

For the first time a hexanuclear Th(IV) glycine complex was observed in aqueous solution. The species $[Th_6(\mu_3\text{-}O)_4(\mu_3\text{-}OH)_4(H_2O)_6(Gly)_6(HGly)_6]^{6+}$ was preserved in a crystal to determine its structure [1].

Thermodynamic studies on the Th(IV)/glycine complexes are rare. Sergeev et al. [2, 3] determined a equilibrium constant of the 1 : 1 complex based on potentiometric titration data to log K = 8.90. Bismondo et al. [4] reinvestigated the system based on potentiomentic and calorimetric measurements and determined three formation constants (log K_1 = 2.55, log K_2 = 1.66 and log K_3 = 1.33). The authors of both studies assumed the formation of monomeric complexes in solution and excluded explicitly the potential formation of polymeric species.

So far, no structural data of the Th(IV)-glycine species in solution are available. Furthermore, no crystal structures were determined which may provide at least hints on potential coordination of the species in solution. The lack of information motivates a spectroscopic investigation of the Th(IV) glycine complexes.

EXAFS spectra, shown in Fig. 1, were recorded on samples with 0.05 M Th(IV) in 1 M glycine with pH ranging from 0.5 to 3.2.

The spectrum at pH 0.5 shows a single peak representing mononuclear complexes of $[Th(OH_2)_n]^{4+}$ and $Th(OH)_n^{(4-n)+}$ with $n \leq 2$. With increasing pH, the first peak in the Fourier transform becomes more asymmetric and finally splits. A second peak at R+Δ = 3.75 Å appears, and its intensity rises with increasing pH. This latter feature represents a Th-Th scattering interaction and indicates the occurrence of a hexanuclear complex. This complex is stable until pH 3.2. At higher pH values precipitates a crystalline material. The EXAFS spectrum of this solid is identical with that of the solution at pH 3.2 indicating that the structure of the solution species remains preserved in the crystal structure.

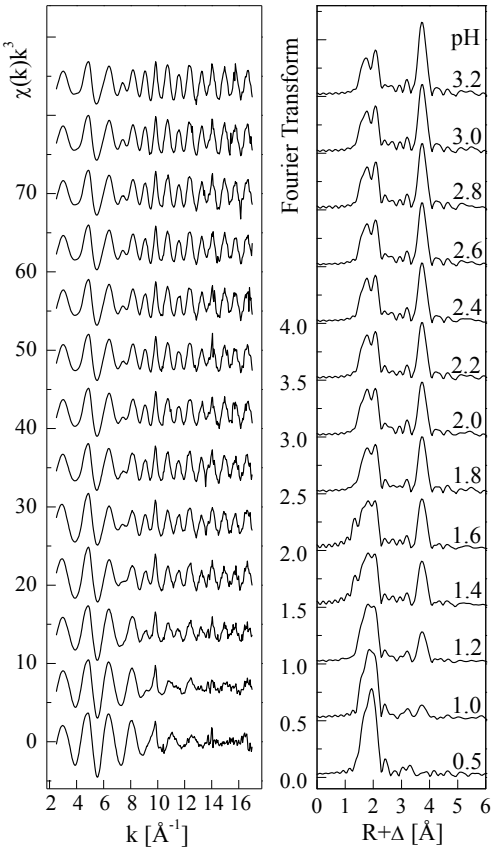

Fig. 1: Th L_3-edge k^3-weighted EXAFS data (left) and the corresponding Fourier Transforms (right) of a sample series with 0.05 M Th(IV), 1 M glycine, pH range of 0.5–3.2.

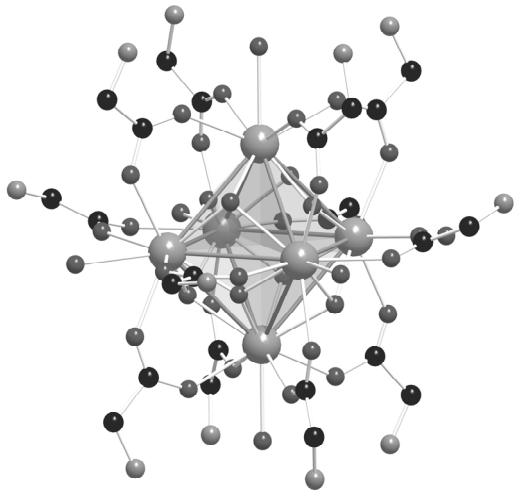

Fig. 2: The $[Th_6(\mu_3\text{-}O)_4(\mu_3\text{-}OH)_4(H_2O)_6(Gly)_6(HGly)_6]^{6+}$ unit. Th: big balls, O: dark grey, C: black, N: light grey.

A drawing of the crystal structure is shown in Figure 2. The complex consists of a hexanuclear core with six Th(IV) atoms arranged at the corners of a nearly regular octahedron. Each of the eight faces of the octahedron is bridged by either a μ_3-O or a μ_3-OH, resulting in a total of four μ_3-O and four μ_3-OH per hexanuclear core. The twelve edges of the octahedron are bridged by the carboxylic group of the glycine ligands through a *syn-syn* coordination. The 12 COO^- groups of the glycine ligands compensate the charge of the $[Th_6(\mu_3\text{-}O)_4(\mu_3\text{-}OH)_4]^{12+}$ core. Of the twelve glycine ligands are six Gly^-, and six HGly ligands, whose positive charge is compensated by three NO_3^- and three ClO_4^- counter ions. The electron density distribution of the coordinated glycine ligands is different from the free forms and influences the deprotonation behaviour of the gycine nitrogen. In the crystal structure appears an equimolar ratio of Gly^- and HGly at lower pH than that expected for the free ligand [1].

The observation of the hexanuclear complex corresponds with both, the onset of the Th(IV) hydrolysis at the one hand, and the deprotonation of the carboxylic function of glycine at the other hand. This results in a competing reaction between hydrolysis and ligation. The hydrolysis results in a polymerization via oxo and hydroxo bonds, whereas the carboxylic function of glycine results in the formation of 12 terminating chelate rings, preventing further polymerization of the hexanuclear polymer.

[1] Hennig, C. et al. (2012) *Dalton Trans.* **41**, 12818–12823.
[2] Sergeev, G.M et al. (1973) *Radiokhimija,* **15**, 619.
[3] Sergeev, G.M. et al. (1980) *Radiokhimija*, **22**, 536.
[4] Bismondo, A. et al. (1983) *Inorg. Chim. Acta,* **74**, 21–24.

Uranyl(VI) "yl"-oxygen exchange via $(UO_2)_2(OH)_2^{2+}$

S. Tsushima

Szabó and Grenthe [1] have shown by NMR spectroscopy that the "yl"-oxygen exchange in uranyl(VI) takes place via binuclear complex $(UO_2)_2(OH)_2^{2+}$. Here, DFT calculations were performed to explore the "yl"-oxygen exchange pathway involving $(UO_2)_2(OH)_2^{2+}$.

Two recent studies [1, 2] independently suggested that the exchange between "yl"-oxygen and oxygen in solvent water takes place via a bi-nuclear $(UO_2)_2(OH)_2^{2+}$ and possibly via other poly-nuclear hydroxo species. DFT calculation were performed to study the mechanism of "yl"-oxygen exchange involving $(UO_2)_2(OH)_2^{2+}$.

CALCULATIONS. DFT calculations were performed in aqueous phase employing the B3LYP functional through the use of the conductor-like polarizable continuum model using Gaussian 03. The small-core effective core potential and the corresponding basis set were used for U and O. For H, valence triple zeta plus polarization basis was used. The Gibbs energy correction to the electronic energy was calculated at the B3LYP level from the vibrational energy levels and the molecular partition functions. Transition states were identified through a single imaginary frequency that describes the translation movement across the energy barrier.

RESULTS. First, direct proton transfer from the bridging OH (**a**) or from the coordinating H_2O (**b**) to the "yl"-oxygen in $(UO_2)_2(OH)_2(H_2O)_6^{2+}$ was investigated. The activation enthalpy $\Delta^{\ddagger}H$ was found to be 180.9 kJ mol^{-1}. and 170.4 kJ mol^{-1} for (**a**) and (**b**), respectively, which are too high compared to the experimental value of 80 ± 14 kJ mol^{-1}[1].

Since a direct proton transfer from either the OH or the H_2O ligand to the "yl"-oxygen was found to be unlikely, another stepwise proton transfer mechanism has been studied here as depicted in Fig. 1. In this pathway, the primary reaction is the cleavage of one of the two OH bridges in $(UO_2)_2(OH)_2(H_2O)_6^{2+}$ (**I** → **II**) which is followed by a twist of the two equatorial planes (**II** → **III**). The pathway then continues with the formation of new oxo bridge (**III** → **IV**). This oxo bridge formation has a very small activation barrier of 3.8 kJ mol^{-1} and also the Gibbs energy difference between the complexes with and without the oxo bridge is only 1.3 kJ mol^{-1}. The oxo bridge formation is followed by cleavage of the OH bridge (**IV** → **V**). Since the ΔG of the reaction is +27.4 kJ mol^{-1} cleavage of the OH bridge clearly destabilizes the complex. Finally, a proton transfer takes place between two OH ligands in complex **V** leading to the formation of new oxo ligand and a water molecule (**VI**). The $\Delta^{\ddagger}H$ of the proton transfer (**V** → **VI**) is 10.1 kJ mol^{-1}, and the activation enthalpy relative to **I** is 93.4 kJ mol^{-1}.

In the final step, a proton is transferred from a water molecule to the oxo bridge in complex **VI**. The reaction takes place first by reorganization of the UO_3 unit on the right-hand-side of **VI** resulting in the formation of **VII**. This is followed by a proton transfer from coordinating H_2O to the oxo bridge (**VII** → **VIII**). The latter reaction has an activation barrier of 94.7 kJ mol^{-1} relative to **I** and has the highest activation barrier relative to complex **I** so

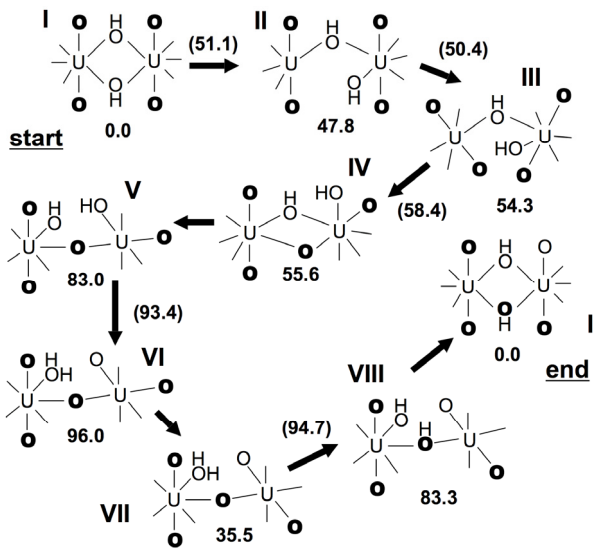

Fig. 1: Illustration of the stepwise proton transfers in $(UO_2)_2(OH)_2^{2+}$ leading to the oxygen exchange between O_{yl} and OH^- ligand. Coordinating waters which are not involved in proton transfer are omitted for clarity. Gibbs energy (and activation enthalpies in parentheses) relative to the precursor are given in kJ mol^{-1}.

that the rate determining step in the entire pathway is the **VII** → **VIII** transition. Large stabilization by the transition **VI** → **VII** is indicative of relatively low activation barrier but this step may have $\Delta^{\ddagger}H$ greater than 94.7 kJ mol^{-1} relative to complex **I** and may slightly increase the overall activation barrier.

Finally, complex **I** follows the following reaction:

$$(UO_2)_2(OH)_2^{2+} + 2H^+ \leftrightarrow 2UO_2^{2+} + 2H_2O \qquad (1)$$

The reaction (1) is known to be a rapid equilibrium, and there is a fast exchange of oxygen in OH^- of $(UO_2)_2(OH)_2^{2+}$ and that in solvent water [3].

The "yl"-oxygen exchange mechanism in Fig. 1 is consistent with the previous experiments of Szabó and Grenthe. The activation enthalpy of 94.7 kJ mol^{-1} agrees with their value of 80 ± 14 kJ mol^{-1}. Previous studies have suggested that a discrepancy of 15 kJ mol^{-1} (94.7 versus 80 kJ mol^{-1}) is acceptable between theory and experiment.

The present study confirms the oxygen exchange mechanism via the binuclear $(UO_2)_2(OH)_2^{2+}$ complex proposed by Szabó and Grenthe [1] and also by Mashirov et al.[2].

ACKNOWLEDGEMENTS. I acknowledge the Center for Information Services and High Performance Computing, Technische Universität Dresden, Dresden, Germany, for the use of supercomputer.

[1] Szabó, Z. et al. (2007) *Inorg. Chem*. **46**, 9372–9378.
[2] Mashirov, L.G. et al. (2004) *C. R. Chimie* **7**, 1179–1184.
[3] Cole, D.A. et al. (1967) *J. Phys. Chem.* **71**, 2771–2775.

Luminescence properties of uranyl ions in chloride media in frozen samples

A. Osman, G. Geipel

Luminescence of uranyl ions is often quenched by ions in the solution like carbonate and chloride. It is known that in case of carbonate ions this dynamic quench effect decreases if the samples are frozen. We report for the first time on the luminescence of the uranyl ion in chloride solutions under frozen conditions.

It is well known that uranium(VI) forms very weak complexes with chloride. The NEA database [1] selects stability constants of

UO_2Cl^+ $\log \beta_1 = 0.17 \pm 0.02$

UO_2Cl_2 $\log \beta_2 = -1.1 \pm 0.4$.

A species distribution calculated with these data at pH = 1 using MEDUSA [2] shows that the yield of the first chloride complex does not exceed 0.1% at chloride concentrations less than 1.0×10^{-3} M. Therefore, it cannot be expected that this complex can be detected by luminescence measurements at room temperature. Additionally, it is well known that chloride ions have a dynamic quench effect on the luminescence of the uranyl ion [3]. Therefore, the determination of uranyl ions in chloride containing solutions may be erroneous. By measuring the samples in a frozen state, the dynamic quench effect of the chloride ions decreases and it becomes easier to detect the luminescence of species in the sample.

EXPERIMENTAL. A series of chloride working standard solutions (10^{-5}, 5×10^{-5}, 10^{-4}, 5×10^{-4}, 10^{-3}, 5×10^{-3} M) were prepared in 10 mL volumetric flasks. For each chloride solution a 5×10^{-5} M UO_2^{2+} was added. The pH was set to 1 (theoretically/ calculated value) by adding 1 mL of 1 M $HClO_4$, and eventually by a pH meter after TRLFS measurement. Measured pH values were very consistent with calculated values. For each sample TRLFS measurement was carried out at both room temperature (RT) and cold temperature (cryo).

RESULTS. TRLFS data showed at room temperature a strong quench effect with increasing chloride concentrations (Fig. 1). No peak shift in the spectra was obtained. The intensity data (sum of counts of the total spectrum) were evaluated by the Stern-Volmer equation. The dynamic quench constant $k_q\tau_0$ has found to be 3260 ± 93 Mol^{-1}.

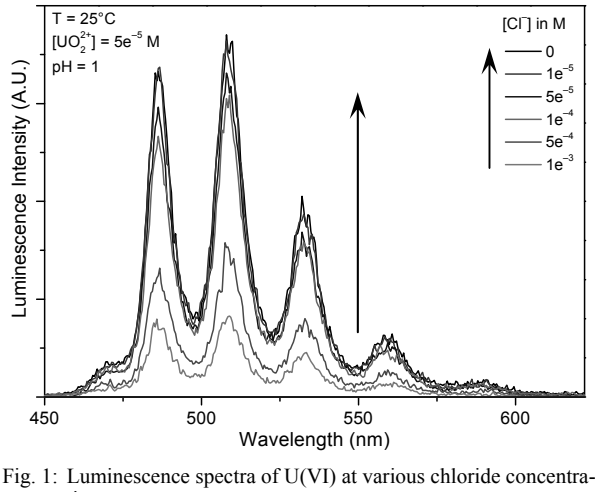

Fig. 1: Luminescence spectra of U(VI) at various chloride concentrations at room temperature.

Additionally, a decrease in fluorescence lifetime was also observed with increasing chloride concentrations.

By observing both effects, it can be stated that chloride ions achieve a collisional quench effect on the luminescence of the uranyl ion. By use of the assigned lifetime for the uranyl ion without the chloride quencher of 2.16 µs, we assign the collisional quench constant k_q to be $2.9 \times 10^9 \pm 2.13 \times 10^7$.

On the contrary, cryo-TRLFS measurements showed a luminescent species represented by higher intensities and strong red shifts of about 5 nm for all peaks positions comparing to the free uranyl ion (Fig. 2). An increase in the luminescence lifetimes was also observed.

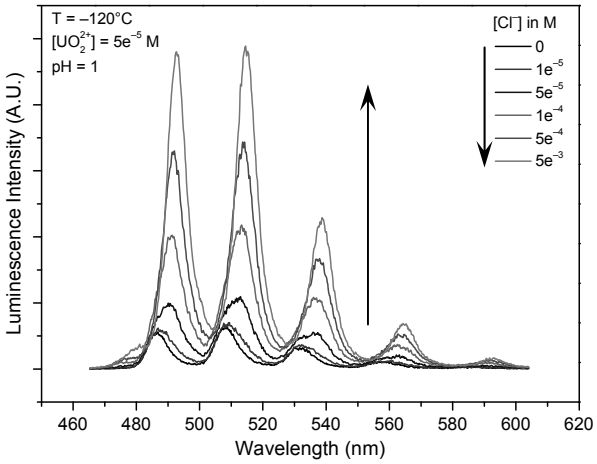

Fig. 2: Luminescence spectra of U(VI) at various chloride concentrations at 153 K.

The luminescence intensity increases by a factor of 5 from 0 to 5.0×10^{-3} M Cl^-, whereas the luminescence lifetime increases from about 340 µs to 490 µs.

In addition, five samples of aqueous 5.0×10^{-5} M U(VI) at pH 1 were prepared without adding any chloride. A pH electrode (filled with 3 M KCl) was immersed in all solutions with the following time interval; 0, 15, 30, 45, 60 minutes. Chloride concentration was determined in each solution. Cryo-TRLFS spectra showed the same effect (peak shift and increase in luminescence lifetime) as seen in the previous experiment. After 60 minutes, pH measurement the luminescence intensity reaches values comparable to 1.0×10^{-3} M Cl^-. This is a clear proof that pH glass electrode release a significant amount of chloride in the solution during pH adjustment.

Therefore, an important conclusion of this work is that the uncontrolled contamination of uranyl solutions with chloride by pH-measurements can be lead to errors, both in luminescence intensity and lifetime. This might explain the range of τ for the free uranyl ion from 1.1 to 2.0 µs.

ACKNOWLEDGEMENTS. We appreciate and thank the German Academic Exchange Service (DAAD) for financial support.

[1] Guillaumont R. et al. (2003) *Chemical Thermodynamics Vol. 5*, Elsevier, Amsterdam.

[2] Puigdomenech, I. (2002) MEDUSA Windows interface to the MS-DOS versions of INPUT, SED and PREDOM: Computer Programs Drawing Equilibrium Diagrams. *Trita-OOK-3010*, RIT, Stockholm Sweden (1983), Version 29.

[3] Nagasaki, S. et al. (1996) internal report.

The new Sunlite system for time-resolved laser-induced luminescence spectroscopy of lanthanide elements

A. Heller

A new, tunable laser system was installed at the Institute of Resource Ecology. The system is tailor-made especially for TRLFS measurements of lanthanides. First test measurements with Ce, Tb, Gd and Magnevist™ as well as the direct $^7F_0$ excitation of Eu are reported.

EXPERIMENTAL. The laser system consists of a pump laser (POWERLITE Precision II 9020), a tunable OPO/OPA (SUNLITE EX OPO) and a doubler unit (FX-1). The system was purchased from Excel Technology, Continuum. The Powerlite is an injection seeded, narrow bandwidth Nd-YAG laser. The Sunlite is pumped with 355 nm and the emitted wavelength can be tuned between 450 and 700 nm (signal) or 720–1750 nm (idler). For excitation wavelengths in the blue region, the FX-1 unit is used and the emitted wavelength can be tuned between 230 and 430 nm (doubled signal or doubled idler). The detection system consists of a spectrograph (270 M, Horiba) and an ICCD camera (i-Spectrum one, Horiba). To test the system, aqueous solutions of $CeCl_3$, $TbCl_3$, $GdCl_3$, Magnevist™ and $EuCl_3$ have been measured.

RESULTS. The UV-vis spectrum of Ce^{3+} exhibits three strong absorption bands between 250 and 300 nm. Hence, these wavelengths were used for excitation of the Ce^{3+} ion. The emission spectra are characterized by one broad band at 320–400 nm, which can be resolved into two single peaks (Fig. 1, Tab. 1) and show a bi-exponential decay of the emission intensity.
In the case of Tb^{3+}, the absorption spectrum exhibits up to nine peaks in the range of 250–400 nm. The most prominent one was used as the excitation wavelength for TRLFS measurements. The emission spectrum of Tb^{3+} exhibits four peaks between 450 and 650 nm (Fig. 1, Tab. 1) and shows a mono-exponential decay curve.

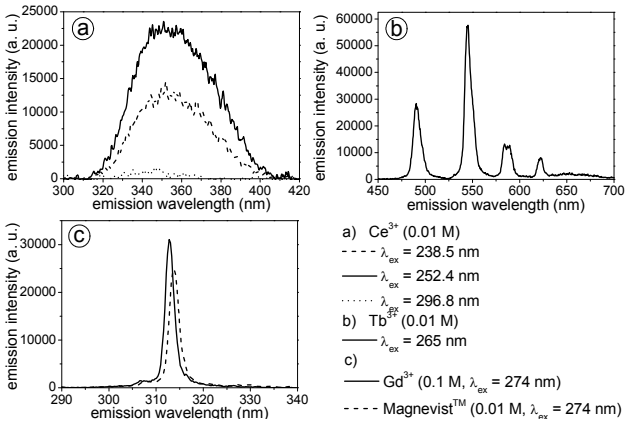

Fig. 1: Emission spectra of a) Cerium, b) Terbium and c) Gadolinium and Magnevist™ in aqueous solutions.

The UV-vis spectra of Gd^{3+} and Magnevist™, a Gd-based contrast enhancing agent used in magnetic resonance imaging, show one main absorption maximum at 273 and 274 nm, respectively, which was used for excitation. The emission spectra are characterized by each one sharp peak, which is shifted by 1 nm to higher wavelengths for Magnevist™ (Fig. 1, Tab. 1). Furthermore, the emission intensity of Magnevist™ is significantly enhanced, compared to that of the Gd^{3+} ion. In both cases, mono-exponential decay curves were measured. Hence, complexation of Gd^{3+} leads to a red-shift of the absorption as well as the emission maximum, an enhanced luminescence intensity and a significantly prolonged lifetime.

Tab. 1: Spectroscopic parameters of the measured Ln^{3+} aqua ions.

Parameter[a]	Ce	Tb	Gd	Magnevist™
λ_{ex} (nm)	238.5 / 252.4 / 296.8	265.0	273.0	274.0
Literature	250–266[1,2]	265, 365[3,4]	273, 275[5,6]	-
λ_{em} (nm)	342.5 / 365.5	488.5[b] / 542.8[b] / 581.8 / 587.4 / 622.2[b]	313.0	314.0
Literature	300–450[1,2]	485–702[3,4]	310–315[5,6]	313.0[7]
τ (µs)	10 ± 1 57 ± 1	428 ± 20	665 ± 150	4500 ± 500
Literature	0.04–0.05[1,2]	390–570[3,4]	200–3000[5,6]	5000 ± 150[7]

[a]λ_{ex} = excitation wavelength; λ_{em} = emission wavelength; τ = emission lifetime; [b]emission peak with shoulder.

Luminescence spectroscopy of Eu^{3+} is usually performed using a broad-band excitation with 395 nm into the $^5L_6$ state. To probe the existence of multiple Eu^{3+} species in one solution, it is helpful to excite with 578–580 nm directly into the degenerated $^7F_0$ state. In the case of two co-existing species, this would yield two excitation maxima with two different lifetimes. The application of the direct $^7F_0$ excitation was tested for Eu^{3+} in methanol on the Sunlite system and compared with broad-band excitation measurements recorded on a Panther EX OPO system. Steady-state spectra and luminescence decay curves are in very good agreement for both excitation methods (Fig. 2).

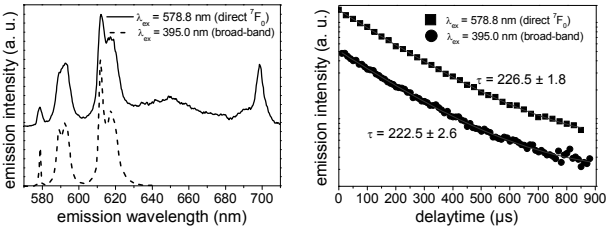

Fig. 2: Comparison of Eu^{3+} emission spectra after different excitation.

[1] Okada, K. et al. (1985) *Mol. Phys.* **54**, 1293–1306.
[2] Azenha, M. et al. (2008) *New J. Chem* **32**, 1531–1535.
[3] Kondrat'eva, E.V. et al. (1960) *Opt. Spektrosk.* **8**, 132–135.
[4] Kim, B Y. et al. (2010) *Electrochem. Comm.* **12**, 1005–1008.
[5] Baumann, M. (1988) *Bull. Chem. Soc. Jap.* **61**, 1399–1400.
[6] Poluektov, N. S. et al. (1972) *Zh. Prikl. Spektrosk.* **12**, 67–70.
[7] Moutiez, E. et al. (1997) *Analyst* **122**, 1347–1352.

NUCLEAR REACTOR

SAFETY & TRANSMUTATION

The Molten Salt Fast Reactor as transmutation system in the view of the nuclear phase-out in Germany

B. Merk, U. Rohde

A study has been performed in order to find an optimal transmutation system for minor actinides based on a Molten Salt Fast Reactor (MSFR). The use of such a system offers the possibility of burning the leftover at the end of the transmutation phase by adding a deep burning phase. The combination of these two phases within one system allows reaching transmutation rates of more than 90%.

The basic development and design of a molten salt reactor with fast neutron spectrum (MSFR) is the target of the EVOL project in FP7. The MSFR offers certain advantages in the view of transmutation compared to solid fuelled fast reactor types. These are especially the:

- avoidance of the solid fuel production with unavoidable minor actinide losses,
- avoidance of multiple recycling including the requested transports,
- improved reactor core stability due to strong negative feedback effects,
- uninterrupted irradiation of the minor actinides due to hot salt cleaning instead of aqueous reprocessing,
- reduction of losses in the reprocessing, since the fission products and not the TRUs are separated.

These advantages make the molten salt reactors more attractive for transmutation than the established technology of sodium cooled reactors [1, 2], even when this technology is mature and it has been used for the fundamental demonstration of the possibility of the transmutation of minor actinides [3]. In a molten salt reactor, the nuclear fuel is used in form of a salt, mostly fluoride salt like UF_4, which is dissolved in a carrier salt like LiF. The nuclear part of the salt can be configured only of transuranium isotopes (TRU – Pu, Am, Cm) as fissile part (fertile free), or the fissile part can be mixed with a fertile part based on salt consisting of U-238 or Th-232.

Long term operation studies for the MSFR are performed using the lattice code HELIOS [4] for different configurations – a core with U-238 fertile, a fertile free core, and a core with Th-232 as a fertile material. For all cases, the transmutation potential is determined, and a significant improvement in the transmutation performance for the case with Th-232 as a fertile material is demonstrated. For the detailed understanding, the time evolution of different important isotopes is analyzed and the amount of fissile and transmutation material for the startup is determined.

Based on the results of the optimized transmutation in a system with Th-232 as fertile component, the operation is optimized by an additional second phase. The goal of transmutation in Germany can not only be to transmute efficiently in a transmuter operation phase. Additionally, it is to burn as efficiently as possible the leftover of the transmuter operation phase. The phase with TRU fuel feeding into the core is finished when all available TRUs have been inserted. Transmutation in the German view is focused on the determination of the maximum transmutation efficiency and on an as much as possible reduction of the leftover of TRUs at the end of transmuter reactor life due the phase out decision. This is a prerequisite, since there is no future reactor foreseen and the leftovers have to be put into a final repository. This minimum leftover is achieved by a deep burning phase utilizing the U-233 bred in the blanket of the core, during the operation time, as feed. It is demonstrated, that transmutation rates up to more than 90% can be reached, while the production of undesired high elements is very limited. A rough approximation based on these results leads to the required number of about 4 reactors of 3000 MW and an operation time of ~ 50 years in transmutation and ~ 35 years in the deep burn mode for the transmutation of the German TRU stockpile [2, 4]. The impressive reduction of the leftover in the deep burn phase can easily be recognized in Fig. 1.

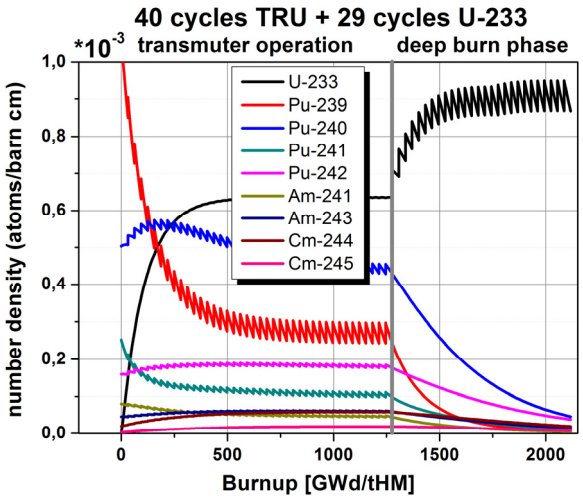

Fig. 1: Evolution of the isotope inventory during the transmuter operation and the deep burn phase.

The studies have been completed by an investigation to tackle one of the possible show stoppers in the design of a MSFR. Traditionally, the radiation damage of the most irradiated materials is one of the major challenges in all fast GEN-IV systems. These are the vessels containing the salt in a MSFR, while these are the fuel assemblies in all solid fuelled reactors which are replaced periodically due to the burnup of the contained nuclear fuel. The investigation has shown that it is possible to shield the safety related outer vessel of a MSFR by an appropriate design. Nevertheless, it has to be accepted that this shielding increases the size of the system significantly [5].

[1] Merk, B. et al. (2013) Intl. Conf. on Fast Reactors and Related Fuel Cycles: Safe Techn. and Sustainable Scenarios, Paris, France.
[2] Merk, B. et al. (2013) *PLoS One*, submitted.
[3] Merk, B. et al. (2013) *PLoS One*, submitted.
[4] Villarino, E.A. et al. (1992) *Nucl. Sci. Eng.* **112**, 16–32.
[5] Merk, B.et al. (2013) International Congress on Advances in Nuclear Power Plants (ICAPP '13), Jeju, Korea. accepted.
[6] Merk, B. et al. (2013) *Ann. Nucl. Energy*, invited.

Shielding and activation calculations in support of MYRRHA

A. Ferrari, J. Konheiser, B. Merk

In the frame of the FP7 European project Central Design Team (CDT), an extensive simulation study has been done to assess the main shielding problems in view of the construction of the MYRRHA accelerator-driven system at SCK·CEN in Mol (Belgium). The main results of the shielding and activation analysis will have important implications in the design solutions.

The CDT European project worked with the goal to design the Fast Spectrum Transmutation Experimental Facility (FASTEF) to demonstrate efficient transmutation of high level waste and associated ADS technology. The MYRRHA facility, which should start the construction phase in 2015, will be based on this design. The heart of the system is a lead-bismuth eutectic (LBE) cooled reactor, working both in critical and subcritical mode. The neutrons needed to sustain fission in the sub-critical mode are produced via spallation processes by a proton beam (600 MeV, 4 mA) provided by a linear accelerator and hits a LBE spallation target located inside the reactor core (Fig. 1). Among the many challenges of the design, radiation shielding and minimization of induced activation are key points.

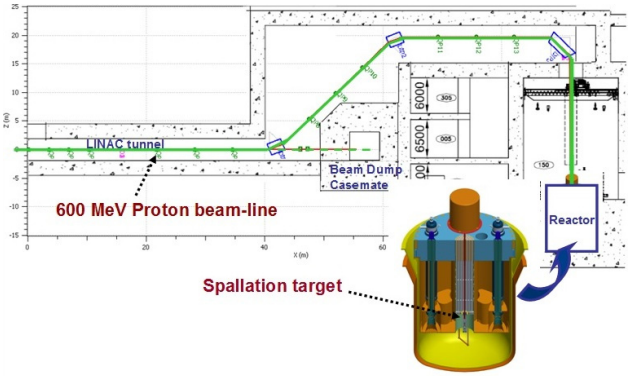

Fig. 1: Final part of the FASTEF-MYRRHA proton beamline.

SHIELDING ANALYSIS. The general problem of the radiation containment can be divided into two parts: the shielding of the accelerator tunnel and the shielding of the reactor building. The first problem has been addressed in [1] and [2]. From these studies of the neutron production and the radioactivity induced in typical materials by the MYRRHA proton beam, the design optimization of the elements devoted to the partial or the total beam absorption was derived. To assess the shielding of the reactor core, both critical and sub-critical operation modes have been studied [3]. Since in FASTEF the reactor is foreseen to operate at 100 MW core power in the critical mode and at 94 MW in the subcritical one, the critical mode exhibits the highest lateral neutron fluence at the fuel level, and can be reasonably considered as the conservative case for the lateral radiation containment. At the contrary, because of the backscattered radiation from the spallation target and due to the presence of the beam pipe channel, the subcritical operation drives the vertical design. An extensive simulation study has been done using two Monte Carlo codes: MCNPX, used in CDT to build the official core models in both the operation modes, and FLUKA, which has the unique possibility to compute, in the same

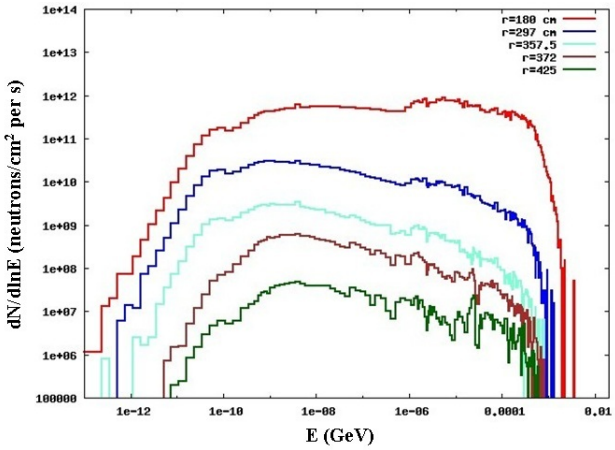

Fig. 2: Neutron spectra at increasing radial distances in the hottest horizontal segment across the core middle plane (FLUKA).

simulation, the transport of the coupled prompt (due to the ADS in operation) and residual radiation (due to the activated materials). Starting from the MCNPX model of the core, the radiation fields have been fully characterized on suitable surfaces around the core and used as input of a second row of FLUKA simulations, where complex source terms have been used. The FLUKA/MCNPX comparison of the neutron fluence rates (Fig. 2) inside the core vessel at different radial and vertical distances from the core barrel, which shows a very good agreement at the percent level, has been used to validate the FLUKA analysis. Dose distributions (Fig. 3) have been then evaluated from the core vessel to the external containment and the shielding walls in the horizontal direction, up to the last magnet of the proton beam-line and the final roof in the vertical one. Moreover, the activation of key materials has been characterized for typical irradiation patterns. This simulation work addressed the optimization of key elements of the design, from the cover plate to the local shielding structure above the last magnet.

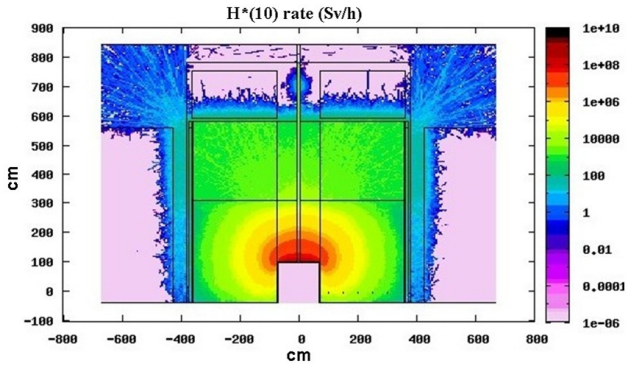

Fig. 3: Prompt H*(10) rate in and around the in-vessel structures.

ACKNOWLEDEGMENTS. The research leading to these results has received funding from the European Atomic Energy Community Seventh Framework Program (FP7/2007-2013) under Grant Agreement no. 232527.

[1] Biarrotte, J.-L. et al. (2012) *CDT Report D2.4*, p. 43–56.
[2] Ferrari, A. et al. (2013) *Proc. SATIF-11*, Tsukuba, Japan (OECD/NEA Publication, Paris).
[3] Sarotto, M. et al. (2012) *CDT Report D2.2*, p. 76–90 and p. 137–150.

Fluence calculations of surveillance specimens of the VVER-440

J. Konheiser, G. Borodkin[1]

[1]Department of Nuclear Plant Safety Scientific and Engineering (SEC-NRS) of Rostechnadzor, Moscow, Russia

Reactor pressure vessel (RPV) is a non-restorable reactor equipment and its lifetime may restrict the plant life time at a whole. Surveillance specimen (SS) programs for RPV materials are one of the most important parts of in-service inspection programs that are necessary for realistic and reliable assessment of RPV residual lifetime. The described work was performed as a part of a Russian-German scientific and technical cooperation.

For the investigation of the RPV embrittlement problem, it is necessary to evaluate the radiation loading parameters (fluences and spectra). The determination of these fluences is the main task of the reactor dosimetry. The fluences are calculated by different codes and the results are checked against measurement data. Neutron-activation measurements were carried out at ex-vessel positions of VVER-440 reactor. They provide the basis for validation of calculated neutron fluence of the surveillance specimens.

CALCULATION. The neutron and gamma fluences were calculated by the Monte Carlo program TRAMO [1] and by a three-dimensional synthesis method, based on the 2D discrete ordinates code DORT [2]. TRAMO is a multigroup Monte Carlo code for neutron and gamma transport calculations developed at HZDR. The code is especially dedicated to problems of reactor dosimetry and shielding. DORT is an internationally used program. The calculations with this code were carried out by SEC-NRS. A 60° sector had to be used for the calculation model; the corresponding geometrical and material information was provided from the investigated unit. The necessary source data were calculated based on the power data of the cycle of unit. The source distribution was given pin-wise in the outer fuel assembly rows.

MEASUREMENT. The measurements were carried out by Russian colleagues of SEC-NRS at Unit 3 of the Kola NPP during a whole cycle. In positions near the core mid-plane and of the critical weld detectors were installed at several azimuthal positions. Likewise, at the azimuthal position of the maximum flux of the core sixteen detectors were evenly distributed vertically. As neutron activation dosimeters mainly the isotopes ^{54}Fe and ^{58}Ni were used. The measured reaction rates give information on the fast neutron fluence integrated over the energy.

RESULTS. Local high resolution neutron spectra are available for all monitors. The statistical errors are around 1.0% for most of the group values. Based on these spectra, the reaction rates of ^{54}Fe(n,p)^{54}Mn and ^{58}Ni(n,p)^{58}Co have been determined. Values of 0.93 to 1.02 were determined for the calculation to experiment ratios (C/E) of the monitors on the horizontal plane of the critical weld which can be interpreted as very good agreement. There is the tendency that too large values were calculated for the monitors of core mid-plane and for the vertical monitors (except for the uppermost two). The value of C/E ratios ranged from 0.99 to 1.16.

The comparisons between the results of TRAMO and DORT calculations showed a very good agreement. The differences between both calculations are up to 5%.
For the investigation of surveillance specimens it is very important to know the uncertainties in the neutron and gamma fluences. One of these uncertainties is that the orientations of specimens in the channel and, hence, the positions of the specimens to the core are not known. Therefore, the minimum and maximum fluences of specimens were determined in dependence on the orientation of the specimen to the core with the help of TRAMO calculations. Figure 1 shows the possible neutron fluences greater 1 MeV in the specimens as a function of the height. The differences could be up to 30%.

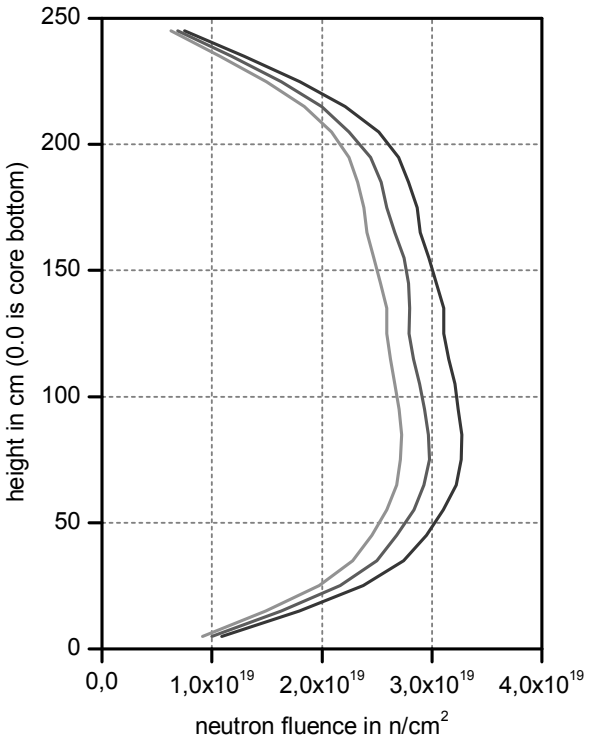

Fig. 1: The smallest (left curve), the average (middle curve) and the largest (right curve) calculated neutron fluences (> 1 MeV) in the Surveillance specimens in dependence on the height.

In addition, the lead factors of the surveillance specimens were determined. The maximum allowed fluence of the RPV (end of life fluence) is already achieved after two cycles in some specimens. The lead factors on the corresponding positions are very large. This is due to the fact that the specimens are located in the downcomer (nearer to the core) which has to be considered in the interpretation of the results.

ACKNOWLEDGEMENTS. This work was supported partly by the bilateral scientific-technical cooperation agreement between Germany and Russia through a project of the Ministry of Economics and Technology of Germany.

[1] Barz, H.-U. et al. (1998) *Report FZR-245.*
[2] Rhoades, W. et al. (1991) *TORT/DORT: Two-and Three Dimensional Discrete Ordinates Transport,* CCC-543.
[3] MacFarlane, R. E. et al. (1994), *The NJOY Nuclear Data Processing System (Version 91), Los Alamos,* LA-12740-M.

High conversion Th-U233 fuel assembly for current generation of PWRs

D. Baldova, E. Fridman

This study presents the development of a high conversion Th-U233 fuel assembly for existing Pressurized Water Reactors (PWRs) which can potentially improve utilization of natural resources, through the exploitation of vast thorium resources and the reduction in natural uranium demand. The proposed fuel assembly has the typical 17×17 PWR fuel lattice and standard outer dimensions. Each fuel assembly is subdivided into two regions seed and blanket, where the breeder blanket region is supplied by neutrons generated in the seed region.

This paper presents the results of the neutronic optimization study of a high conversion Th-U233 seed-blanket (SB) fuel assembly that can be used in the current generation of PWRs without any changes in the core design. The main goal is to maximize the conversion ratio through the optimization of the fuel composition and moderate modification of the fuel pin dimensions while preserving standard PWR fuel assembly lattice pitch and outer dimensions as well as using "typical" oxide fuel. The calculations were performed taking into account the target fuel cycle length of 12 months with 3-batch reloading scheme. The seed fuel pins have a standard radius of 0.4095 cm, while the blanket pin radius was enlarged in order to increase resonance capture in blanket and thus enhance the breeding potential. The parameters of the reference SB fuel assembly are given in Tab. 1 and the layout can be seen in Fig. 1. The neutronic optimization was performed with the deterministic transport code HELIOS [1] on the fuel assembly lattice level. The fuel cycle length and the core k-eff were approximated using Non-Linear Reactivity Model [2]. As an alternative to the conversion ratio the instant to initial fissile inventory ratio (FIR) was considered.

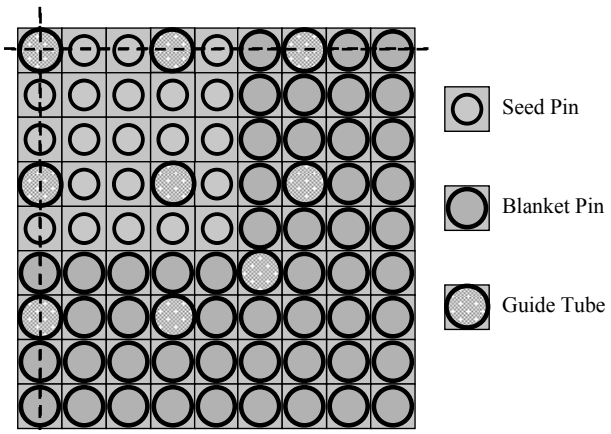

Fig. 1: 1/4th of the 17×17 SB fuel assembly.

Tab. 1: Operating parameters of the SB fuel assembly.

Pin pitch [cm]	1.26
Seed fuel pellet radius [cm]	0.4095
Seed cladding outer radius [cm]	0.4750
Blanket fuel pellet radius [cm]	0.5300
Blanket cladding outer radius [cm]	0.6155
Guide tube inner radius [cm]	0.5715
Guide tube outer radius [cm]	0.6120
Seed/Blanket fuel material	$U233O_2$-ThO_2
Seed fissile content [wt.-%]	2.50-12.50
Blanket fissile content [wt.-%]	0.5-2.5
Power density [W/cm^3]	70
Number of Seed pins	72
Number of Blanket pins	192
Number of Guide tube	25

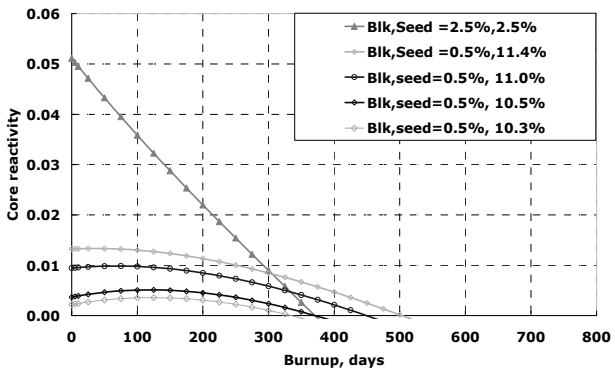

Fig. 2: Core reactivity.

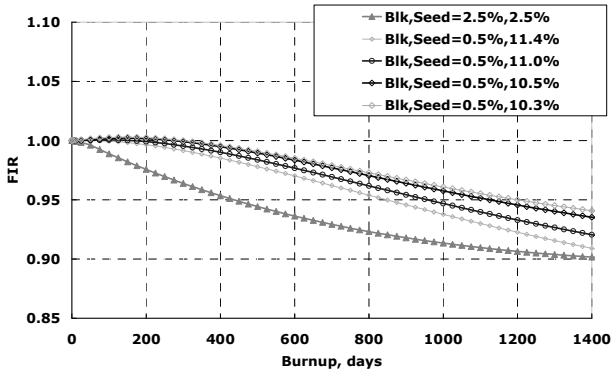

Fig. 3: Fissile inventory ratio (FIR) vs. burnup.

RESULTS. The 2D assembly lattice level neutronic analyses show that the SB assembly with optimized U233 content of 10.5 wt.-% and 0.5 wt.-% in seed and blanket regions can achieve the fuel cycle length of 370 EFPD in the 3-batch core (Fig. 2). In this case the FIR of about 0.97 (Fig. 3) can be achieved. It must be noted that the depletion calculations were performed with reduced average power density of 70 W/cm^3, since the high U233 content in the seed will cause strong power peeking in this part and may negatively affect the safety from thermal hydraulics point of view. In the future a detailed thermal hydraulic analysis must be performed in order to estimate the safe power density limits.

[1] Studsvik Scandpower (2008) *HELIOS Methods*.
[2] Driscoll, M. J. et al. (1990) *The Linear Reactivity Model for Nuclear Fuel Management*, Am. Nucl. Soc., LaGrange Park, U.S.A.
[3] Volaski, D. et al. (2009) *Proc. Global 2009*, Paris, France.

Post-test calculations of a ROCOM main steam line break experiment

S. Kliem, P. Apanasevich[1]
[1]Helmholtz-Zentrum Dresden-Rossendorf, Institute of Fluid Dynamics, Dresden, Germany

A coolant mixing experiment for a main steam line break scenario has been conducted at the Rossendorf Coolant Mixing Model (ROCOM). This experiment was used for a post-test calculation by means of the Computational Fluid Dynamics (CFD) code ANSYS CFX. All physical effects observed in the experiment can be reproduced by the code. The boundary in the downcomer between perturbed and unperturbed coolant has been calculated nearly at the same position as in the experiment. Quantitative differences between experiment and calculations can be seen in the structure of the inflowing overcooled water stripe.

ROCOM is a four-loop test facility for the investigation of coolant mixing operated with water at room temperature (Fig. 1). The facility models a KONVOI-type reactor with all details important for the coolant mixing along the flow path, from the cold-leg nozzles up to the core inlet, at a linear scale of 1:5. Special attention was given to components which significantly influence the velocity field, such as the core barrel with lower core support plate and core simulator, perforated drum in the lower plenum, and inlet and outlet nozzles [1]. The facility is operated with demineralized water at room temperature. Salt water is used to alter the local electrical conductivity of the fluid in order to label a specific volume of water and thus simulate an overcooled slug of coolant. The distribution of this tracer in the test facility is measured by special own developed wire-mesh electrical conductivity sensors, which allow a high-resolution measurement of the transient tracer concentration with regard to space and time.

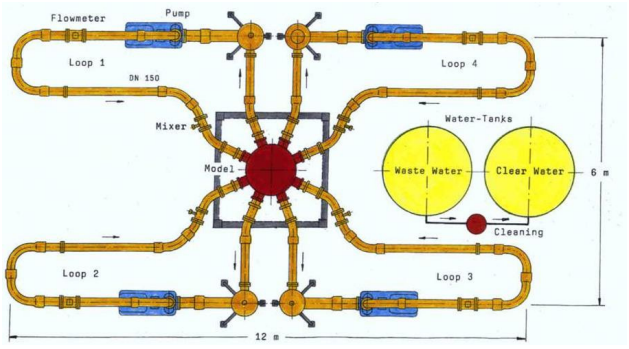

Fig. 1: Sketch of the ROCOM test facility.

EXPERIMENT. An experiment on the coolant mixing during a postulated main steam break accident in a pressurized water reactor has been conducted at the ROCOM test facility. Such an accident is characterized by a considerable reduction of the coolant temperature (up to 100 K) in one of the loops. During the experiment, water with higher density (simulating the lower temperature) was injected into loop 1 of the facility. This water mixes with the coolant arriving in the vessel from the other three loops. After some time, a quasi-stationary mixing pattern establishes in the downcomer. Figure 2 shows the distribution of the tracer in the downcomer of the facility. The data is shown as relative values between 0 and 100% by relating them to the initial perturbation. A boundary layer between perturbed and unperturbed (0% tracer) coolant is to be seen.

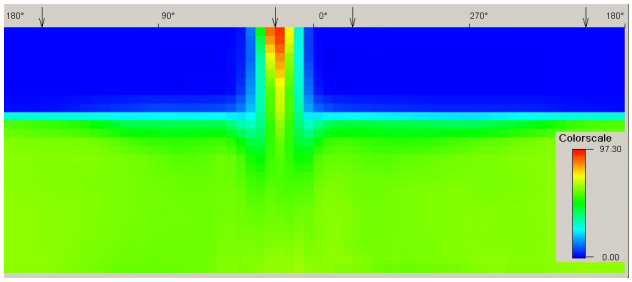

Fig. 2: Measured tracer distribution in the downcomer.

SIMULATION. One of the goals of the described experiment was the creation of data for the validation of CFD codes. The CFD code for simulating this mixing experiment was ANSYS CFX [2]. ANSYS CFX is an element-based finite-volume method with first and second-order discretization schemes in space and time. A coupled algebraic multigrid algorithm is used to solve linear systems arising from discretization. An ANSYS CFX model for the main part of the test facility was created starting from the cold legs over the downcomer and core till the hot legs. It consists of about 4×10^6 elements (Fig. 3).

Fig. 3: Outline of the ROCOM ANSYS-CFX calculation grid.

The calculation reproduces the structure of the coolant distribution in the downcomer; the boundary between the sectors is predicted nearly at the same vertical position. It can be seen that the inflowing overcooled water stripe has a different structure than in the experiment.

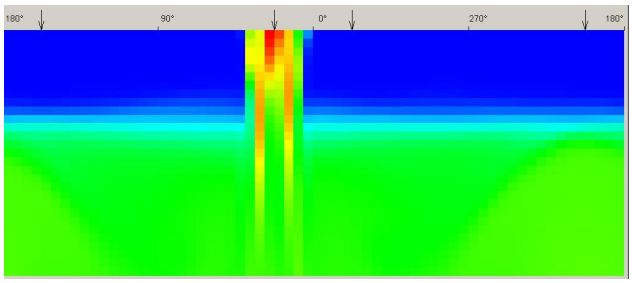

Fig. 4: Calculated tracer distribution in the downcomer (same color scale as Fig. 2).

ACKNOWLEDGEMENTS. The ROCOM experiment was conducted within the OECD PKL2 project. The corresponding boundary conditions were derived from a PKL-experiment conducted by AREVA NP Germany.

[1] Kliem, S. et al. (2008) *Nucl. Eng. Design* **238**, 566–576.
[2] ANSYS-CFX (2012) *ANSYS-CFX User's Guide*, Canonsburg.

Coupling of the reactor dynamics code DYN3D with the general-purpose fluid dynamics code ANSYS-CFX: test simulations in the one-phase region

A. Grahn, L. Tiborcz,[1] S. Kliem
[1]Budapest University of Technology and Economics, Budapest, Hungria

A coupling procedure with a commercially available fluid flow solver is being developed in order to improve the hydraulic simulation accuracy of reactor core simulations. At the current stage, coupled neutronic/hydraulic simulations with subcooled, non-boiling coolant flow can be performed.

In order to get the correct feedback on the core reactivity, analyses of postulated reactivity initiated accidents in nuclear reactors require the coupled solution of the neutron transport equation, the equations of heat conduction in the fuel and the heat and momentum transport in the coolant. The code DYN3D developed at Helmholtz-Zentrum Dresden-Rossendorf is a neutron kinetic core model, which solves in its basic version the three-dimensional neutron diffusion equation in two energy groups for fuel assemblies with rectangular and hexagonal cross sections [1]. DYN3D's thermal hydraulic part is based on a strictly one-dimensional representation of the coolant flow within each fuel assembly. However, the heat exchange between the fuel rods and the coolant flowing through the reactor core leads to complex three-dimensional flow-patterns, such as cross-flow between fuel assemblies and vortices behind obstacles. The computational fluid dynamics (CFD) code ANSYS-CFX [2] is the reference CFD code of the German CFD Network in Nuclear Reactor Safety. One of the goals of the cooperation inside this network is the development of CFD software for the simulation of multi-dimensional flows in reactor cooling systems. This includes the coupling of the CFD code ANSYS-CFX with the 3D neutron kinetic core model of DYN3D, in order to extend the description of the coolant flow and of the convective heat transport to three dimensions. This may finally lead to more plausible temperature and power distributions in the core.

COUPLING METHOD. The coupling approach is based on the selection of best-in-class software tools for the simulation of each of the phenomena to be described by the coupled codes. For this, the module predicting the coolant flow within DYN3D is replaced by a fully three-dimensional CFD simulation using ANSYS-CFX. A detailed and spatially resolved modeling of the whole reactor core down to the fuel pin level in a CFD code is not feasible for practical applications at present and in the foreseeable future. Currently, acceptable computation times can be achieved only by modeling the reactor core as a porous region. The interface between the two codes was therefore chosen to be at the heat-transfer level. The heat transfer from the fuel assemblies is calculated by DYN3D based on the boron concentration field, on the coolant's physical properties as well as on the flow velocity supplied by ANSYS-CFX, and is passed back to ANSYS-CFX as a volumetric heat source. ANSYS-CFX acts as the master program; DYN3D is implemented as a set of subroutines. A 3D volume mesh-to-mesh transfer of field quantities between ANSYS-CFX and DYN3D was implemented taking into account the largely different mesh resolutions used in the two codes.

SIMULATION EXAMPLE. A transient pressurized water reactor simulation with a perturbation of the coolant temperature in one quadrant at the core inlet (Fig. 1) is shown here for demonstration. The simulated reactor is operated at 18596 kg/s coolant mass flow and 15.8 MPa pressure. The nominal power is 3500 MW. The computational grid used by DYN3D contains 2701 cells, while the hydraulic simulation of CFX is carried out on a refined mesh with 717,000 elements. The computed temperature distributions at the core outlet and in the central vertical cross section after 18 s are shown in Fig. 2. It can be seen that the hydraulic simulation by a dedicated CFD program allows for greater detail in the computed distributions. Fig. 3 shows the simulation of the flow around a blocked zone of the core. Due to reduced cooling behind the obstacle the coolant temperature rises above its usual value.

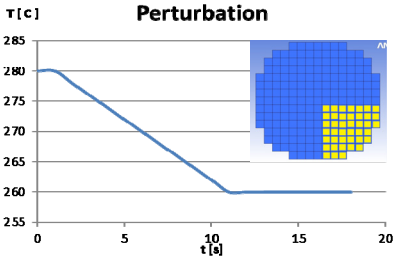

Fig. 1: Perturbed coolant temperature at core inlet.

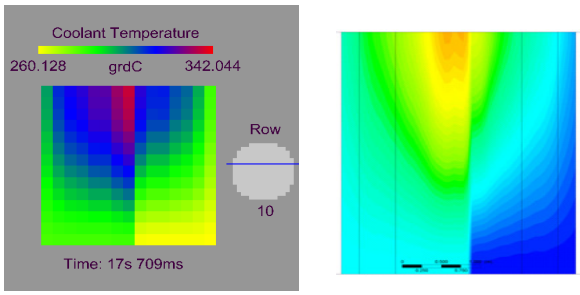

Fig. 2: Coolant temperature in vertical cross section of the core; left: DYN3D standalone, right: coupled DYN3D-CFX simulation.

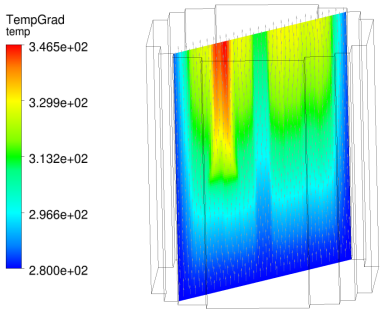

Fig. 3: Coolant flow around blocked zone in a fuel assembly Perturbed coolant temperature at core inlet.

ACKNOWLEDGEMENT. The project was funded by the German Federal Ministry of Economics and Technology (Contract numbers 150 1328 and 150 1358).

[1] Grundmann, U. et al. (2000) Proc. PHYSOR2000.
[2] ANSYS Inc. (2009), ANSYS-CFX User's Guide, Canonsburg, PA.

Steady state analysis of Sodium Fast Reactor cores using DYN3D-Serpent codes sequence

R. Rachamin, E. Fridman

The main objective of this study is to demonstrate the feasibility of using DYN3D for the modeling of Sodium cooled Fast Reactors (SFRs). A representative SFR core was modeled using the Serpent-DYN3D code sequence and the results were compared with those produced by 2D full core Monte Carlo solution. Very good agreement between the codes was observed for the core integral parameters and power distribution.

The advanced multi-group nodal diffusion code DYN3D [1], is currently being extended to the analysis of Sodium-cooled Fast Reactor (SFR) cores. Thermo-physical properties of sodium (such as thermal conductivity, density, viscosity, etc.) were included into the thermal-hydraulics module database. The development of thermo-mechanical model (to account for the core thermal expansion effects) is planned for the near future. The main objective of this study is to demonstrate the feasibility of using DYN3D for the modeling of SFR cores. For this purpose, a 2D model of the "working horse" mixed oxide fuel (MOX) SFR core (Fig. 1), proposed in the frame of the Collaborative Project (CP) on European Sodium Fast Reactor (ESFR) [2], was considered. The homogenized Few-group constants to be used by DYN3D were generated using the Monte Carlo (MC) reactor physics code Serpent [3], which was especially designed to generate homogenized constants for practically any reactor concept.

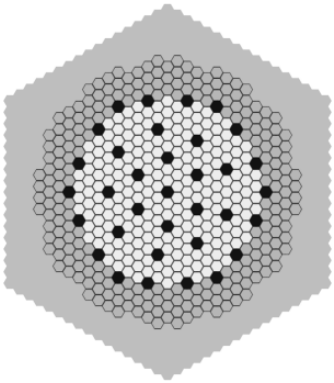

Fig. 1: Radial layout of the ESFR core; light grey: inner MOX fuel assemblies (14.5 wt.-% Pu), dark grey: outer MOX fuel assemblies (17.0 wt.-% Pu), black: control assemblies, grey: radial reflector.

FEW-GROUP CROSS SECTION GENERATION METHODOLOGY. The Few-group cross sections for the ESFR analysis were generated in 24-group energy structure [4]. The 24-group cross sections for the fuel assemblies not facing the non-multiplying regions were generated in an infinite assembly lattice calculation (Fig. 2a). In order to account for the strong spectral transition between the fuel assemblies and neighboring non-multiplying regions, the super-cell configuration presented in Fig. 2b was used to generate the 24-group cross sections for control assembly and surrounding fuel assemblies. The 24-group data sets for the outermost fuel assemblies facing the radial reflector and radial reflector itself were generated using the radial reflector model depicted in Fig. 2c.

FULL CORE RESULTS. 2D full core depletion calculations were performed using Serpent and DYN3D codes. The calculations were carried out at a constant power density of 206 W/cm^3 for a total of 2050 effective full power days (EFPD). The few-group cross section sets employed by DYN3D were generated, for each burnup step, using Serpent according to the methodology presented in the previous section. The results of the full core Serpent MC calculations served as a reference for verification of the DYN3D performance. Figure 3 presents the core k-eff as a function of burnup. It can be seen that the k-eff curves calculated by DYN3D and Serpent agree very well. The maximum difference is about 32 pcm. These results suggest that the DYN3D code with cross section library generated using Serpent can be reliably used for the analysis of fast reactors.

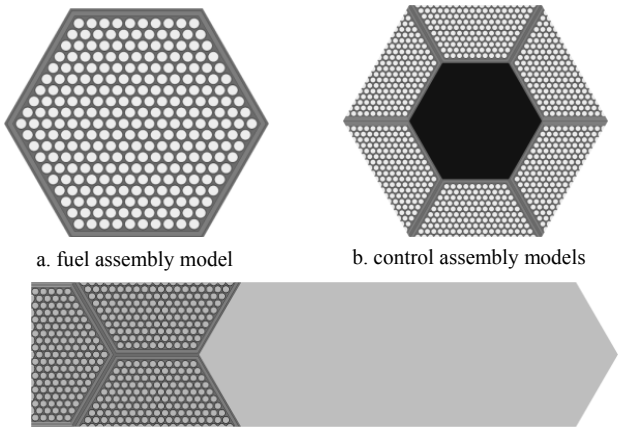

Fig. 2: Models for Few-group cross section generation.

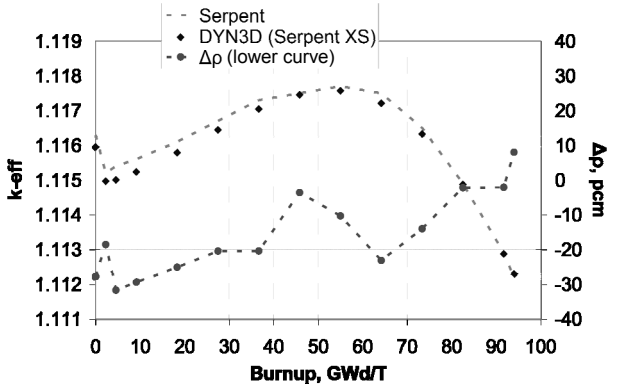

Fig. 3: k-eff as a function of burnup: Serpent vs. DYN3D.

[1] Grundmann, U. et al. (2000) *Proc. PHYSOR 2000*, Pittsburgh, U.S.A.
[2] Fiorini, G.L. et al. (2011) *Nucl. Eng. Des*. **241**, 3461–3469.
[3] Leppänen, J. (2007) D.Sc. Thesis, Helsinki University of Technology, Helsinki, Finland.
[4] Fridman, E. et al. (2013) *Ann. Nucl. Energy* **53**, 354–363.

Application of the reactor dynamics code DYN3D for prismatic High Temperature Reactors

S. Baier, E. Fridman, S. Kliem, U. Rohde

The reactor dynamics code DYN3D [1, 2] was extended to study steady state and transient behavior of prismatic High Temperature Reactors (HTRs). For this purpose, an appropriate heat conduction model is necessary to include 3D heat conduction and to reproduce the multi-level structure of the reactor core. Within this study a short description of the heat conduction model and a few results are presented.

The prismatic HTR is a GEN-IV reactor concept to produce electrical power and to make use of high-grade heat for various industrial processes. The core consists of hexagonal fuel assemblies made of graphite with cylindrical holes for the coolant gas helium and for holding the fuel compacts. The latter contain highly robust tristructural isotropic (TRISO) coated fuel particles.

METHODOLOGY. A 3D heat conduction model was developed and coupled with the already existing coolant channel flow model in DYN3D. For temperature calculations, the hexagonal prismatic fuel assembly is radially divided into six equilateral triangles and then axially divided into nodes of equal height. Node-averaged temperatures of each fuel, fuel coatings, compact, and graphite matrix are calculated. Thus, the heat conduction model consists of a system of coupled heat conduction equations for each component. This system is solved with a finite volume method and the Crank-Nicolson method [3]. The neutronic calculation is performed in multi-energy-groups diffusion approximation. The temperature-dependent cross section data for the diffusion equation are generated using the Monte Carlo code Serpent [4] modeling each individual TRISO particle.

RESULTS. The test calculations are performed for the core in Fig. 1. The green assemblies contain fuel, the white and blue assemblies represent the outer and inner reflector, respectively. For the chosen transient a steady state with inserted control rod (assembly 41 in Fig. 1) was prepared. The initial power is 600 MW. Physical properties of the materials are taken from [5] and geometrical properties from [6]. During time evolution, the control rod was withdrawn with constant velocity within the time interval t = 5–105 s. Figure 2 shows the temporal evolution of the released power and the temperatures. During control rod withdrawal the absorption cross section becomes smaller and, thus, more neutrons are available for fission and the power increases dramatically. Due to the increased heat release the fuel temperature also increases. All other temperatures follow this trend with some delay. Due to the negative temperature feedback of fuel, compact and graphite block the power decreases and the temperatures follow this behavior. The system eventually relaxes to a new steady state with increased power and temperatures. The differences of graphite, compact and fuel temperature indicate the necessity of the multi-level heat conduction model because the feedback coefficients are very sensitive on temperature changes.
Additional analysis of steady state temperature and power distributions and other transients show that DYN3D-HTR

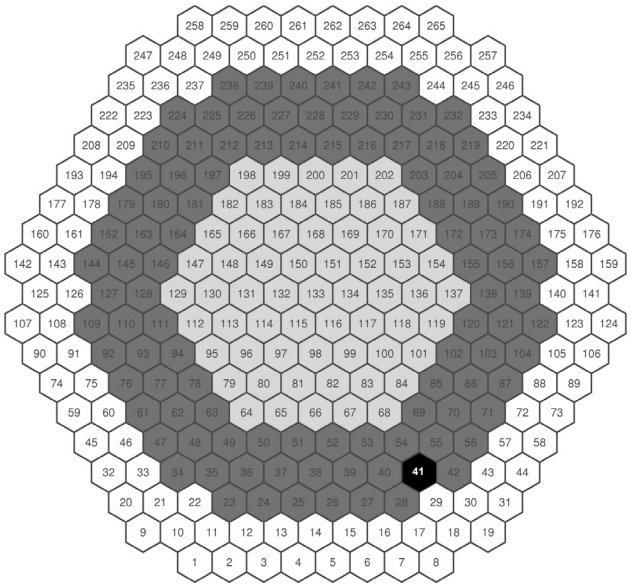

Fig. 1: Test core: *dark grey*: fuel assemblies, *white*: outer reflector, *light grey*: inner reflector, *black*: fuel assembly with inserted control rod.

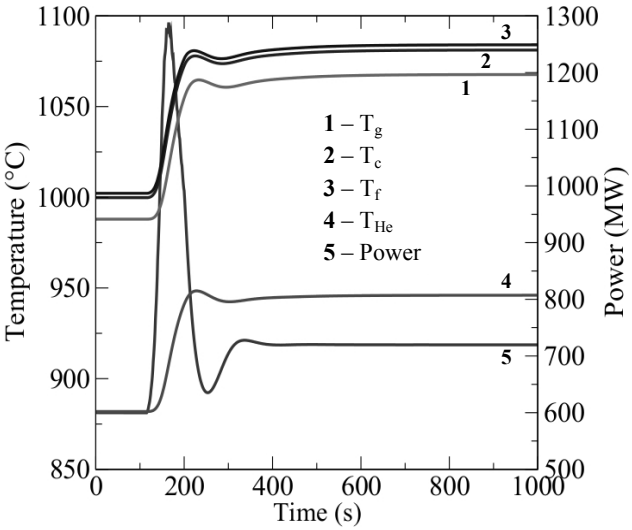

Fig. 2: Temporal evolution of the released power and the temperatures of graphite block (T_g), compact (T_c), fuel (T_f), and coolant (T_{He}) for a control rod ejection transient.

is an appropriate tool to perform steady state and transient analysis for prismatic HTRs.
Next, verification on benchmark exercises is planned.

ACKNOWLEDGEMENTS. This project was funded by BMWF, grant No. 1501358.

[1] Grundmann, U. et al. (2000) *Proc. PHYSOR2000*.
[2] Manera, A. et al. (2005) *Nucl. Eng. Des.* **235**, 1517–1535.
[3] Baier, S. et al. (2012) *Proc. HTR2012*.
[4] Leppänen, J. (2011) PSG2/Serpent Mote Carlo Reactor Physics Burnup Calculation Code, http://montecarlo.vtt.fi.
[5] Cho, N. Z. et al. (2009) *Ann. Nucl. Energy* **36**, 448–457.
[6] Lee, K.-H. et al. (2008) *Nucl. Eng. Des.* **238**, 2654–2667.

The trigonal-geometry simplified P_3 neutron transport and diffusion approaches of the nodal reactor code DYN3D

S. Duerigen, E. Nikitin[1]

[1]Institute of Nuclear Techniques, Budapest University of Technology and Economics, Budapest, Hungary

The reactor dynamics code DYN3D is a 3-D best-estimate tool for simulating steady states and transients of Light Water Reactors. It comprises a three-dimensional neutron-kinetics model, a thermal-hydraulics core module, and a fuel-rod model. Several versions of the DYN3D code are available including diffusion and simplified P_3 (SP_3) neutron transport options. In this article, the advantage of the SP3 method in trigonal geometry over the respective diffusion approach is demonstrated.

To improve the accuracy of the DYN3D [1] neutronics model, a transport approximation higher than diffusion theory has been developed. A trigonal-geometry simplified P_3 (SP_3) neutron transport approach for hexagonal reactor cores has been implemented in the code [2] in addition to the trigonal-geometry diffusion model [3]. This geometry is of particular importance for existing Russian-type power water reactors as well as for innovative reactor concepts.

THEORY. The behavior of a nuclear reactor is governed by the transport of neutrons and the interactions between neutrons and matter. As there are seven independent variables in the neutron transport equation, the solution of transport problems is difficult. The P_N approximation of the transport equation is quite accurate for planar geometry problems. However, expanding the P_N equations to multi-dimensional geometries is exceedingly complicated. The simplified P_N (SP_N) approximation of the neutron transport equation is obtained by expanding the angular flux in Legendre polynomials. Truncating the series expansion after the third-order term yields the P_3 and – generalizing to multi-dimensional geometries – eventually the SP_3 equations.

The high cost of solving core dynamics problems forces the use of methods based on coarse mesh elements. Therefore, a nodal approach is implemented in the code DYN3D. A nodal method allows a reactor core to be handled with large volume elements, so-called nodes, in which the global neutron flux distribution is characterized in terms of only a small number of parameters.

This approach is derived on trigonal geometries. A particular advantage in developing a nodal method for reactor cores with hexagonal fuel assembly geometry on a trigonal basis is the possibility of mesh refinement. In Fig. 1, the refinement mode is illustrated in a schematic manner.

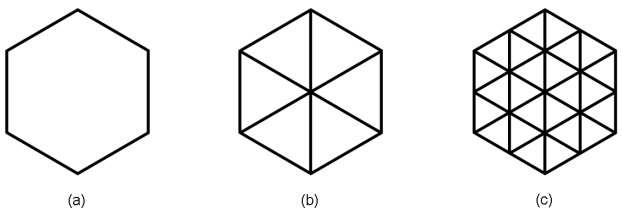

Fig. 1: Hexagonal fuel assembly (a) with triangular subdivision (b) and one subsequent refinement level (c).

RESULTS. In order to show the advantage of the trigonal DYN3D SP_3 model (DYN3D-TRISP3) in comparison to the respective diffusion approach (DYN3D-TRIDIF), a two-dimensional hexagonal benchmark problem with anisotropic scattering is presented.

The considered 30° core sector consists of three material types: one type of hexagonal fuel assemblies (material 1) and two types of reflector assemblies (materials 2 + 3). Whereas material 2 allows solely scattering, material 3 features pure absorption. Thus, the neutron flux is dominated by a strong migration process in direction to the absorber. In such a case, the importance of a method capable of representing anisotropic flux behavior becomes obvious.

Using vacuum outer boundary conditions, the SP_5 transport reference solution has been obtained by the finite-element code TRIVAC [4].

DYN3D-TRISP3 and DYN3D-TRIDIF calculations have been run applying the refinements of 6 and 6144 trigonal nodes per assembly. In Fig. 2, the normalized reference flux distribution of the considered core sector and the respective relative errors determined by DYN3D are depicted. Especially in the outer reflector region, DYN3D-TRISP3 superiorly represents the flux distribution in comparison to DYN3D-TRIDIF by more than an order of magnitude.

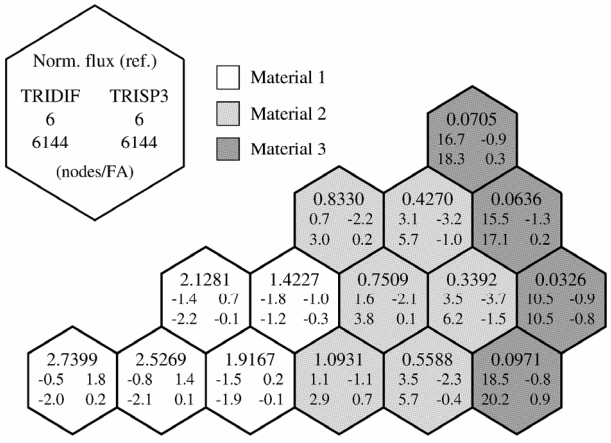

Fig. 2: Core configuration of the benchmark problem. Normalized reference neutron flux distribution and relative errors (%) determined by DYN3D-TRISP3 and DYN3D-TRIDIF for the nodalizations 6 and 6144.

CONCLUSION. By means of the presented benchmark problem, anisotropy effects are quantitatively identified and the superiority of the trigonal DYN3D SP_3 method over the respective diffusion model is clearly demonstrated.

[1] Grundmann, U. et al. (2000) *Proc. PHYSOR 2000*.
[2] Duerigen. S. et al. (2012) *Kerntechnik* **77**, 226–229.
[3] Duerigen, S. et al. (2012) *Proc. 22nd AER Symposium*.
[4] Hébert, A. (2012) *Tech. Rep. IGE-293*, École Polytechnique, Montreal, Canada.

Serpent Monte-Carlo code: an advanced tool for few-group cross section generation

E. Fridman

Serpent is a continuous-energy Monte Carlo reactor physics code especially developed for reactor physics applications. The main objective of this study is to demonstrate the applicability of Serpent for generation of homogenized few-group constants for existing and advanced reactor designs.

Serpent is a continuous-energy Monte Carlo (MC) reactor physics code recently developed at VTT, Finland [1]. Serpent is especially designed to generate homogenized constants for deterministic 3D core analysis. Recently, some new calculation methods related to the production of homogenized few-group constants were implemented in the Serpent code including homogenization in leakage-corrected criticality spectrum [2, 3], group constant generation in reflectors and other non-fissile regions [3], and improved treatment of neutron-multiplying scattering reactions [3]. The capability to generate homogenized few-group constants can be considered as one of the most attractive features of Serpent. Being a MC code, Serpent is capable of handling complex geometries without any major approximations and can be used for producing cross section data for virtually any fuel or reactor type. The demonstration of the Serpent capability to generate few-group cross sections for different reactor systems is the main topic of this study.

DESCRIPTION OF THE REFERENCE CORES. In this study three core designs were selected for demonstration of the Serpent modeling capabilities:

- A typical Westinghouse Pressurized Water Reactor (PWR) core loaded with 193 all fresh UO_2 17×17 fuel assemblies at different enrichment levels. Some of the assemblies contain Wet Annular Burnable Absorber (WABA) rods.
- A simplified version of the prismatic High Temperature Gas Cooled Reactor (HTGR) core developed by Idaho National Laboratory (INL) in the frame of Next Generation Nuclear Plant project [4]. One of the unique features of prismatic HTGR cores is the use of tristructural isotropic (TRISO) fuel particles randomly dispersed in graphite fuel elements which are, in turn, placed in graphite blocks with cooling channels.
- A Sodium Fast Reactor (SFR) core with enriched uranium carbide (UC) fuel developed as a part of the effort to design fast reactor with low enriched uranium based on a once-through fuel cycle [5, 6].

General core layouts and some basic operation parameters of the three considered systems are given in Table 1.

MODELING APPROACH. For each core the following analysis procedure was applied. Initially, few-group cross section sets for the core components were produced by the Serpent code. Then, these few-group cross section sets were used by the multi-group nodal diffusion code DYN3D [7] for full-core analysis. Finally, the nodal results were compared with the full-core reference solution obtained using Serpent MC calculations. In all examples, fixed thermal hydraulic conditions were considered. The few-group constants were generated in 2, 12, and 24 energy group structures for PWR, HTGR, and SFR cores respectively in order to correctly account for the particular neutron spectral effect of the each system.

RESULTS. The results of calculations are summarized in Table 2. For all core models, the results of the Serpent full core MC simulations agree very well with those of the DYN3D calculations performed with the Serpent cross-section sets. The relative difference in k-eff is about 170, 133, and 26 pcm for PWR, HTGR, and SFR cores respectively. For all cases the average difference in the radial power distribution is lower than 1% and the maximum difference does not exceed 2%.

Tab. 1: Selected core models.

	PWR	HTGR	SFR
Core layout	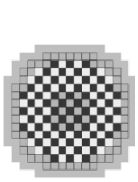	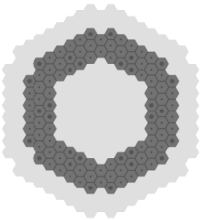	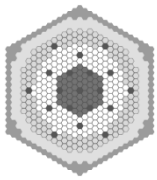
Power [MW]	3300	600	2400
Coolant	H_2O	He	Na
Moderator	H_2O	Graphite	–
Fuel	UO_2	UO_2	UC

Tab. 2: Results summary.

Core type	PWR	HTGR	SFR
k-eff, Serpent*	1.00187	1.39859	1.09802
k-eff, DYN3D	1.00016	1.40126	1.09772
Δρ DYN3D vs. Serpent [pcm]	−170	133	−26
Max. diff. in radial power [%]	1.0	1.0	1.7
Av. diff. in radial power [%]	0.7	0.4	0.5

*In Serpent calculations $\sigma_{k\text{-}eff}$ is about 0.00007.

CONCLUSIONS. In this study, we demonstrate by numerical examples the feasibility of the MC code Serpent for generating homogenized few-group constants for existing and advanced reactor designs. Extending the use of the continuous-energy MC method to lattice physics and group constant generation is a topic that is gaining more and more attention from the international reactor physics community since the method is not limited to any particular technology. This capability can be considered as particularly valuable for developing advanced reactor concepts for the future.

[1] http://montecarlo.vtt.fi.
[2] Fridman, E. et al. (2011) *Ann. Nucl. Energy* **38**, 921–929.
[3] Fridman, E. et al. (2012) *Proc. PHYSOR 2012*, Knoxville, U.S.A.
[4] MacDonald, P. E. et al. (2003) INEEL/EXT-03-00870.
[5] Fei, T. et al. (2011) *Trans. Am. Nucl. Soc.* **104**, 734–735.
[6] Fridman, E. et al. (2013) *Ann. Nucl. Energy* **53**, 354–363.
[7] Grundmann, U. et al. (2000) *Proc. PHYSOR 2000*, Pittsburgh, U.S.A.

TRANSURANUS fuel performance calculations for OECD RIA fuel codes benchmark

L. Holt

TRANSURANUS is a fuel performance code developed by the European Institute for Transuranium Elements. Simulations with TRANSURANUS were done in the frame of an OECD reactivity initiated accident (RIA) fuel codes benchmark. The simulations showed a good agreement with other fuel performance codes for parameters like injected energy, central fuel temperature and location of the maximum fuel temperature. Nevertheless, the mechanical loading model has still to be improved in the code for RIA. TRANSURANUS allows improving the level of detail of reactor transient simulations at HZDR.

OVERVIEW ABOUT THE SCENARIO. A reactivity initiated accident (RIA) can occur due to a control rod ejection in a pressurized water reactor (PWR) or a control rod drop in a boiling water reactor (BWR). This kind of transient has a pulse width of around 30 ms in German power reactors depending on the core loading, the worth of the ejected/ dropped control rod and the reactor state.
During this short time period a high amount of energy is injected in the fuel rod. The resulting sharp increase of the fuel temperature can cause transient fission gas release and mechanical loading on the cladding due to pellet cladding mechanical interaction or cladding ballooning and finally to a burst of the fuel rod as shown in Fig. 1 [1]. Fuel cladding failure must be avoided because the hot fuel can then interact directly with the coolant, leading to the release of radioactive fission products to the environment in the worst-case scenario.

Fig. 1: Post-test appearance of the rodlet VA-1, which was tested in a RIA simulation test in the NSRR reactor in Japan [1].

RIA belongs to the category of design basis accidents; thence, the reactor must be constructed to handle the consequences without environmental impact. Fuel performance codes are used in the safety analysis for checking the corresponding RIA safety criteria. Actual criteria are based on the fuel rod enthalpy threshold depending on the fuel burn-up. Accordingly, phenomena like corrosion, oxide spallation, hydrogen pickup and high burn-up structure formation in the fuel have to be taken into account. Future RIA experiments aim at analyzing these phenomena in detail.
At HZDR, the fuel performance code TRANSURANUS [2] has been used for fuel rod modeling since 2010. Usually, the fuel rod behavior is modeled in thermo hydraulic and neutronic computer codes in a simplified manner. Thence, more reliable safety analyses are possible by including knowledge and experience from TRANSURANUS simulations.

EXPERIMENTAL. In the frame of the OECD RIA benchmark, data from several RIA experiments [3] were provided and calculated with different fuel performance codes world-wide.
The provided cases were or will be conducted on similar PWR rods. Within the benchmark, re-calculations as well as blind calculations were performed. The fuel was irradiated up to a maximum local burn-up close to 75 MWd/kg in the power reactor Vandellos-2 in Spain. After post irradiation examinations (PIE) in hot labs, the fuel rods were refabricated to short test rodlets and were or will be tested under RIA conditions in the NSRR reactor in Japan or the CABRI facility in France.

Tab. 1: Specification of the calculated benchmark cases [3].

Case	Rod	Specific conditions
1	CIP0-1	Real test in sodium, CABRI sodium loop facility
2	CIP3-1	Simulated test in water (boiling inhibited), CABRI water loop facility
3	CIP3-1	Simulated test in water (clad outer temperature prescribed and use of flat axial power profile), CABRI water loop facility

RESULTS OF SIMULATION. Besides real experimental cases as #1, simulated test cases as #2 or #3 were determined to concentrate on the fuel performance modeling and to eliminate the influence of differences in thermo hydraulic modeling. The TRANSURANUS simulations done by HZDR showed a very good agreement in injected energy, variation of enthalpy, central fuel temperature, maximum fuel temperature and location of the maximum fuel temperature [3] although the validation of TRANSURANUS is still in progress for RIA. The code showed a stable numerical behavior which is really an important issue for very narrow, but high power pulses occurring in RIA. Nevertheless, TRANSURANUS underestimated the elongation of the fuel stack and the cladding. Thence, a new material correlation will be considered for fuel cladding behavior under high strain rates in case of highly irradiated cladding materials. Furthermore, transient thermo-hydraulic models aren't included in TRANSURANUS. The thermo-hydraulic conditions have to be given as boundary conditions to the fuel performance code. For that purpose, the TRANSURANUS code will be coupled in the near future with the HZDR's reactor dynamics code DYN3D, providing boundary conditions for fuel performance analysis in a consistent way.

ACKNOWLEDGEMENTS. The author would like to thank the organizers of the OECD RIA fuel codes benchmark, especially Marc Petit from IRSN in France for the technical support. The project is funded by E.ON Kernkraft within the knowledge preservation program in German nuclear safety research.

[1] Nuclear Energy Agency (2010) *Nuclear Fuel Behaviour Under Reactivity-initiated Accident (RIA) Conditions*, OECD/NEA.
[2] Lassmann, K. (1992) *J. Nucl. Mater.***188**, 295–302.
[3] Nuclear Energy Agency (2013) *RIA fuel codes benchmark*, OECD-NEA, Vol. 1–2, in progress.

Accident Management in case of Station Blackout

P. Tusheva, F. Schäfer, S. Kliem

Station blackout (total loss of AC power supply) is one of the dominant accidents taken into consideration at performing accident analysis. In case of the assumption of multiple failures of safety systems it leads to a severe accident. To prevent an accident to turn into a severe one or to mitigate the consequences, accident management measures have to be performed. The behaviour of the nuclear power plant and possibilities for application and optimization of accident management measures following a station blackout accident are investigated [1]. The analyses have been performed with the computer code ATHLET [2].

The reactor safety issues are of primary importance for preserving the health of the population and ensuring no release of radioactivity and fission products into the environment. A part of the nuclear research focuses on improvement of the safety of existing nuclear power plants. After shutting down the reactor the residual heat has to be removed from the reactor core. In case of station blackout, and under the additional assumption of the loss of the reserve power from the diesel generators, the active safety systems are not operable and cannot deliver water for cooling of the reactor core. Only the systems operating on passive principles are functional, but with limited amount of water. Without any preventive or mitigative measures depletion of the primary side, resulting in core uncovery, core heat up, cracking of the fuel claddings, release of fission products, core degradation and later on failure of the reactor pressure vessel under high pressure conditions is to be expected. This will cause challenges to the containment structures and possibly to the environment.

NUMERICAL ANALYSIS. The analyses are focused on investigations of the possibilities for management of accidents. To avoid or to delay the heating up of the core different accident management measures [3, 4] can be applied. The effectiveness and possible optimization of countermeasures are analyzed for a generic pressurized water reactor type VVER-1000. The influence of the initiation criteria and the effect of the availability of components on the course of the accident as well as the time margins for the operators are additionally addressed. A computer model of the main components of a nuclear power plant has been built (Fig. 1).

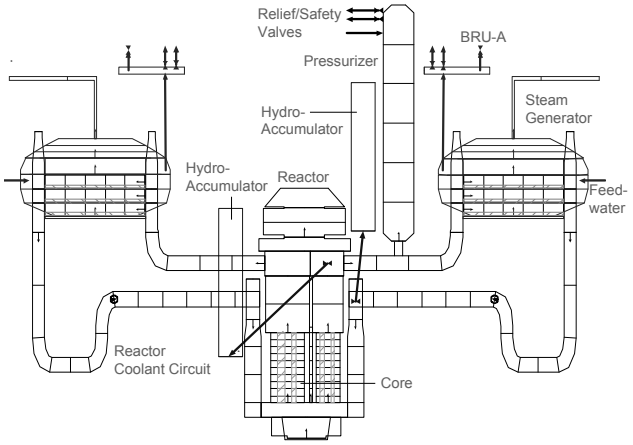

Fig. 1: Computer model, nodalization scheme.

The model includes the whole reactor cooling system with primary and secondary side as well as the essential safety systems. As basic accident management measures (AMM) the secondary side depressurization (SSD) and the primary side depressurization (PSD) are analyzed. In an accident, first SSD and, if not successful, also PSD or SSD and PSD in sequence can be applied. Depressurization on secondary side and primary side respectively is performed by manual opening of a certain number of relief or safety valves (on steam generators' secondary side for SSD and on the pressurizer for PSD; Fig. 1). SSD would allow reduction of the secondary pressure and, thus, passive feeding of the steam generators' secondary side from the feedwater system. In this way, the depletion of the steam generators and the pressure rise in the primary circuit can be delayed. SSD is a very efficient way to reduce the primary circuit pressure without an early release of primary coolant to the containment. With increasing primary pressure and temperatures, PSD can be applied to reduce the primary pressure by full opening of the pressurizer relief and safety valves and so to trigger the injection from the hydro-accumulators (passive system).

RESULTS. Figure 2 shows the main results of the simulations: Case 1-no AMM; Case 2-PSD at $T_{core\ exit}$ > 650 °C; Case 3-SSD after 30 min; Case 4-combination of SSD and PSD. The criterion for assessment of the measures effectiveness is the fuel elements cladding temperature. With SSD and PSD final core heat-up can be significantly delayed (~ 12 h compared to 2 h and 17 min for Case 1).

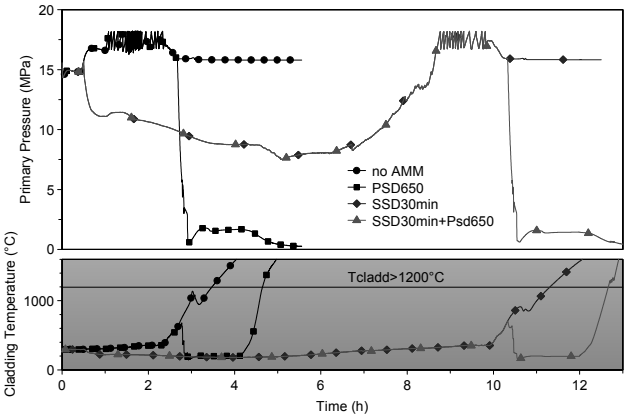

Fig. 2: Primary pressure and cladding temperatures evolution in time.

ACKNOWLEDGEMENTS. The authors would like to acknowledge the support of GRS (Germany), INRNE, Kozloduy NPP and EI (Bulgaria) in the discussions.

[1] Tusheva, P. et al. (2012) *Investigation on Optimzation of Accident Management Measures following a Station Blackout Accident in VVER-1000 Pressurized Water Reactor*, ICAPP'12, Paper 12159.
[2] Lerchl, G. et al. (2009) ATHLET *Mod 2.2 Cycle A User's Manual,* Gesellschaft für Anlagen- und Reaktorsicherheit (GRS) mbH.
[3] Cherubini, M. et al. (2008) *Nucl. Eng. Des.* **238**, 74–80.
[4] Pavlova, M.P. et al. (2007) *Prog. Nucl. Eng.* **49**, 409–427.

- ARTICLES (PEER-REVIEWED)
- EXTENDED ABSTRACTS, REPORTS, CONTRIBUTIONS
- LECTURES, ORAL PRESENTATIONS
- POSTERS
- DOCTORAL THESES
- MASTER, DIPLOMA, BACHELOR

ARTICLES (PEER-REVIEWED)

Abrasonis, G.; Wintz, S.; Liedke, M.O.; Aksoy Akgul, F.; Krause, M.; Kuepper, K.; Banerjee, D.; Liu, Z.; Gemming, S.
Environment controlled dewetting of Rh−Pd bilayers: A route for core−shell nanostructure synthesis
Journal of Physical Chemistry C 116, 14401–14407 (2012).

Barkleit, A.; Acker, M.; Bernhard, G.
Europium(III) complexation with salicylic acid at elevated temperatures
Inorganica Chimica Acta 394, 535–541 (2012).

Bartolome, J.; Bartolome, F.; Garcia, L.M.; Figueroa, A.I.; Repolles, A.; Martinez, M.J.; Luis, F.; Magen, C.; Selenska-Pobell, S.; Pobell, F.; Reitz, T.; Schönemann, T.; Herrmannsdörfer, T.; Merroun, M.; Geissler, A.; Wilhelm, F.; Rogalev, A.
Strong paramagnetism of gold nanoparticles deposited on a *Sulfolobus acidocaldarius* S-layer
Physical Review Letters 109, 247203-247201-247203-247205 (2012).

Baumann, N.; Arnold, T.; Lonschinski, M.
TRLFS study on the speciation of uranium in seepage water and pore water of heavy metal contaminated soil
Journal of Radioanalytical and Nuclear Chemistry 291, 673–679 (2012).

Behrends, T.; Krawczyk-Bärsch, E.; Arnold, T.
Implementation of microbial processes in the performance assessment of spent nuclear fuel repositories
Applied Geochemistry 27, 453–462 (2012).

Bilodid, Y.; Ovdiienko, I.; Mittag, S.; Kuchin, A.; Khalimonchuk, V.; Leremenko, M.
Assessment of spectral history influence on PWR and WWER core
Kerntechnik 77, 278–285 KT11025 (2012).

Borodkin, P.G.; Borodkin, G.I.; Khrennikov, N.N.; Konheiser, J.
Application of ex-vessel neutron dosimetry combined with in-core measurements for correction of neutron source used for RPV fluence calculations
Journal of ASTM International 9 (2012). DOI: 10.1520/JAI104022

Chaumont, A.; Klimchuk, O.; Gaillard, C.; Billard, I.; Ouadi, A.; Hennig, C.; Wipff, G.
Perrhenate complexation by uranyl in traditional solvents and in ionic liquids: a joined molecular dynamics/spectroscopic study
Journal of Physical Chemistry B 116, 3205–3219 (2012).

Deplanche, K.; Merroun, M.L.; Casadesus, M.; Tran, D.T.; Mikheenko, I.P.; Bennett, J.A.; Wood, J.; Jones, I.P.; Attard, G.A.; Selenska-Pobell, S.; Macaskie, L.E.
Microbial synthesis of core/shell gold/palladium nanoparticles for applications in green chemistry
Journal of the Royal Society Interface 9, 1705–1712 (2012).

Duerigen, S.; Fridman, E.
The simplified P3 approach on a trigonal geometry of the nodal reactor code DYN3D
Kerntechnik 77, 226–229 (2012).

Erkut, C.; Penkov, S.; Fahmy, K.; Kurzchalia, T.V.
How worms survive desiccation: Trehalose pro water
Worm 1, 61–65 (2012).

Foerstendorf, H.; Heim, K.; Rossberg, A.
The complexation of uranium(VI) and atmospherically derived CO_2 at the ferrihydrite-water interface probed by time-resolved vibrational spectroscopy
Journal of Colloid and Interface Science 377, 299–306 (2012).

Frost, L.; Moll, H.; Bernhard, G.
Aqueous uranyl benzoate species characterized by different spectroscopic techniques
Radiochimica Acta 100, 297–303 (2012).

Gaillard, C.; Klimchuk, O.; Ouadi, A.; Billard, I.; Hennig, C.
Evidence for the formation of $UO_2(NO_3)_4^{2-}$ in an ionic liquid by EXAFS
Dalton Transactions 41, 5476–5479 (2012).

Gezahegne, W.A.; Hennig, C.; Tsushima, S.; Planer-Friedrich, B.; Scheinost, A.C.; Merkel, B.J.
EXAFS and DFT investigations of uranyl-arsenate complexes in aqueous solution
Environmental Science & Technology 46, 2228–2233 (2012).

Gückel, K.; Rossberg, A.; Brendler, V.; Foerstendorf, H.
Binary and ternary surface complexes of U(VI) on the gibbsite/water interface studied by vibrational and EXAFS spectroscopy
Chemical Geology 326–327, 27–35 (2012).

Heine, K.B.; Fairweather, K.A.; Heine, A.; Clegg, J.K.; Jolliffe, K.A.
Unusual non-head-to-tail chains in the crystal structure of glycyl-L-glutamyl-L-phosphoseryl-L-leucine
Acta Crystallographica Section C 42, 839–845 (2012).

Heller, A.; Barkleit, A.; Foerstendorf, H.; Tsushima, S.; Bernhard, G.
Curium(III) citrate speciation in biological systems: An europium(III) assisted spectroscopic and quantum chemical study
Dalton Transactions 41, 13969–13983 (2012).

Hennig, C.; Takao, S.; Takao, K.; Weiss, S.; Kraus, W.; Emmerling, K.; Scheinost, A.C.
Structure and stability range of a hexanuclear Th(IV) – glycine complex
Dalton Transactions 41, 12818–12823 (2012).

Hildebrand, H.; Franke, K.
A new radiolabeling method for commercial Ag^0 nanopowder with ^{110m}Ag for sensitive nanoparticle detection in complex media
Journal of Nanoparticle Research 14, 1142 (2012).

Huber, F.; Schild, D; Vitova, T.; Rothe, J.; Kirsch, R.; Schaefer, T.
U(VI) removal kinetics in presence of synthetic magnetite nanoparticles
Geochimica et Cosmochimica Acta 96, 154–173 (2012).

Ikeda-Ohno, A.; Tsushima, S.; Hennig, C.; Yaita, T.; Bernhard, G.
Dinuclear complexes of tetravalent cerium in an aqueous perchloric acid solution
Dalton Transactions 41, 7190–7192 (2012).

Konheiser, J.; Mittag, S.; Viehrig, H.W.
Application of different nuclides in retrospective dosimetry
DOI: *10.1520/JAI103925*
Journal of ASTM International 9 (2012).

Kozmenkov, Y.; Rohde, U.; Baranaev, Y.; Glebov, A.
Simulation of RUTA-70 reactor with CERMET fuel using DYN3D/ATHLET and DYN3D/RELAP5 coupled codes
Kerntechnik 77, 249–257 (2012).

Kozmenkov, Y.; Rohde, U.; Manera, A.
Validation of the RELAP5 code for the modeling of flashing-induced instabilities under natural-circulation conditions using experimental data from the CIRCUS test facility
Nuclear Engineering and Design 243, 168–175 (2012).

Krawczyk-Bärsch, E.; Lünsdorf, H.; Arnold, T.; Bok, F.; Steudtner, R.; Pedersen, K.; Lehtinen, A.; Brendler, V.
Immobilization of uranium in biofilm microorganisms exposed to groundwater seeps over granitic rock tunnel walls in Olkiluoto, Finland
Geochimica et Cosmochimica Acta 96, 94–104 (2012).

Kremleva, A.; Zhang, Y.; Shor, A.M.; Krüger, S.; Joseph, C.; Raditzky, B.; Schmeide, K.; Sachs, S.; Bernhard, G.; Rösch, N.
Uranyl(VI) complexation by sulfonate ligands: a relativistic Density Functional and TRLFS study
European Journal of Inorganic Chemistry 2012, 3636–3644 (2012).

Lippold, H.; Eidner, S.; Kumke, M.U.; Lippmann-Pipke, J.
Diffusion, degradation or on-site stabilisation – identifying causes of kinetic processes involved in metal-humate complexation
Applied Geochemistry 27, 250–256 (2012).

Lucks, C.; Rossberg, A.; Tsushima, S.; Foerstendorf, H.; Scheinost, A.C.; Bernhard, G.
Aqueous uranium(VI) complexes with acetic and succinic acid: speciation and structure revisited
Inorganic Chemistry 51, 12288–12300 (2012).

Lütke, L.; Moll, H.; Bernhard, G.
Insights on the uranium(VI) speciation with *Pseudomonas fluorescens* on a molecular level
Dalton Transactions 41, 13370–13378 (2012).

Martinavicius, A.; Abrasonis, G.; Scheinost, A. C.; Danoix, R.; Danoix, F.; Stinville, J. C.; Talut, G.; Templier, C.; Liedke, O.; Gemming, S.; Moeller, W.
Nitrogen interstitial diffusion induced decomposition in AISI 304L austenitic stainless steel
Acta Materialia 60, 4065–4076 (2012).

Marques Fernandes, M.; Baeyens, B.; Dähn, R.; Scheinost, A.C.; Macé, N.; Bradbury, M.H.
U(VI) sorption on montmorillonite: a macroscopic and microscopic study
Geochimica et Cosmochimica Acta 93, 262–277 (2012).

Merk, B.; Glivici-Cotruță, V.
Solutions without space-time separation for ADS experiments: overview on developments and applications
Science and Technology of Nuclear Installations, 140946 (2012).

Merk, B.; Glivici-Cotruță, V.; Weiß, F.P.
On the use of different analytical solutions for recalculation of the YALINA-Booster experiment SC3A
Progress in Nuclear Energy 58, 11–20 (2012).

Merk, B.; Rohde, U.
An analytical solution for the consideration of the effect of adjacent fuel assemblies; extension to hexagonal VVER-440 type fuel assemblies
Kerntechnik 77, 230–239 (2012).

Merk, B.; Weiß, F.P.; Fridman, E.; Kliem, S.
Use of zirconium-based moderators to enhance feedback coefficients in a MOX-fueled sodium-cooled fast reactor
Nuclear Science and Engineering 171, 136–149 (2012).

Moll, H.; Bernhard, G.
A TRLFS study of curium(III) naphthalene and hydroxyquinoline complexes in aqueous solution
Polyhedron 31, 759–766 (2012).

Müller, K.; Foerstendorf, H.; Meusel, T.; Brendler, V.; Comarmond, M.J.; Lefèvre, G.; Payne, T.E.
Sorption of U(VI) at the TiO_2 – water interface: an in situ vibrational spectroscopic study
Geochimica et Cosmochimica Acta 76, 191–205 (2012).

Prieur, D.; Martin, P.M.; Lebreton, F.; Delahaye, T.; Jankowiak, A.; Laval, J.P.; Scheinost, A.C.; Dehaudt, P.; Blanchart, P.
Alpha self-irradiation effect on the local structure of the $U_{0.85}Am_{0.15}O_{2+x}$ solid solution
Journal of Solid State Chemistry 194, 206–211 (2012).

Rohde, U.; Baier, S.; Duerigen, S.; Fridman, E.; Kliem, S.; Merk, B.
Development and verification of the coupled 3D neutron kinetics/thermal-hydraulics code DYN3D-HTR for the simulation of transients in block-type HTGR
Nuclear Engineering and Design 251, 412–422 (2012).

Rohde, U.; Pivovarov, V.A.; Matveev, Y.A.
Studies on Boiling Water Reactor design with reduced moderation and analysis of reactivity accidents using the code DYN3D-MG
Kerntechnik 77, 240–248 (2012).

Saeki, M.; Sasaki, Y.; Nakai, A.; Ohashi, A.; Banerjee, D.; Scheinost, A.C.; Foerstendorf, H.
Structural study on 2,2′-(Methylimino)-bis(N,N-Dioctylacetamide) complex with $Re(VII)O_4^-$ and $Tc(VII)O_4^-$ by ^1H NMR, EXAFS, and IR Spectroscopy
Inorganic Chemistry 51, 5814–5821 (2012).

Schmeide, K.; Sachs, S.; Bernhard, G.
Np(V) reduction by humic acid: Contribution of reduced sulfur functionalities to the redox behavior of humic acid
Science of the Total Environment 419, 116–123 (2012).

Schmidt, H.; Asztalos, A.; Bok, F.; Voigt, W.
New iron(III) nitrate hydrates: $Fe(NO_3)_3 \cdot xH_2O$ with x = 4, 5 and 6
Acta Crystallographica Section C 68, i29–i33 (2012).

Schott, J.; Acker, M.; Barkleit, A.; Brendler, V.; Taut, S.; Bernhard, G.
The influence of temperature and small organic ligands on the sorption of Eu(III) on Opalinus Clay
Radiochimica Acta 100, 315–324 (2012).

Stockmann, M.; Hirsch, D.; Lippmann-Pipke, J.; Kupsch, H.
Geochemical study of different-aged mining dump materials in the Freiberg mining district, Germany
Environmental Earth Sciences 68, 1153–1168 (2012).

Sundman, O.; Persson, P.; Banerjee, D.; Ohman, L.O.
Interactions between $GaO_4Al_{12}(OH)_{24}(H_2O)_{12}^{7+}$ and cellulosic materials
Journal of Colloid and Interface Science 374, 250–257 (2012).

Takao, K.; Takao, S.; Scheinost, A.; Bernhard, G.; Hennig, C.
Formation of soluble hexanuclear neptunium(IV) nano-clusters in aqueous solution: growth termination of actinide(iv) hydrous oxides by carboxylates
Inorganic Chemistry 51, 1336–1344 (2012).

Takao, K.; Tone, Y.; Hennig, C.; Inoue, S.; Tsubomura, T.
Simplest homoleptic metal-centered tetrahedrons, $[M(OH_2)_4]^{2+}$, in 1-ethyl-3-methylimidazolium tetrafluoroborate ionic liquid (M = Co, Ni, Cu)
Inorganic Chemistry 51, 4850–4854 (2012).

Tomczak, A.; Sontheimer, J.; Drechsel, D.; Hausdorf, R.; Gentzel, M.; Shevchenko, A.; Eichler, S.; Fahmy, K.; Buchholz, F.; Pisabarro, M.T.
3D profile-based approach to proteome-wide discovery of novel human Chemokines
PlosOne 7, e36151 (2012).

Tondera, C.; Laube, M.; Wimmer, C.; Kniess, T.; Mosch, B.; Großmann, K.; Pietzsch, J.
Visualization of cyclooxygenase-2 using a 2,3-diarylsubstituted indole-based inhibitor and confocal laser induced cryofluorescence microscopy at 20 K in melanoma cells in vitro
Biochemical and Biophysical Research Communications 430, 301–306 (2012).

Tsushima, S.
"yl"-oxygen exchange in uranyl(VI) ion: a mechanism involving $(UO_2)_2(\mu\text{-}OH)_2^{2+}$ via U-Oyl-U bridge formation
Inorganic Chemistry 51, 1434–1439 (2012).

Tusheva, P.; Schäfer, F.; Reinke, N.; Altstadt, E.; Kliem, S.
Study on severe accidents and countermeasures for VVER-1000 reactors using the integral code ASTEC
Kerntechnik 77, 271–277 (2012).

Zänker, H.; Schierz, A.
Engineered nanoparticles and their identification among natural nanoparticles
Annual Review of Analytical Chemistry 5, 107–132 (2012).

Zirnstein, I.; Arnold, T.; Krawczyk-Bärsch, E.; Jenk, U.; Bernhard, G.; Röske, I.
Eukaryotic life in biofilms formed in a uranium mine
MicrobiologyOpen 1, 83–94 (2012).

▶ EXTENDED ABSTRACTS, REPORTS, CONTRIBUTIONS

Baumann, N.; Arnold, T.; Lonschinski, M.
Speciation of uranium in seepage and pore waters of heavy metal-contaminated soil
Bio-Geo Interactions in Metal-Contaminated Soils (Kothe, E.; Varma, A., eds.), Springer, Berlin, 131–142 (2012).

Foerstendorf, H.; Müller, K.; Steudtner, R.
International Workshop on Advanced Techniques in Actinide Spectroscopy (ATAS 2012) – Abstract Book
Wissenschaftlich-Technische Berichte / Helmholtz-Zentrum Dresden-Rossendorf; HZDR-027 2012 - ISSN: 2191-8708 (2012).

Krawczyk-Bärsch, E.; Lünsdorf, H.; Pedersen, K.; Arnold, T.; Bok, F.; Steudtner, R.; Lehtinen, A.; Brendler, V.
Redox behavior of uranium in biofilms and groundwater seeps, sampled from the granitic rock walls in the ONKALO tunnel (Finland)
4th Annual Workshop, Proceedings of the Collaborative Project "Redox Phenomena Controlling Systems" (7EC FP CP ReCosy), Jan. 23-26, 2012, Karlsruhe, Germany, KIT Scientific Reports 7626: KIT Scientific Publishing, Karlsruhe, Germany, 241-251 (2012).

Rohde U.; Apanasevich, P.; Baier, S.; Duerigen, S.; Fridman, E.; Grahn, A.; Kliem, S.; Merk, B.
Entwicklung einer Version des Reaktordynamikcodes DYN3D für Hochtemperaturreaktoren
Wissenschaftlich-Technische Berichte / Helmholtz-Zentrum Dresden-Rossendorf; HZDR-023 2012 - ISSN: 1437-322X (2012).

Schmeide, K.; Gürtler, S.; Müller, K.; Steudtner, R.; Joseph, C.; Bok, F.; Brendler, V.
Sorption of U(VI) and Np(V) onto diorite from Äspö HRL
1st Workshop Proceedings of the Collaborative Project "Crystalline Rock Retention Processes" (7th EC FP CP CROCK), KIT Scientific Reports 7629, KIT Scientific Publishing, Karlsruhe, 169–180 (2012).

Schmeide, K.; Joseph, C.; Sachs, S.; Steudtner, R.: Raditzky, B.; Günther, A.: Bernhard, G.
Characterization and quantification of the influence of clay organics on the interaction and diffusion of uranium and americium in the clay
Interaction and transport of actinides in natural clay rock with consideration of humic substances and clay organics, KIT Scientific Reports 7633, KIT Scientific Publishing (Marquardt, C. M., ed.), Karlsruhe, Annex B, Report No. 1 (2012).

Schmeide, K.; Joseph, C.; Sachs, S.; Steudtner, R.; Raditzky, B.; Günther, A.; Bernhard, G.
Joint Project: Interaction and transport of actinides in natural clay rock with consideration of humic substances and clay organics. Characterization and quantification of the influence of clay organics on the interaction and diffusion of uranium and americium in the clay
Wissenschaftlich-Technische Berichte / Helmholtz-Zentrum Dresden-Rossendorf; HZDR-017 2012 - ISSN: 2191-8708 (2012).

▶ LECTURES, ORAL PRESENTATIONS

Arnold, T.
Combining Confocal Laser Scanning Microscopy (Clsm) and Laser-Induced Fluorescence Spectroscopy (LIFS) to study the interactions of biofilms with uranium
MARC IX – 9th International Conference on the Methods and Applications of Radioanalytical Chemistry, March 25-30, 2012, Kailua-Kona, Hawaii, U.S.A..

Baier, S.; Fridman, E.; Kliem, S.; Rohde, U.
Extension and application of the reactor dynamics code DYN3D for Block-type High Temperature Reactors
HTR2012 – 6th International Topical Meeting on High Temperature Reactor Technology, Oct. 28–Nov. 01, 2012, Tokyo, Japan.

Baier, S.; Rohde, U.; Kliem, S.; Fridman, E.
Development and implementation of a 3D heat conduction model for (very) High Temperature Reactors into the reactor dynamics code DYN3D
ICONE20 – 20th International Conference on Nuclear Engineering, July 30– Aug. 03, 2012, Anaheim, U.S.A..

Baldova, D.; Fridman, E.
High Conversion Th-U233 fuel assembly for current generation of PWRs
PHYSOR 2012 – Advances in Reactor Physics – Linking Research, Industry, and Education, April 15–20, 2012, Knoxville, Tennessee, U.S.A..

Breynaert, E.; Dom, D.; Scheinost, A.C.; Kirschhock, C.E.A.; Maes, A.
Interaction of selenite with iron sulphide minerals: a new perspective
Goldschmidt 2012, Earth in Evolution, June 24–29, 2012, Montreal, Canada.

Breynaert, E.; Dom, D.; Scheinost, A.C.; Kirschhock, C.E.A.; Maes, A.
Interaction of selenite with iron sulphide minerals: a new perspective
5th International Meeting on "Clays in Natural and Engineered Barriers for Radioactive Waste Confinement", Oct. 22–25, 2012, Montpellier, France.

Cowan, T.
Applications of laser-matter interaction at ultra-high intensity
Workshop on Laser-Plasma Interaction at Ultra-High Intensity ENLITE – 2nd Dresden Exchange oN Laser-plasma Interaction ThEory, April 16–20, 2012, Dresden, Germany.

Cowan, T.
Beschleunigung der Beschleunigung: Lasergetriebene Strahlungsquellen und ihre Anwendungen
ZIH Colloquium, April 26, 2012, Dresden, Germany.

Cowan, T.
Dresden projects in Ultra-High- Intensity physics with PW lasers
Science with PW-class lasers, Jan. 23–24, 2012, Paris, France.

Cowan, T.
Helmholtz beamline at European XFEL status & next steps
Peak Brightness Collaboration @ XFEL Users Meeting, Jan. 26, 2012, Hamburg, Germany.

Cowan, T.
The Helmholtz beamlines at the European XFEL and FAIR
Joint IZEST – Helmholtz Beamlines Workshop 2012, April 23–25, 2012, Darmstadt, Germany.

Cowan, T.
Ion acceleration in ultra-intense laser-matter interactions, and applications in radiation oncology
Kolloquium, May 09, 2012, Chemnitz, Germany.

Cowan, T.
Science with high-power lasers at the European XFEL
503. WE-Heraeus-Seminar Free-Electron Lasers: from Fundamentals to Applications, April 10–13, 2012, Bad Honnef, Germany.

Duerigen, S.; Bilodid, Y.; Fridman, E.
The trigonal nodal SP3 method of the code DYN3D — verification on pin level
Jahrestagung Kerntechnik, May 22–24, 2012, Stuttgart, Germany.

Duerigen, S.; Bilodid, Y.; Fridman, E.; Mittag, S.
A trigonal nodal SP3 method with mesh refinement capabilities - development and verification
PHYSOR 2012 – Advances in Reactor Physics – Linking Research, Industry, and Education, April 15–20, 2012, Knoxville, Tennessee, U.S.A..

Duerigen, S.; Nikitin, E.; Mittag, S.
Verification of the trigonal-geometry diffusion and SP3 models of the code DYN3D
22nd Symposium of Atomic Energy Research (AER) on VVER Reactor Physics and Reactor Safety, Oct. 01–05, 2012, Pruhonice, Czech Republic.

Dulnee, S.; Banerjee, D.; Rossberg, A.; Scheinost, A.C.
Tin sorption to magnetite nanoparticles under anoxic conditions
Goldschmidt 2012, Earth in Evolution, June 24–29, 2012, Montreal, Canada.
Mineralogical Magazine 76, 1668 (2012).

Ferrari, A.
Neutronics analysis around the spallation target for the MYRRHA ADS design
13th International Conference on Nuclear Reaction Mechanisms, June 11–15, 2012, Varenna, Italy.

Ferrari, A.; Biarrotte, J.L.; Perrot, L.; Saugnac, H.; Vandeplassche, D.
Shielding and activation studies for the design of the MYRRHA proton beamline
SATIF-11 – 11th Workshop on Shielding Aspects of Accelerators, Targets and Irradiation Facilities, Sept. 11–14, 2012, Tsukuba, Japan.

Ferrari, A.; Di Maria, S.; Sarotto, M.; Stankovskiy, A.
Shielding and activation calculations for the MYRRHA ADS design in the subcritical operation mode
ICRS12 – 12th International Conference on Radiation Shielding, Sept. 02–07, 2012, Nara, Japan.

Foerstendorf, H.
Keine Ahnung von der Strahlung – Unbemerkte alltägliche Radioaktivität
Kreuz-Uni am Evangelischen Kreuzgymnasium Dresden, Nov. 19, 2012, Dresden, Germany.

Foerstendorf, H.; Müller, K.; Heim, K.; Meusel, T.; Brendler, V.
Surface complexation of U(VI) at the mineral-water interface probed by time-resolved vibrational spectroscopy – Identification of binary and ternary surface species
Uranium biogeochemistry: transformations and applications, March 11–16, 2012, Ascona, Switzerland.

Franke, K.
Untersuchung des Lebenszyklus von TiO_2- und Ag^0-Nanopartikeln - NanoTRACK
2. Clustertreffen der Fördermaßnahmen NanoCare und NanoNature, March 13–14, 2012, Frankfurt/Main, Germany.

Franke, K.; Hildebrand, H.; Schymura, S.
Radiolabelling of engineered nanoparticles for environmental particle tracing - HZDR – cyclotron facility – radionuclide production
JRC-QNano-seminar, June 15, 2012, Ispra, Italia.

Franzen, C.; Hering, D.; Jordan, N.
The impact of salinity on the sorption of selenate onto aged gamma-Al_2O_3 in the context of salt dome repositories
EMC2012 – European Mineralogical Conference, Spet. 02–06, 2012, Frankfurt/Main, Germany.

Franzen, C.; Jordan, N.; Mueller, K.
Influence of temperature on the sorption of selenate onto anatase
Experimental Mineralogy Petrology and Geochemistry, March 04–07, 2012, Kiel, Germany.

Fridman, E.; Leppänen, J.
Revised methods for Few-group cross sections generation in the Serpent Monte Carlo code
PHYSOR 2012 – Advances in Reactor Physics – Linking Research, Industry, and Education, April 15–20, 2012, Knoxville, Tennessee, U.S.A..

Fridman, E.; Leppänen, J.
Serpent Monte Carlo code: new methods for few-group cross section generation
Jahrestagung Kerntechnik, May 22–24, 2012, Stuttgart, Germany.

Fridman, E.; Shwageraus, E.
Demonstration of the Serpent Monte-Carlo code applicability to Few-group constants generation for existing and advanced reactor concepts
26th Conference of the Nuclear Societies in Israel, Feb. 21–23, 2012, Dead Sea, Israel.

Fritsch, K.
Für den Laboreinsatz optimierte Kalibrationsmethode für pH-Elektroden bei hohen Ionenstärken
2. Workshop des Verbundprojekts „Rückhaltung endlagerrelevanter Radionuklide im natürlichen Tongestein und in salinaren Systemen“, April 04, 2012, Cologne, Germany.

Glivici-Cotruță, V.; Merk, B.
Analytical solutions for ADS experiments. development and application
International Conference Dedicated to the 50th Anniversary of BFS Critical Facility, Feb. 28–March 01, 2012, Obninsk, Russia.

Gückel, K.; Comarmond, M.J.; Payne, T.E.; Chong, E.; Mokher-Shahin, L.
Radionuclide sorption studies of Co, Cs and Sr onto soils from an Australian legacy radioactive waste site
12th South Pacific Environmental Radioactivity Association Conference, Oct. 16–19, 2012, Sydney, Australia.

Gückel, K.; Foerstendorf, H.; Brendler, V.
Comparative investigation of the neptunium(V) sorption onto gibbsite by means of ATR FT-IR spectroscopy
4th EuCheMS Chemistry Congress, Aug. 26–30, 2012, Prague, Czech Republic.

Gückel, K.; Foerstendorf, H.; Rossberg, A.
The impact of atmospheric carbonate on the sorption of actinyl (V/VI) ions onto gibbsite studied by in situ ATR FT-IR and EXAFS spectroscopy
Helmholtz-Koordinierungstreffen 2012, Jan 23–24, 2012, Karlsruhe, Germany.

Heller, A.; Barkleit, A.; Sachs, S.; Bernhard, G.
Cm(III) and Eu(III) speciation in human body fluids and cell culture media studied by luminescence spectroscopy
4th Speciation Seminar, May 29–31, 2012, Montpellier, France.

Hennig, C.
Formation and structure of hexanuclear actinide(IV) carboxylates
University of Grenoble I, Institute of Earth Science, Jan. 17, 2012, Grenoble, France.

Hennig, C.
Structure and formation of hexanuclear actinide(IV) complexes
Johannes Gutenberg Universität Mainz, Institut für Kernchemie, Jan. 23, 2012, Mainz, Germany.

Hennig, C.; Meyer, M.
A short description of the Rossendorf Beamline at ESRF – and one scientific example of French-German collaboration: the formation of polynuclear actinide(IV) carboxylates
German-French research for nuclear safety: Chemistry of the f-elements, Feb. 22–23, 2012, Strasbourg, France.

Hennig, C.; Takao, S.; Takao, K.; Weiss, S.; Kraus, W.; Emmerling, F.; Meyer, M.; Scheinost, A.C.
Hexanuclear actinide(IV) carboxylates formed by competition between ligation and hydrolysis
XAFS15 – 15th International Conference on X-ray Absorption Fine Structure, July 22–28, 2012, Beijing, China.

Hildebrand, H.; Franke, K.; Freyer, A.; Bilz, E.; Mehnert, R.; Mai, E.; Isaacson, C.; Schirmer, K.; Ammann, A.; Sigg, L.
Investigation of the life cycle of nanoparticles by means of [^{44,45}Ti]TiO_2 and [^{110m}Ag]Ag^0 – Research project NanoTrack
NanoSAFE'12, Nov. 13–15, 2012, Grenoble, France.

Hildebrand, H.; Schymura, S.; Franke, K.
Radiolabelling of commercial Ag^0 and TiO_2 nanoparticles with ^{110m}Ag and $^{44/45}$Ti for life-cycle studies and results from the QNANO research stay at JRC
JRC-QNano-seminar, June 15, 2012, Ispra, Italia.

Höhne, T.; Grahn, A.; Kliem, S.
CFD studies of the insulation material transport inside the reactor pressure vessel under LOCA conditions
CFD4NRS-4, The Experimental Validation and Application of CFD and CMFD Codes in Nuclear Reactor Technology, Sept. 10–12, 2012, Daejeon, Korea.

Hurel, C.; Clement, L.; Jordan, N.; Weiß, S.; Marmier, N.
Nanoscale TiO_2 particles: relationship between surface properties and toxicity measurements
Interfaces Against Pollution, June 11–14, 2012, Nancy, France.

Jordan, N.; Ritter, A.; Foerstendorf, H.; Scheinost, A.C.; Heim, K.; Weiß, S.; Brendler, V.
Sorption of Se(VI) and Se(IV) oxyanions onto maghemite: a macroscopic and spectroscopic study
Selen2012 – Selenium in geological, hydrological and biological systems, Oct. 08–09, 2012, Karlsruhe, Germany.

Jordan, N.; Ritter, A.; Heim, K.; Foerstendorf, H.
Different types of outer-sphere complexes of selenate ions on mineral surfaces
Helmholtz-Koordinierungstreffen 2012, Jan 23–24, 2012, Karlsruhe, Germany.

Joseph, C.; Fritsch, K.; Steudtner, R.; Schmeide, K.
U(VI)-Sorption und -Diffusion an/in Tonmineralen und Opalinuston – Einfluss von pH, Ionenstärke und Organika
3. Workshop des Verbundprojekts „Rückhaltung endlagerrelevanter Radionuklide im natürlichen Tongestein und in salinaren Systemen“, Oct. 29–30, 2012, Munich, Germany.

Joseph, C.; van Loon, L.R.; Jakob, A.; Steudtner, R.; Schmeide, K.; Sachs, S.; Bernhard, G.
Do elevated temperatures and organic matter influence the U(VI) diffusion through argillaceous rock?
5th International Meeting on "Clays in Natural and Engineered Barriers for Radioactive Waste Confinement", Oct. 22–25, 2012, Montpellier, France.

Kirsch, R.; Fellhauer, D.; Altmaier, M.; Charlet, L.; Fanghänel, T.; Scheinost, A.
Plutonium redox chemistry under anoxic conditions in the presence of iron(II) bearing minerals
Goldschmidt 2012, Earth in Evolution, June 24–29, 2012, Montreal, Canada.
Mineralogical Magazine 76, 1942 (2012)

Kliem, S.
Research on reactor physics for the enhancement of the safety of nuclear reactors
International Seminar Series of the Universitas Gadjah Mada, Jan 30–Feb. 03, 2012, Yogyakarta, Indonesia.

Kliem, S.; Schäfer, F.; Tusheva, P.
The Fukushima reactor accident - Reasons, background and consequences
International Seminar Series of the Universitas Gadjah Mada, Jan 30–Feb. 03, 2012, Yogyakarta, Indonesia.

Konheiser, J.; Ferrari, A.
Uncertainties in activity calculations of different nuclides in rector steels by neutron radiation
ICRS-12 – 12th International Conference on Radiation Shielding, RPSD-2012 – 17th Topical Meeting of the Radiation Protection and Shielding Division of the American Nuclear Society, Sept. 02–07, 2012, Nara, Japan.

Krawczyk-Bärsch, E.; Lünsdorf, H.; Pedersen, K.; Arnold, T.; Bok, F.; Steudtner, R.; Lehtinen, A.; Brendler, V.
Combined approach of microsensor and EF-TEM/EELS studies to study the speciation of uranium in biofilms and in the surrounding bulk solution
MARC IX – 9th International Conference on the Methods and Applications of Radioanalytical Chemistry, March 25-30, 2012, Kailua-Kona, Hawaii, U.S.A..

Krawczyk-Bärsch, E.
The influence of microorganisms on the speciation and mobilization of uranium in acid mine drainage and crystalline rock environments
Institute of Geology of Ore Deposits (IGEM), Laboratory of Radiogeology, Russian Academy of Science, SUE SIA "RADON", Nov. 22–23, 2012, Moscow, Russia.

Krawczyk-Bärsch, E.
Vorstellung und Diskussion der Untersuchungen des HZDR zur Rolle von Mikroorganismen bei der Endlagerung radioaktiver Abfälle
Meeting with representants of PromTekhnologii (VNIPI PT), Moscow, July 12–13, 2012, Peine, Germany.

Kretzschmar, J.; Barkleit, A.; Paasch, S.; Brunner, E.
Lanthanide induced linkage of phosphorylated organic acids
Festkörper-NMR-Methoden und Anwendungen in der Materialforschung, July 29–Aug. 02, 2012, Oberjoch, Germany.

Kulenkampff, J.; Gründig, M.; Schikora, J.; Zakhnini, A.; Lippmann-Pipke, J.
Long-term spatiotemporal monitoring of diffusion processes in Opalinus drill cores with GeoPET and parameterization with Comsol Multiphysics
5th International Meeting on "Clays in Natural and Engineered Barriers for Radioactive Waste Confinement", Oct. 22–25, 2012, Montpellier, France.

Kulenkampff, J.; Schikora, J.; Zakhnini, A.; Gründig, M.; Lippmann-Pipke, J.
Ansätze zur Bestimmung heterogener Diffusionsparameter auf Bohrkernskala mit Hilfe von Na-22-PET-Diffusionsmessungen und Modellsimulationen
2. Workshop des Verbundprojekts „Rückhaltung endlagerrelevanter Radionuklide im natürlichen Tongestein und in salinaren Systemen", April 04, 2012, Cologne, Germany.

Lippmann-Pipke, J.; Erzinger, J.; Zimmer, M.; Kujawa, C.; Boettcher, M.S.; van Heerden, E.; Bester, A.; Cason, E.; Reches, Z.
Long-term, on-site borehole monitoring of gases released from an "active" fault system at 3.6 km depth, TauTona Gold Mine, South Africa
GeoFuture Workshop, Nov. 28–29, 2012, Potsdam, Germany.

Lippold, H.; Lippmann-Pipke, J.
Radiotracer studies on the kinetics and equilibrium characteristics of adsorption of humic matter
Goldschmidt 2012, Earth in Evolution, June 24–29, 2012, Montreal, Canada.
Mineralogical Magazine 76, 2015 (2012).

Lütke, L.; Moll, H.; Bachvarova, V.; Geißler, A.; Selenska-Pobell, S.; Bernhard, G.
Interaction of U(VI) with bacterial isolates from Äspö and Mont Terri
Helmholtz-Koordinierungstreffen 2012, Jan 23–24, 2012, Karlsruhe, Germany.

Lütke, L.; Moll, H.; Bachvarova, V.; Selenska-Pobell, S.; Bernhard, G.
Insights into the U(VI) speciation with bacterial isolates from Äspö and Mont Terri
IRS Institutskolloqium, Nov. 15, 2012, Hannover, Germany.

Lütke, L.; Moll, H.; Bachvarova, V.; Selenska-Pobell, S.; Bernhard, G.
Insights on the U(VI) speciation with bacterial isolates from Äspö and Mont Terri
ISMEC – International Symposium on Metal Complexes 2012, June 18–22, 2012, Lisbon, Portugal.

Mansel, A.; Franke, K.
Production and purification of ^{56}Co at the Leipzig cyclotron
EuCheMS International Conference on Nuclear and Radiochchemistry (NRC-8), Sept. 16–21, 2012, Como, Italy.

Martin, P.M.; Belin, R.B.; Prieur, D.; Delahaye, T.; Gavilan, E.; Lebreton, F.; Robisson, A.C.; Dumas, J.C.; Scheinost, A.C.
Local structure and charge distribution of Am bearing nuclear oxide fuels: $(U,Am)O_{2\pm x}$ and $(U,Pu,Am)O_{2-x}$
Plutonium Futures - The Science 2012, July 15–20, 2012, Cambridge, United Kingdom.

Merk, B.
Core/system modeling and simulation: state-of-the-art, R&D needs and new ideas
Technical Meeting to Identify Innovative Fast Neutron Systems Development Gaps, Feb. 29–March 02, 2012, Vienna, Austria.

Merk, B.
German SFR research and european sodium fast reactor project
International Workshop on Prevention and Mitigation of Severe Accidents in Sodium-cooled Fast Reactors, June 12–13, 2012, Tsuruga, Japan.

Merk, B.
On the possible gain of the application of the sp3 solution in nodal codes
PHYSOR 2012 – Advances in Reactor Physics – Linking Research, Industry, and Education, April 15–20, 2012, Knoxville, Tennessee, U.S.A..

Merk, B.
Subcriticality determination in accelerator driven systems (ADS)
Technical Meeting to Identify Innovative Fast Neutron Systems Development Gaps, Feb. 29–March 02, 2012, Vienna, Austria.

Merk, B.; Kliem, S.
On the safety evaluation methodology applied in Germany after the Fukushima event
Technical Meeting on Impact of the Fukushima Event on Current and Future Fast Reactor (FR) Designs, March 19–23, 2012, Dresden, Germany.

Merk, B.; Rohde, U.
An analytical solution for the consideration of the effect of adjacent fuel assemblies; comparison of rectangular and hexagonal structures
PHYSOR 2012 – Advances in Reactor Physics – Linking Research, Industry, and Education, April 15–20, 2012, Knoxville, Tennessee, U.S.A..

Merk, B.; Weiß, F.P.
On the effect of different placing ZrH moderator material on the performance of a SFR core
PHYSOR 2012 – Advances in Reactor Physics – Linking Research, Industry, and Education, April 15–20, 2012, Knoxville, Tennessee, U.S.A..

Merk, B.; Weiß, F.P.
On the use of fine distributed moderating material to enhance feedback coefficients in fast reactors
Innovative Fast Reactor Designs with Enhanced Negative Reactivity Feedback Features, Feb. 27–29, 2012, Vienna, Austria.

Merk, B.; Weiß, F.P.
On the use of moderating material to enhance the feedback coefficients in SFR cores with high minor actinide content
ICAPP'12 – International Congress on Advances in Nuclear Power Plants, June 24–28, 2012, Chicago, U.S.A..

Moll, H.; Bachvarova, V.; Lütke, L.; Geissler, A.; Selenska-Pobell, S.; Bernhard, G.
Curium(III) and europium(III) speciation studies with Mont Terri Opalinus clay isolates
Mont Terri Project: Joint HT-MA-BN-GD-PCC Meeting, Feb. 06–07, 2012, St. Ursanne, Switzerland.

Moll, H.; Lütke, L.; Bachvarova, V.; Geissler, A.; Krawczyk-Bärsch, E.; Selenska-Pobell, S.; Bernhard, G.
Mikrobielle Diversität im Tongestein (Opalinus-Ton) und Wechselwirkung dominanter Mikroorganismen mit Actiniden – Vorhaben BMWi 0210618
10. Projektstatusgespräch zu BMWi- und BMBF-geförderten FuE-Projekten der Endlagerforschung und der Nuklearen Sicherheitsforschung, Nov. 13–14, 2012, Karlsruhe, Germany.

Moll, H.; Lütke, L.; Sachs, S.; Schmeide, K.; Bernhard, G.
The impact of the Äspö ground water bacterium *Pseudomonas fluorescens* on the speciation of plutonium
Plutonium Futures - The Science 2012, July 15–20, 2012, Cambridge, United Kingdom.

Müller, K.
Endlagerung radioaktiver Abfälle: Wie tief muss man graben für eine Million Jahre Sicherheit?
Tag des offenen Labors, May 12, 2012, Dresden, Germany.

Müller, K.
Endlagerung radioaktiver Abfälle: Wie tief muss man graben für eine Million Jahre Sicherheit?
Lange Nacht der Wissenschaften in Dresden, July 06, 2012, Dresden, Germany.

Rachamin, R.; Elias, E.; Galperin, A.
Loss of coolant accident analysis for IRR 1
26th Conference of the Nuclear Societies in Israel, Feb. 21–23, 2012, Dead Sea, Israel.

Rachamin, R.; Galperin, A.; Fridman, E.
Conceptual design of a pressure tube light water reactor with variable moderator control
PHYSOR 2012 - Advances in Reactor Physics, April 15–20, 2012, Knoxville, Tennessee, USA.

Rachamin, R.; Elias, E.; Galperin, A.
loss of coolant accident analysis for IRR 1
26th Conference of the Nuclear Societies in Israel, Feb. 21–23, 2012, Dead Sea, Israel.

Rachamin, R.; Galperin, A.; Fridman, E.
Innovative pressure tube light water reactor with variable moderator control
26th Conference of the Nuclear Societies in Israel, Feb. 21–23, 2012, Dead Sea, Israel.

Raff, J.
Abgeschaut aus der Natur: Biobasierte Nanoverbundmaterialien für die Wasserbehandlung
nANO meets water IV, Nov. 08, 2012, Oberhausen, Germany.

Raff, J.
Entwicklung und Bewertung neuer photokatalytisch aktiver Verbundmaterialien zur Eliminierung von Arzneimittelreststoffen im Projekt NanoPharm
2. Clustertreffen der BMBF-Fördermaßnahmen NanoCare und NanoNature, March 13–14, 2012, Frankfurt/Main, Germany.

Raff, J.
Neue biotechnologische Verfahren zur (Rück)Gewinnung seltener Industriemetalle
Gesellschaft zur Förderung von Medizin-, Bio- und Umwelttechnologien e.V. (GMBU), Arbeitsgruppe "Funktionelle Schichten", March 07, 2012, Dresden, Germany.

Raff, J.
Was das Leben auf den Hinterlassenschaften des Uranerzbergbaus mit Zwergen zu tun hat
Vom Molekül zum Muster (Selbstorganisationsphänomene in der Biologie), Vortragsreihe vom COM-LABBIO, May 08, 2012, Dresden, Germany.

Raff, J.; Lehmann, F.; Moll, H.; Kutschke, S.; Pollmann, K.
Advanced biotechnology for extraction and recovery of metals
GeoHannover 2012, Oct. 01–03, 2012, Hannover, Germany.

Richter, A.; Bok, F.; Brendler, V.
THEREDA – A thermodynamic database for increasing confidence in waste disposal
Goldschmidt 2012, Earth in Evolution, June 24–29, 2012, Montreal, Canada.
Mineralogical Magazine 76, 2283 (2012).

Rohde, U.; Kozmenkov, Y.
Application of the method of uncertainty and sensitivity evaluation to results of PWR LBLOCA analysis calculated with the code ATHLET
22nd Symposium of Atomic Energy Research (AER) on VVER Reactor Physics And Reactor Safety, Oct. 01–05, 2012, Pruhonice, Czech Republic.

Rohde, U.; Kozmenkov, Y.
Validation of the RELAP5 code for the modeling of flashing-induced instabilities under natural circulation conditions using experimental data from the CIRCUS test facility
Scientific Workshop on Reactor Dynamics and Safety 2012, Sept. 13–14, 2012, Dresden, Germany.

Sabau, A.; Lomenech, C.; Marmier, N.; Jordan, N.; Barkleit, A.; Brendler, V.; Toulhoat, N.; Pipon, Y.; Moncoffre, N.; Giffaut, E.
Rétention de l'europium par la calcite : de l'adsorption à l'incorporation dans le matériau
XIIIe Journées Nationales de Radiochimie et Chimie Nucléaire, Oct. 04–05, 2012, Nantes, France.

Sauerzapf, S.; Zakhnini, A.; Weber, W.; Pietrzyk, U.; Mix, M.
Analyse und Optimierung einer Positronenreichweitenkorrektur innerhalb der iterativen Rekonstruktion für die Kleintierbildgebung
43. Jahrestagung der Deutschen Gesellschaft für Medizinische Physik, Sept. 26–29, 2012, Jena, Germany.

Scheinost, A.C.
Nuclear waste management: Current research at ROBL/ESRF
Expert Panel: Industry's needs for advanced characterisation, by neutron and synchrotron X-ray techniques, of materials for civil nuclear power, April 03–04, 2012, Grenoble, France.

Scheinost, A.C.; Rossberg, A.
Uranium at solid/water interfaces: Lessons to be learned from X-ray absorption spectroscopy
Uranium biogeochemistry: transformations and applications, March 11–16, 2012, Ascona, Switzerland.

Scheinost, A.C.; Rossberg, A.
Uranium at solid/water interfaces: Lessons to be learned from X-ray absorption spectroscopy
Seminaire de l'Institut de minéralogie et de physique des milieux condensés, Nov. 29, 2012, Paris, France.

Schmeide, K.; Gürtler, S.; Müller, K.; Steudtner, R.; Joseph, C.; Bok, F.; Brendler, V.
Sorption of U(VI) and Np(V) onto diorite from Äspö HRL
1st Workshop of the Project "Crystalline rock retention processes" (CROCK), May 22–24, 2012, Stockholm, Sweden.

Schott, J.; Acker, M.; Barkleit, A.; Brendler, V.; Bernhard, G.
The Sorption of Eu(III) on Opalinus Clay at elevated Temperatures and in Presence of Organics
Workshop "Kompetenzerhaltung in der Kerntechnik", May 23–24, 2012, Stuttgart, Germany.

Schott, J.; Acker, M.; Barkleit, A.; Taut, S.; Brendler, V.
Characterization of a solid Eu-borate species by TRLFS
BMWi-Verbundprojekttreffen „Rückhaltung endlagerrelevanter Radionuklide im natürlichen Tongestein und in salinaren Systemen,,, Oct. 29–30, 2012, Garching, Germany.

Schott, J.; Barkleit, A.; Acker, M.; Brendler, V.; Bernhard, G.
Complexation of Eu(III) with borates
BMWi-Verbundprojekttreffen „Rückhaltung endlagerrelevanter Radionuklide im natürlichen Tongestein und in salinaren Systemen“, April 03–04, 2012, Köln, Germany.

Schymura, S.; Cydzik, I.; Bulgheroni, A.; Simonelli, F.; Holzwarth, U.; Kozempel, J.; Franke, K.; Gibson, J.
Strategies for the radiolabelling of carbon nanoparticles
NanoSAFE'12, Nov. 13–15, 2012, Grenoble, France.

Schymura, S.; Hildebrand, H.; Cydzik, I.; Simonelli, F.; Bulgheroni, A.; Holzwarth, U.; Kozempel, J.; Freyer, A.; Bilz, E.; Gibson, N.; Franke, K.
Radiolabelling of engineered nanoparticles – different strategies for Ag^0-NP, TiO_2-NP and MWCNT
Cycleur Meeting 2012, Nov. 28–30, 2012, Ispra, Italy.

Schymura, S.; Hildebrand, H.; Franke, K.
CNT-Modification and radiolabelling at the HZDR
Seminar at the JRC-cyclotron facility within the Qnano project: "Be-7 Recoil labelling of multi-wall carbon nanotubes", June 04–15, 2012, Ispra, Italy.

Selenska-Pobell, S.; Reitz, T.; Merroun, M.
Interactions of U(VI) with archaea: what is different than with bacteria?
Goldschmidt 2012, Earth in Evolution, June 24–29, 2012, Montreal, Canada.
Mineralogical Magazine 76, 2352 (2012)

Steudtner, R.; Müller, K.; Jäckel, E.; Meyer, R.; Schmeide, K.; Günther, A.
Uranium chemistry in citric acid solution
4th EuCheMS Chemistry Congress, Aug. 26–30, 2012, Prague, Czech Republic.

Stockmann, M.; Brendler, V.; Schikora, J.; Britz, S.; Flügge, J.; Noseck, U.
Smart K_d-concept based on Surface Complexation Modeling
Goldschmidt 2012, Earth in Evolution, June 24–29, 2012, Montreal, Canada.
Mineralogical Magazine 76, 2412 (2012).

Tusheva, P.; Schaefer, F.; Kliem, S.
Investigations on optimization of accident management measures following a station blackout accident in a VVER-1000 pressurized water reactor
ICAPP'12 – International Congress on Advances in Nuclear Power Plants, June 24–28, 2012, Chicago, U.S.A..

Vogel, M.
Vorstellung und Bewertung des Beitrags zur Erreichung des Meilensteins im Projekt Nanopharm
Meilenstein-Treffen zum Projekt Nanopharm, April 19, 2012, Köthen, Germany.

Zakhnini, A.; Kulenkampff, J.; Lippmann-Pipke, J.; Pietrzyk, U.
GATE-Based simulation in GeoSciences
OpenGATE Collaboration Meeting, May 03–04, 2012, Athens, Greece.

Zänker, H.; Weiss, S.; Hennig, C.; Dreissig, I.
Actinide(IV)-silica colloids and their potential geochemical implications
E-MRS 2012 SPRING MEETING, May 15–17, 2012, Strasbourg, France.

Zänker, H.; Weiss, S.; Hennig, C.; Dreissig, I.
Silica-stabilized actinide(IV) colloids at near-neutral pH
Goldschmidt 2012, Earth in Evolution, June 24–29, 2012, Montreal, Canada.
Mineralogical Magazine 76, 2581 (2012).

▶ POSTERS

Arab-Chapelet, B.; Tamain, C.; Martin, P.M.; Rivenet, M.; Scheinost, A.C.; Grandjean, S.; Abraham, F.
XRD and XAS structural characterization of mixed-valence plutonium(III,IV) oxalate hydrates used to obtain controlled particle shape of plutonium oxide
Plutonium Futures - The Science 2012, July 15–20, 2012, Cambridge, United Kingdom.

Barkleit, A.; Acker, M.; Geipel, G.; Bernhard, G.
Time-resolved laser-induced fluorescence spectroscopy (TRLFS) of aqueous Am(III) complexes at ambient and elevated temperature
ATAS 2012 – International Workshop on Advanced Techniques in Actinide Spectroscopy, Nov. 05–07, 2012, Dresden, Germany.

Bitto, F.; Kretzschmar, J.; Brendler, E.; Kroke, E.
NMR Investigations of the intra- and intermolecular exchange phenomena of the 3,5-dimethylpyrazolylsilane ClSi(pz*) and related compounds
4th EuCheMS Chemistry Congress, Aug. 26–30, 2012, Prague, Czech Republic.

Bok, F.; Brendler, V.; Richter, A.
THEREDA - One Database for thermodynamic and sorption data
Experimental Mineralogy Petrology and Geochemistry, March 04–07, 2012, Kiel, Germany.

Fritsch, K.; Schmeide, K.
Investigation of the mobility of uranium (VI) in argillaceous rock at higher salinity
7. Graduate Students Seminar, Oct. 08–10, 2012, Schöneck, Germany.

Gückel, K.
Structural analysis of surface species of U(VI) on gibbsite – A combined approach using ATR FT-IR, EXAFS spectroscopy and DFT-calculations
ACTINET ThuL Spring School in Actinide Chemistry, March 26–30, 2012, Karlsruhe, Germany.

Gückel, K.; Tsushima, S.; Foerstendorf, H.; Rossberg, A.
Structural analysis of the aqueous $(UO_2)_2CO_3(OH)_3^-$-complex – A combined approach using ATR FT-IR spectroscopy and DFT calculations
ATAS 2012 – International Workshop on Advanced Techniques in Actinide Spectroscopy, Nov. 05–07, 2012, Dresden, Germany.

Günther, A.; Vogel, M.; Roßberg, A.; Raff, J.; Bernhard, G.
Combination of spectroscopic methods for the identification of U(VI) spezies formed by selected bacteria, algae and fungi
ATAS 2012 – International Workshop on Advanced Techniques in Actinide Spectroscopy, Nov. 05–07, 2012, Dresden, Germany.

Hildebrand, H.; Franke, K.
Investigation of the life cycle of nanoparticles by means of radiolabelling – NanoTRACK
2. Clustertreffen der BMBF-Fördermaßnahmen NanoCare und NanoNature, March 13–14, 2012, Frankfurt/Main, Germany.

Hildebrand, H.; Franke, K.; Gibson, N.; Cydzik, I.; Simonelli, F.; Bulgheroni, A.; Holzwarth, U.; Bilz, E.; Freyer, A.
Radiolabelling of engineered silver and titania nanoparticles as a tool for sensitive detection of nanoparticle release from surface coatings
NanoSAFE'12, Nov. 13–15, 2012, Grenoble, France.

Husar, R.; Weiß, S.; Dreißig, I.; Hennig, C.; Brendler, E.; Zänker, H.
Investigation of actinide(IV)-silica colloids at near-neutral pH
7. Graduate Students Seminar, Oct. 08–10, 2012, Schöneck, Germany.

Husar, R.; Weiß, S.; Zaenker, H.; Bernhard, G.
Investigations into the formation of neptunium(IV)-silica colloids
ATAS 2012 – International Workshop on Advanced Techniques in Actinide Spectroscopy, Nov. 05–07, 2012, Dresden, Germany.

Kretzschmar, J.; Barkleit, A.; Paasch, S.; Brunner, E.
Lanthanide induced linkage of bifunctional organic acids
GDCh FGMR 34th Annual Discussion Meeting - Advanced Magnetic Resonance for the Study of Dynamics in Biomolecules and Materials, Sept. 17–20, 2012, Halle/Saale, Germany.

Lederer, F.; Kutschke, S.; Pollmann, K.
Recombinant production of genetically modified S-layer proteins in different expression systems
Annual Conference of the Association for General and Applied Microbiology (VAAM), March 18–21, 2012, Tübingen, Germany.

Lindner, K.; Günther, A.; Bernhard, G.
Complexation behaviour of U(VI) and Eu(III) with Schiff Bases investigated by laserinduced spectroscopy
ATAS 2012 – International Workshop on Advanced Techniques in Actinide Spectroscopy, Nov. 05–07, 2012, Dresden, Germany.

Lindner, K.; Günther, A.; Bernhard, G.
Laser-induced spectroscopy - A method for the determination of complexation behaviour of metals by organic ligands
7. Graduate Students Seminar, Oct. 08–10, 2012, Schöneck, Germany.

Lindner, K.; Günther, A.; Bernhard, G.
Spectroscopic Studies of Complexation Behaviour of Uranium(VI) by Schiff Bases
EuCheMS International Conference on Nuclear and Radiochchemistry (NRC-8), Sept. 16–21, 2012, Como, Italy.

Moll, H.; Lütke, L.; Raff, J.; Brendler, V.; Bernhard, G.
Curium(III) as intrinsic luminescence probe for direct speciation studies in biogeochemical systems
ATAS 2012 – International Workshop on Advanced Techniques in Actinide Spectroscopy, Nov. 05–07, 2012, Dresden, Germany.

Poetsch, M.; Mansel, A.; Schnorr, R.; Haupt, S.; Kersting, B.
Selective Extraction of 85Sr2+ with modified Calix[4]arenes in a liquid-liquid system
ATAS 2012 – International Workshop on Advanced Techniques in Actinide Spectroscopy, Nov. 05–07, 2012, Dresden, Germany.

Poetsch, M.; Mansel, A.; Schnorr, R.; Haupt, S.; Kersting, B.
Selective liquid-liquid extraction of Sr-85 with modified calixarenes
NRC-8 – International Conference on Nuclear and Radiochemistry, Sept. 16–21, 2012, Como, Italia.

Sabău, A.; Marmier, N.; Jordan, N.; Lomenech, C.; Barkleit, A.; Toulhoat, N.; Pipon, Y.; Moncoffre, N.; Brendler, V.; Giffaut, E.
Interaction between europium and calcite: macroscopic and spectroscopic studies
5th International Meeting on "Clays in Natural and Engineered Barriers for Radioactive Waste Confinement", Oct. 22–25, 2012, Montpellier, France.

Sauerzapf, S.; Zakhnini, A.; Weber, W.; Pietrzyk, U.; Mix, M.
Korrekturen für nichtreine und hochenergetische Positronenstrahler in der Kleintierbildgebung unter Verwendung von Monte-Carlo Simulationen
Die 50. Jahrestagung der Deutschen Gesellschaft für Nuklearmedizin, April 25–28, 2012, Bremen, Germany.

Schikora, J.; Kulenkampff, J.; Gründig, M.; Lippmann-Pipke, J.
Modelling and simulation of 4D GeoPET measurements with COMSOL Multiphysics 4.2a
EGU General Assembly 2012, April 22–27, 2012, Vienna, Austria.

Schmeide, K.; Gürtler, S.; Müller, K.; Steudtner, R.; Joseph, C.; Bok, F.; Brendler, V.
Sorption of U(VI) and Np(V) onto diorite from Äspö HRL
1st Workshop of the Project "Crystalline rock retention processes" (CROCK), May 22–24, 2012, Stockholm, Sweden.

Schott, J.; Barkleit, A.; Acker, M.; Brendler, V.
Investigation of the Eu(III)-$B(OH)_3$-organic system
7. Graduate Students Seminar, Oct. 08–10, 2012, Schöneck, Germany.

Schymura, S.; Franke, K.; Lippmann-Pipke, J.
Rapid carbon nanotube modification and radiolabelling for particle tracing applications
2. Clustertreffen der BMBF-Fördermaßnahmen NanoCare und NanoNature, March 13–14, 2012, Frankfurt/Main, Germany.

Schymura, S.; Weiß, S.; Zänker, H.; Franke, K.
Colloidal stability of modified carbon nanotubes
NanoSAFE'12, Nov. 13–15, 2012, Grenoble, France.

Suhr, M.; Fischer, S.; Günther, T.; Raff, J.; Pollmann, K.
Investigation of metal binding by cell wall components of Gram-positive bacteria studied by QCM-D
5th International Symposium on Biosorption and Bioremediation, June 24–28, 2012, Prague, Czech Republic.

Suhr, M.; Günther, T.; Raff, J.; Pollmann, K.
Adsorption kinetics of cell wall components of gram positive bacteria on technical surfaces studied by QCM-D
Annual Conference of the Association for General and Applied Microbiology (VAAM), March 18–21, 2012, Tübingen, Germany.

Thomas, L.; Sauerzapf, S.; Mix, M.; Zakhnini, A.; Gaens, M.; Axer, M.; Pietrzyk, U.
A simulation study to determine the influence of low-energy bremsstrahlungs photons on the acquisition of very rare coincidence events from Yttrium-90 decay
Die 50. Jahrestagung der Deutschen Gesellschaft für Nuklearmedizin, April 25–28, 2012, Bremen, Germany.

Veeramani, H.; Qafoku, N.; Pruden, A.; Monsegue, N.; Kukkadapu, R.; Murayama, M.; Newville, M.; Lanzirotti, A.; Scheinost, A.C.; Hochella, M.F.
Abiotic U(VI) reduction by biogenic mackinawite
Goldschmidt 2012, Earth in Evolution, June 24–29, 2012, Montreal, Canada.

Vogel, M.; Lehmann, F.; Bobeth, C.; Kutschke, S.; Pollmann, K.; Raff, J.
Neue photokatalytisch aktive Verbundmaterialien zur Eliminierung von pharmazeutischen Reststoffen - Teilprojekt: Herstellung und Charakterisierung von photokatalytischen S-Layer basierten Nanokompositen
2. Clustertreffen der BMBF-Fördermaßnahmen NanoCare und NanoNature, March 13–14, 2012, Frankfurt/Main, Germany.

Weinert, U.; Pollmann, K.; Strehlitz, B.; Raff, J.
Inspired by nature: novel biosensors based on an assembly of self-assembling S-layer proteins, aptamers and fluorescence dyes
bio-inspired Materials, March 20–23, 2012, Potsdam, Germany.

Weinert, U.; Strehlitz, B.; Pollmann, K.; Raff, J.
Developing sensory layers as combination of S-layer proteins, aptamers and fluorescence dyes
Nanofair 2012, June 12–13, 2012, Dresden, Germany.

Zirnstein, I.; Arnold, T.; Krawczyk-Bärsch, E.; Wobus, A.; Röske, I.
Biofilms in a uranium contaminated acid mine drainage environment
1st Transnational Workshop "GETGEOWEB": Genomics and Transcriptomics in Geobiotechnolgy and White Biotechnology, October 29–30, 2012, Freiberg, Germany.

Zirnstein, I.; Arnold, T.; Krawczyk-Baersch, E.; Wobus, A.; Röske, I.
Retrieval and biodiversity of biofilms of an underground uranium mine
Biofilms 5 International Conference, Dec. 10–12, 2012, Paris, France.

▶ DOCTORAL THESES

Eichler, S.
Structure, Function and Dynamics of G-Protein coupled Receptors
Technische Universität Dresden, Dresden, Germany (2012).

Kirsch, R.
Abiotische Reduktion von Pu und Sb: Reaktionsmechanismen und Kinetik
Université Joseph Fourier, Grenoble, France (2012).

Tusheva, P.
Modelling and analysis of severe accidents for VVER-1000 reactors
Technische Universität Dresden, Dresden, Germany (2012).
Available as: Wissenschaftlich-Technische Berichte, HZDR-025, Helmholtz-Zentrum Dresden-Rossendorf; Dresden (2012).

▶ MASTER, DIPLOMA, BACHELOR

Drechsel, N.
Isolierung und Charakterisierung von Zellwandbestandteilen grampositiver Mikroorganismen
University of Applied Sciences, Mittweida, Germany (2012).

Gürtler, S.
Sorption von U(VI) und Np(V) an Äspö-Granit unter anaeroben Bedingungen
Hochschule Fresenius, University of Applied Sciences, Zwickau, Germany (2012).

Kruse, C.
Untersuchungen der Sorptionsprozesse von Uran(VI) an Mineraloxiden bei höheren Temperaturen
University of Applied Sciences, Zittau/Görlitz, Germany (2012).

Meusel, T.
Schwingungsspektroskopische Untersuchung der Speziation von U(VI) in Lösungen und an der Oberfläche von Titandioxid bei hohen Temperaturen
Technische Universität Dresden, Dresden, Germany (2012).

Meyer, R.
Spektroskopische Untersuchungen von Uran(VI)-Oberflächenprozessen in Gegenwart von Citronen-und Oxalsäure an den Modelloxiden SiO_2und α-Fe_2O_3
University of Applied Sciences, Dresden, Germany (2012).

Poetsch, M.
Wechselwirkungsstudien von Radionukliden mit makrozyklischen, multifunktionalen Chelatliganden
University Leipzig, Leipzig, Germany (2012).

Ritter, A.
Sorption von Selen an Maghemit
Hochschule Fresenius, University of Applied Sciences, Zwickau, Germany (2012).

Sauerbier, M.
Funktionalisierung von S-layer Proteinen mit Aptameren
Technische Universität Dresden, Dresden, Germany (2012)

Schikora, J.
Simulation von Diffusions-Adsorptionsprozessen in natürlichem Gesteinsmaterial mit COMSOL Multiphysics
Technische Universität Dresden, Dresden, Germany (2012).

- SEMINARS (TALKS OF VISITORS)
- WORKSHOPS
- TEACHING ACTIVITIES

SEMINARS

T. Sasaki
Institute for Chemical Research, Kyoto University, Kyoto, Japan
Topics in solution chemistry of environmentally important actinide species
January 27, 2012

D. Reed
Los Alamos National Laboratory, U.S.A.
Actinide solubility and oxidation-state distribution in the waste isolation pilot plant
January 27, 2012

S. Keller
Molecular Biophysics, University of Kaiserslautern, Germany
Reconstitution and folding of membrane proteins: case studies on KcsA and Mistic
February 07, 2012

M. Solioz
University Bern, Switzerland
How organisms handle copper - from genetic models to genetic diseases
May 09, 2012

K. G. van den Boogart
Helmholtz Institute Freiberg for Resource Technology, Freiberg, Germany
Statistischer Umgang mit geologischen Zusammensetzungsdaten
May 25, 2012

J. Gutzmer
Helmholtz Institute Freiberg for Resource Technology, Freiberg, Germany
Geometallurgy
May 29, 2012

B. Daus
Department Groundwater Remediation, Helmholtz Centre for Environmental Research, Leipzig, Germany
Elemental speciation in environmental science
June 04, 2012

R. Marsac
Institute for Waste Disposal, Karlsruhe Institute of Technology, Karlsruhe, Germany
Control of rare earth elements speciation by humic acis: role of the binding sites heterogeneity
June 14, 2012

M. Urbanová
Institute of Chemical Technology, Prague, Czech Republic
Chiroptical studies of biologically interesting structures and interactions
June 18, 2012

D. Waite
Civil and Environmental Engineering, The University of New South Wales, Sydney, Australia
New insights into contaminant redox transformations mediated by iron and silver assemblages
June 21, 2012

J. Matschullat
Institute of Mineralogy, Technische Universität Bergakademie Freiberg, Freiberg, Germany
Mit Arsen leben – Ergebnisse einer interdisziplinären Komplexstudie zu Stoffdispersion, Humanbiomonitoring und Risikoreduktion in SE-Brasilien
July 16, 2012

Y. Petrushenko
CYCLOTRON Science & Research Establishment, National Science Center - Kharkov Institute of Physics & Technology, Kyiv, Ukraine
Radiation effects in multicomponent solids and radionuclide productions: two aspects of research
August 24, 2012

F. Winde
Faculty Natural Sciences: School of Environmental Sciences and Development, North-West University (NWU), Potchefstroom, South Africa
Uran im Trinkwasser? Ein Überblick über Ausmaß und Risiken bergbaubedingter und natürlicher Kontamination in Südafrika
August 30, 2012

A. Gorbushina
Federal Institute for Materials Research and Testing and Institute of Geological Sciences, Freie Universität Berlin, Berlin, Germany
Rock-inhabiting fungi and phototrophs on bare rock surfaces
September 11, 2012

E. Breynaert
Centrum voor Oppervlaktechemie en Katalyse, KU Leuven, The Netherlands
Interaction of selenite with iron sulphide minerals: a new perspective
October 05, 2012

H. Shao
Department Environmental Informatics, Helmholtz Centre for Environmental Research, Leipzig, Germany
Recent developments of reactive transport in OpenGeoSystems
October 12, 2012

N. Musat
Helmholtz Centre for Environmental Research, Leipzig, Germany
NanoSIMS technology at the cutting edge – imaging single-cells at nano-scale
November 30, 2012

M. Zavarin
Lawrence Livermore National Laboratory, Glenn T. Seaborg Institute, Livermore, CA, U.S.A.
Environmental transport of actinides: probing biochemical processes at femtomolar to millimolar concentrations and nanometer to kilometer scales
December 13, 2012

▶ WORKSHOPS (ORGANIZED BY THE IRE)

Colloquium in honor of 65th birthday of Prof. Dr. G. Bernhard

HZDR, Dresden, Germany, January 05, 2012.

Boeßert, W.
VKTA – Nuclear Engineering and Analytics Inc., Dresden, Germany

Gloe, K.
Technische Universität Dresden, Dresden, Germany

Nitsche, H.
Dept of Chemistry, University of California, Berkeley, U.S.A.

Trautmann, N.
Institute for Nuclear Chemistry, Johannes Gutenberg Universität, Mainz, Germany

Helmholtz Meeting "Research on Waste Repositories", Institute for Waste Disposal (INE), KIT, Karlsruhe, Institute of Resource Ecology (IRE), HZDR, Dresden, and Institute of Energy and Climate Research (IEK), FZJ, Jülich, Germany

KIT, Karlsruhe, Germany, January 23–24, 2012.

Adam, C.
Charakterisierung von partitioningrelevanten Lanthaniden- und Actiniden-nPrBTP-Komplexen mittels NMR-Spektroskopie

Alekseev, E. V.
Actinides Solid State Chemistry at IEK-6

Finkeldei, S.
Die Konditionierung von Minoren Actiniden in ZrO_2 basierten Keramiken

Foerstendorf, H.
Different types of outer-sphere complexes of selenate ions on mineral surfaces

Gückel, K.
The impact of atmospheric carbonate on the sorption of actinyl (V/VI) ions onto gibbsite studied by in situ ATR FT-IR and EXAFS spectroscopy

Heberling, F.
The calcite-water interface: insights from surface diffraction, zetapotential measurements, and coprecipitation experiments

Lütke, L.
Interaction of U(VI) with microbial isolates from Äspö and Mont Terri

Niemeyer, I.
Internationale Kernmaterialüberwachung (Safeguards) – F&E im IEK-6

Pölz, S.
Numerische Effizienzkalibrierung von Teilkörperzählern mit Hilfe von anthropomorphen Phantomen

Polly, R.
Quantum chemical study of the sorption of trivalent actinides on mineral surfaces

Raff, J.
Radio-ecological research as a basis for the development of new biotechnological methods for the recovery of rare metals

Rozov, K.
Synthesis, characterization and stabilities of Cl-bearing layered double hydroxides (LDHs)

International Workshop on Advanced Techniques for Actinide Spectroscopy (ATAS 2012)

HZDR, Dresden, Germany, November 05–07, 2012.

(Only lectures are noted. Complete abstract book available at: www.hzdr.de/atas)

Baker, R.J. (Trinity College Dublin, Ireland)
Uranium(IV) luminescence: new tricks for an old dog

Creff, G. (IPNO, France)
Study of uranyl and thorium complexation with phosphorylated biomolecules

Dumas, T. (HZDR, Germany)
XAS study of actinide and lanthanide hexacyanoferrates

Foerstendorf, H. (HZDR, Germany)
In situ identification of the U(VI) surface speciation on iron oxide phases by ATR FT-IR spectroscopy

Guillaumont, D. (CEA, France)
Experimental and theoretical structures of actinide ions with oxygen-donor ligands in organic solution

Heller, A. (HZDR, Germany)
Spectroscopic and quantum chemical study of the curium(III) and europium(III) citrate speciation in biological systems

Heuser, J. (FZJ, Germany)
Short-range order investigations of $LnPO_4$ using Raman spectroscopy

Hofmann, S. (KIT, Germany)
Surface interaction studies of Ln(III)/ An(III) with site-selective time resolved laser fluorescence spectroscopy

Huittinen, N. (University of Helsinki, Finland)
The specific sorption of Y(III) onto γ-alumina: a solid-state ^{1}H MAS NMR study

Kremleva, A. (Technical University Munich, Germany)
Density functional computational studies of uranyl(VI) complexation on solvated surfaces of clay minerals

Kretzschmar, J. (HZDR, Germany)
Eu^{3+} in NMR spectroscopy - a helpful tool in tracking binding sites

Li, J. (Tsinghua University, China)
Recent advances of computational spectroscopy in actinide chemistry

Lübke, M. (Mainz University, Germany)
Spectroscopic study of the reaction of neptunium(V) with synthetic nanocrystalline mackinawite (FeS)

März, J. (Technische Universität Dresden, Germany)
Fluorescent complexes of tripodal amides: TRLFS and multinuclear NMR spectroscopic studies

Martínez-Torrents, A. (Universitat Politècnica de Catalunya, Spain)
Uranium speciation studies at alkaline pH and in presence of peroxide using TRLFS

Mason, H. (LLNL, U.S.A.)
Actinide NMR research at Lawrence Livermore National Laboratory

Merroun, M. (University of Granada, Spain)
Application of spectroscopic and microscopic techniques in bacterial/actinide interaction studies

Persson, P. (Umeå University, Sweden)
In-situ infrared spectroscopic studies of reactions at water-mineral interfaces

Polly, R. (KIT, Germany)
Quantum mechanical and spectroscopic investigation of the corundum water interface and sorption of lanthanides and actinides on this surface

Reiller, P. (CEA, France)
Commonalities and dissimilarities of Eu(III) interactions by simple organic acids and humic substances: complexation and sorption on Al_2O_3.

Rothe, J. (KIT, Germany)
Soft X-ray spectromicroscopy of natural organics affecting actinide mobility - an overview

Saito, T. (The University of Tokyo, Japan)
Application of multi-mode factor analysis as a robust data reduction tool for time-resolved laser fluorescence spectroscopy

Schmidt, M. (KIT, Germany)
X-ray reflectivity investigations on the interfacial reactivity of actinides

Szabó, Z. (KTH, Stockholm, Sweden)
^{17}O NMR study of the oxygen exchange between uranyl(VI) oxygen and water oxygen in strongly alkaline solutions

Vitova, T. (KIT, Germany)
Actinide speciation with high-energy resolution X-ray absorption spectroscopy and inelastic
X-ray scattering

Yang, P. (PNNL, U.S.A.)
Computational studies on coordination, energetics, and spectra of actinyl ions in the natural environment

Status-Seminar 2012:
„Nuclear Safety Research – From Reactors to Disposal“

HZDR, Dresden, Germany, December 11–12, 2012.

Baumann, N.
Uranium contents in plant compartments from plants grown on a uranium contaminated site

Domaschke, K.
Self-organizing maps as an alternative for high dimensional data analysis

Dulnee, S.
Interfacial reactions of Sn(II) with mineral surfaces: EXAFS and surface complexation modeling

Dumas, Th.
EXAFS and XANES study of plutonium incorporation in iron minerals

Fischermeier, E.
Metal transport across membranes

Franke, K.
Radiolabeling of engineered nanoparticles – different strategies for Ag^0-NP, TiO_2-NP and Multi-Wall Carbon Nanotubes

Gagell, C.
Microbial investigations in uranium contaminated mine environments

Gückel, K.
Investigation of the neptunium(V) sorption onto gibbsite by means of ATR FT-IR spectroscopy

Hennig, C.
Formation and structure of polynuclear actinide(IV) carboxylates in aqueous solution

Holt, L.
The European fuel performance code TRANSURANUS – Current developments and safety analysis for high burn-up fuel in power reactors

Jordan, N.
Uptake of Se(IV) oxyanions onto maghemite

Kozmenkov, Y.; Rohde, U.
Statistical approach to realistic analysis of large break loss-of-coolant accident in PWR

Kretzschmar, J.
Nuclear Magnetic Resonance spectroscopy @ IRE – Possibilities and limitations

Martin, Ph. (CEA Cadarache, France)
Application of X-ray absorption spectroscopy for nuclear fuel research

Merk, B.
Molten Salt Fast Reactor

Moll, H.
The interaction of the Äspö ground water bacterium Pseudomonas fluorescens with plutonium

Poetsch, M.
Interaction studies of radionuclides with macrocyclic, multifunctional chelate ligands

Rossberg, A.
Another way to gain information from high dimensional data: data mining with self-organizing artificial neural networks

Scheinost, A.C.
ROBL Status Report 2012

Schmeide, K.
Sorption of U(VI) and Np(V) onto diorite from Äspö Hard Rock Laboratory

Steudtner, R.
Uranium chemistry in citric acid solution

Tsushima, S.
Uranyl(VI) chemistry in strong alkaline solution: $UO_2(OH)_5^{3-}$ or $UO_3(OH)_3^{3-}$?

TEACHING ACTIVITIES

Lectures

Bernhard, G.
Radiochemistry
Technische Universität Dresden
Summer term 2012

Environmental chemistry
Technische Universität Dresden
Summer term 2012

Brendler, V.
Radiochemie 2
University of Applied Sciences, Dresden
Summer term 2012

Fahmy, K.
Biophysics
Dresden-International-PhD-Programme (DIPP), Technische Universität Dresden, Winter term 2012/2013

Biophysikalische Methoden
Modul in "Soft Condensed Matter and Biophysics"
Winter term 2012/2013

UV-vis and infrared spectroscopy
BIOTEC-Master-Course, Technische Universität Dresden
Winter term 2012/2013

Kretzschmar. J.
Seminar: "Strukturbestimmung"
Technische Universität Dresden
Summer term 2012

Lippold, H.
Radiochemistry and radiopharmacology – part II: origin, properties and applications of ionising radiation
University of Leipzig
Summer term 2012

Lippold, H.
Radioanalytics
Lecture within the post-graduate course "Analytics and spectroscopy", University of Leipzig
Summer term 2012

Raff, J.
Mikrobiologie
University of Applied Sciences, Dresden
Winter term 2012/2013

Courses

- The laboratory course "Radiochemistry" was provided from August 6th to 10th and from 13th to 17th, 2012, as a part of a module of the chemistry master degree program at the Technische Universität Dresden.

  Advisers:

Dr. Barkleit, A.	Husar, R.	Mickein, K.
Drobot, B.	Kretzschmar, J.	Müller, M.
Fritsch, K.	Lederer, F.	Rumpel, A.
Gagell, C.	Lindner, K.	Schott, J.
Gückel, K.	Lütke, L.	Suhr, M.
Heim, H.	Osman, A.A.A:	Zirnstein, I.

- The IRC provided one experiment "Alpha spectrometric isotope dilution analysis of uranium" of the laboratory course "Instrumental Analysis" held by the Institute for Analytical Chemistry, Technische Universität Dresden, during winter term.

  Advisers:

Winter term 2011-12	*Winter term 2012-13*
Fischer, S.	Fritsch K.
Dr. Foerstendorf, H.	Lindner, K.
Husar, R.	Mickein, K.
Schott, J.	Schott, J.
Suhr, M.	Weiß, S.
Weiß, S.	

- Biophysics course of the Dresden-International-Graduate School
  December 03-07, 2012

  Advisers:

Dr. Fahmy, K.	Philip, J.
Groß, M.	Sayed, A.
Oertel, J.	

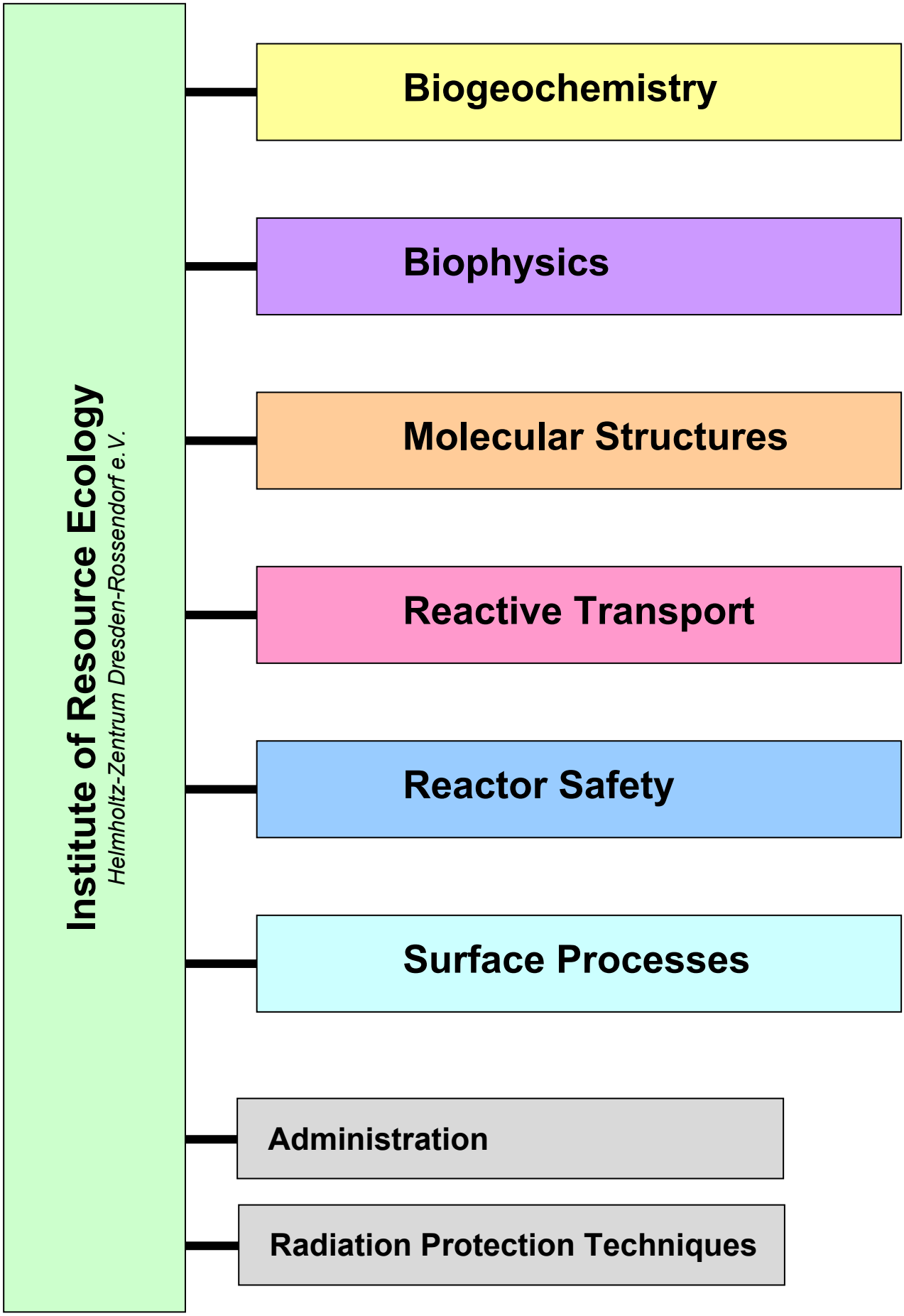
Institute of Resource Ecology
Helmholtz-Zentrum Dresden-Rossendorf e.V.
Biogeochemistry
Biophysics
Molecular Structures
Reactive Transport
Reactor Safety
Surface Processes
Administration
Radiation Protection Techniques

Dr. V. Brendler (Acting director)
Prof. Dr. habil. G. Bernhard

ADMINISTRATION:
Gorzitze, Jana; Mauersberger, Anke; Berndt, Ronny (Sysad)
Glückert, Marion (ESRF); Gerstner, Katrin (FS Leipzig)

RADIATION PROTECTION TECHNIQUES:
Heim, Heidemarie; Falkenberg, Dirk; Henke, Steffen; Hiller, Bernd; Rumpel, Annette

D I V I S I O N S

BIOGEO-CHEMISTRY

Dr. Geipel, Gerhard

Dr. Arnold, Thuro
Dr. Baumann, Nils
Drobot, Björn
Dudek, Monika
Flemming, Katrin
Gagell, Corinna
Dr. Geißler, Andrea
Grambole, Genia
Dr. Großmann, Kay
Dr. Günther, Alix
Dr. Heller, Anne
Heller, Sylvia
Dr. Krawczyk-Bärsch, Evelyn
Lindner, Katja
Lütke, Laura
Dr. Matys, Sabine
Dr. Moll, Henry
Müller, Manuela
Dr. Raff, Johannes
Dr. Sachs, Susanne
Seibt, Jana
Dr. Selenska-Pobell, Sonja
Dr. Vogel, Manja
Zirnstein, Isabel

BIOPHYSICS

Dr. habil. Fahmy, Karim

Abu Shark, Sawsan E.
Bobeth, Caroline
Fischermeier, Elisabeth
Günther, Tobias
Kummer, Ulrike
Lederer, Franziska
Dr. Oertel, Jana
Philipp, Jenny
Sayed, Ahmed M. T.
Suhr, Matthias
Dr. Tsushima, Satoru
Weinert, Ulrike

MOLECULAR STRUCTURES

Dr. habil. Scheinost, Andreas C.

Dr. Banerjee, Dipanjan
Dulnee, Siriwan
Dr. Dumas, Thomas
Exner, Jörg
Fengler, Matthias
Dr. Hennig, Christoph
Dr. Kirsch, Regina
Dr. Rossberg, André

External Ph. D. students
Attia, Enas M. H.
Brockmann, Sina
Müller, Mathias
Müller, Melanie
Obeid, Muhammad H.
Osman, Ahmed. A. A.
Sabau, Andrea

REACTIVE TRANSPORT

Dr. Lippmann-Pipke, Johanna

Bütow, Claudia
Claus, Benjamin
Dr. Franke, Karsten
Gruhne, Stefan
Gründig, Marion
Dr. Hildebrand, Heike
Dr. Kulenkampff, Johannes
Korn, Nico
Dr. Lippold, Holger
Lösel, Dagmar
Dr. Mansel, Alexander
Mickein, Kathleen
Schößler, Claudia
Schymura, Stefan
Zakhnini, Abdelhamid

REACTOR SAFETY

Dr. Kliem, Sören

Dr. Baier, Silvio
Baldova, Daniela
Bilodid, Yurii
Dürigen, Susan
Dr. Ferrari, Anna
Dr. Fridman, Emil
Glivici-Cotruta, Varvara
Gommlich, André
Dr. Grahn, Alexander
Holt, Lars
Hoffmann, Alexander
Dr. Hristov, Hristo V.
Konheiser, Jörg
Kozmenkov, Yaroslav
Litskevich, Dzianis
Dr. Merk, Bruno
Rachamin, Reuven
Dr. Rohde, Ulrich
Dr. Schäfer, Frank
Dr. Tusheva, Polina

SURFACE PROCESSES

Dr. Foerstendorf, Harald (Acting head)

Dr. Barkleit, Astrid
Dr. Bok, Frank
Eckardt, Carola
Fischer, Sarah
Franzen, Carola
Fritsch, Katharina
Gückel, Katharina
Gürtler, Sylvia
Heim, Karsten
Hempel, Diana
Husar, Richard
Dr. Ikeda, Atsushi
Dr. Jordan, Norbert
Joseph, Claudia
Kretzschmar, Jerome
Müller, Christa
Dr. Müller, Katharina
Neubert, Heidrun
Dr. Richter, Anke
Richter, Constanze
Ritter, Aline
Schaefer, Ursula
Dr. Schmeide, Katja
Schott, Juliane
Dr. Steudtner, Robin
Dr. Stockmann, Madlen
Weiß, Stephan
Dr. Zänker, Harald

GUEST SCIENTISTS

Comarmond, M. Josick	*Institute for Environmental Research, Australian Nuclear Science and Technology Organisation, Menai, Australia*
Gordienko, Pavel	*National Research Center "Kurchatov Institute", Moscow, Russia*
Hofinger, Jürgen	*Namos GmbH, Dresden, Germany*
Lehrer, Tamar	*Technion - Israel Institute of Technology Civil and Environmental Engineering Haifa, Israel*
Nikitin, Evgeny	*Institute of Nuclear Techniques, Budapest University of Technology and Economics, Budapest, Hungary*
Radeva, Galina	*Institute of Molecular Biology, Bulgarian Academy of Sciences, Sofia, Bulgaria*
Roos, Steffen	*Namos GmbH, Dresden, Germany*
Sabau, Andrea	*Laboratoire de Radiochimie Sciences Analytiques et Environnement, Université Nice Sophia Antipolis, France*
Smyrek, Anna	*Institute of Waste Disposal, Karlsruhe Institute of Technology, Karlsruhe, Germany*
Solioz, Marc	*Department of Clinical Pharmacology, University of Berne, Berne, Switzerland*
Tiborcz, Livia	*Institute of Nuclear Techniques, Budapest University of Technology and Economics, Budapest, Hungary*
Visnak, Jakub	*Faculty of Nuclear Sciences and Physical Engineering, Czech Technical University, Prague, Czech Republic*
Zavarin, Mavrick	*Lawrence Livermore National Laboratory, Glenn T. Seaborg Institute, Livermore, CA, U.S.A.*

MASTER/DIPLOMA/BACHELOR

Domaschke, Kristin	Kruse, Carsten	Schikora, Johannes
Drechsel, Nancy	Meyer, Ronny	
Gröschel, Annett	Poetsch, Maria	

GRADUATE ASSISTANTS, STUDENT ASSISTANTS, TRAINEES

Bauer, Saskia	Hartenauer, Anne	Kuczera, Mirco	Stoll, Madeleine
Bittner, Lars	Hering, David	Mathys, Nadine	Trepte, Paul
Doll, Katharina	Hevesi, Martin Jens	Mieth, Juliane	Wengrzik, S.
Domaschke, Steffen	Hille, Frank	Peuker, Lisa Christin	Zabelt, Denise
Friebel, Michael	Jäckel, Elisabeth	Pufe, Johanna	Zechel, Susanne
Goretzki, Gudrun	Körner, Paul	Scholl, Susanne	

ACKNOWLEDGEMENTS

The Institute of Resource Ecology is one of the eight institutes of the Helmholtz-Zentrum Dresden-Rossendorf e.V. (HZDR). As registered, non-profit institution, the HZDR is supported by the authorities of the Federal Government and the Free State of Saxony. In addition to the basic funding, the financial support of the projects listed below by the given organizations and companies is greatfully acknowledged.

FUNDING ORGANIZATION / COMPANY	PROJECT TITLE	CONTRACT NO.
Commission of the European Communities (EU)	ACTINET Integrated Infrastructure Initiative (ACTINET-I3)	*232631*
	CROCK Crystalline Rock Retention Processes	*FP7-269658*
	EVOL Evaluation and Viability of Liquid Fuel Fast Reactor Systems	*FP7-249696*
	FREYA Fast Reactor Experiments for hYbrid Applications	*FP7-2696665*
	HEXANE Heavy Elements X-ray Absorption Spectroscopies Network	*230807*
	NURISP Nuclear Reactor Integrated Simulation Project	*232124*
	RECOSY Redox phenomena controlling systems	*212287*
	SARGEN IV Safety Assessment for Reactors of Generation IV	*FP7-295446*
	UMBRELLA Using microbes for the regulation of heavy metal mobility at ecosystem and landscape scale: An integrative approach for soil remediation by geobiological processes	*226870*
Bundesministerium für Wirtschaft und Technologie (BMWi) & Bundesministerium für Bildung und Forschung (BMBF)	Conditioning Grundlegende Untersuchungen zur Immobilisierung langlebiger Radionuklide mittels Einbau in endlagerrelevante Keramiken	*02NUK021B*
	DIL Water Untersuchungen zur Entwicklung neuer Biokompositmaterialien zur Entfernung von Schadstoffen aus Abwässern	*02WA1223*
	ESTRAL-TV2 Verbundprojekt: Realitätsnahe Einbindung von Sorptionsprozessen in Transportprogramme für die Langzeitsicherheitsanalyse	*BMWi 02E10528*
	IMMORAD Grundlegende Untersuchungen zur Immobilisierung langlebiger Radionuklide durch die Wechselwirkung mit endlagerrelevanten Sekundärphasen	*02NUK019D*
	Mikrobielle Diversität im Tongestein (Opalinus-Ton) und Wechselwirkung dominanter Mikroorganismen mit Actiniden	*BMWi 02E10618*
	NanoTrack Untersuchung des Lebenszyklus von Nanopartikeln anhand von [^{45}Ti]TiO_2 und [^{105}Ag]Ag0	*03X0078A*
	Partitioning II Verbundprojekt: Multifunktionelle Komplexbildner mit N, O, S-Donorfunktionen für d- und f-Elemente	*BMBF-FZK 02NUK014B*
	P&T Partitioning and Transmutation	*FKZ: 1501446*

FUNDING ORGANIZATION / COMPANY	PROJECT TITLE	CONTRACT NO.
	Radionuklide in der Umwelt	
	Verbundprojekt: Rückhaltung endlagerrelevanter Radionuklide im natürlichen Tongestein und in salinaren Systemen – Geochemisches Verhalten und Transport von Radionukliden (Np, U, Pu und weitere RN) in salinaren Systemen in Gegenwart endlagerrelevanter Organika	*BMWi 02E10971*
	Strahlung und Umwelt II Verbundprojekt: Radionuklide in der Umwelt, ihr Transport in die Nahrungsketten zum und im Menschen, Teilprojekt F	*BMBF-FZK 02NUK015F*
	VESPA Verbundprojekt: Verhalten langlebiger Spalt- und Aktivierungsprodukte im Nahfeld eines Endlagers und Möglichkeiten ihrer Rückhaltung	*FZK-BMWi 02E10790*
	WEIMAR	*BMWi 02 E 11072B*
	WTZ-Russland- Fluenzberechnungen	*FKZ: 1501403*
Deutsche Forschungsgemeinschaft (DFG)	ATAS Workshop	*STE 2225/1-1*
	Imaging and image simulation of organic target compound migration between different biogeochemical interfaces of a soil horizon using position emission tomography and the lattice Boltzmann equation approach (BIG)	*LI 872/5-1*
	Sorptions- und Redoxreaktionen von SN II und Sn IV an der Magnetite/Wasser-Grenzfläche in An- und Abwesenheit organischer Liganden (Zinn-Redox)	*SCHE 509/3-1*
	Surface processes of Np species on selected mineral oxides. From sorption to precipitation	*MU 3207/1-1*
	Transport von CNP	
Project Management Jülich & BMBF	Nano Track Untersuchung des Lebenszyklus von Nanopartikeln	
	NANOPHARM Neue photokatalytisch aktive Verbundmaterialien zur Eliminierung von pharmazeutischen Reststoffen	*03X0094G*
ANDRA, Paris, France	Pollutant Trapping	*RCOT ASEV 110027*
Bundesamt für Strahlenschutz (BfS)	THEREDA-SZ II Vervollständigung einer Thermodynamischen Standarddatenbasis	*WS 2051-8732-9*
BMBF & DLR	AptaSens Aptamer modifizierte bakterielle Oberflächenstrukturen für die Entwicklung neuer Sensoren	*01RB0805A*
E.ON, Hannover	MCNP Rechnungen	*4500063558/KME/0701*
	Datensatzerstellung Vor-Konvoi-Anlage	*4500047740/KME/0701*
	DYN3D Analyse von Neutronenflussrauschen	*4500081577/KME/0701*
	Entwicklung eines Modells thermo mechanisches Brennstabverhalten	*4570157785/IQ4/0701/NB*

FUNDING ORGANIZATION / COMPANY	PROJECT TITLE	CONTRACT NO.
VGB Powertech	Kopplung Neutronik/ Thermohydraulik für DWR	*SA "AT" 41/09 A*
	Kopplung Neutronik/ Thermohydraulik für SWR (TU Dresden)	*SA "AT" 41/09 C*
TÜV SÜD	Reaktorberechnungen für WWER-1000-Reaktoren	*500601247*
STFI	Textilien S-Layer	
UJV Rez, a.s.	DYN3D für UJV Wartung 2012/2013	*150178*
SAB Förderbank, Dresden, Germany	Spezialanalytik WISMUT	
	SYNCOPE Synergetische Kopplung von Energieträgern für effiziente Prozesse	*100109023*
SCK•CEN, Studiecentrum voor Kernenergie, Brussels, Belgium	Mont Terri BN-experiment ph 17	

INDEX OF AUTHORS